

**FABRICATION, STRUCTURE, AND
ELECTROCHEMICAL PROPERTIES OF
ELECTROSPUN METAL-METAL OXIDE/CARBON
COMPOSITE NANOFIBERS**



**A Thesis Submitted in Partial Fulfillment of the Requirements for the
Degree of Doctor of Philosophy in Physics
Suranaree University of Technology
Academic Year 2016**

การประดิษฐ์ โครงสร้างและสมบัติเคมีไฟฟ้าของเส้นใยนาโนอิเล็กทรอนิกส์ของ
โลหะ-โลหะออกไซด์/คาร์บอนคอมโพสิต



วิทยานิพนธ์นี้เป็นส่วนหนึ่งของการศึกษาตามหลักสูตรปริญญาวิทยาศาสตรดุษฎีบัณฑิต

สาขาวิชาฟิสิกส์

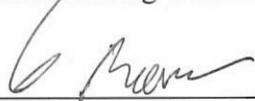
มหาวิทยาลัยเทคโนโลยีสุรนารี

ปีการศึกษา 2559

**FABRICATION, STRUCTURE AND ELECTROCHEMICAL
PROPERTIES OF ELECTROSPUN METAL-METAL
OXIDE/CARBON COMPOSITE NANOFIBERS**

Suranaree University of Technology has approved this thesis submitted in partial fulfillment of the requirements for the Degree of Doctor of Philosophy.

Thesis Examining Committee



(Asst. Prof. Dr. Worawat Meevasana)

Chairperson




(Prof. Dr. Santi Maensiri)

Member (Thesis Advisor)



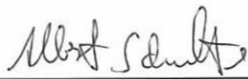
(Asst. Prof. Dr. Montree Sawangphruk)

Member




(Assoc. Prof. Dr. Prayoon Songsiriritthigul)

Member



(Assoc. Prof. Dr. Albert Schulte)

Member



(Prof. Dr. Sukit Limpijumnong)

Vice Rector for Academic Affairs
and Innovation



(Prof. Dr. Santi Maensiri)

Dean of Institute of Science

ชเนศ สิ้นธุ์ประจิม : การประดิษฐ์ โครงสร้าง และสมบัติเคมีไฟฟ้าของเส้นใยนาโนอิเล็กทรอนิกส์
โครงสร้างของโลหะ-โลหะออกไซด์/คาร์บอนคอมโพสิต (FABRICATION,
STRUCTURE AND ELECTROCHEMICAL PROPERTIES OF
ELECTROSPUN METAL-METAL OXIDE/CARBON COMPOSITE NANOFIBERS)
อาจารย์ที่ปรึกษา : ศาสตราจารย์ ดร.สันติ แม่นศิริ, 236 หน้า.

ในงานวิจัยนี้ได้ทำการประดิษฐ์เส้นใยนาโนคาร์บอนและคอมโพสิตของคาร์บอนร่วมกับอนุภาคโลหะและ/หรือโลหะออกไซด์ในกลุ่มของนิกเกิล ซิลเวอร์ และแมงกานีส (CNF, NiO_x/CNF, AgO_x/CNF, MnO_x/CNF, and AgO_x-MnO_x/CNF) โดยเริ่มจากใช้เทคนิคอิเล็กโตรสปินนิ่งสำหรับประดิษฐ์เส้นใยนาโนคอมโพสิตของสารละลายโพลีอะครีโลไนไตรล์ ที่เตรียมในอัตราร้อยละ 10 ร่วมกับสารตั้งต้นของโลหะที่ร้อยละ 20 เทียบกับพอลิเมอร์โดยละลายในไดเมทิลฟอร์มาไมด์ (DMF) จากนั้นนำเส้นใยที่ได้ไปเผา (calcination) เพื่อให้เปลี่ยนเป็นเส้นใยนาโนคาร์บอนและคาร์บอนคอมโพสิตซึ่งประกอบด้วยสามขั้นตอนคือ การเสถียร (stabilization) การคาร์บอนไนเซชัน (carbonization) และแอคติเวชัน (activation) สารตัวอย่างที่เตรียมได้ถูกนำไปตรวจสอบสมบัติทางสัณฐานวิทยา เสถียรภาพทางความร้อน หมู่ฟังก์ชันทางเคมีเชิงพื้นผิว โครงสร้างเชิงผลึก สมบัติความพรุนและสถานะทางเคมี โดยใช้เทคนิคกล้องจุลทรรศน์แบบส่องกราด (SEM) กล้องจุลทรรศน์แบบส่องผ่าน (TEM) การวิเคราะห์เสถียรภาพทางความร้อน (TGA) ฟลูออรีนฟูเรียร์อินฟราเรด (FTIR) การเลี้ยวเบนของรังสีเอกซ์ (XRD) และการดูดกลืนรังสีเอกซ์ (XAS) สมบัติเชิงไฟฟ้าเคมีของขั้วไฟฟ้าที่เตรียมจากวัสดุคอมโพสิตที่ประดิษฐ์ขึ้น ถูกศึกษาโดยสามวิธีคือ โวลแทมเมตรี (CV) การประจุที่กระแสคงที่ (GCD) และอิเล็กโตรเคมีคัลอิมพีแดนซ์สเปกโทรสโกปี (EIS)

เส้นใยนาโนพอลิเมอร์คอมโพสิตที่เตรียมได้มีขนาดเส้นผ่าศูนย์กลางเฉลี่ย 265 ± 643 นาโนเมตรและลดลงประมาณร้อยละ 25 หลังจากเผาเปลี่ยนเป็นคาร์บอน จากการตรวจสอบด้วยเทคนิคการวิเคราะห์ทางความร้อนและรามานสเปกโทรสโกปีพบว่าเส้นใยนาโนคาร์บอนส่วนใหญ่จะประกอบด้วยคาร์บอนอสัณฐานประมาณร้อยละ 80 รวมอยู่กับอีกร้อยละ 20 ของอนุภาคนาโนของสารโลหะที่เสริมเข้าไป ในส่วนการวัดการดูดซับก๊าซไนโตรเจนพบว่า AgO_x-MnO_x/CNF มีพื้นที่ผิวจำเพาะสูงสุดที่ 812 ตารางเมตรต่อกรัม ซึ่งมีค่าเป็นสองเท่าของเส้นใยนาโนคาร์บอนบริสุทธิ์

อันเนื่องมาจากอนุพูนขนาดเล็กจำนวนมากที่มีขนาดเฉลี่ย 0.6-0.9 นาโนเมตร มีปริมาตรสูงถึง 0.36 ลูกบาศก์เซนติเมตรต่อกรัม

การศึกษาสมบัติเชิงเคมีไฟฟ้าของขั้วไฟฟ้าที่ประดิษฐ์จากตัวอย่างที่ได้เตรียมขึ้นพบว่ามีรูปแบบการเก็บประจุสามรูปแบบ รูปแบบแรกคือการเก็บแบบประจุไฟฟ้าสองชั้น (EDLC) โดยสังเกตจากความคล้ายคลึงของกราฟโวลแทมเมตริกซึ่งพบในวัสดุ CNF Ni/CNF และ Ag/CNF และมีค่าการประจุที่ประมาณ 63-130 ฟารัดต่อกรัม ตามลำดับ ส่วนรูปแบบที่สองซึ่งพบในขั้วไฟฟ้า MnO_x/CNF มีเฉพาะค่าการประจุแฝง (pseudocapacitance) จากปฏิกิริยาเคมีของแมงกานีสออกไซด์ที่เสริมเข้าไป มีค่าประมาณ 38 ฟารัดต่อกรัม รูปแบบที่สามสังเกตได้ทั้งใน Ni-NiO/CNF และ AgO_x-MnO_x/CNF คือการร่วมกันระหว่างแบบประจุไฟฟ้าสองชั้นอันเนื่องมาจากพื้นที่ผิวจำเพาะสูงและการประจุแฝงของอนุภาคนาโนของโลหะออกไซด์ ส่งผลให้มีค่าความจุรวมสูงสุดที่ 94-204 ฟารัดต่อกรัม ยิ่งไปกว่านั้นการเสริมเข้าไปของอนุภาคนาโนได้ส่งผลต่อค่าความต้านทานภายใน (ESR) ของตัววัสดุคอมโพสิตอย่างมีนัยสำคัญ ทำให้ได้ค่าความต้านทานอยู่ระหว่าง 237-627 มิลลิโห์ม สมบัติที่น่าสนใจอีกประการคือวัสดุที่ประดิษฐ์ขึ้นสามารถรักษาความสามารถของการคายประจุได้สูงกว่าร้อยละ 80 หลังการทดสอบประจุซ้ำอย่างน้อย 1000 รอบ



สาขาวิชาฟิสิกส์

ปีการศึกษา 2559

ลายมือชื่อนักศึกษา _____

ลายมือชื่ออาจารย์ที่ปรึกษา _____

TANAYT SINPRACHIM : FABRICATION, STRUCTURE AND
ELECTROCHEMICAL PROPERTIES OF ELECTROSPUN METAL-
METAL OXIDE/CARBON COMPOSITE NANOFIBERS. THESIS
ADVISOR : PROF. SANTI MAENSIRI, D.Phil. 236 PP.

CARBON NANOFIBERS/ELECTROSPINNING/MANGANESE OXIDE
/SILVER/ELECTROCHEMICAL/SUPERCAPACITOR

In this study, carbon-based bare and composite nanofibers (i.e., pure CNF, NiO_x/CNF, AgO_x/CNF, MnO_x/CNF, and AgO_x-MnO_x/CNF) were fabricated by electrospinning of 10 wt.% polyacrylonitrile-based (PAN) in DMF and 20 wt.% metal precursors comparing to PAN. The as-spuns were subsequently calcined to obtain as composited CNF using three steps of stabilization, carbonization and activation. The morphology, thermal stability, surface functional chemistry, microstructures, crystallinity, chemical state, and porosity of the samples were investigated by scanning electron microscopy (SEM), transmission electron microscopy (TEM), thermogravimetric analysis (TGA), Fourier-transform infrared spectroscopy (FTIR), Raman spectroscopy, X-ray diffraction (XRD), X-ray absorption spectroscopy (XAS) and Brunauer-Emmett-Teller (BET) techniques. The electrochemical properties of the samples were studied by using cyclic voltammetry (CV), galvanostatic charge-discharge (GCD), and electrochemical impedance spectroscopy (EIS).

The as-spun nanofibers have average diameter sizes between 265-643 nm and ~25% of these sizes were reduced after calcination. TGA and Raman spectroscopy revealed that the most samples consisted of matrix amorphous carbon of around 80% composited with the nanometal reinforcement of around 20%. The measurement of N₂

isotherm of the samples revealed the highest surface area of $812 \text{ m}^2 \text{ g}^{-1}$ for $\text{AgO}_x\text{-MnO}_x/\text{CNF}$ almost two times greater than that the value of bare CNF. This high value was due to the plentiful micropores average sizes of 0.6-0.9 nm yielding the high volume of $0.36 \text{ cm}^3 \text{ g}^{-1}$ in the $\text{AgO}_x\text{-MnO}_x/\text{CNF}$.

The studying of electrochemical properties of the prepared samples revealed that the energy storage mechanism of the electrodes can be divided into three features. Firstly, the bare CNF, Ni/CNF and Ag/CNF presented likely rectangular CV of EDLC behavior with the capacitances of 63-130 F g^{-1} . Secondly, the MnO/CNF electrode displayed mainly pseudocapacitive behavior from the redox reaction of manganese reinforcement with the capacitance of 38 F g^{-1} . Thirdly, both the Ni-NiO/CNF and $\text{AgO}_x\text{-MnO}_x/\text{CNF}$ electrodes stored the charge by a combination of both EDLC forming on high surface area of carbon matrix together and the pseudocapacitive process of metal and/or metal oxides composited in each electrode, showing the high specific capacitance of 94-204 F g^{-1} . Moreover, the internal DC resistances (ESR) of each composite were significantly changed by adding of nanometal reinforcement resulting in the resistance value of $\sim 273\text{-}627 \text{ m}\Omega$. Furthermore, most the electrodes showed the imposing cycling capacity retention more than 80% at 1000 cycles.

School of Physics

Student's Signature _____

Academic Year 2016

Advisor's Signature _____

CONTENTS

	Page
ABSTRACT IN THAI.....	I
ABSTRACT IN ENGLISH	III
ACKNOWLEDGEMENTS.....	V
CONTENTS.....	VI
LIST OF TABLES.....	XI
LIST OF FIGURES.....	XIV
LIST OF ABBREVIATIONS.....	XXVI
 CHAPTER	
I INTRODUCTION.....	1
1.1 Background and motivation.....	1
1.2 Objectives of the research.....	5
1.3 Scope of study.....	6
1.4 Location of the research.....	6
1.5 Anticipated outcomes.....	6
1.6 Outline of thesis.....	7
II LITERATURE REVIEWS.....	8
2.1 Carbon nanofibers.....	8
2.1.1 Precursor of electrospun nanofibers.....	9
2.1.2 Electrospinning process.....	10

CONTENTS (Continued)

	Page
2.1.3 Carbonization and graphitization process.....	15
2.1.4 Activation process.....	20
2.1.5 Application of carbon nanofibers.....	22
2.2 Supercapacitor.....	23
2.2.1 Working principle of capacitor.....	23
2.2.2 Working principle of supercapacitors.....	25
2.2.3 Electrode materials of supercapacitor.....	35
2.3 Theoretical approach and electrochemical study for supercapacitors.....	43
2.3.1 Potentiostat cyclic voltammetry.....	44
2.3.2 Galvanostat charge/discharge testing.....	47
2.3.3 Electrochemical impedance spectroscopy.....	50
III RESEARCH METHODOLOGY.....	54
3.1 Material.....	54
3.2 Apparatus.....	56
3.3 Fabrication of metal-metal oxide carbon-based nanofibers.....	57
3.3.1 Preparation of precursor solutions.....	57
3.3.2 Electrospinning of nanofibers.....	63
3.3.3 Calcination and activation of as-spun nanofibers.....	64
3.4 Material characterizations.....	67
3.4.1 Thermogravimetric analysis.....	67
3.4.2 Scanning electron microscopy.....	67

CONTENTS (Continued)

	Page
3.4.3 Transmission electron microscopy.....	68
3.4.4 Surface area and porosity.....	68
3.4.5 Fourier transform infrared spectroscopy.....	71
3.4.6 Raman spectroscopy.....	71
3.4.7 X-ray diffraction.....	74
3.4.8 X-ray absorption near edge structure.....	75
3.5 Electrochemical property evaluation.....	76
3.5.1 Electrode preparation.....	76
3.5.2 Electrolyte preparation.....	76
3.5.3 Electrochemical cell setup.....	78
3.5.4 Cyclic voltammetry.....	78
3.5.5 Galvanostat charge/discharge testing.....	78
3.5.6 Electrochemical impedance spectroscopy.....	79
IV RESULTS AND DISCUSSION.....	80
4.1 Fabrication of electrospun carbon-based composite nanofibers.....	82
4.1.1 Effect of applied voltage on the morphology of electrospun nanofibers.....	82
4.1.2 Effect of nickel concentration on morphology and microstructure of electrospun nanofibers.....	84
4.2 Characterization and electrochemical properties of nickel clusters composite carbon-based nanofibers (NiO _x /CNF).....	89

CONTENTS (Continued)

	Page
4.2.1 Characterization of CNF, NiO/CNF, Ni/CNF, and Ni-NiO/CNF.....	89
4.2.2 Morphology of CNF, Ni/CNF, NiO/CNF, and Ni-NiO/CNF.....	94
4.2.3 Microstructure of CNF, Ni/CNF, NiO/CNF, and Ni-NiO/CNF.....	96
4.2.4 Surface area and porosity of CNF, Ni/CNF, NiO/CNF, and Ni- NiO/CNF.....	107
4.2.5 Electrochemical properties of CNF, NiO/CNF, Ni/CNF, and Ni- NiO/CNF.....	110
4.3 Characterization and electrochemical properties of silver and/or manganese cluster composite carbon-based nanofibers (AgO _x -MnO _x / CNF).....	129
4.3.1 Fabrication of CNF, AgO _x /CNF, MnO _x /CNF, and AgO _x -MnO _x / CNF.....	129
4.3.2 Characterization of as-spun and calcined pure PAN, AgNO ₃ / PAN, Mn(NO ₃) ₂ /PAN, and AgNO ₃ -Mn(NO ₃) ₂ /PAN.....	130
4.3.3 Electrochemical properties of pure CNF, AgO _x /CNF, MnO _x / CNF, and AgO _x - MnO _x /CNF electrodes.....	155
4.3.4 Effect of calcination temperature on physical and electrochemical properties of AgO _x -MnO _x /CNF.....	179
4.3.5 Effect of electrolyte on electrochemical properties of AgO _x - MnO _x /CNF.....	186

CONTENTS (Continued)

	Page
4.3.6 AgO _x - MnO _x /CNF electrode comparing to the commercial capacitors.....	197
V CONCLUSIONS.....	201
5.1 CNF.....	201
5.2 NiO _x /CNF.....	202
5.3 AgO _x /CNF.....	203
5.4 MnO _x /CNF.....	204
5.5 AgO _x - MnO _x /CNF.....	205
5.6 Suggestion.....	206
REFERENCES.....	207
APPENDIX.....	233
CURRICULUM VITAE.....	236

LIST OF TABLES

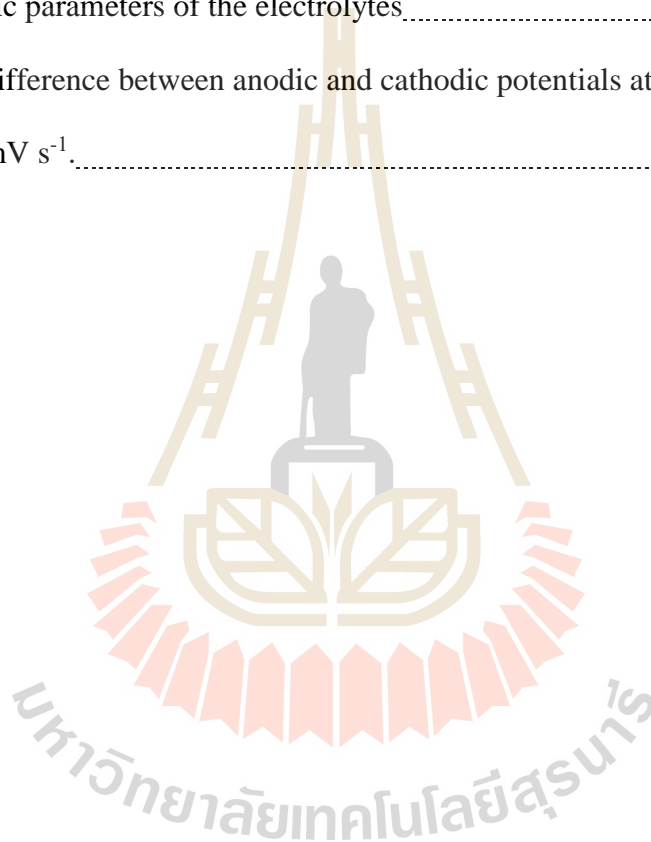
Table	Page
2.1	Variables of the electrospinning process divided into different categories 13
2.2	Current manufacturers of SCs for utility-scale applications 34
2.3	Carbon-based materials used for supercapacitor electrodes 37
2.4	Conductive polymers used for supercapacitor electrode 40
2.5	Case study of metal oxides for supercapacitor electrodes 42
2.6	The impedance of resistor, warburg, and capacitor depending on the value of α 51
2.7	The impedance of equivalent circuit component 52
3.1	List of weight content of raw materials for the preparation of PAN-based solution 62
3.2	List of weight content of raw materials for the preparation of AgNO ₃ -Mn(NO ₃) ₂ /PAN solution 63
3.3	Calcination procedure of each composite 65
3.4	List of materials used for aqueous electrolyte preparation 77
4.1	Average diameter of all fiber and particle size of CNF, AgO _x /CNF, MnO _x /CNF and AgO _x -MnO _x -CNF nanofibers 96
4.2	Structural parameters of the carbon, cubic nickel, and cubic nickel oxide observing from electrospun (a) CNF, (b) NiO/CNF, (c) NiO, (d) Ni/CNF, and (e) Ni-NiO/CNF 99

LIST OF TABLES (Continued)

Table	Page
4.3	Relevant parameters of the peaks fitted to the Raman spectra of the various composited CNF.....107
4.4	The textural parameters of CNF, Ni/CNF, NiO/CNF, and Ni-NiO/CNF, obtained by BET, MP, and BJH method.....109
4.5	Kinetic parameters derived from the Nyquist plots for CNF, NiO/CNF, Ni/CNF and Ni-NiO/CNF electrodes.....128
4.6	Average diameter of all fiber and particle size of AgO _x and MnO _x embedded nanofibers.....136
4.7	The textural parameters of CNF, AgO _x /CNF, MnO _x /CNF, and AgO _x -MnO _x /CNF, obtained by BET, MP, and BJH method.....144
4.8	Relevant parameters of the peaks fitted to the Raman spectra of the various CNF, AgO _x /CNF, MnO _x /CNF, and AgO _x -MnO _x /CNF.....148
4.9	Element chemical states mapping in AgO _x /CNF, MnO _x /CNF, and AgO _x -MnO _x /CNF obtaining from linear combination fitting.....154
4.10	Comparison of specific capacitance and cycle life of composite CNF-based related to MnO _x All values are measured using the three-electrode system.....171
4.11	Kinetic parameters derived from the Nyquist plots for CNF, AgO _x /CNF, MnO _x /CNF, and AgO _x -MnO _x /CNF electrodes.....174
4.12	The textural parameter of AgO _x -MnO _x /CNF calcined at 500, 700, and 900 °C.....180

LIST OF TABLES (Continued)

Table	Page
4.13 Structural parameters of the carbon, cubic Ag, and spinel Mn ₃ O ₄ observing from electrospun AgO _x - MnO _x /CNF prepared at different calcination temperatures of 500, 700, and 900 °C.....	183
4.14 Kinetic parameters of the electrolytes.....	189
4.15 The difference between anodic and cathodic potentials at small scan rate of 2 mV s ⁻¹	194



LIST OF FIGURES

Figure	Page
1.1 Sketch of Ragone plot of various energy storage and conversion devices. The indicated areas are rough guidelines.....	2
2.1 Fibrous carbon materials in different sizes.....	9
2.2 Schematic diagram of electrospinning system.....	11
2.3 Various strategies used to prepare the electrospun composite nanofibers.....	14
2.4 A schematic shows the various models of oxidization of PAN.....	16
2.5 A schematic shows the thermal chemistry of PAN carbonization which involves dehydrogenation and denitrogenation eventually leading to partially graphitic structures.....	17
2.6 Model for a crystallite of a carbon material (a) stack of layers and structure of an individual layer with difference size of p.....	20
2.7 Schematic diagram of a conventional capacitor.....	24
2.8 Representation of a supercapacitor. An illustration of the potential drop at the electrode, electrolyte interface, and equivalent circuit model for a supercapacitor.....	27
2.9 Taxonomy of electrochemical capacitors (modified from.....)	28
2.10 (a) The Helmholtz and (b) Stern model of the electrical double layer formed at an interface in aqueous electrolyte. IHP refers to the distance of the closest approach of ions and OHP refers to that of nonspecifically adsorbed ions.....	30

LIST OF FIGURES (Continued)

Figure	Page
2.11	Cyclic voltammograms of the samples at a scan rate of 20 mVs^{-1}36
2.12	Cyclic voltammogram of a PEDOT nanofiber mat in EMIBF ₄ .(mPEDOT) = 2.0 mg, scan rate $v = 5 \text{ mVs}^{-1}$ 41
2.13	CV curves of (a) NiO/CA nanofibers at different scan rates of 5, 10 and 20 mV s^{-1} , calcined at $500 \text{ }^{\circ}\text{C}$, in 6.0 M KOH solution, (b) NiO, NiO/CA at the scan rates of 5 mV s^{-1} , calcined at $500 \text{ }^{\circ}\text{C}$, in 6.0 M KOH solution, and (c) NiO/CA nanofibers at the 1st and 300th cycles at the scan rates of 5 mV s^{-1} , calcined at $500 \text{ }^{\circ}\text{C}$, in 6.0 M KOH solution 41
2.14	Cyclic voltammetry potential waveform..... 45
2.15	Typical cyclic voltammogram of EDLC..... 46
2.16	Typical cyclic voltammogram of electrode with chemical redox reaction.... 46
2.17	The charge/discharge constant current for galvanostat method..... 48
2.18	Typical charge/discharge profile with the presence of self-discharge..... 48
2.19	A schematic comparison of charge and discharge behavior for an ideal capacitor and battery..... 49
2.20	Nyquist plot of (a) an ideal electrical EDLC and (b) an ideal pseudocapacitor..... 53
2.21	(a) Nyquist plot of a CPE for different values of α , (b) Nyquist plot of a pseudocapacitor including a CPE instead of C_{dl} 53
3.1	Schematic representation of composite CNF fabrication process and experimental apparatus..... 54

LIST OF FIGURES (Continued)

Figure	Page
3.2	(a) The SP04-electrospinning system for electrospun composite nanofibers fabrication and (b) the rotating drum collector.....57
3.3	Diagram showing the preparation of pure PAN solution.....59
3.4	Diagram showing the preparation of the composite precursor solution.....60
3.5	Diagram showing the preparation of AgNO ₃ -Mn(NO ₃) ₂ /PAN precursor solution.....61
3.6	Diagram showing the electrospinning setup.....64
3.7	(a) Diagram showing the typical calcination process consisting of three steps, including stabilization, carbonization, and activation. (b) The expected composite carbon nanofibers after calcination.....66
3.8	Instrumentation setup of sample calcination.....67
3.9	Type of sorption isotherms and hysteresis loops.....69
3.10	Schematic diagram of the principle of Raman scattering: (a) inelastic scattering of an optical quantum hitting the materials; (b) term diagram; (c) Raman spectra. Because the vibration of atoms in the excited state is much less than that of the ground state atoms, the Stokes line is stronger than the anti-Stokes line73
3.11	Diagram represents the principles of XRD.....74
3.12	Schematic representation of a working electrode preparation.....76
3.13	Three-electrode electrochemical cell setup. Reference electrode (RE) is Ag/AgCl, counter electrode (CE) is platinum wire, and working electrode (WE) are prepared from the fabricated samples.....79

LIST OF FIGURES (Continued)

Figure	Page
3.14 Electrochemical experiment setup. Inset: Three-electrode electrochemical cell setup. Reference electrode (RE) is Ag/AgCl, counter electrode (CE) is platinum wire, and working electrode (WE) are prepared from the fabricated samples.....	79
4.1 (a) The electrospun nanofibers sheet on aluminum foil, (b) it was cut as a dimension of around 1.5×4 cm before putting in the crucible for calcination, and (c) the sample after calcination.....	82
4.2 SEM images of Ni(NO ₃) ₂ /PAN (5 wt.%) electrospun at various applied voltages of (a) 8 kV, (b) 10 kV, (c) 12 kV, and (d) 14 kV. The histograms on the right-hand side show the average size distribution of each condition (TCD:18 cm; flow rate:0.5 ml h ⁻¹).....	83
4.3 Average diameter of the as-spun Ni(NO ₃) ₂ -5%/PAN at the various applied voltages of 8, 10, 12, and 14 kV (TCD: 18 cm; flow rate: 0.5 ml h ⁻¹).....	84
4.4 SEM images of as-spun Ni(NO ₃) ₂ /PAN fabricated using voltage of 12 kV at the various Ni(NO ₃) ₂ concentrations of (a) 0, (b) 5, (c) 10, and (d) 20 wt.%. The histograms on right-hand side show the average size distribution of each species (the samples were spun using a flow rate of 0.5 ml h ⁻¹ and TCD of 18 cm).....	86
4.5 SEM images of NiO _x /CNF calcined at 900 °C the with the various Ni(NO ₃) ₂ precursor concentrations of (a) 0, (b) 5, (c) 10, and (d) 20 wt.%. Right-hand, the histogram of the average size of each species.....	87

LIST OF FIGURES (Continued)

Figure	Page
4.6	Average diameter of the as-spun and calcined Ni(NO ₃) ₂ /PAN at the various Ni(NO ₃) ₂ concentrations of 0, 5, 10, and 20 wt.% comparing to PAN (applied voltage: 12 kV; flow rate: 0.05 ml h ⁻¹ ; TCD: 10 cm).88
4.7	(a) TGA and (b) DSC curves of as-spun PAN nanofibers reinforced with different Ni(NO ₃) ₂ concentrations of 0, 5, 10, and 20 %. The TGA-DSC analysis was carried out in N ₂ atmosphere (heating rate: 10 °C min ⁻¹ ; flow rate: 100 ml min ⁻¹).92
4.8	(a) TGA of CNF, Ni/CNF, NiO/CNF, and Ni-NiO/CNF carried out in an air atmosphere, the temperature ranged from 25-1000 °C, and a heating rate of 10 °C min ⁻¹ . (b) The plot of carbon and non-carbon content determined from TGA of various composite CNF.93
4.9	SEM images of (a) as-spun Ni(NO ₃) ₂ /PAN (20 wt.%) and (b) calcined samples. (c) TEM images of the calcined sample.94
4.10	A schematic crystal structure of the cubic (a) Ni and (b) NiO97
4.11	XRD patterns of CNF (500 °C in argon), NiO/CNF (500 °C in air+argon), NiO (500 °C in air), Ni/CNF (500 °C in argon → 900 °C in argon), and Ni-NiO/CNF (500 °C in air+argon → 900 °C in argon atmosphere).98
4.12	(a) Ni K-edge XANES of as-spun Ni(NO ₃) ₂ /PAN, NiO, and Ni foil. (b-d) Ni chemical mapping of each sample using Linear combination fitting.101
4.13	FTIR spectra of as-spun PAN, Ni(NO ₃) ₂ /PAN and the calcined samples.104

LIST OF FIGURES (Continued)

Figure	Page
4.14 Raman spectra of CNF (500 °C in argon), NiO/CNF (500 °C in air+argon), Ni/CNF (500→900 °C in argon), and Ni-NiO/CNF (500 °C in air+argon → 900 °C in argon). The dash lines are Gaussian fitting.....	106
4.15 (a) N ₂ adsorption and desorption isotherm (solid line (ADS) and dash line (DES)), (b) micropore distribution by MP plot, and (inset) mesopore distribution from BJH plot of CNF, Ni/CNF, NiO/CNF, and Ni-NiO/CNF.....	108
4.16 Cyclic voltammograms of (a) CNF, (b) Ni/CNF, (c) NiO/CNF, (d) Ni-NiO/CNF, and (e) specific capacitance as a function of scan rate	112
4.17 Cyclic voltammograms of (a) CNF, (b) Ni/CNF, (c) NiO/CNF, (d) Ni-NiO/CNF measuring for different potential windows of 1.0, 1.2, 1.4, and 1.5 V at scan rate of 20 mV s ⁻¹	115
4.18 (a) Specific capacitance and (b) energy density of CNF, Ni/CNF, NiO/CNF, and Ni-NiO/CNF at different applied potential windows.....	117
4.19 The linear voltage-time profiles of GCD measurement of (a) CNF, (b) Ni/CNF, (c) NiO/CNF, and (d) Ni-NiO/CNF as the function of current.....	119
4.20 (a) Discharged specific capacitance and (b) IR-drop of CNF, Ni/CNF, NiO/CNF, and Ni-NiO/CNF as a function of current density.....	121

LIST OF FIGURES (Continued)

Figure	Page
4.21 (a) A Ragone plot comparing between energy and power density of each electrode varying the discharge current density of 0.5, 1, 2, 5, and 10 A g ⁻¹ . (b) Cycling stability at a current density of 5 A g ⁻¹ for up to 1000 cycles.....	123
4.22 Charge/discharge profile at -1-0 V at various cycles of 2nd, 10th, 100th, 500th, and 1000th of (a) CNF, (b) NiO/CNF, (c) Ni/CNF, and (d) NiO/CNF electrode, insets presented typical continued cycling.....	124
4.23 Nyquist plot and an equivalent circuit of (a – d) CNF, NiO/CNF, Ni/CNF, and Ni-NiO/CNF at a perturbation amplitude of 0.1 V. (e – h) Enlarged picture of each sample at high-frequency region.....	126
4.24 (a) Capacitance as a function of frequency. (b) The imaginary part in impedance of all electrodes.....	127
4.25 (a) TGA and (b) DSC curves of as-spun PAN, AgNO ₃ /PAN, Mn(NO ₃) ₂ /PAN, and AN/AgNO ₃ -Mn(NO ₃) ₂	132
4.26 (a) TGA of CNF, AgO _x /CNF, MnO _x /CNF, and AgO _x - MnO _x /CNF carried out at the temperature ranged from 25-1000 °C in an air atmosphere and a heating rate of 10 °C min ⁻¹ . (b) The plot of carbon and non-carbon content determined from TGA of various composite CNF.....	134
4.27 SEM images of as-spun (a,e) PAN, (b,f) AgNO ₃ /PAN, (c,g) Mn(NO ₃) ₂ /PAN, and (d,h) AgNO ₃ -Mn(NO ₃) ₂ /PAN (flow rate: 0.35 ml h ⁻¹ , TDC: 18 cm, applied voltage: 12 kV).....	137

LIST OF FIGURES (Continued)

Figure	Page
4.28 SEM images of (a,e) CNF, (b,f) AgO _x /CNF, (c,g) MnO _x /CNF, and (d,h) AgO _x - MnO _x /CNF.....	138
4.29 TEM images of (a) CNF, (b) AgO _x /CNF, (c) MnO _x /CNF, and (d) AgO _x - MnO _x /CNF. Figures e, f, g, and h are a high magnification of each sample.....	139
4.30 (a) N ₂ adsorption and desorption isotherm (solid line (ADS) and dash line (DES)), (b) Micropore distribution by MP plot, and (inset) Mesopore distribution from BJH plot of CNF, AgO _x /CNF, MnO _x /CNF, and AgO _x - MnO _x /CNF.....	142
4.31 Schematic represents the textural carbon structure and the reinforcement of (a) CNF, (b) AgO _x /CNF or AgO _x -MnO _x /CNF, and (c) MnO _x /CNF.....	143
4.32 (a) FTIR spectra of as-spun PAN, Mn(NO ₃) ₂ /PAN, Ag NO ₃ /PAN, and AgNO ₃ -Mn(NO ₃) ₂ /PAN and (b) CNF, AgO _x /CNF, MnO _x /CNF, and AgO _x - MnO _x /CNF.....	146
4.33 Raman shift of CNF, AgO _x /CNF, MnO _x /CNF, and AgO _x - MnO _x /CNF.....	148
4.34 A schematic picture of the (a) cubic and (b) spinel structure; star means the intermediary cation sites that denote considerable cation disorder.....	149
4.35 XRD patterns of CNF, AgO _x /CNF, MnO _x /CNF, and AgO _x - MnO _x /CNF....	150
4.36 (a) Ag L3-edge XANES of the as-prepared samples and various oxide compounds. (b) Ag chemical mapping of the nanofibers using Linear combination fitting.....	152

LIST OF FIGURES (Continued)

Figure	Page
4.37 (a) Mn K-edge XANES of the as-prepared samples and various oxide compounds. (b) Mn chemical mapping of the nanofibers using Linear combination fitting.....	153
4.38 Cyclic voltammograms of (a) CNF, (b) AgO _x /CNF, (c) MnO _x /CNF, and (d) AgO _x - MnO _x /CNF as the function of scan rate.....	159
4.39 Cyclic voltammograms of CNF, AgO _x /CNF, MnO _x /CNF, and AgO _x -MnO _x /CNF at (a) 500, (b) 20, and (d) 2 mV s ⁻¹ . (d) The specific capacitance as the function of scan rate.....	160
4.40 (A) Specific capacitance normalized by BET surface area and average pore size for carbon. Drawing of solvated ions residing in pores structure (B) greater than 2 nm, (C) between 1 and 2 nm, and (D) less than 1 nm	163
4.41 A schematic represents the capacitive mechanism of the composite carbon nanofibers of this work in three scan rate regions of (a) low ($v < 10 \text{ mV s}^{-1}$), (b) mid ($10 \text{ mVs}^{-1} < v < 100 \text{ mV s}^{-1}$), and (c) high ($v > 100 \text{ mV s}^{-1}$) scan rate.....	164
4.42 The linear voltage-time profiles of GCD measurement of (a) CNF, (b) AgO _x /CNF, (c) MnO _x /CNF, and (d) AgO _x - MnO _x /CNF as the function of current density.....	166
4.43 (a) The comparison of linear voltage-time profiles of CNF, AgO _x /CNF, MnO _x /CNF, and AgO _x - MnO _x /CNF at a current density of 10 A g ⁻¹ . (b) The specific capacitance as the function of current density.....	167

LIST OF FIGURES (Continued)

Figure	Page
4.44	Charge/discharge profile at -1-0 V at various cycles of 2nd, 10th, 100th, 500th, and 1000th of (a) CNF, (b) AgO _x /CNF, (c) MnO _x /CNF, and (d) AgO _x - MnO _x /CNF electrode, insets presented typical continued cycling. 169
4.45	(a) A Ragone plot for CNF, AgO _x /CNF, MnO _x /CNF, and AgO _x - MnO _x /CNF varying the discharge current density of 0.5, 1, 2, 5, and 10 A g ⁻¹ . (b) Cycling stability at a current density of 5 A g ⁻¹ for up to 1000 cycles. 170
4.46	(a) Nyquist plot of all electrodes at a perturbation amplitude of 0.1 V and (b) enlarged spectra at high frequency (inset is the equivalent circuit using for impedance fitting). 175
4.47	The relationship between pore features and impedance curves obtaining from EIS 177
4.48	(a) Capacitance as a function of frequency. (b) The imaginary part in impedance of all electrodes. 178
4.49	N ₂ adsorption/desorption isotherm of AgO _x - MnO _x /CNF calcined at 500, 700, and 900 °C. 180
4.50	(a) XRD patterns and TEM pictures of AgO _x - MnO _x /CNF prepared at different calcination temperature of (b) 500, (c) 700, and (d) 900 °C. 182
4.51	Cyclic voltammograms of the AgO _x - MnO _x /CNFs which were calcined at differences temperature of 500, 700, and 900 °C. 185
4.52	The specific capacitance as the function of scan rate of AgO _x - MnO _x /CNF calcined at difference temperature of 500, 700, and 900 °C. 186

LIST OF FIGURES (Continued)

Figure	Page
4.53 (a-d) CV profiles of AgO _x - MnO _x /CNF electrode in the different electrolytes as scan rate range between 2-500 mV s ⁻¹ . (e-g) Comparison of CV profiles at high, mid, and small scan rate.	190
4.54 Specific capacitance of AgO _x - MnO _x /CNF electrode measured in different electrolytes as the function of scan rate.	192
4.55 (a-c) CV profiles of AgO _x - MnO _x /CNF electrode in the difference KOH molarities as the scan rate range between 2-500 mV s ⁻¹ . (d-f) Comparison of CV profile at high, mid, and small scan rate.	195
4.56 Specific capacitance of AgO _x - MnO _x /CNF electrode measured in different molar of KOH as the function of scan rate.	197
4.57 (a) Pressed- AgO _x - MnO _x /CNF nickel foam for the supercapacitor electrode. (B) A schematic represented a manufacturing of two-electrode AgO _x - MnO _x /CNF supercapacitor.	199
4.58 CV of AgO _x - MnO _x /CNF supercapacitor measured compared to commercial products.	200

LIST OF ABBREVIATIONS

ADS	=	Adsorption isotherm
BET	=	Brunauer-Emmett-Teller method
BJH	=	Barrett-Joyner-Halenda method
CF	=	Carbon fiber
CNF	=	Carbon nanofibers
CNT	=	Carbon nanotubes
CV	=	Cyclic voltammetry
DES	=	Desorption isotherm
DMF	=	N, N-dimethylformamide
DSC	=	Differentiate scanning calorimetry
EDLC	=	Electrical double layer capacitor
EIS	=	Electrochemical impedance spectroscopy
FE-SEM	=	Field emission scanning electron microscopy
GCD	=	Galvanostatic charge/discharge
GDL	=	Gas diffusion layer
IUPAC	=	The International Union of Pure and Applied Chemistry
MO	=	Metal oxide
MP	=	Micropore
PAN	=	Polyacrylonitrile
PEO	=	Polyethylene Oxide

LIST OF ABBREVIATIONS (Continued)

PVA	=	Poly (vinyl alcohol)
PVDF	=	Poly (vinylidene fluoride)
PVP	=	polyvinyl alcohol
SC	=	Supercapacitor
SEM	=	Scanning electron microscopy
TCD	=	Tip-Collector-Distance
TEM	=	Transmission electron microscopy
TGA	=	Thermogravimetric analysis
XANES	=	X-ray near edge structure
XRD	=	X-ray diffraction

CHAPTER I

INTRODUCTION

1.1 Background and motivation

The exponential growth of human activities has caused more and more energy consumption around the world. It is hard to find new energy resources to meet the infinite demand. Moreover, daily life now relies on such electronic devices as smart phones, wireless computers, survey instruments, medical devices, and even electronic vehicles (Crabtree and Lewis, 2007). Therefore, the challenge is how to produce more energy or to recharge new energy of these storage devices in only a short time. The functional uses of these devices can be described by a Ragone plot as shown in Figure 1.1. Batteries and capacitors have long been used as conventional energy storage devices. The process of charging or discharging a battery always takes a long time in comparison with other devices, for example, capacitors can only store a small amount of energy. This limitation hinders the development of portable electronic devices. In order to fill this gap, scientists have turned to new electronics devices, such as supercapacitors, fuel cells, etc. After several decades of research, supercapacitors have now become impressive devices, and they occupy the largest area of the Ragone plot by showing high energy and power density simultaneously. While the energy density of supercapacitors is much higher than conventional dielectric capacitors, it is still less than that of batteries and fuel cells. Most of the available commercial supercapacitors have specific energy densities of less than 10 Wh kg^{-1} , which is 3 to 15 times smaller than that of batteries (150 Wh kg^{-1} is possible for lithium-ion batteries). Thus, there

has been a strong research interest in increasing the energy performance of supercapacitors to bring them close to or even greater than the capacity of batteries (Zhang and Zhao, 2009). In particular, the most important aspects for the development of electric energy storage devices is how to increase energy density, power density, lifetime, and to make greater savings in costs. In order to produce high-performance devices, it is necessary to use new technology.

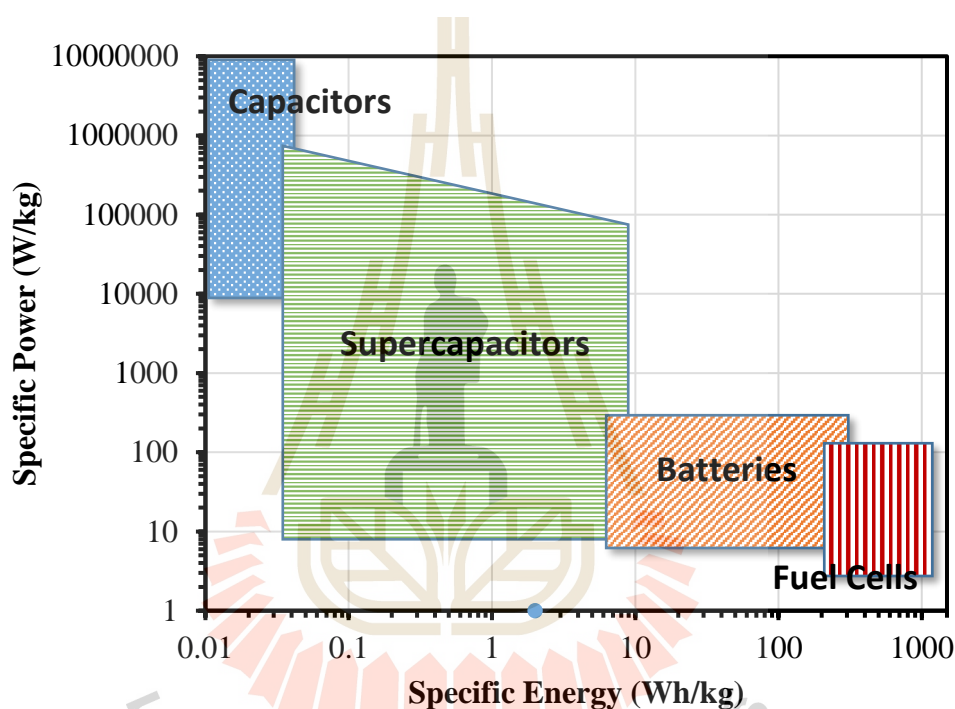


Figure 1.1 Sketch of Ragone plot of various energy storage and conversion devices. The indicated areas are rough guidelines (Kötz and Carlen, 2000).

For example, carbon-based nanofibers (CNF) are an impressive choice and have been widely studied for the technological advancement of energy storage devices. They are attractive materials because of their high specific surface area of up to 2000 $\text{m}^2 \text{g}^{-1}$, high porosity, light weight and high stability. Porous carbon provides capacitance in excess of 200 F g^{-1} , and an operating potential of up to 1.2 V. The capacitive mechanism is provided mainly by electrical double layer capacitance

resulting in high power density (Kim *et al.*, 2009). Furthermore, the transition metal oxides embedding carbon nanofibers have been specifically considered for the application of electrolytic energy storage devices because they possess both high pseudocapacitance from the chemical redox reaction and double layer capacitance at the same time. For example, the composite CNF reinforced with various metal oxides, such as cobalt-manganese oxide, nickel oxide, vanadium oxide, copper oxide, titanium dioxide, and ruthenium oxide have been reported as promising materials (Zhang *et al.*, 2009; Kim *et al.*, 2013; Zhao *et al.*, 2011). The CNF-based materials can be manufactured by several techniques, such as chemical vapor deposition (CVD) (Thakur *et al.*, 2009), template synthesis (Han and Hyeon, 1999), self-assembly (Fleaca and Le Normand, 2014), phase separation (Zhang and Hsieh, 2009), and electrospinning (Kidkhunthod *et al.*, 2016; Chronakis, 2005). Among these techniques, electrospinning has been recognized as an efficient technique for CNF preparation, as the fibrous size can be controlled and it is easy to add reinforcement. The polymer sources such as polyacrylonitrile (PAN), polyvinylpyrrolidone (PVP) and polyaniline (PANI), etc. have been employed as the carbon precursors. They were prepared as a solution and converted into nanofibers by electrostatic force. With a strong electric field between a steel nozzle and a conductive drum which induces them to move along an electric field and to collect on the drum and form a non-woven mat of electrospun nanofibers. The mat can be calcined into composite CNF by heat treatment including stabilization and carbonization in an atmosphere of inert gasses, such as argon (Qing and Sigmund, 2014) or nitrogen (Zussman *et al.*, 2005). Moreover, the specific surface area of CNF can be improved by an activation process with different reactive effects, such as KOH (Yoon *et al.*, 2004), steam (Kim *et al.*, 2004) and CO₂ (Tavanai *et al.*,

2009). The electrospun CNF obtained displayed typical diameters of a few hundred nanometers up to several microns (Gu *et al.*, 2005), soft and flexible (Kim *et al.*, 2011). In addition, the electrospun CNF matrix which was reinforced by a transition metal oxide also expresses surprising textural, electrical, and electrochemical properties. These remarkable characteristics of CNF are useful for various applications (Huang *et al.*, 2003). Among these, metal oxide composite CNF has been used and play an important role in the electrode active materials of electrical energy storage devices, such as fuel cells, batteries, capacitors, solar cells, and especially for supercapacitors (SC). It provides high supercapacitor performance by combining both an electrical double layer capacitor (EDLC) and pseudocapacitance.

In this work, we have focused on the electrode materials of a supercapacitor in the form of a composite of three components: metal, metal oxide, and carbon nanofibers. First, metal is a good conductive material, which should improve the conductivity of its host. Second, metal oxide always presents higher capacitance (pseudocapacitance) than carbon or polymer-based electrodes because of its redox reaction. However, the redox reaction could harm some structures resulting in a shorter lifetime of the device. Finally, carbon nanofibers play an important role in electrode materials because of their attributes of a high surface area and high porosity. In this research, the fabrication, structure, and electrochemical properties of the electrospun metal-metal oxide-carbon composite nanofibers are investigated. The fabricated composite nanofibers are characterized by various techniques, including thermogravimetric analysis (TGA), differential scanning calorimetric method (DSC), scanning electron microscopy (SEM), transmission electron microscopy (TEM), X-ray diffraction (XRD), Fourier transform infrared spectroscopy (FTIR), Fourier transform

Raman spectroscopy (FT-Raman), X-ray absorption spectroscopy (XAS), the Brunauer–Emmett–Teller method (BET), cyclic voltammetry (CV), galvanostatic charge/discharge testing (GCD) and electrochemical impedance spectroscopy (EIS). The effects of metal and metal oxide phases on the electrochemical properties of the fabricated composite nanofibers are investigated and discussed.

1.2 Objectives of the research

1.2.1 To fabricate carbon nanofibers (CNF) and carbon nanofibers composited with metal and metal oxide, such as CNF, M/CNF, MO/CNF and M-MO/CNF (M = Ni, Ag, and Mn) by the electrospinning technique.

1.2.2 To study the effects of temperature and gas atmosphere on the structure and phase composition of carbon-based composite nanofibers.

1.2.3 To characterize the fabricated carbon-based composite nanofibers by TGA, DSC, SEM, TEM, XRD, FTIR, Raman spectroscopy, XAS, and the BET method.

1.2.4 To study the electrochemical performance of the fabricated carbon-based composite nanofibers using CV, GCD, and EIS techniques and compare to the other works.

1.3 Scope of study

1.3.1 This work focuses on the fabrication of carbon-based composite nanofibers reinforced with three species of transition metal: NiO_x; MnO_x; and AgO_x compared to pristine CNF.

1.3.2 The polymer source is fixed at 10 wt.%, while the metal sources are varied at 0, 5, 10, 20, and 40 (for CNF/AgO_x-MnO_x) wt.% compared to polymer content.

1.3.3 The morphology, the microstructure, and the electrochemical performance of the fabricated carbon-based composite nanofibers are compared.

1.3.4 The effect of the calcination temperature on the physical and electrochemical properties was only observed for CNF/AgO_x-MnO_x.

1.4 Location of the research

Advanced Materials Physics Laboratory (AMP), School of Physics, Institute of Science, Suranaree University of Technology, Nakhon Ratchasima, Thailand

1.5 Anticipated outcomes

1.5.1 Acquirement of skills in the fabrication of electrospun carbon-based composite nanofibers of pristine CNF, CNF/NiO_x, CNF/MnO_x, CNF/AgO_x, and CNF/AgO_x-MnO_x.

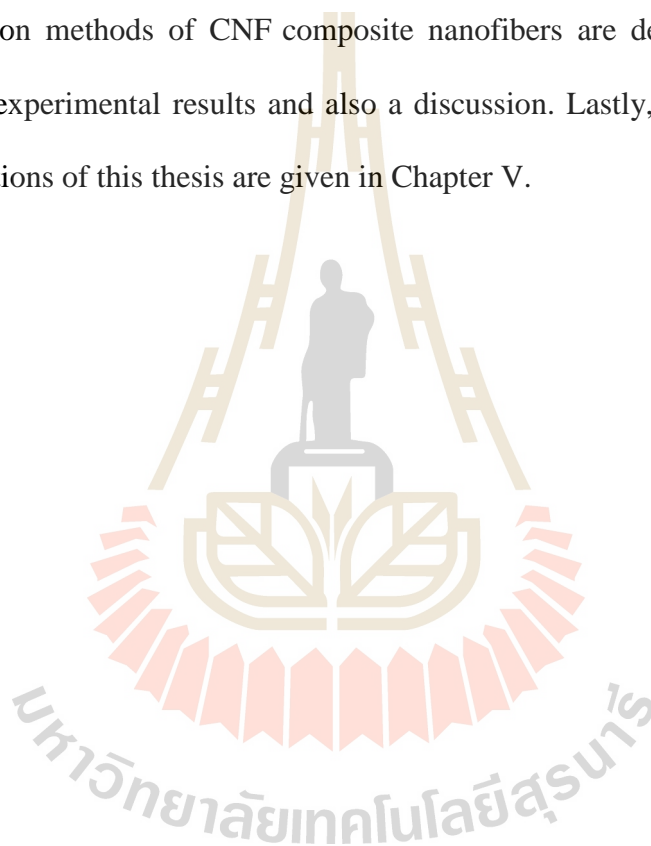
1.5.2 Skills in the characterization of electrospun carbon-based composite nanofibers.

1.5.3 Understanding of the electrochemical performance of the electrospun carbon-based composite nanofibers.

1.5.4 Publications in International ISI journals.

1.6 Outline of thesis

This thesis is divided into five chapters. The first chapter is the introduction of the thesis. Chapter II describes a brief literature review of information concerning the structure, synthesis method, and potential applications of carbon-based materials, CNF. Furthermore, the theory approach concerning the physical and electrochemical properties are also described in this section. Chapter III, the preparation and characterization methods of CNF composite nanofibers are described. Chapter IV presents the experimental results and also a discussion. Lastly, the conclusions and recommendations of this thesis are given in Chapter V.



CHAPTER II

LITERATURE REVIEWS

2.1 Carbon nanofibers

Recently, fibrous carbon materials have been attracting the attention of scientists and engineers. In the 1960s, carbon fibers were developed as an important material for modern science and technology, and they were produced from various carbon precursors via a melt-spinning process. Among the many material precursors, Polyacrylonitrile (PAN) has been used as the principal precursor, associated with various modifications in processing, such as the use of some additives, oxidative stabilization of as-spun PAN fibers at a low temperature, and stretching during stabilization and carbonization. Isotropic pitches, anisotropic mesostructure pitches and phenolic resins have also been the predecessors of carbon fibers. The catalytic chemical vapor deposition process has also produced carbon fibers (vapor-grown carbon fiber, VGCF) (Endo *et al.*, 1999), which are different in structure and properties from those produced via melt-spinning. In the center of VGCFs, thin tubes consisting of straight carbon layers were found, which were later reported to be produced by arc-discharging and were named carbon nanotubes (CNT). The diameters of fibrous carbon materials are in the nanometer range, such as 7 nm for single-walled CNT, compared to the diameters of carbon fibers, which are often a few micrometers. Fibrous carbon materials with diameters in the range of 10^1 – 10^3 nm, i.e. intermediate between carbon nanotubes and carbon fibers are shown in Figure 2.1 , called “carbon nanofibers

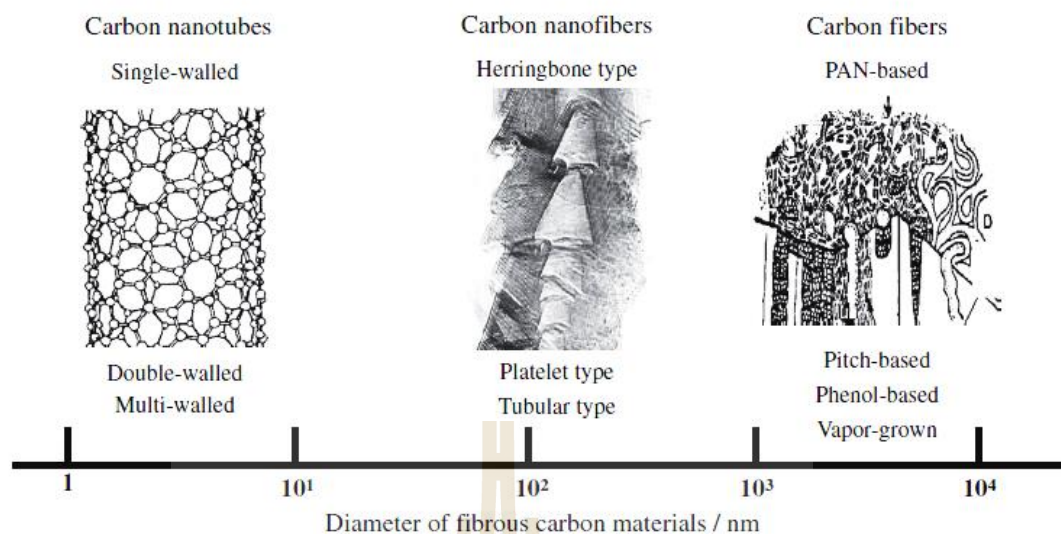


Figure 2.1 Fibrous carbon materials in different sizes (Inagaki *et al.*, 2013).

2.1.1 Precursor of electrospun nanofibers

The majority of carbon materials are usually produced from carbon-rich organic precursors by heat treatment in an inert gas atmosphere which process is known as carbonization. The ultimate properties of this carbon are dependent on a number of critical factors, such as the carbon precursor, its dominant condensation state during carbonization, processing conditions, and the structural and textural properties of the products (Inagaki and Radovic, 2002). The polymer precursors such as polyacrylonitrile (PAN), polyvinylpyrrolidone (PVP), polyvinylidene fluoride (PVDF), polyethylene (PE), PVA (poly(vinyl alcohol)) or poly(methylmethacrylate) (PMMA) polymers are commonly used to fabricate carbon materials (Inagaki *et al.*, 2004). Among these precursors, PAN, containing 68% carbon, is currently the most widely used precursor for carbon nanofibers. PAN is commercially obtained by suspension or an aqueous dispersion polymerization process, in the presence of catalysts, such as ferric cation, anion persulfate and bisulfite. The polymerization occurs when the formation of a complete polymeric molecule rising from an

acrylonitrile monomer takes place by the addition of free radicals from the same monomer or from different monomers. The polymer chain formed grows due to the high reactivity double bond. According to Masson and Morgan, the redox system originates from free radicals in an aqueous acid medium, pH 2 to 3.5, at a relatively low temperature, 40-60 °C. The most common redox system comprises an oxidizer (potassium persulfate or potassium chlorate), a reducing agent (sodium bisulfite, sulfur dioxide or sodium metabisulfite) and a catalyst (ferrous iron) (Fleming *et al.*, 2014).

2.1.2 Electrospinning process

Electrospinning, which may be considered to be a variant of the electrostatic spinning process, is currently the only technique that is able to produce continuous ultrafine fibers from submicrometer to nanometer diameters. The first patent of electrospinning was given in 1934 (Anton, 1934) in order to produce filament materials which is recognized as the most efficient technique to produce polymer nanofibers (Huang *et al.*, 2003; Nataraj *et al.*, 2012). When a high voltage (usually in the range of 1 to 30 kV) is applied, the drop ejector nozzle in the polymer solution becomes highly electrified with the load uniformly distributed over the surface. As a result, the drop of the polymer solution suffers from two kinds of Coulomb electrostatic forces, the repulsion between the surface charges and the forces exerted by the external electric field. Under the action of these electrostatic interactions, a drop of a solution is distorted into a conical shape known as the Taylor cone (Yarin *et al.*, 2001; Kalayci *et al.*, 2005). Since the electric field strength has exceeded a threshold value, the electrostatic force can overcome the surface tension of the polymer solution and thus force the solution through the nozzle jet ejector. Along the way, the electrified jet ejector nozzle travels to the collector as shown in Figure 2.2, in the process of

stretching and elongating the jet and depending on the physical characteristics of the polymer solution, the jet can break up into droplets or remain as nanofibers. The evaporation of the solvent and solidification of the polymer leads to the formation of particles or nanofibers. Moreover, the jet bending before collecting on the target is also caused by the induction of a very nonuniform electric field. This process caused the nanofibers to form randomly on the collector (Yang *et al.*, 2008).

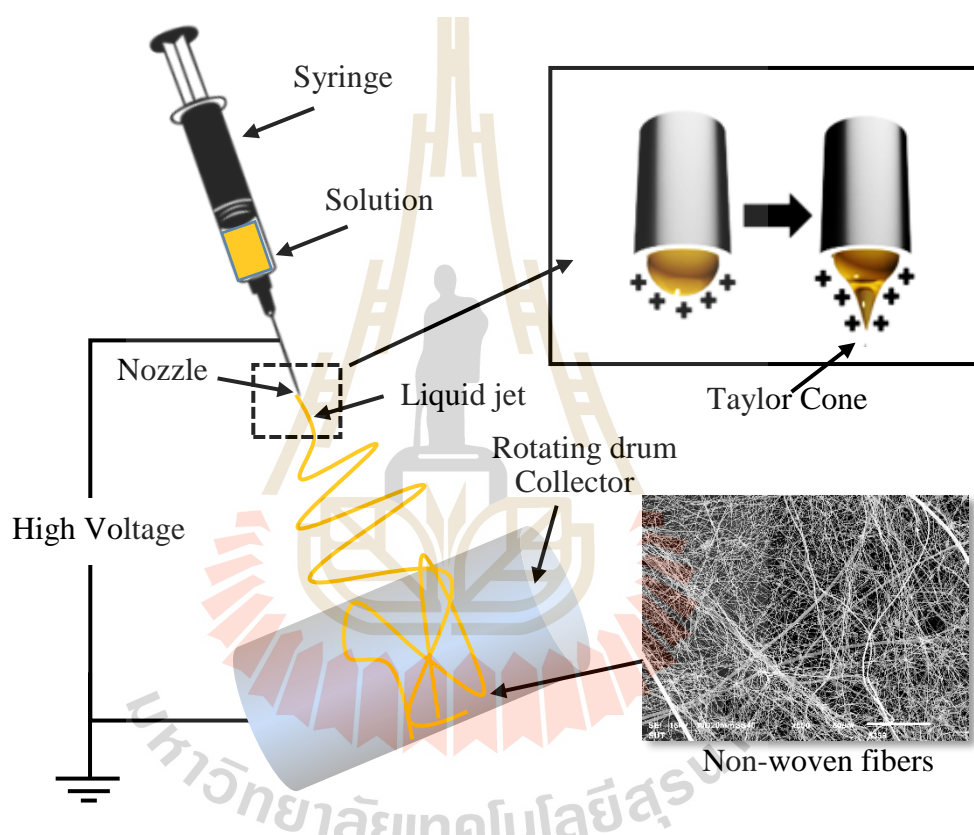


Figure 2.2 Schematic diagram of electrospinning system (Gong and Wu, 2012).

Process control in the electrospinning technique is typically limited to identifying the operating conditions that produce fibers with acceptable properties. However, within a laboratory setting, even with these conditions identified, it is reported that there still remains significant differentiation in the quality of the materials produced. These variations are a result of an incomplete understanding or hearing of

all the process variables. There are many factors influencing the morphology of the fibers or fibrous constructs produced and these can be divided into solution parameters, process parameters and ambient parameters, which are listed in Table 2.1.

Currently, electrospinning has become an attractive technique in the production of nanofibers. Its advantages are a controllable size and that it is easy to add the other substrates simultaneously with the main product in order to form composite nanofibers as shown in Figure 2.2 (Li *et al.*, 2008; Beachley and Wen, 2009; Lisunova *et al.*, 2010; Zhang *et al.*, 2010; Katepalli *et al.*, 2011; Kim *et al.*, 2011; Kim *et al.*, 2011; Xiang *et al.*, 2011; Sarlak *et al.*, 2012). Moreover, there are many tactics to make them as the composite as demonstrated in Figure 2.3.

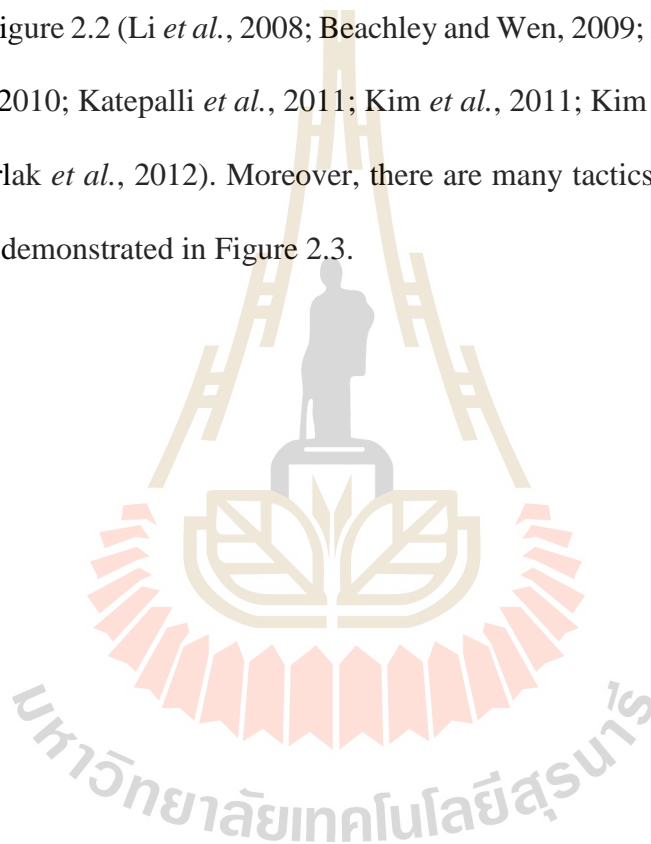


Table 2.1 Variables of the electrospinning process divided into different categories (Bosworth and Downes, 2011).

Solution parameter	Process parameter	Ambient parameter
Material selection	Electromagnetic field	Humidity
Solvent selection	Spinning distance	Temperature
Concentration	Solution flow rate	Atmosphere
Viscosity	Spinneret morphology	Gas/Air
Dielectric constant	Collector morphology	
Conductivity		
Surface tension		
Elasticity		

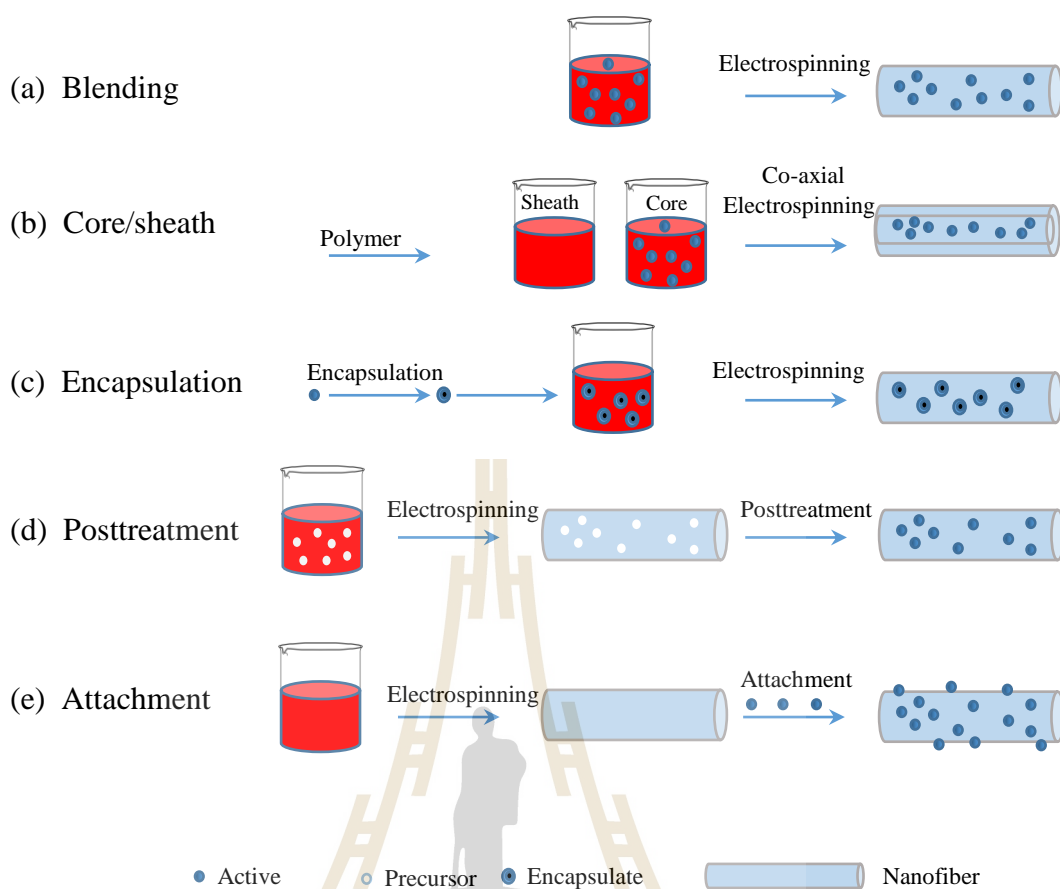


Figure 2.3 Various strategies used to prepare the electrospun composite nanofibers (Haider *et al.*, 2015).

2.1.3 Carbonization and graphitization process

The polymer precursors can be converted into carbon by a heat treatment called carbonization. This process commonly consists of stabilization, carbonization or metallization, and sometimes an activation process. In the stabilization step, the linear PAN polymers are first converted into a cyclic structure. However, cyclization is a very complicated process and there are still differences of conception on the reaction mechanisms. Different models have been proposed for the cyclization of PAN molecules as summarized in Figure 2.4. A cyclization and dehydration of structure are proposed in Figure 2.4(a) in which the structure is often cited as the product of low-temperature stabilization. At the mid temperature, the crosslink structures could be formed as shown in Figure 2.4(b). Since both structures contain no oxygen, an oxidized structure is proposed as in Figure 2.4(c), a ladder structure is also proposed as in Figure 2.4(d), and the contribution of a nitrene structure is shown as in Figure 2.4(e). A different structure also has been tried to include in the oxidized molecules, such as the structures in Figure 2.4(f), Figure 2.4(g), and Figure 2.4(h). Unreacted nitrile groups are demonstrated in (g) and (h) due to the random initiation sites and the atactic nature of PAN. The orientation in the pyrolysis step is sustained by the strong intermolecular hydrogen bonding and the rigidity of the ladder structure. (Huang, 2009).

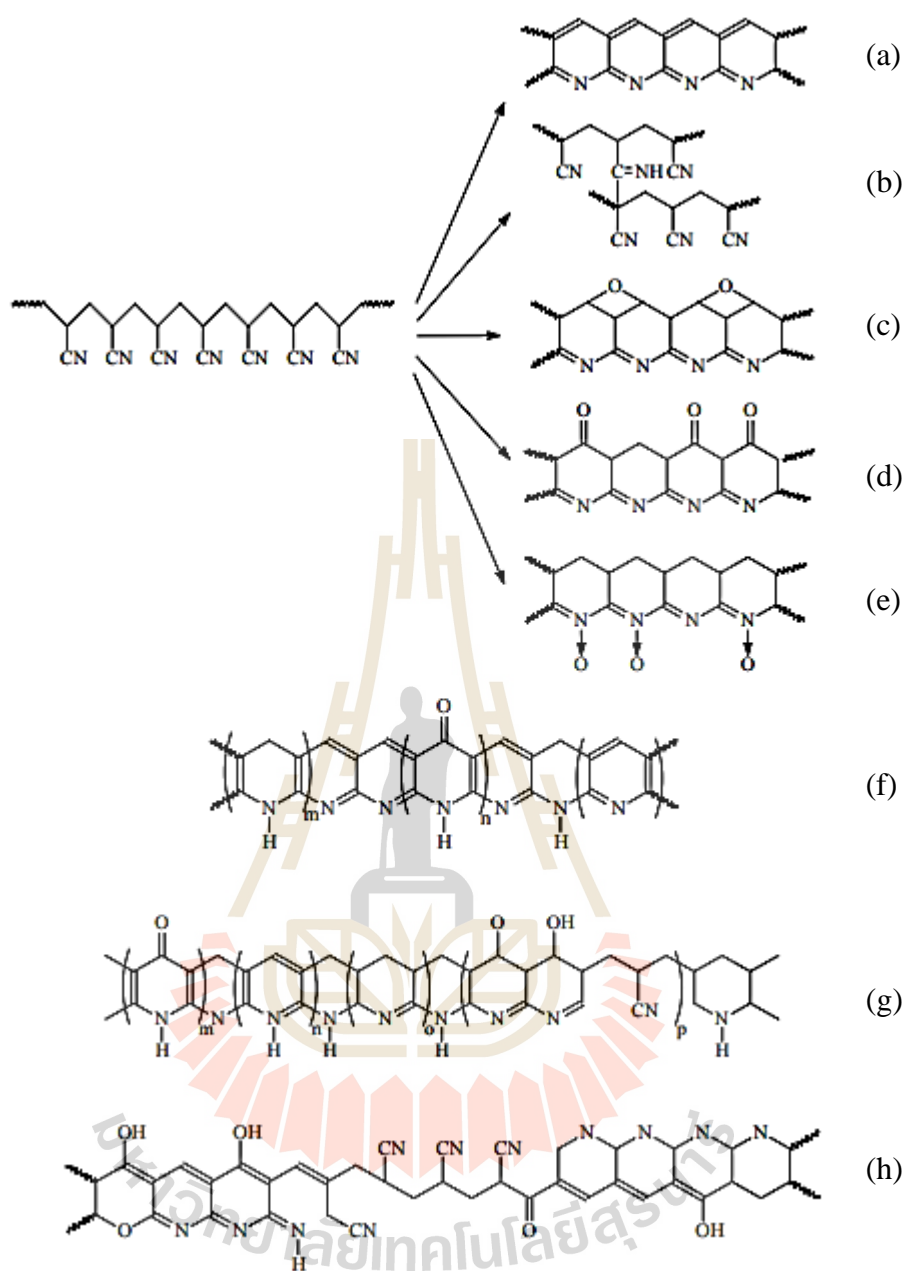


Figure 2.4 A schematic shows the various models of oxidization of PAN during heat treatment (Huang, 2009).

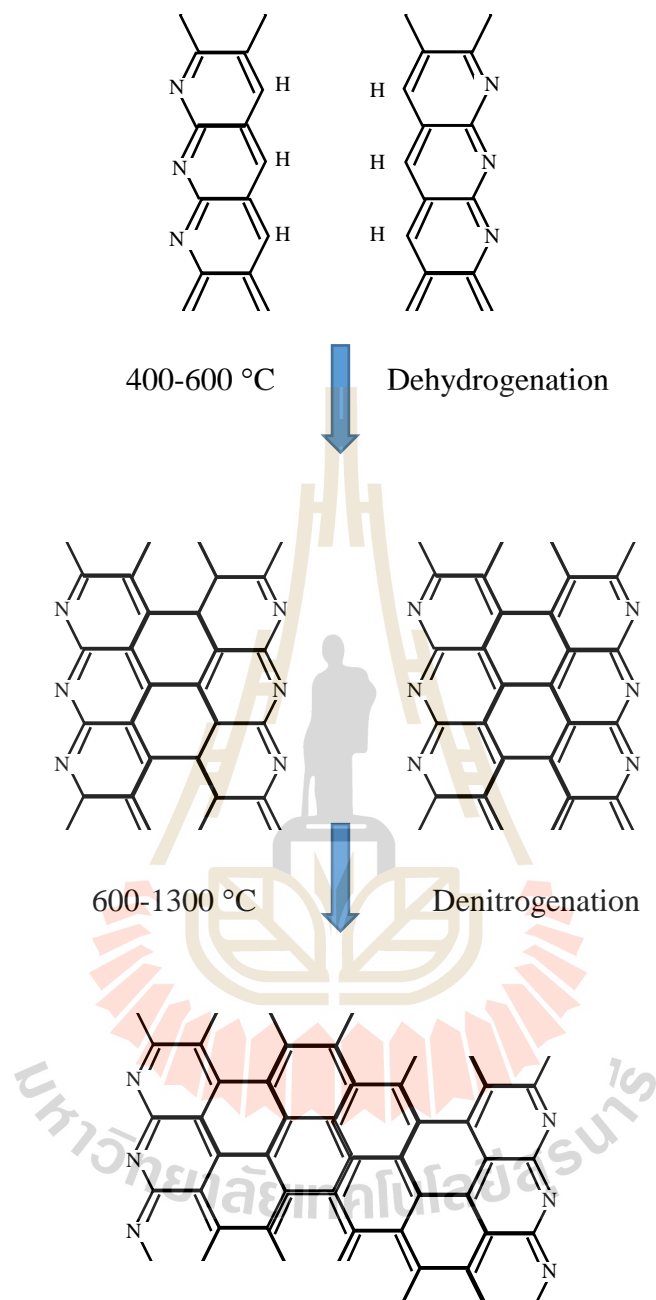


Figure 2.5 A schematic shows the thermal chemistry of PAN carbonization which involves dehydrogenation and denitrogenation eventually leading to partially graphitic structures (Huang, 2009).

The carbonization is conducted at high temperature in inert gas continuously after stabilization. The importance of stretching in this step is still under debate. The fiber diameter is reduced by the removal of the non-carbon elements. At the early stages of carbonization, crosslinking reactions arise in the oxidized PAN. The cyclized structure starts to link up in a lateral direction by dehydration and denitrogenation. A planar structure can be formed with the basal planes directed along the fiber axis (Figure 2.5). These fibers are generally called “high strength” fibers. The strength of a carbon fiber is observed to increase with the carbonization temperature and the maximum strength is monitored at around 1500 °C. Further increase in temperature results in increased modulus but reduced tensile strength. Too fast a carbonization rate introduces defects in carbon fibers while a low carbonization rate causes the loss of too much nitrogen at the previous stages of carbonization, a certain amount of which is preferred to achieve high strength carbon fibers (Huang, 2009).

Moreover, the more graphitic carbon can be also improved by preparation in high-temperature conditions (Kim *et al.*, 2015). The structural changes produced in carbon materials by high-temperature heat treatment, grinding, or neutron irradiation is always accompanied by changes in crystallite size. These processes are usually considered separately. The graphitization of carbon materials at 2500–3000 °C reduces crystallite growth. By contrast, consideration of the processes taking place in carbon materials is confined to crystallization induced by high-temperature heat treatment or amorphization induced by grinding or neutron irradiation. Such approaches are incapable, however, of adequately describing the observed variations in the lattice parameters of carbon materials with crystallite size. In carbon materials consisting of crystallites less than 100 nm in size, the lattice parameters a and c are smaller and

larger than those in graphite, respectively. In terms of the theory of phase transformations, this behavior can be explained as due to a corrugation of graphite layers as a result of the attachment of carbon atoms. By analogy with intercalation compounds, various configurations and, accordingly, several metastable phases may be expected to result, without changes in interatomic distances. In this approach, the changes in interplanar spacing must be larger in more defect-rich crystallites. However, the intercalation capacity of large crystallites is higher, whereas experimental data indicate that the largest changes in lattice parameters occur in fine particle carbon materials. The crystallites of carbon from the model in Figure 2.6 are described by parameters including number of layer dimensions ($p = 1, 2, 3\dots$), atom per layer (N), a-axis layer dimension (L_a), and interatomic C-C bond distance (R_{C-C}), and these can be calculated by equations as follow (Belenkov, 2001; Fujimoto *et al.*, 1994).

$$R_{C-C} = A + 0.25B \left(3 - \frac{1}{p} \right) \quad (2.1)$$

$$N = 6p^2 \quad (2.2)$$

$$L_a = 2R_{C-C} \cos 30^\circ (2p - 1) \quad (2.3)$$

where the coefficients $A = 0.1068$ and $B = 0.0472$ nm (Belenkov, 2001).

In addition, the in plane graphite crystalline size as demonstrated in Figure 2.6 (c) can be also determined from the I_D/I_G as reported by Knight and White (1989). The L_a (nm) is evaluated by the followed equation;

$$L_a = C_\lambda \left(\frac{I_D}{I_G} \right)^{-1} \quad (2.4)$$

Where C_λ is a constant, ~ 4.4 .

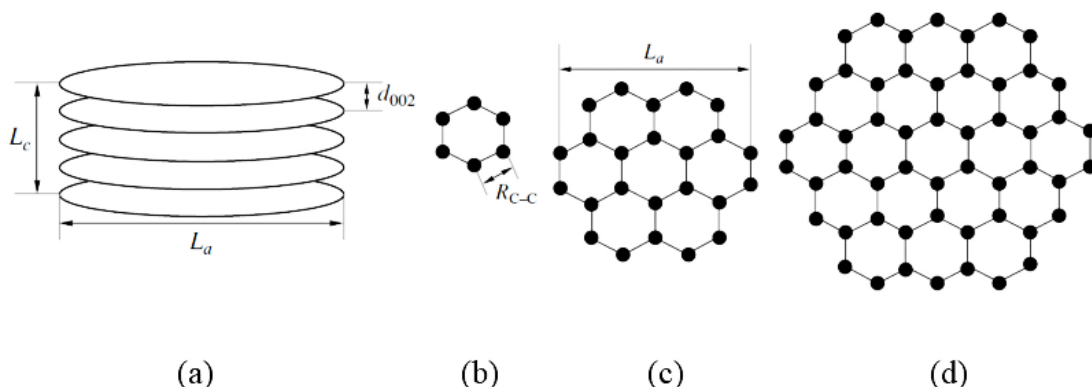


Figure 2.6 Model for a crystallite of a carbon material (a) stack of layers and structure of an individual layer with difference size of $p =$ (b) 1, (c) 2, and (d) 3 (Belenkov, 2001).

2.1.4 Activation process

The methods used to improve carbon porosity are known as activation processes. Normally, carbon has a rather low porosity and its structure consists of elementary crystallites with a large number of interstices between them. The spaces tend to be filled with ‘disorganized’ carbon residues (tars) that block the pore entrances. Activation opens these pores and can also cause additional porosity. Varying the carbon precursor and activation conditions (particularly temperature, time and gaseous environment) allows some control over the resulting porosity, pore-size distribution, and the nature of the internal surfaces. Although carbon manufacturers closely guard their procedures for the activation of commercial carbons, the processes can be collected into two general categories: thermal activation and chemical activation.

Thermal activation, sometimes referred to as physical activation, entails the modification of a carbon char by controlled gasification and is usually operated at

temperatures between 700 and 1100 °C in the presence of suitable oxidizing gasses, such as steam (Girgis *et al.*, 2002), carbon dioxide (San Miguel *et al.*, 2003), air, or mixtures of these gasses (Nataraj *et al.*, 2012). During gasification, the oxidizing atmosphere greatly improves the pore volume and surface area of the sample in virtue of a controlled carbon ‘burn-off’ and the elimination of volatile pyrolysis products. The level of burn-off is, perhaps, the most important factor governing the quality of the activated carbon and is directed by the temperature and duration of activation. A high degree of activation is completed by increased burn-off, but the additional activity is attended by a decrease in carbon strength, a lower density, reduced yield, and pore widening. The activation mechanism for carbon dioxide and steam are illustrated as follows.



Chemical activation is usually processed at slightly lower temperatures (~400–700 °C) and involves the dehydrating action of certain agents such as phosphoric acid, zinc chloride, and potassium hydroxide. Post-activation washing of the carbon is usually needed to remove residual reactants as well as any inorganic residue (sometimes referred to as ash) that initiates from the carbon precursor or is introduced during activation. Exceptionally high surface area materials ($> 2500 \text{ m}^2 \text{ g}^{-1}$) were prepared with potassium hydroxide activation techniques (Pandolfo and Hollenkamp, 2006).

2.1.5 Application of carbon nanofibers

The applications of nanofibers into electronic devices are dominant in batteries (Gopalan *et al.*, 2008; Jung *et al.*, 2011; Kim *et al.*, 2013; Lee *et al.*, 2012) and supercapacitors (Huang *et al.*, 2007; Kim *et al.*, 2012; Kim *et al.*, 2011; Kim and Yang, 2003; Kim *et al.*, 2012). For supercapacitors, as-spun polymer-based nanofibers or carbonized nanofibers have been applied as the electrode material. The nonwoven web obtained from the electrospinning has been used to produce activated carbon nanofibers through the stabilization, carbonization and activation processes. The activated carbon nanofibers have a highly specific surface area from shallow pores size. The superficial pores could be formed due to the nanosize in fibers diameters through the activation resulting in enhanced specific capacitance at an elevated current density (Kim and Yang, 2003).

The electrospinning of PAN/DMF (Gu *et al.*, 2005; Gu *et al.*, 2005; Tekmen *et al.*, 2010; Yu *et al.*, 2010; Dhakate *et al.*, 2011; Kim *et al.*, 2011; Prahsarn *et al.*, 2011; Wang *et al.*, 2012; Yu *et al.*, 2012; Singh *et al.*, 2013) was processed, and fibers with diameters ranging from 200 nm to 1200 nm were achieved depending on the electrospinning conditions, including applied voltage, conductivity, and viscosity of solution etc. Morphology and size distribution of fibers were investigated at various concentrations and applied voltages. Fibers with a diameter over 1000 nm were made at a concentration of 12 wt.%. Uniform PAN nanofibers were obtained at a concentration of 8 -10 wt.% under an applied voltage of 10-20 kV. For a solution with a concentration of 6 wt.%, fibers with spindle-like beads were gained at lower applied voltage, and uniform nanofibers were obtained at higher applied voltage (Gu *et al.*, 2005).

2.2 Supercapacitors

2.2.1 Working principle of capacitor

A capacitor is a passive component that stores energy in an electrostatic field rather than in chemical form. As shown in Figure 2.7, it consists of two parallel electrodes (plates) separated by a dielectric. The capacitor is charged by applying a potential difference (voltage) across the electrodes, which causes positive and negative charges to migrate toward the surface of electrodes of opposite polarity. When charged, a capacitor connected in a circuit will act as a voltage source for a short time. Its capacitance (C), which is measured in farads (F), is the ratio of electric charge on each electrode (Q) to the potential difference between them (V) so that:

$$C = \frac{Q}{V} \quad (2.7)$$

For a conventional capacitor, C is proportional to the area (A) of each electrode and the permittivity (ϵ) of the dielectric is inversely proportional to the distance (D) between the electrodes so that:

$$C = \frac{\epsilon_0 \epsilon_r A}{D} \quad (2.8)$$

where ϵ_0 is the permittivity of free space and ϵ_r is the dielectric constant (or relative permittivity) of the material between the plates. Therefore, the three main factors that determine the capacitance of a capacitor are

- plate area (common to the two electrodes)
- separation distance between the electrodes
- properties of the dielectric (insulator) used.

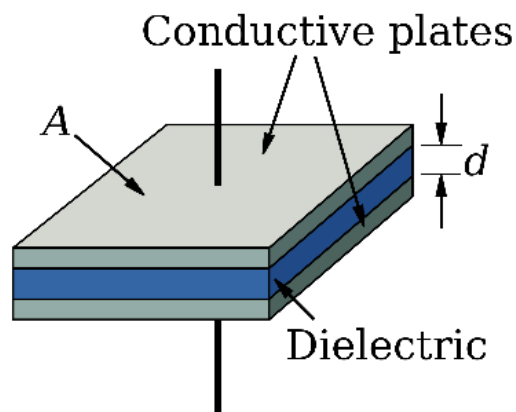


Figure 2.7 Schematic diagram of a conventional capacitor.

Two primary attributes of a capacitor are its energy and power density, both of which can be expressed as a quantity per unit weight (specific energy or power) or per unit volume. The energy E (J) stored in a capacitor is related to the charge Q (C), at each interface and the potential difference V (V), and therefore it is directly proportional to its capacitance:

$$E = \frac{1}{2} CV^2 \quad (2.9)$$

Maximum energy is achieved when V is at a maximum, which is usually limited by the breakdown strength of the dielectric. In general, power (P) is the rate of energy delivery per unit time. The resistance of the internal components of the capacitor (e.g., current collectors, electrode materials, dielectric/electrolyte, and separators) needs to be taken into account in order to determine P for a certain capacitor. The resistance of these components is usually measured in aggregate and collectively referred to as the equivalent series resistance, ESR (Ω). The ESR , by introducing a voltage drop, determines the maximum voltage of the capacitor during discharge and therefore limits the maximum energy and power of a capacitor. The measurement of power for capacitors is often measured at matched impedance (i.e., the resistance of the load is

assumed to be the same as the capacitor ESR) which corresponds to the maximum power P_{max} , given by:

$$P_{max} = \frac{V^2}{4ESR} \quad (2.10)$$

even though the resistance of a good capacitor is typically much lower than that of the connected load, the actually delivered peak power, although still very high, is usually lower than P_{max} (Lu *et al.*, 2013).

However, the conventional capacitor can store little energy due to its limited charge storage area and geometrically it contains the separation distance between the two charged plates. Therefore, a new generation has been developed based on the electrical double layer capacitive and pseudocapacitive process as the supercapacitors.

2.2.2 Working principle of supercapacitors

Supercapacitor (SC) is also known as ultracapacitor, an electrochemical capacitor, and electrical double layer capacitor (EDLC). It was first modeled by Helmholtz in 1874 (Fripp, 1876), later explained by several groups of researchers such as Gouy and Chapman, and the precious principle is known as Gouy-Chapman-Stern-Grahame model (Simon *et al.*, 1998). As described by the Ragone plot in Figure 1.1, the SCs were developed in order to fill the gap between electronic cells like batteries and conventional capacitors, which provide a longer term of charging/discharging than a battery and which store more energy than a normal capacitor.

The construction of SCs is always different from that of conventional capacitors because there is no solid dielectric separation between the two electrodes. The SC is generally manufactured with two current collectors, porous material electrodes, an electrolyte, and a separator as shown in Figure 2.9. During the charging

process, one of the electrodes is positive and the other is negative. The method for SC to store energy is in principle based on two types of capacitive process: the EDLC from the electrostatic process and the pseudocapacitance from the chemical process of the reversible redox reaction of reactive electrode materials.



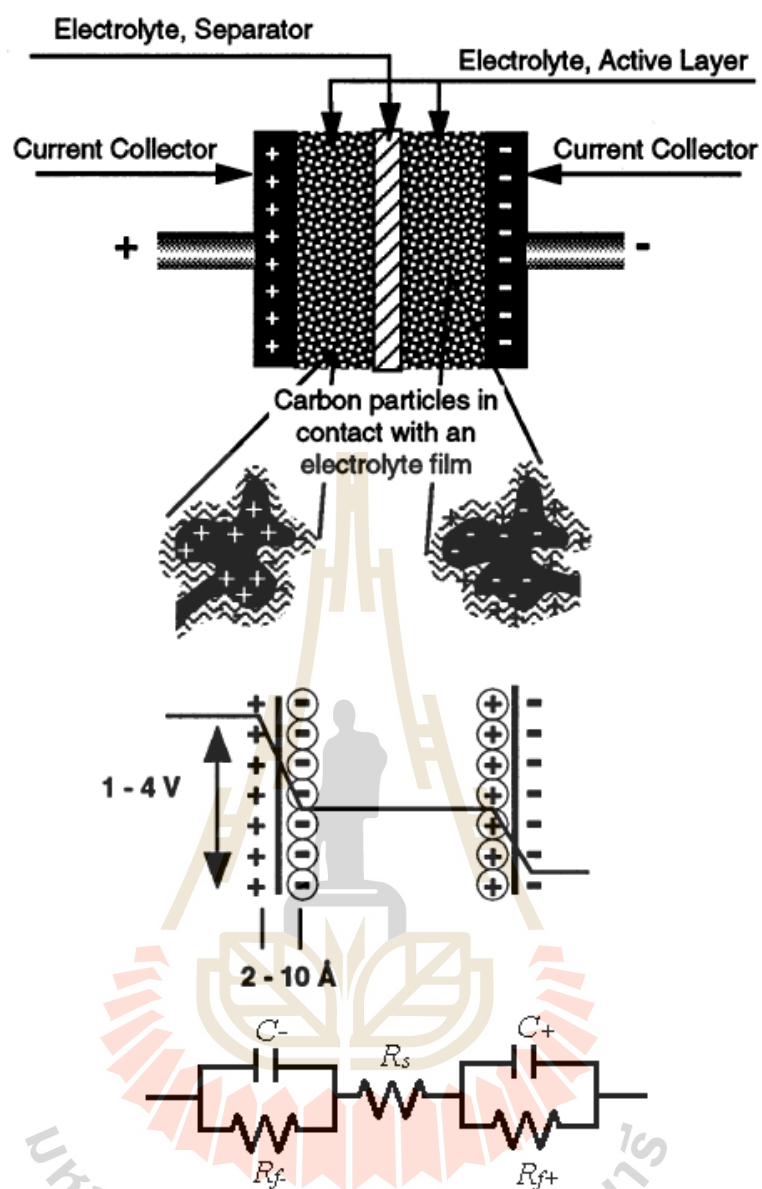


Figure 2.8 Representation of a supercapacitor. An illustration of the potential drop at the electrode, electrolyte interface, and equivalent circuit model for a supercapacitor (Kötz and Carlen, 2000).

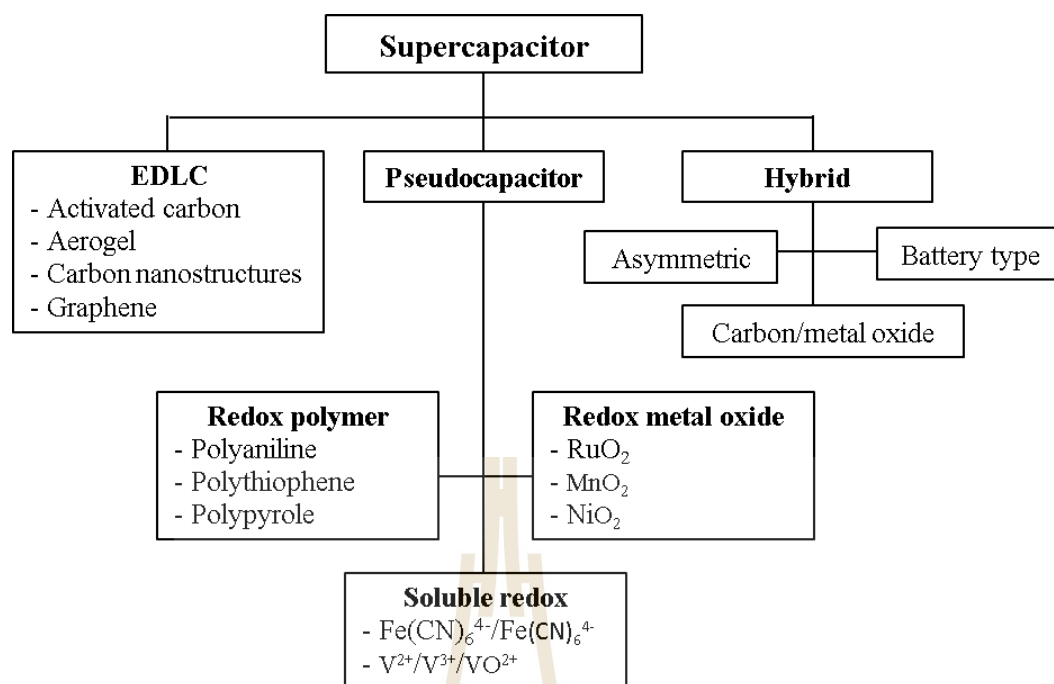


Figure 2.9 Taxonomy of electrochemical capacitors (Shukla *et al.*, 2012).

2.2.2.1 Electrical double layer capacitor (EDLC)

EDLC is based on the operating principle of an electrical double layer that is formed at the interface between the porous material and an electrolyte. A porous material, such as activated carbon, is used as an electrode. The principle behind the capacitor is shown in Figure 2.10. They move electrical charges between two electrodes rather than performing any chemical process, and they maintain cycle ability longer than batteries (Gualous *et al.*, 2003). When active electrode materials come in contact with the electrolyte, the positive and negative poles are distributed relative to each other over an extremely short distance which is in the range of 2-10 Å. Such a phenomenon is known as an electrical double-layer. When an external electric field is applied, the electrical double-layer that is formed in the vicinity of the porous electrode surface within the electrolytic fluid is used as the fundamental capacitor structure. This is the charging process. When the capacitor is discharged, the ions move away from

the electrodes and then generate the energy. Charge separation occurs on polarization at the electrode/electrolyte interface, producing what Helmholtz described in 1853 as the double-layer capacitance. The capacitive mechanism of EDLC also obeys the equations (2.7) and (2.8) capacitance principle. As the distance D decreases to an extreme point to a very small double-layer distance ($d \approx 2\text{-}10 \text{ \AA}$), the capacitance then reaches a very high value ($>10^3$ of the conventional capacitor) compared to the conventional capacitors. The thickness of the double layer is usually given as being approximately $1.5k^{-1}$, where k^{-1} is the Debye-Hückel length:

$$K^{-1} = \sqrt{\varepsilon\varepsilon_0 k T c^0 z_i^2 e_0^2} \quad (2.11)$$

where c^0 is the bulk z:z electrolyte concentration, ε is the relative dielectric permittivity of the solvent, ε_0 is the permittivity of the vacuum, k is the Boltzmann constant, T is the temperature, z is the ion charge and e_0 is the elementary charge. For $z = 1$, the approximate k^{-1} values calculated for electrolyte concentrations of 1×10^{-3} , 1×10^{-5} and 1×10^{-7} M are 10 nm, 100 nm and 1 mm, respectively. The thickness of the double layer also depends on the potential: the larger the difference between the electrode potential and the potential of zero charges (the potential at which the excess charge on the electrode equals zero), the smaller is the Debye-Hückel length (Stojek, 2010). Some theoretical works (Dzubiella and Hansen, 2005) and experimental studies (Teschke and De Souza, 1999; Palmer *et al.*, 1952) suggest that the dielectric constant of water near charged surfaces is in the range of 5–20 which is much smaller than the value of 78 for bulk water. The capacitive mechanism is explained by Gouy and Chapman, and Stern (GCS model) and Geary (Conway *et al.*, 1951) as presented in Figure 2.10(b).

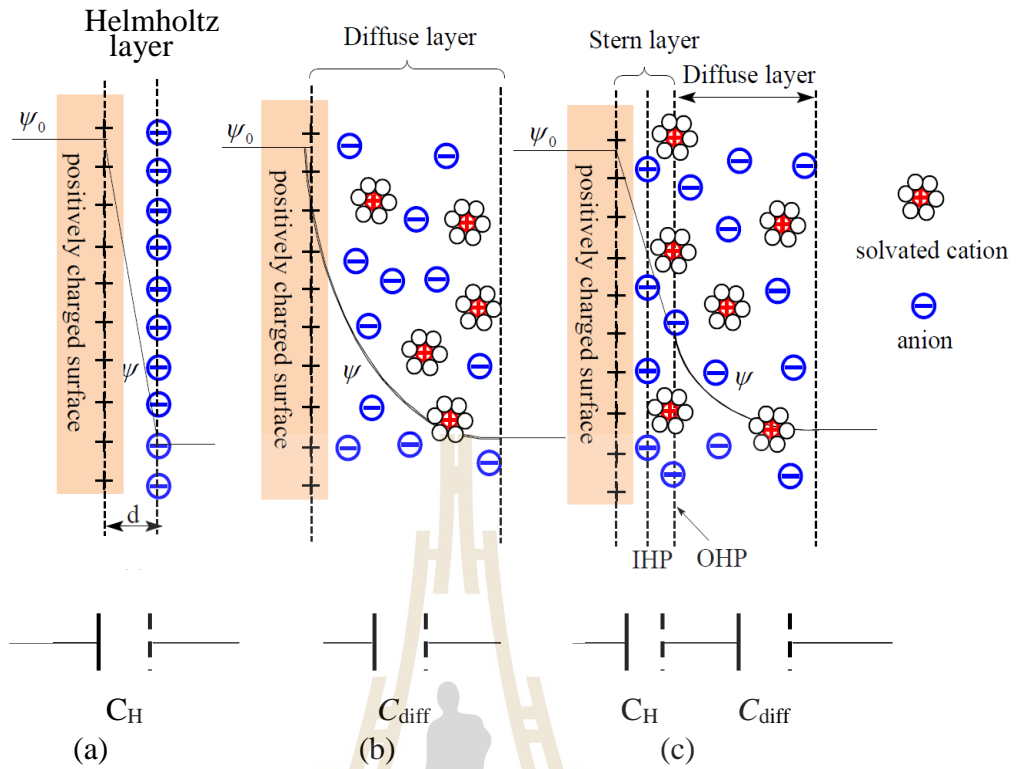


Figure 2.10 (a) The Helmholtz, (b) the Gouy-Chapman model, and (c) Stern model of the electrical double layer formed at an interface in aqueous electrolyte. IHP refers to the distance of the closest approach of ions and OHP refers to that of nonspecifically adsorbed ions. The OHP is also the plane where the diffuse layer begins. ϕ_0 is the potential at the electrode surface (Lu *et al.*, 2013).

The capacitance in the EDLC (C_{dl}) can be treated as the combination of the capacitance from two regions, the Stern type of compact double layer capacitance (C_H) and the diffusion region capacitance (C_{diff}). Thus, C_{dl} can be expressed as follows:

$$\frac{1}{C_{dl}} = \frac{1}{C_H} + \frac{1}{C_{diff}} \quad (2.12)$$

where C_{diff} is obtained as:

$$C_{diff} = \frac{\epsilon_r \epsilon_0 A}{\lambda_D} \cosh\left(\frac{e\phi_{diff}}{2k_B T}\right) \quad (2.13)$$

where ϕ_{diff} is the potential drop across the diffuse layer, e the electron charge, k_B is the Boltzmann constant, and T is the absolute temperature, and λ_D is the characteristic Debye length which, for monovalent electrolytes, is defined as:

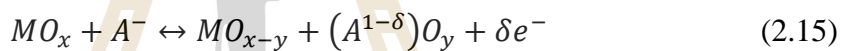
$$\lambda_D = \left(\frac{\epsilon_r \epsilon_0 k_B T}{2e^2 c_\infty}\right)^{1/2} \quad (2.14)$$

where c_∞ is the electrolyte concentration.

The parameters that determine the EDLC behavior at a planar electrode surface include the electric field across the electrode, the type of electrolyte, the solvent in which the electrolyte is dissolved, and the chemical affinity between the electrode surface and the electrolyte ion with an opposite charge to the electrode. Because the electrode is usually a porous material with a high specific surface area, the EDLC behavior at the pore surface of the porous electrode is more complex than that at an infinitely planar surface as ion transportation in a confined system can be drastically affected by the tortuous mass transfer path, the space constraints inside the pores, ohmic resistance associated with the electrolyte, and the wetting behavior of the pore surface by the electrolyte (Zhang and Zhao, 2009).

2.2.2.2 Pseudocapacitors

Pseudocapacitors store energy by the chemical process of a reversible redox reaction. Since the EDLC has been developed, they move electrical charges between two electrodes rather than perform any chemical process, and they maintain cycle ability longer than batteries (Gualous *et al.*, 2003). Moreover, the capacitance can be enhanced by both the double-layer and pseudocapacitance which contribute to the formation of a supercapacitor. Pseudocapacitance, arises on electrodes when the application of a potential induces faradaic current from reactions such as electrosorption or from the oxidation–reduction of electroactive materials (e.g., RuO₂, IrO₂, and Co₃O₄). Firstly, the pseudocapacitance of any metal oxide (MO_x) always originates with electrosorption which occurs when chemisorption of electron donating anions such as Cl⁻, OH⁻ or SO₄²⁻ takes place in a process such as:

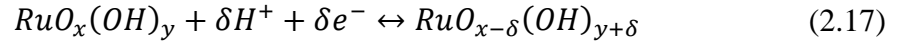


Such an electrosorption reaction of A⁻ anions at the surface of an electrode, and the quantity δe^- are related to the so-called electrosorption valence. Secondly, an exchange of charge across the DL, rather than a static separation of charge across a finite distance, resulting in oxidation–reduction reactions as illustrated:



The electric charges (e^-) are exchanged in this faradaic process, and the energy storage is indirect and analogous to that of a battery (Zhang *et al.*, 2009). A good example of a material with a pseudocapacitive property is ruthenium oxide. Due to its intrinsic reversibility of various surface redox couples and high conductivity, the electrochemical behavior of both amorphous and crystalline forms of ruthenium oxide has been widely studied in acidic electrolyte solution over the past few decades. It has been shown that amorphous hydrous ruthenium oxide (RuO_x · xH₂O) exhibits a much

higher specific capacitance value (720 F g⁻¹) than anhydrous ruthenium oxide. This is attributed to the mixed proton-electron conductivity within as the superficial redox transitions of ruthenium oxide involve the protons and electrons double injecting/expelling according to the following reaction (Zhang and Zhao, 2009):



In the case of a pseudocapacitor, the faradaic impedance has to be taken into account, which can be expressed by a capacitance C_{ps} in series with a charge-transfer resistance R_{CT} (Lu *et al.*, 2013)

$$R_{CT} = \frac{RT}{\alpha n F I_0} \quad (2.18)$$

$$C_{ps} = \frac{nF}{RT} \frac{\theta(1-\theta)}{g\theta(1-\theta)-1} \quad (2.19)$$

where I_0 is concentration and the θ is the saturation coverage of the electrochemical sites and g is a repulsion factor that is negative when repulsive forces occur between each site and positive in the opposite case. By deriving the equation (2.19), the theoretical pseudocapacitance of metal oxide can be obtained from the CV measurement, and the specific capacitance is calculated using the equation as follows (Zhi *et al.*, 2013):

$$C_{ps} = \frac{nF}{MV} \quad (2.20)$$

where n is the mean number of the electrons transferred in the redox reaction, F is the Faraday constant, M is the molar mass of the metal oxide and V is the operating voltage window.

SCs can be distinguished by several criteria such as the electrode material utilized, the electrolyte, or the cell design. With respect to electrode materials, there

are three main categories (Shukla *et al.*, 2012): carbon based, metal oxides, and polymeric materials. However, the electrode is the key part of a supercapacitor, so the literature review will focus on electrode nanomaterials. However, supercapacitors can be classified according to the main electrode material as displayed in Figure 2.4. The commercial products are reported in Table 2.2.

Table 2.2 Current manufacturers of SCs for utility-scale applications (Sharma and Bhatti, 2010).

Company	Device name	Country	Voltage range (V)	Capacitance (F)
AVX	Bestcap	USA	3.5–12	0.022–0.56
Cap XX	Super Capacitor	Australia	2.25–4.5	0.09–2.8
Copper	Power stor	USA	2.5–5.0	0.47–50
ESMA	Capacitor modules	Russia	12–52	100–8000
Maxwell	Boostcap	USA	2.5	1.6–2600
NEC	Super capacitor	Japan	3.5–12	0.01–6.5
Nesscap	EDLC	South Korea	2.7	10–5000
Panasonic	Gold capacitor	Japan	2.3–5.5	0.1–2000

2.2.3 Electrode materials of supercapacitor

Supercapacitors are commonly manufactured using three groups of active materials: carbon-based materials; conducting polymers; and transition metal oxides which provide different capacitive mechanisms.

2.2.3.1 Carbon-based electrode

The precursor of CNF which can be produced by several techniques, such as the vapor grown process (Terasawa and Takeuchi, 2013; Xu *et al.*, 2004; Al-Saleh and Sundararaj, 2009), the electrodeposition process (Chen *et al.*, 2005), the sol-gel process (Aryal *et al.*, 2008), and the electrospinning process (Tanimura *et al.*, 2003; Yang *et al.*, 2003; Gu *et al.*, 2005; Jang *et al.*, 2005). Carbonization in inert gas is always used to convert the precursor into a carbon structure. Carbonization consists of two main processes, stabilization and calcination. The activation process is always applied in order to increase the surface area porosity of the product (Manickam *et al.*, 2013; Yoon *et al.*, 2004; Song *et al.*, 2013). Although chemical activation by KOH or NaOH can be used for this process, some salt remains in the final products. Thus, gas flowing processes take place (Ra *et al.*, 2009). Carbon-based materials have taken the major role in energy storage devices due to their high surface areas, porosity, tunable structures, minimized ohmic resistance, mechanical stability, good wettability by the electrolyte and controllable conductivity (Zhang *et al.*, 2009).

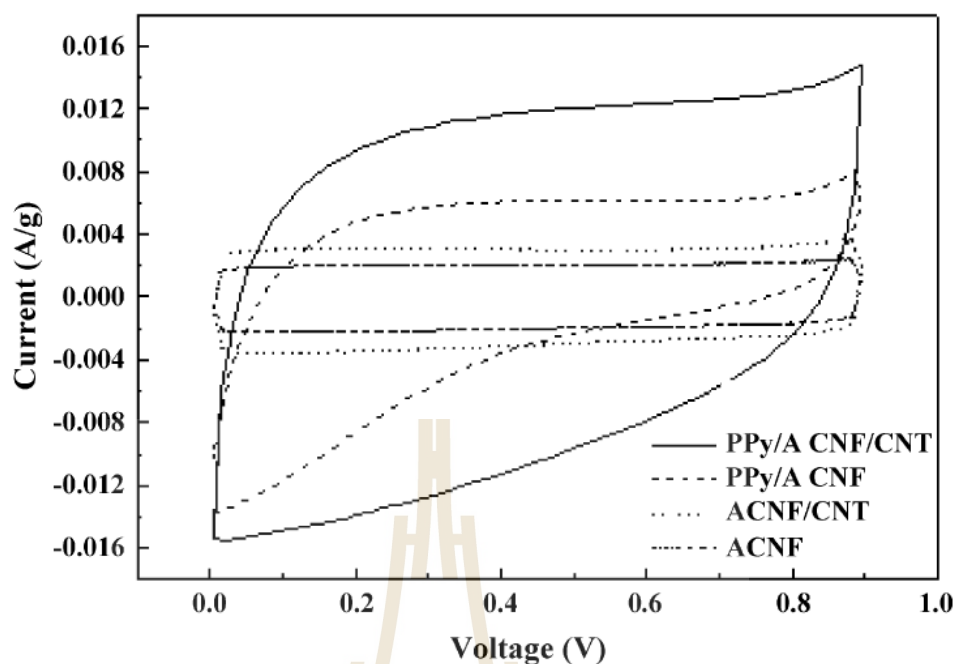


Figure 2.11 Cyclic voltammograms of the samples at a scan rate of 20 mVs^{-1} (Ju *et al.*, 2008).

In the case of capacitor performance, charge storage on carbon electrodes is predominantly capacitive in the supercapacitor. Carbon-based supercapacitors come close to what one could call an electrical double layer capacitor. Cyclic voltammetry of carbon-based electrodes always appears without redox peaks as shown in Figure 2.11. There are contributions from surface functional groups which are generally present on activated carbons which can be charged and discharged giving rise to pseudocapacitance. However, the effect of surface area and porosity are not linearly proportional to a capacitance (Barbieri *et al.*, 2005). The carbon-based electrode materials are reported in Table 2.3.

Table 2.3 Carbon-based materials used for supercapacitor electrodes (Zhang *et al.*, 2009).

Electrode material	Electrolyte	V (V)	C _s (F.g ⁻¹)
Activated carbon (AC)	1MEt ₄ NBF ₄ +PC	1.5	40
Graphite	1MEt ₄ NBF ₄ +PC	3.0	12
Carbon aerogels (CAGs)	1.5MEt ₃ MeNBF ₄ + PC	3.0	160
Mesoporous carbon	30wt% KOH	0.9	180
Meso/macroporous carbon	6MKOH	0.8	130
C60-loaded AC fiber	0.5MH ₂ SO ₄	1.0	172
AC fiber cloth	6MKOH	1.0	208
Single-walled CNT	EMITFSI	2.3	50
Multi-walled CNT sheet	1.96MTEMABF ₄ +PC	2.5	13
CNT/polypyrrole(PPy)/MnO ₂	1.0MNa ₂ SO ₄	0.9	281

2.2.3.2 Conducting polymer-based electrodes

In general, the energy density of redox capacitors consisting of conducting polymers is higher than that of EDLC composed of carbon materials because conducting polymers can store a charge not only in the electrical double layer but also through the rapid faradaic charge transfer of pseudocapacitance. It is therefore not unexpected that a large number of recent publications reported on the synthesis and electrochemical properties of electrically conducting polymer and their derivatives (Mi *et al.*, 2008). PANi nanofibers synthesized in the presence of a cationic surfactant exhibited a specific capacitance of 298 F g^{-1} (Subramania and Devi, 2008). Xu and co-workers (2009) fabricated PANi thin films on a stainless-steel substrate and evaluated the film as a supercapacitor electrode. A relatively high specific capacitance (431 F g^{-1}) and good charge-discharge behaviors were observed. In-situ polymerization of aniline was conducted to coat PANi on the surface of polypyrrole (PPy) nanotubes. The specific capacitances of the PPy/PANi composite were measured to be 416 F g^{-1} in $1 \text{ M H}_2\text{SO}_4$ electrolyte and 291 F g^{-1} in 1 M KCl electrolyte, respectively (Mi *et al.*, 2008). Polythiophene (Pth) and polyparafluorophenylthiophene (PFPT) were also tested as supercapacitor electrodes with energy storage capacities of 260 F g^{-1} for polythiophene and 110 F g^{-1} for PFPT, respectively (Laforgue *et al.*, 1999).

Conducting polymers present a significant disadvantage of a lower life cycle than carbon electrodes because the redox sites in the polymer backbone are not sufficiently stable for many repeated redox processes. Variations of the polymer structure can affect the penetration of electrolyte into pores, as well as the ion mobility within the conducting polymer. The design of the electrode structure is the key to obtaining a stable conducting polymer electrode. Therefore, making composite

structures with conducting polymers supported on porous rigid materials (e.g., carbon monoliths, porous carbon, CNT, and porous silica) has been explored.

Conducting polymer-based materials, such as poly (aniline)-based, poly (pyrrole)-based and poly (3-methylthiophene)-based have been used for the electrodes of a supercapacitor. Their cyclic voltammetry distorts from a rectangular shape (ideal capacitor) and shows oxidation and a reduction peaks. Due to the redox reactions, conducting polymer based electrochemical capacitors have a high capacitance as shown in Figure 2.12. Several case studies of conducting polymer are reported in Table 2.4.

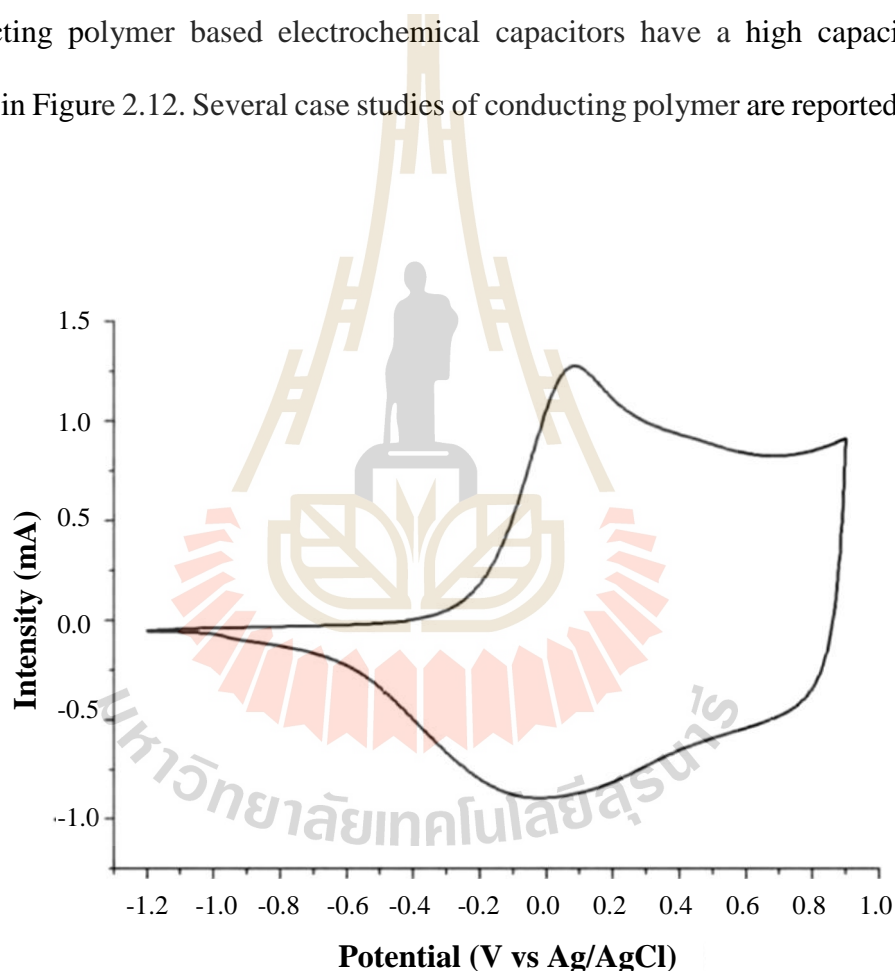


Figure 2.12 Cyclic voltammogram of a PEDOT nanofiber mat in EMIBF₄.(mPEDOT) = 2.0 mg, scan rate $v = 5 \text{ mVs}^{-1}$ (Laforgue, 2011).

Table 2.4 Several conductive polymers used for supercapacitor electrode (Zhang et al., 2009).

Electrode material	Electrolyte	V (V)	C _s (F g ⁻¹)
Poly(3-methylthiophene)	PYR ₁₄ TFSI	3.6	25
Poly(3-methylthiophene)/MnO ₂	1M Na ₂ SO ₄	1.0	381
Polypyrrole/AC	0.5M Pyrrole+0.5Mb-NSA	0.9	345
PANI/MnO ₂	0.1M Na ₂ SO ₄	1.2	715
PANI/AC	6M KOH	0.9	588

2.2.3.3 Metal oxide (MO)-based electrodes

These are produced based on a group of elements which are conductive. These are useful materials to improve the electrical properties of their compounds or composites as well. Metal oxides (MO) are the compound of any metals with oxygen. Transition metal elements in the form of metals or metal oxides are promised as anode materials due to their highly specific capacity and safe operation. They have been applied as a part of energy storage devices, such as an electrode of conventional batteries (Ohzuku and Ueda, 1994) and as a role material of capacitors because their redox reaction can support the enhancement of pseudocapacitance as shown in Figure 2.13 (Ren *et al.*, 2013). Many case studies of metal oxides are reported in Table 2.5.

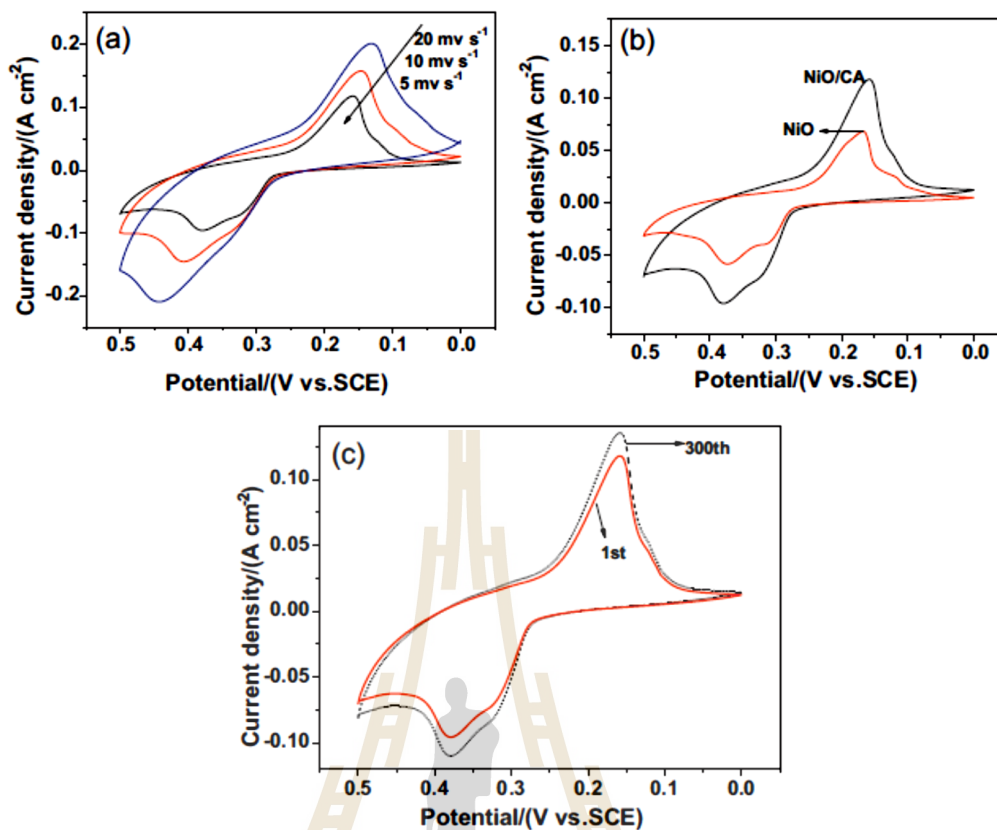


Figure 2.13 CV curves of (a) NiO/CA nanofibers at different scan rates of 5, 10 and 20 mV s⁻¹, calcined at 500 °C, in 6.0 M KOH solution, (b) NiO, NiO/CA at the scan rates of 5 mV s⁻¹, calcined at 500 °C, in 6.0 M KOH solution, and (c) NiO/CA nanofibers at the 1st and 300th cycles at the scan rates of 5 mV s⁻¹, calcined at 500 °C, in 6.0 M KOH solution (Ren *et al.*, 2013).

Table 2.5 Case study of metal oxides for supercapacitor electrodes (Zhang *et al.*, 2009).

Electrode material	Electrolyte	V (V)	C _s (F g ⁻¹)
RuO ₂ .H ₂ O	0.5M H ₂ SO ₄	1.0	650
H ₂ RuO ₄ nanosheet/Au	0.5M H ₂ SO ₄	1.2	620
H _{0.2} RuO _{2.1} .nH ₂ O	0.5M H ₂ SO ₄	1.2	390
RuO ₂ /carbon	PVAhydrogel	0.8	1000
Amorphous Ru _{1-y} Cr _y O ₂ /TiO ₂	1MKOH	0.9	1272
MnO ₂	0.5M K ₂ SO ₄	0.8	261
MnO ₂ /AC	0.65M K ₂ SO ₄	2.2	29
SnO ₂ /carbon aerogel	1M H ₂ SO ₄	1.0	68
Ni(OH) ₂	3% KOH	0.8	578
Ni(OH) ₂ /AC	6M KOH	0.9	194
Cobalt-nickel oxides/CNT	1M KOH	1.0	569
Nickel-basedmischmetal/AC	BMIM-PF ₆	3.0	357
Mo ₂ N/Ta ₂ O ₅	3.5M H ₂ SO ₄	0.8	106
WC/carbon	1M H ₂ SO ₄	0.9	477
MnFe ₂ O ₄	1M LiPF ₆ +EC/EMC	2.5	126
TiN	1M KOH	0.2	238
V ₂ O	2M KCl	0.7	262

2.3 Theoretical approach and electrochemical study for supercapacitors

Most supercapacitors are electrochemical storage devices, so their capacitive mechanisms, performances, and other properties are usually investigated using electrochemical techniques, such as cyclic voltammetry (CV), galvanostatic charge/discharge testing (GCD), electrochemical impedance spectroscopy (EIS), and others. All techniques are normally executed in electrochemical workstations which are generally composed of three main components: a potentiostat/galvanostat (PG), a computer, and an electrochemical cell.

To study an electrochemical property, all three configurations can be performed as two electrodes, three electrodes, and four electrodes. Basically, the current flows through the counter electrode (CE) and the working electrode (WE), and the voltage is measured (or controlled) between the reference electrode (RE) and the working electrode (WE). For a two-electrode cell (the cells are usually assembled like the commercial devices), the voltage measured (or controlled) is the cell voltage since the CE and the RE are shorted; for a three-electrode cell a third electrode is added and it acts as the RE. The RE used for this purpose should exhibit an ideal nonpolarizable behavior, meaning that its voltage is constant over a large range of current densities. In this way, the WE voltage is accurately measured (or controlled). Of course, many plugging combinations are possible, and the only limitation is the imagination of the experimenter. For instance, one can control the cell voltage while measuring the WE voltage or the opposite.

2.3.1 Cyclic voltammetry (CV)

This is a technique widely used by electrochemists because of its versatility, but most of the time this technique is restricted to laboratory cells. Actually, large devices lead to very large volumes of current from several hundred to thousands of amps, which could be technically difficult to handle. At the laboratory or material scale it is an accurate technique that enables:

- qualitative and pseudo-quantitative studies
- kinetic analysis by scanning a huge range of scan rates (ν)
- voltage window determination ($\Delta V = |V - V_0|$)

This technique is operated by applying a linear voltage to an electrode between two voltage limits to measure the resulting current. The applied voltage is as follows:

$$V(t) = V_0 + \nu t \quad (2.21)$$

Where V and V_0 are the voltage boundary and initial voltage, respectively. ν is the scan rate (V s^{-1}), and t is the duration time as shown in Figure 2.14. From the CV curve, the information of capacitive mechanisms is described by the characteristic CV curve as demonstrated in Figure 2.15 for EDLC and Figure 2.16 for pseudocapacitor. The specific capacitance of a supercapacitor cell (C_{cv}) can be calculated according to equations (2.22) or (2.23):

$$C_{cv} = \frac{1}{m\nu\Delta V} \int I(V)dV \quad (2.22)$$

$$C_{cv} = \frac{1}{m\Delta V} \int I(t)dt \quad (2.23)$$

The energy density (E_{cv}) can be calculated by equation;

$$E_{cv} = \frac{1}{2} C_{cv} (\Delta V^2) \quad (2.24)$$

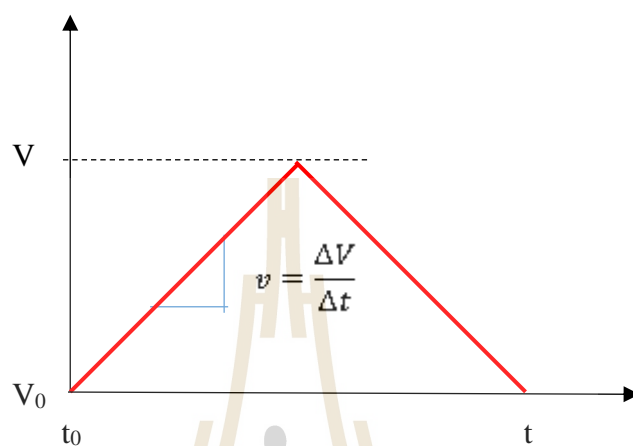


Figure 2.14 Cyclic voltammetry potential waveform.

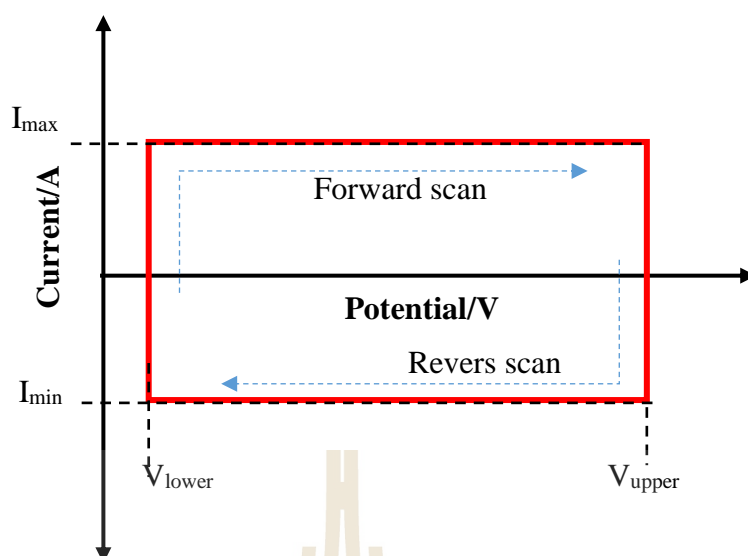


Figure 2.15 Typical cyclic voltammogram of EDLC.

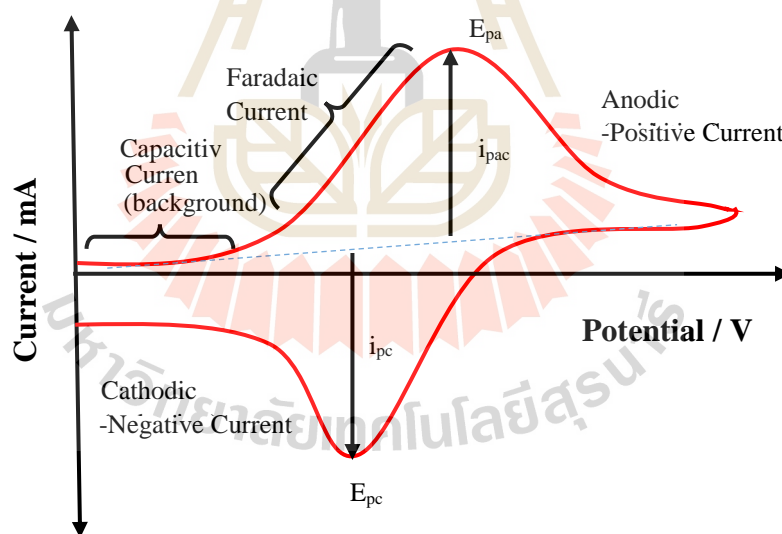


Figure 2.16 Typical cyclic voltammogram of electrode with chemical redox reaction

(<http://urrjaa.blogspot.com/2013/08/cyclic-voltammetry-urrjaa-p0110-2013.html>).

2.3.2 Galvanostatic charge/discharge testing (GCD)

For GCD technique, the potential of a supercapacitor is linear, or almost linear, with respect to the charge/discharge duration time ($dV/dt = \text{constant}$) during a constant current operation (Figure 2.17), so that can be exactly pinpointed. In contrast, most batteries exhibit a relatively constant operating voltage because of the thermodynamics of battery reactants (Figure 2.19). As a result, their SOC cannot be measured precisely. From a GCD curve, the specific capacitance of a supercapacitor cell (C_{GCD}) can be calculated according to equation (2.25).

$$C_{GCD} = \frac{I}{m} \times \frac{\Delta t}{\Delta V} \quad (2.25)$$

Where I is the discharge current (A), m is the mass of active materials (g), ΔV is the potential during the discharge process (V), and Δt is the discharge time (s). However, if the discharge potential displayed as a nonlinear curve as a function of time which attributed resistive behavior of the electrode as shown in Figure 2.18. Stoller and Ruoff (Stoller and Ruoff, 2010) recommend that the specific capacitance should be calculated by using two datum points from the discharge curve with equation (2.26).

$$\frac{\Delta V}{\Delta t} = \frac{(V_{\max} - 1/2 V_{\max})}{(t_2 - t_1)} \quad (2.26)$$

Where t_2 and t_1 are the discharge times at the points of maximum potential (V_{\max}) and half of the maximum voltage ($1/2 V_{\max}$).

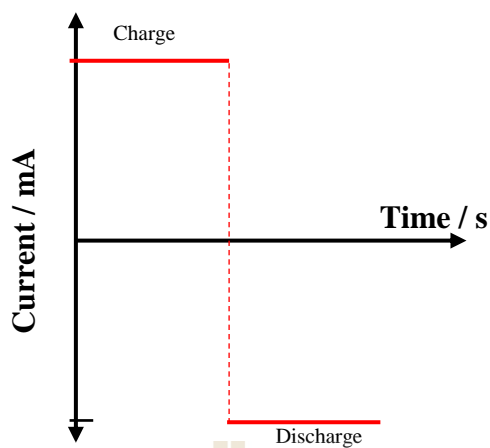


Figure 2.17 The charge/discharge constant current for galvanostatic method.

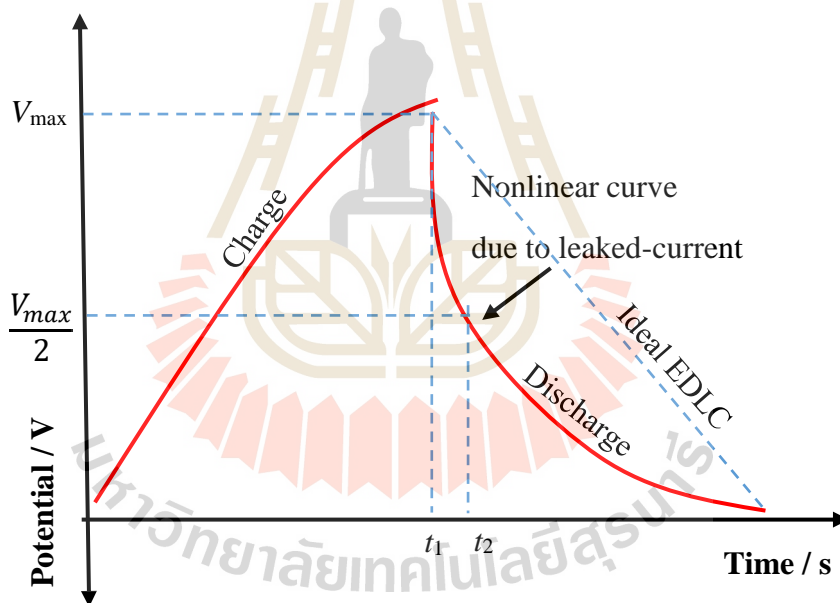


Figure 2.18 Typical charge/discharge profile with the presence of nonlinear due to resistive behavior.

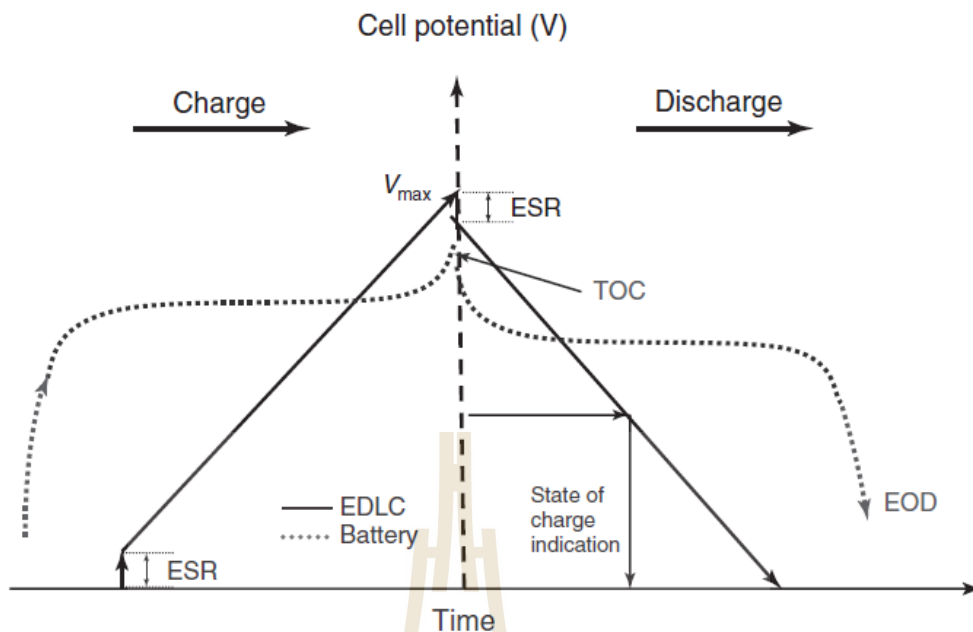


Figure 2.19 A schematic comparison of charge and discharge behavior for an ideal capacitor and battery (JINTAO, 2012).

Energy density and power density are two important parameters to evaluate the capacitive performance of a supercapacitor cell. The energy density is the capacity to perform work, whereas the power density exhibits how fast the energy is delivered. The maximum energy stored (E_{\max} , Wh kg⁻¹) and power delivered (P_{\max} , W kg⁻¹) for a supercapacitor cell is given respectively in equations (2.27) and (2.28) (Zhi *et al.*, 2013).

$$E_{\max} = \frac{1}{2}CV^2 \quad (2.27)$$

$$P_{\max} = \frac{V^2}{4(ESR)} \quad (2.28)$$

Where ESR is equivalent series resistance of the cell (Ω). However, the power density can be also obtained from equation (2.29) (Zhi *et al.*, 2012).

$$P = \frac{E}{t} \quad (2.29)$$

Where t is the discharge time.

2.3.3 Electrochemical impedance spectroscopy (EIS)

Electrochemical impedance is the response of an electrochemical system (electrochemical cell) to an applied potential. The frequency dependence of this impedance can reveal underlying chemical processes of the electrochemical cell. The EIS study is always measured with a large timescale (from microseconds to hours), meaning that electrochemical processes are parted depending on their own time constant. In addition, such measurements are made under steady-state conditions that allow acquisition times high enough to get accurate measurements. Finally, in contrast to the previous techniques, small excitation signals are employed, permitting linearization of current–voltage characteristics. Actually, this last point means that this technique can be carried out by controlling either the current or the voltage, thus measuring either the voltage or the current. Here, the voltage control technique is focused on, but the same remarks or conclusions could be driven by controlling the current. In this technique, the response of electrochemical system is very nonlinear, so the observed frequency response behavior is fitted according to equivalent-circuit models of various complexities, supposedly simulating the behavior of the actual system, which evaluates the so-called “transfer function”. These equivalent circuit elements are commonly used: resistances, R ; capacitances, C ; Warburg impedance, W ; diffusion element, T , constant phase element, CPE ; and inductances, L . Their real or imaginary frequency response in the impedance Z is summarized in Table 2.7. The impedance of CPE (Z_{CPE}) is expressed as followed:

$$Z_{CPE} = \frac{1}{Y_0(j\omega)^\alpha} \quad (2.30)$$

where α is the dispersion exponent and Y_0 is the magnitude of the admittance ($= 1/Z$) at $\omega = 1 \text{ rad s}^{-1}$ ($\sim 0.16 \text{ Hz}$). Three particular situations can be found depending on the value of α are shown in Table 2.6.

Table 2.6 The impedance of resistor, Warburg, and Capacitor depending on the value of α .(Conway, 2013).

	$\alpha = 0$	$\alpha = 0.5$	$\alpha = 1$
Impedance	Resistor	Warburg	Capacitor
	$R = \frac{1}{Y_0}$	$W = \frac{1}{Y_0(j\omega)^{0.5}}$	$Z_{CPE} = \frac{1}{j\omega Y_0}$

$$\sigma = \frac{1}{(\sqrt{2} \cdot Y_0)} \quad (2.31)$$

In addition, Warburg coefficient (σ) obtained from equation (2.31) also being discussed and the most EIS results always reported using Nyquist plot of real (Z') and imaginary part (Z'') as displayed in Figure 2.20 (Conway, 2013; Lu *et al.*, 2013). The complex capacitance ($C(\omega)$), which obtained from EIS are expressed as followed.

$$C(\omega) = C'(\omega) - jC''(\omega) \quad (2.32)$$

$$C'(\omega) = \frac{-Z''(\omega)}{\omega|Z(\omega)|^2} \quad (2.33)$$

$$C''(\omega) = \frac{-Z'(\omega)}{\omega|Z(\omega)|^2} \quad (2.34)$$

where $C'(\omega)$ and $C''(\omega)$ are the respective real and imaginary part of complex capacitance. $Z'(\omega)$ and $Z''(\omega)$ are the real and imaginary part of complex impedance (Z), respectively. ω is angular frequency (Zhi *et al.*, 2012).

$$\tau = \frac{1}{f(\omega)} \quad (2.35)$$

Where τ is the time constant (s) and f_ω is the resonance frequency (Hz).

In this study the EIS was monitored over the frequency range, 10 mHz to 100 kHz at 0.1 V. The equivalent circuits of the cells were evaluated using Nova 1.11 software.

Table 2.7 The impedance of equivalent circuit component (Conway, 2013).

Component	$ Z $	Z'	Z''	Φ (rad)
Resistance	R	R	0	0
Capacitance	$1/C\omega$	0	$-1/C\omega$	$\pi/2$
Inductance	$L\omega$	0	$L\omega$	$-\pi/2$

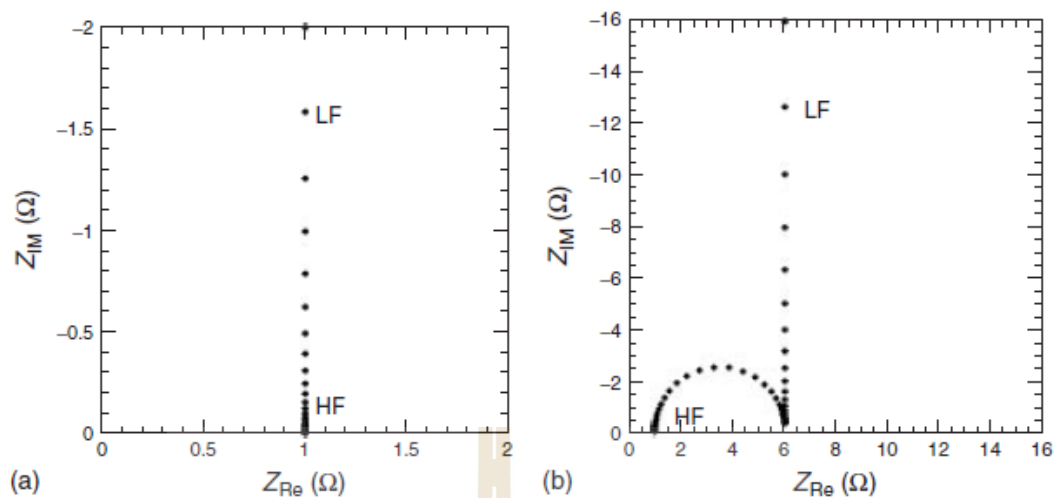


Figure 2.20 Nyquist plot of (a) an ideal electrical EDLC and (b) an ideal pseudocapacitor (Lu *et al.*, 2013).

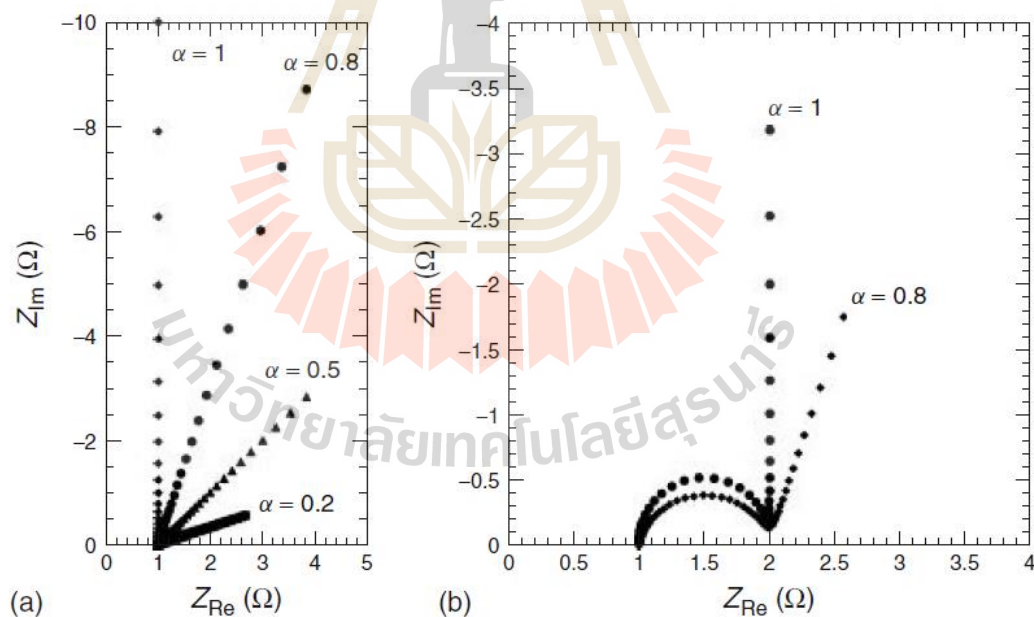


Figure 2.21 (a) Nyquist plot of a CPE for different values of α , (b) Nyquist plot of a pseudocapacitor including a CPE instead of C_{dl} (Lu *et al.*, 2013).

CHAPTER III

RESEARCH METHODOLOGY

This chapter explains the materials, apparatus, and fabrication method. Figure 3.1 represents the whole procedure of material preparation, including preparation of the solution, electrospinning, and calcination. The polymer and metal precursor were prepared as a solution. The precursor solution was changed into nanofibers using the electrospinning system and further calcined as composite carbon nanofibers by using a furnace tube.

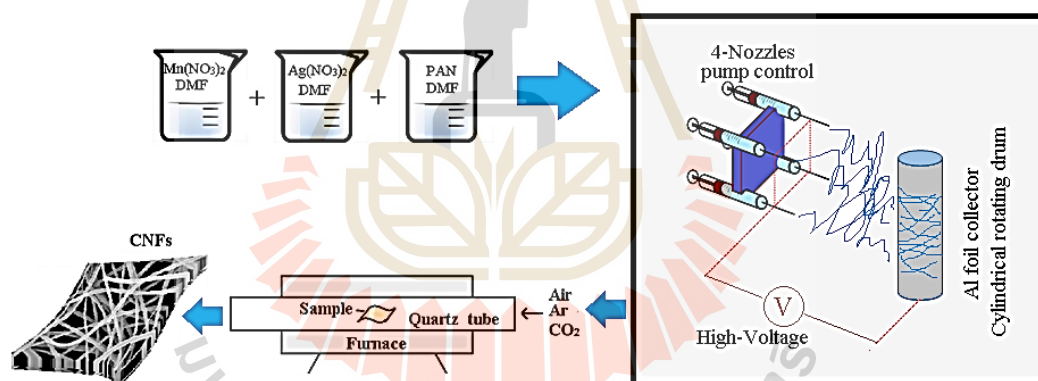


Figure 3.1 Schematic representation of composite CNF fabrication process and experimental apparatus.

3.1 Materials

- Polyacrylonitrile (PAN, Mw 150,000, Sigma-Aldrich, USA)
- Nickel nitrate ($Ni(NO_3)_2$, Sigma-Aldrich, USA)
- Copper nitrate ($Cu(NO_3)_2$, Sigma-Aldrich, USA)
- Silver nitrate ($AgNO_3$, Sigma-Aldrich, USA)

- Manganese nitrate ($\text{Mn}(\text{NO}_3)_2$, Sigma-Aldrich, USA)
- N’N-dimethylformamide (DMF, Sigma-Aldrich, USA)
- Potassium hydroxide (KOH, 90%, Sigma-Aldrich, USA)
- Sodium hydroxide (NaOH, 90%, Sigma-Aldrich, USA)
- Sodium chloride (NaCl, 90%, Sigma-Aldrich, USA)
- Lithium hydroxide (LiOH, 90%, Sigma-Aldrich, USA)
- Sodium sulfate (Na_2SO_4 , 90%, Sigma-Aldrich, USA)
- Lithium hexafluorophosphate (LiPF_6 , Gelon, China)
- Nickel foam 99.99% purity (MTI, USA)
- Stainless needle No.22
- Plastic syringe 10 ml.
- Platinum wire 0.5 mm in diameter (PT541009, ADVENT, England)
- Ag/AgCl reference electrode (Basi, MF-2079, USA)
- Nickel foam (MTI, USA)
- Tweezer
- Copper grid (Tedpellar, USA)
- High temperature silicone rubber O-ring (MTI, USA)
- Aluminum foil
- Copper foil
- Lithium foil (Gelon, China)
- Beaker
- Magnetic stirrer

3.2 Apparatus

- Electrospinning system SP04 (Figure 3.2)
- Furnace tube and Quartz tube, 1 inch in diameter (GSL-1100X,USA)
- Electrochemical station (AUTOLAB-PGSTAT302N, Netherlands)
- Air pump
- Gas feeding system (argon, nitrogen and carbon dioxide)
- Mass flow meter (MTI, USA)
- Quartz tube 50 OD×46 ID×60 L (MTI, USA)
- Vacuum flange for tube sealing (MTI, USA)
- Electric balance
- Ultrasonicator
- Incubator
- Hot Plate & Magnetic stirrer (IKA, C-MAG HS7)
- Hydraulic presser
- Coin cell crimping mold (Gelon, China)
- CO₂ tank

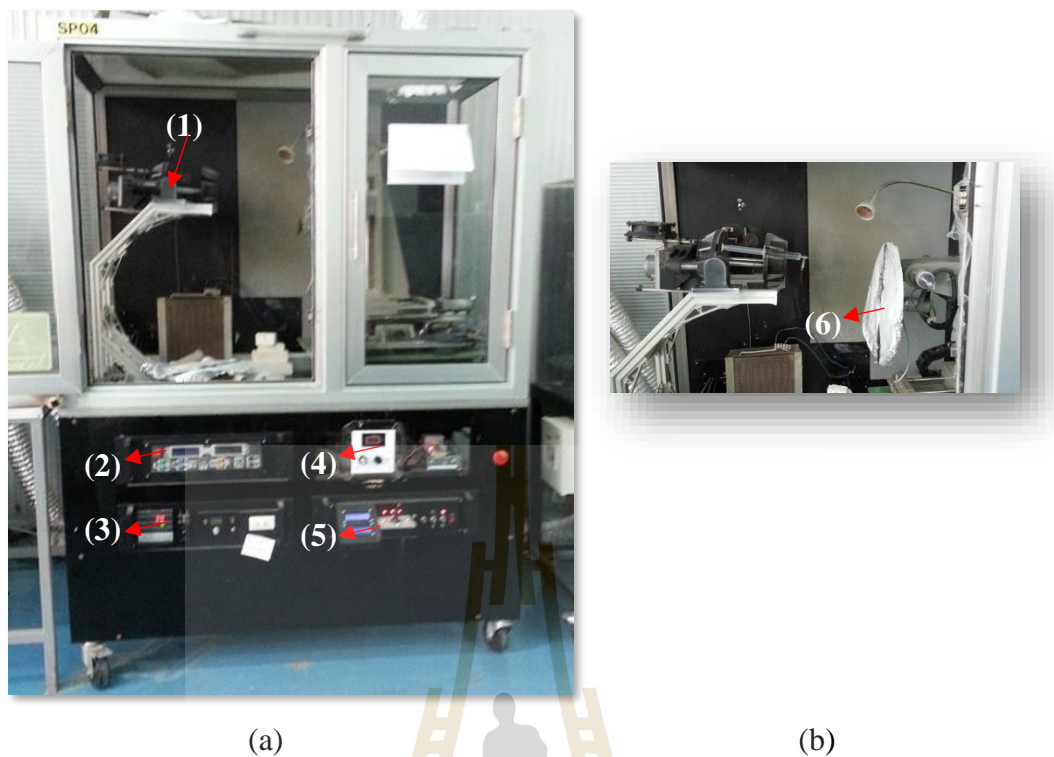


Figure 3.2 (a) The SP04-electrospinning system for electrospun composite nanofibers fabrication and (b) the rotating drum collector.

Figure 3.2 shows the SP04-electrospinning system used to fabricate electrospun composite nanofibers consisted of; 1) six-nozzle syringe pump, 2) pump control, 3) temperature control, 4) high voltage control, 5) drum control, and 6) rotating drum collector.

3.3 Fabrication of metal-metal oxide carbon-based nanofibers

3.3.1 Preparation of precursor solutions

In this work, the three groups of precursor solutions were prepared to obtain the difference CNF-based composite nanofibers, pure PAN for CNF, adding only one type of metal precursor for M/CMF, and two metal substrates simultaneous doping to achieve a more reinforcement of M-MO/CNF.

3.3.1.1 Preparation of pure PAN solution.

In this study, the pure precursor solutions were prepared by dissolving 10 wt.% PAN in DMF as a pristine sample. The solution was strongly stirred at room temperature for 3 h, then ultrasonicated for 3 h at 50 °C and subsequently stirred overnight at room temperature to obtain a homogeneous solution, which was then ready for electrospinning (Figure 3.3).

3.3.1.2 Preparation of precursor Ni(NO₃)₂/PAN, Mn(NO₃)₂/PAN, and AgNO₃/PAN solution.

For the composites, the metal sources including Ni(NO₃)₂, Mn(NO₃)₂, and AgNO₃ were added into a bare PAN/DMF solution with the weight content as listed in Table 3.1. After being strongly stirred at room temperature for 3 h, each solution was then mixed and then followed the same procedure of pure PAN solution preparing as describe above (Figure 3.3). The preparation of the composite precursor solution is shown schematically in Figure 3.4.

3.3.1.3 Preparation of AgNO₃-Mn(NO₃)₂/PAN solution.

The two elements of AgNO₃ and Mn(NO₃)₂ were added according to the ratio of each metal precursor which was varied as shown in Table 3.2 (for example, 20 wt.%), and the whole metal content was also prepared under different conditions as 5 wt.%, 10 wt.%, 20 wt.%, and 40 wt.% for comparison. The preparation of AgNO₃-Mn(NO₃)₂/PAN precursor solution is shown schematically in Figure 3.5.

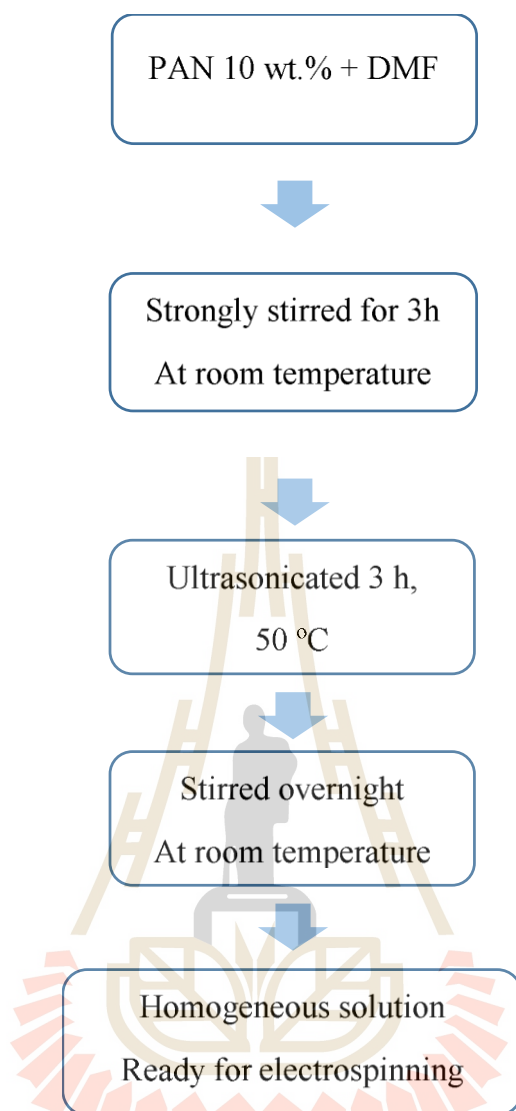


Figure 3.3 Diagram showing the preparation of pure PAN solution.

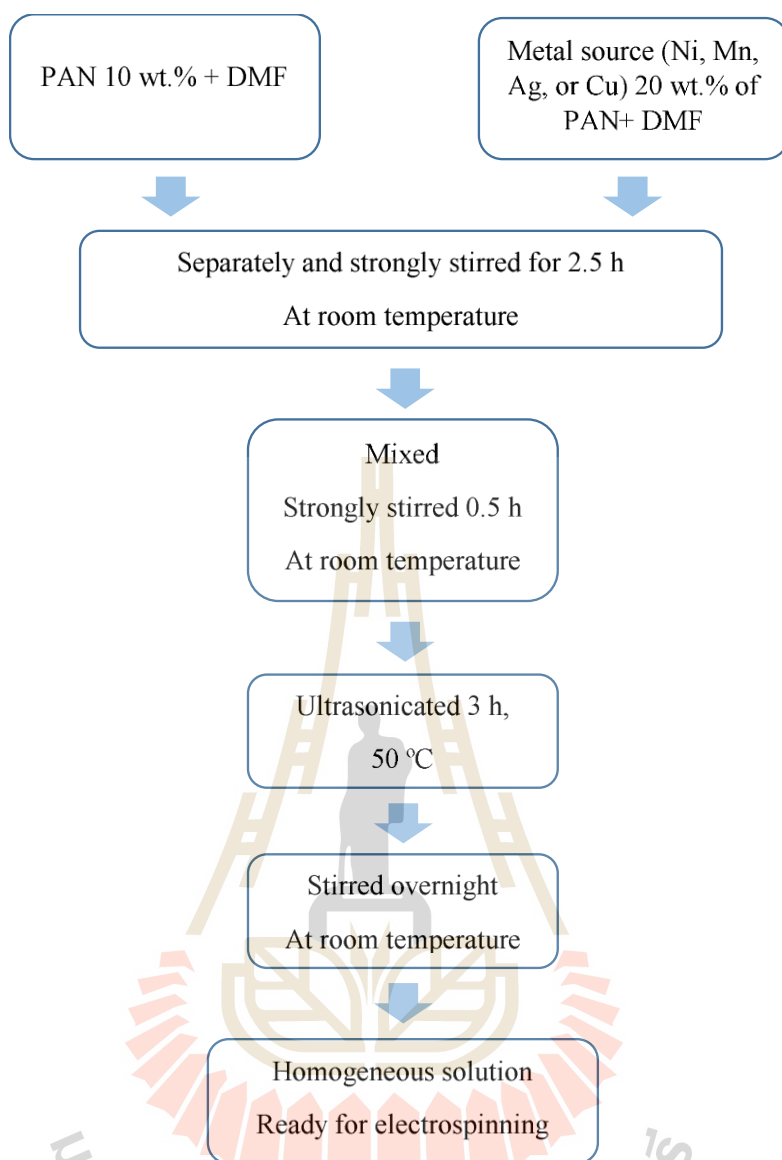


Figure 3.4 Diagram showing the preparation of the composite precursor solution.

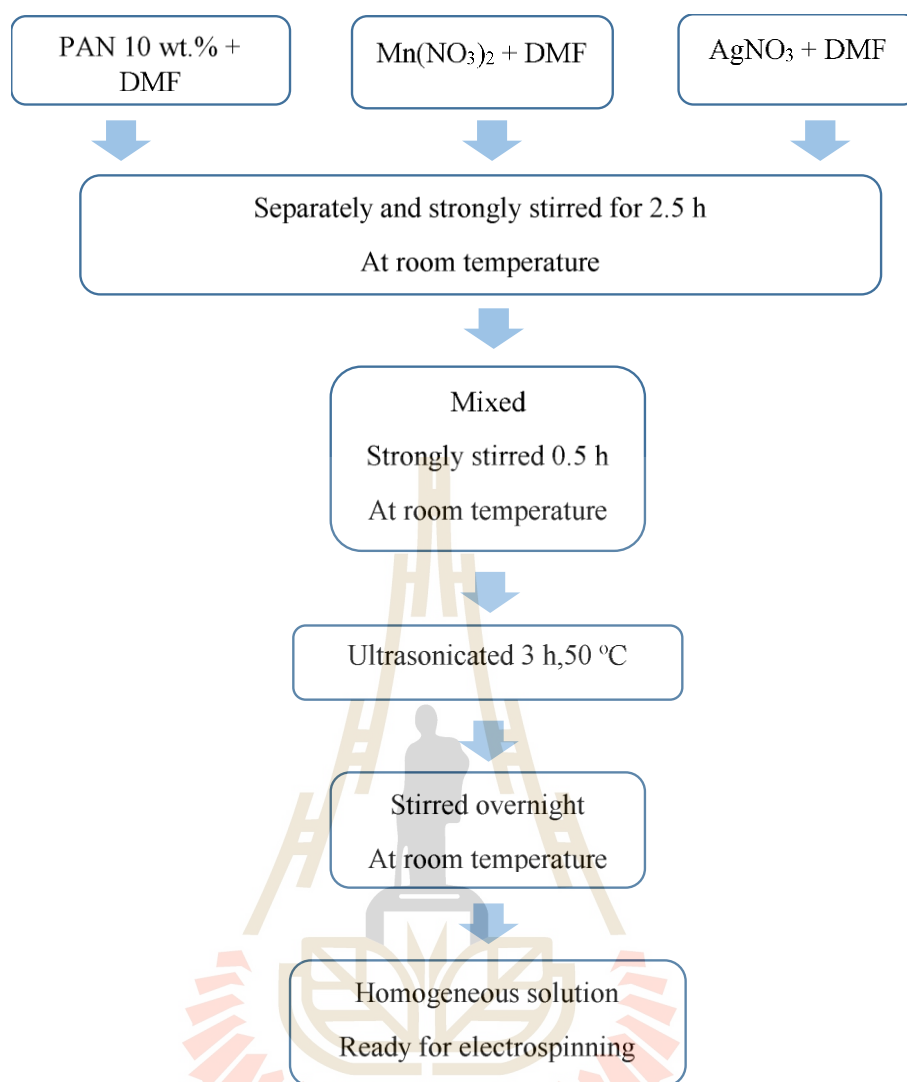


Figure 3.5 Diagram showing the preparation of AgNO₃-Mn(NO₃)₂/PAN precursor solution

Table 3.1 List of weight content of raw materials for the preparation of PAN-based solution.

Sample	The weight content		
	PAN	Metal source	DMF
	(mg)	(mg)	(mg)
PAN	4	-	40
Ni(NO ₃) ₂ /PAN-5 wt. %	4	0.2	40
Ni(NO ₃) ₂ /PAN -10 wt. %	4	0.4	40
Ni(NO ₃) ₂ /PAN -20 wt. %	4	0.8	40
AgNO ₃ /PAN -20 wt. %	4	0.8	40
Mn(NO ₃) ₂ /PAN -20 wt. %	4	0.8	40

Table 3.2 List of weight content of raw materials for the preparation of AgNO₃-Mn(NO₃)₂/PAN solution.

Sample	The weight content			
	PAN (mg)	AgNO ₃ (mg)	Mn(NO ₃) ₂ (mg)	DMF (mg)
Controlled metal source at 20wt% with various ratios				
AgNO ₃ -Mn(NO ₃) ₂ /PAN -20(25:75)	4	0.2	0.6	40
AgNO ₃ -Mn(NO ₃) ₂ /PAN-20(50:50)	4	0.4	0.4	40
AgNO ₃ -Mn(NO ₃) ₂ /PAN -20(75:25)	4	0.6	0.2	40
The ratio of AgNO ₃ :Mn(NO ₃) ₂ sources was controlled and the weight content varied				
AgNO ₃ -Mn(NO ₃) ₂ /PAN -10(25:75)	4	0.1	0.3	40
AgNO ₃ -Mn(NO ₃) ₂ /PAN -20(25:75)	4	0.2	0.6	40
AgNO ₃ -Mn(NO ₃) ₂ /PAN -40(25:75)	4	0.4	1.2	40

3.3.2 Electrospinning of nanofibers

The electrospinning process was setup as exhibited in Figure 3.6, the homogenous precursor solution was loaded into a 10-ml syringe and delivered to a stainless-steel needle (No.22). The parameters for electrospinning were as follows: the applied voltage was 10-12 kV, the tip-collector distance (TCD) was fixed at 18 cm, and the solution flowing rate was 0.3-0.5 ml h⁻¹ depending on the concentration of the metal source added in the precursor solution. The electrospun fibers were collected as a random woven sheet on a rotating aluminum foil drum which was connected to the

ground electrode. The sheet of as-spun nanofibers was removed from the drum every 6 h and then stored in an incubator at 70 °C at least 24 h before calcination.

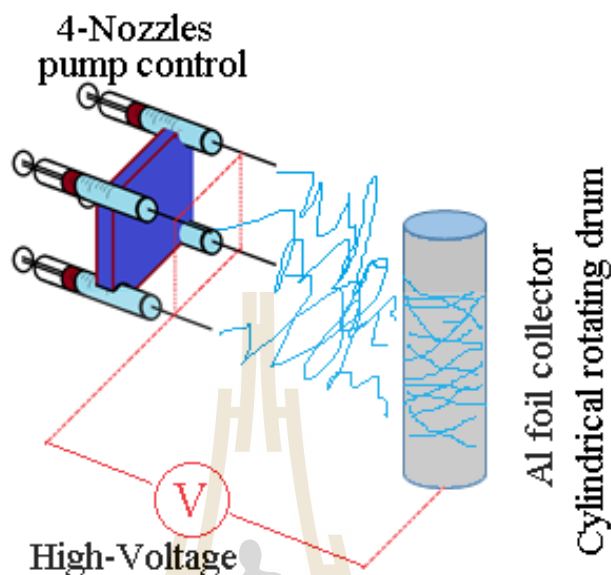


Figure 3.6 Diagram showing the electrospinning setup.

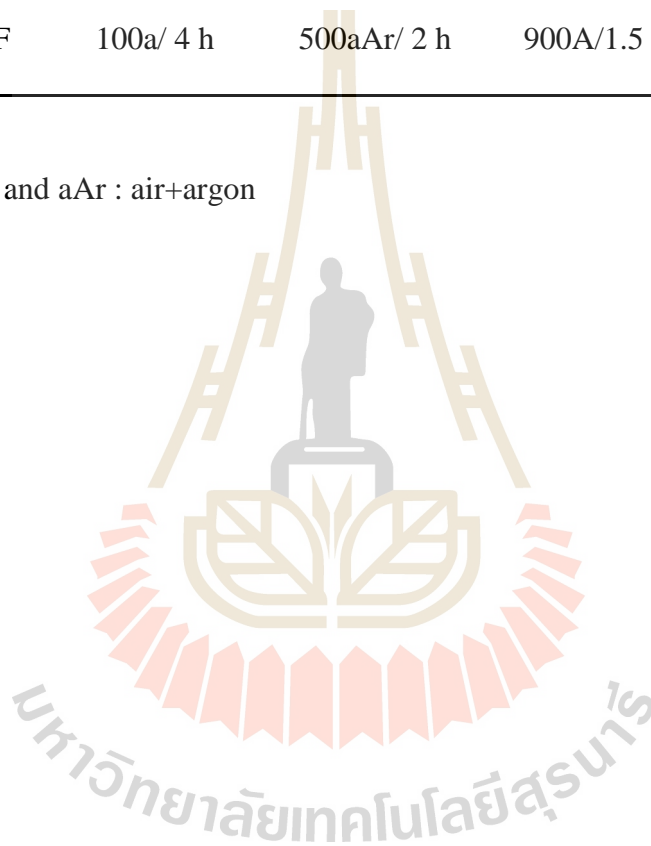
3.3.3 Calcination and activation of as-spun nanofibers

The typical heating process of the overall calcination process consists of three steps, including stabilization, carbonization, and activation as shown schematically in Figure 3.7 which were carried out using the apparatus as described in Figure 3.8. The as-spun sheet was stabilized in a mild temperature of 100 °C using a furnace tube for 4 h under air atmosphere to form an infusible ladder polymer before calcination (Lee *et al.*, 2010). Subsequently, the gas was then switched to argon (300 ml min^{-1}) and the temperature was increased with a heating rate of 5 °C min^{-1} between 500 and 900 °C, and the holding time was 2 h at each step for metallization (Fritsch *et al.*, 1998) and carbonization, respectively. During the last 30 min at 900 °C, the gas was then changed to CO_2 for an activation process (Ra *et al.*, 2009). Finally, the gas was switched back to argon again and cooled down naturally (Table 3.1).

Table 3.3 Calcination procedure of each composite.

Expected sample	Calcination procedure/temperature (°C)			
	Stabilization	Metallization	Carbonization	Activation
CNF	100a/ 4 h	500aAr/ 3.5 h	-	500CO ₂ /0.5 h
NiO/CNF	100a/ 4 h	500aAr/ 3.5 h	-	500 CO ₂ /0.5 h
Ni/CNF	100a/ 4 h	500Ar/ 2 h	900A/1.5 h	900 CO ₂ /0.5 h
Ni-NiO/CNF	100a/ 4 h	500aAr/ 2 h	900A/1.5 h	900 CO ₂ /0.5 h

Note a :air and aAr : air+argon



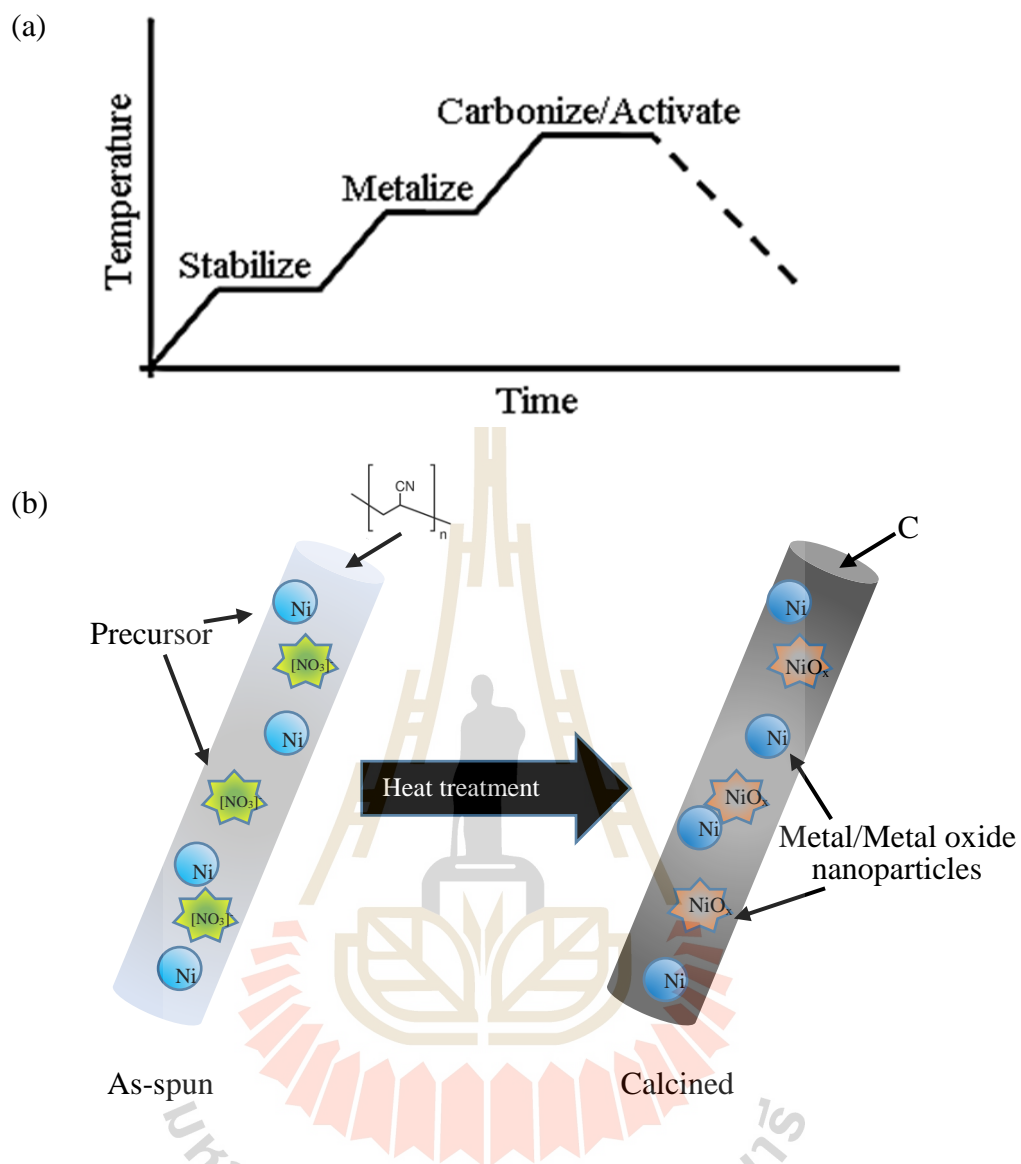


Figure 3.7 (a) Diagram showing the typical calcination process consisting of three steps, including stabilization, carbonization, and activation. (b) The expected composite carbon nanofibers after calcination.

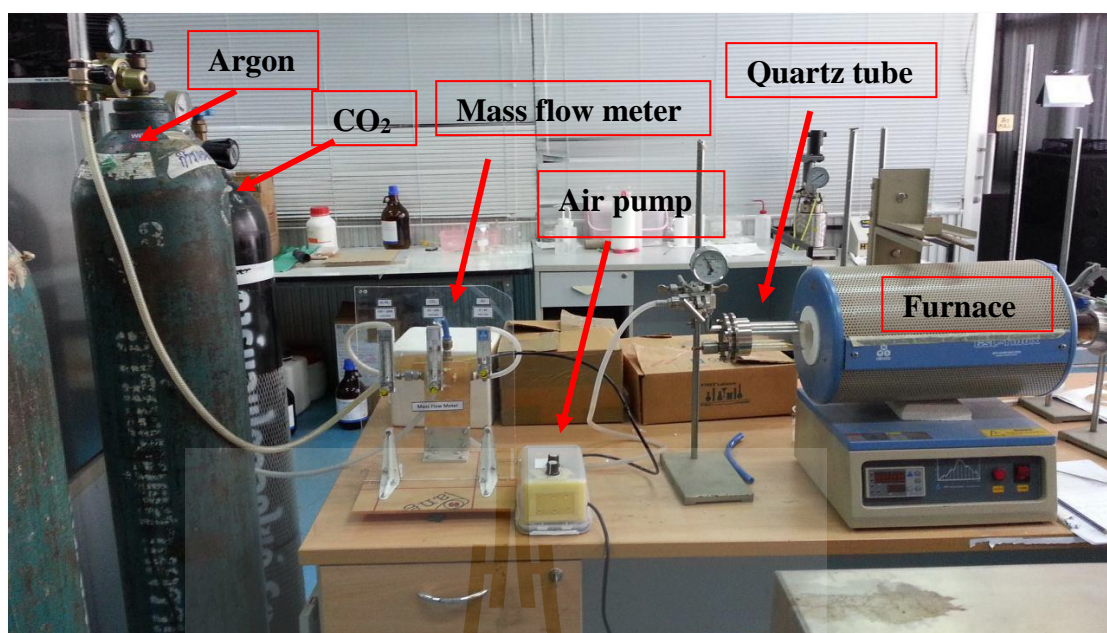


Figure 3.8 Instrumentation setup of sample calcination.

3.4 Materials characterization

3.4.1 Thermogravimetric analysis

The thermogravimetric analysis and differential scanning calorimetry (TGA/DSC) are the techniques used to study the thermal characteristics of substances, especially polymers. The weight losses of the sample during heat treatment are evidence of polymer structure deformation or decomposition that can be helpful for consideration of the proper temperature for calcination of as-spun polymer nanofibers. In this work, the thermal stability and exothermic reaction of all the samples were carried out in N₂ atmosphere (100 ml min⁻¹) in the temperature range of 25-1000 °C with a heating rate of 10 °C min⁻¹ using Mettler TOLEDO.

3.4.2 Scanning electron microscopy

Scanning electron microscopy (SEM) is a powerful technique for materials examination. A high-energy beam of electrons is focused on the surface of the

specimen and which then generates a variety of signals. The signals reveal information about the sample, including external morphology, chemical composition, and the orientation of materials making up the sample. In this work, the samples were held on a metal stub and coated in a vacuum gold coating for 9-12 min⁻¹ before SEM analysis. FESEM JEOL JSM 7800X was employed to investigate external morphologies, such as surface, diameter size, and fibers arrangement etc. of both the as-spun and calcined sample.

3.4.3 Transmission electron microscopy

Transmission electron microscopy (TEM) is a microscopy technique to observe internal morphology and particle size distribution. High resolution images can be recorded by the transmission of electron beams through an ultra-thin specimen, magnified and focused by an objective lens. The specimen needs to be thin enough to be transparent for electrons. In this study, the sample was dispersed in ethanol and then dripped and dried on a copper grid. Bright Field Transmission Electron Microscopy (TEM) FEI Tecnai G2 20 200kV was used to investigate the internal microstructure and the distribution of the reinforcements were embedded in composite CNF.

3.4.4 Surface area and porosity

In surface area and porosity analysis, a sample is exposed to N₂ gas of different pressures at a given temperature (usually at -196 °C, the liquid-nitrogen temperature). Increments of pressure result in increased amounts of N₂ molecules being adsorbed on the surface of the sample. The pressure at which the adsorption equilibrium is established is measured and the universal gas law is applied to determine the quantity of N₂ gas adsorbed. Thus, an adsorption isotherm is obtained

(Figure 3.9). If the pressure is systematically decreased to induce desorption of the adsorbed N₂ molecules, then a desorption isotherm is obtained.

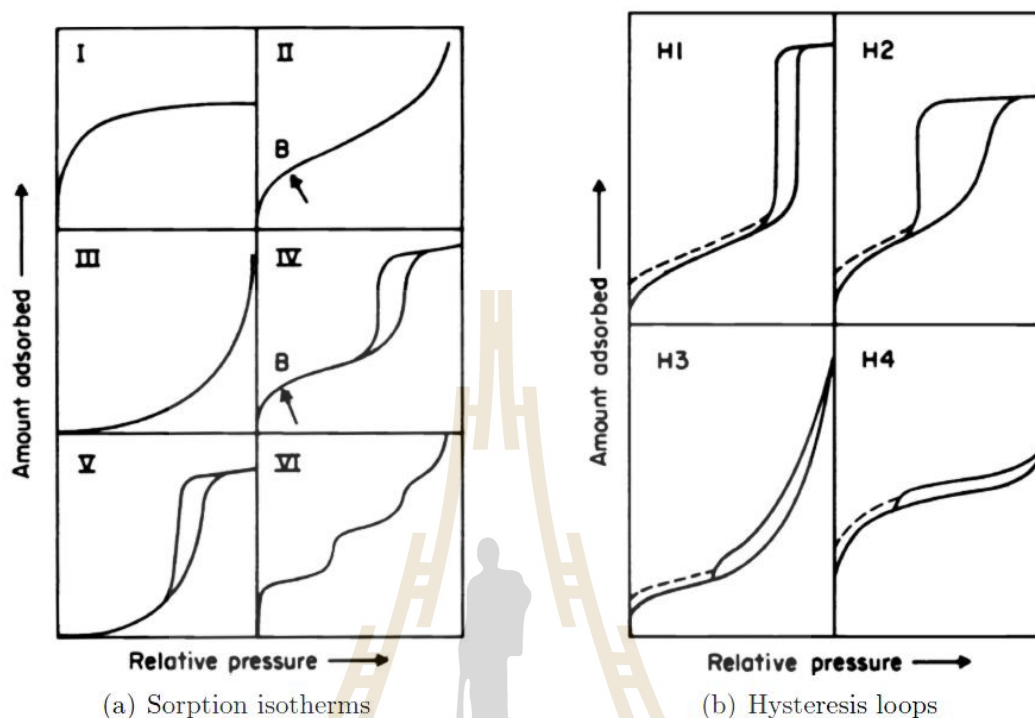


Figure 3.9 Type of sorption isotherms and hysteresis loops (IUPAC 1985, (Gubbins, 2009))

Analysis of the adsorption and desorption isotherms in combination with some physical models yields information about the pore structure of the sample, such as surface area, pore volume, pore size and surface nature (Gubbins, 2009). In this study, the samples were degassed at 150 °C for 6 h and then the N₂ adsorption/desorption isotherms were measured at 77 K using an automatic specific surface area/pore size distribution analyzer BELSORP-miniII. The Brunauer-Emmett-Teller (BET) method was used to describe the specific surface;

$$\frac{1}{W((P_0/P)-1)} = \frac{1}{W_m C} + \frac{C-1}{W_m C} \left(\frac{P}{P_0} \right) \quad (3.1)$$

where W is the weight of gas adsorbed, P/P_0 is the relative pressure, W_m is the weight of adsorbate as monolayer, and C is the BET constant. The total surface area (S_B) can then be derived as follows:

$$S_B = \frac{W_m N A_{CS}}{M} \quad (3.2)$$

where N is Avogadro's number (6.023×10^{23}), M is the molecular weight of the adsorbate, and A_{CS} is adsorbate cross section area (16.2 \AA^2 for nitrogen). The total pore volume (V_T) is derived from the amount of vapor adsorbed at a relative temperature close to unity by the following equation:

$$V_T = \frac{P_a V_{ads} V_m}{RT} \quad (3.3)$$

Where V_{ads} is the volume of gas adsorbed, V_T is the volume of liquid N_2 in total pore, V_m is molar vol. of liquid adsorbate, P_a is ambient pressure, R is gas constant ($8.314 \text{ J K}^{-1} \text{ mol}^{-1}$), and T is ambient temperature. The average pore size is estimated from the pore volume assuming cylindrical pore geometry (type A hysteresis), the average pore radius (r_p) can be expressed as follows:

$$r_p = \frac{2V_T}{S_B} \quad (3.4)$$

The Barrett-Joyner-Halenda method (BJH) and Brunauer's MP (MP) methods were employed to determine the pore character of the samples. The pore size distribution was classified according to three regions:

Micropore < 2 nm < Mesopore < 50nm < Macropore.

3.4.5 Fourier transform infrared spectroscopy

An FTIR spectrometer records the interaction of infrared radiation with a sample by measuring the frequencies at which the sample absorbs the radiation and

the intensities of the absorptions. Chemical functional groups are known to absorb light at specific frequencies. Thus, the chemical structure can be determined from the frequencies recorded. In this thesis work, FTIR spectra were analyzed using Bruker Tensor 27 with a resolution of 4 cm^{-1} in the wavelength range of $400\text{-}4000\text{ cm}^{-1}$. The samples were prepared without potassium bromide mixing (KBr).

3.4.6 Raman spectroscopy

Raman spectroscopy is a popular nondestructive, ambient probing tool to characterize the structure of materials and usually imposes very little constraint on the substrate size. When a light quantum $h\nu_0$ hits a surface, an elastic scattering process, that is, Rayleigh scattering of quanta with energy $h\nu_0$ ensues. This process has the highest probability. However, there also exists an inelastic process in which the vibrational energy is altered by $h\nu_s$. The inelastic process is called Raman scattering and quanta of energy $h\nu_0 \pm h\nu_s$ are emitted. Because vibration of the atoms in the excited state is much less than that of the ground state atoms at ambient temperature according to Boltzmann's law, it is more efficient to excite ground-state atoms to a vibrationally excited state than to receive the decay energy from the vibrating atoms. Hence, the emitted quanta having energy of $h\nu_0 - h\nu_s$ are more prevalent than the emitted quanta with energy of $h\nu_0 + h\nu_s$. The Raman lines corresponding to the quanta with energy of $h\nu_0 - h\nu_s$ are referred to as the Stokes lines whereas the higher energy lines ($h\nu_0 + h\nu_s$) are called the anti-Stokes lines. As the intensities of the anti-Stokes lines are lower, only the Stokes lines are usually recorded in the Raman spectrum. The light scattering process is illustrated in Figure 3.10. Raman spectroscopy is a very effective way to investigate the detailed bonding structure of carbon films. Though there is still debate on the exact relationship between the atom vibration and Raman spectra, the method

is the most widely used to distinguish the bonding type, domain size, and sensitivity to internal stress in amorphous and nanocrystalline carbon films. Raman spectra are usually discussed in the context of diamond versus graphite as carbon films are composed of short distance ordered sp^3 and sp^2 bonds (Chu and Li, 2006).

In this study, Raman Spectroscopy was observed between 100 and 3200 cm^{-1} using JOBIN YVON HORIBA T64000, laser wave length of 532 nm, to characterize the carbon structures of all calcined nanofibers.



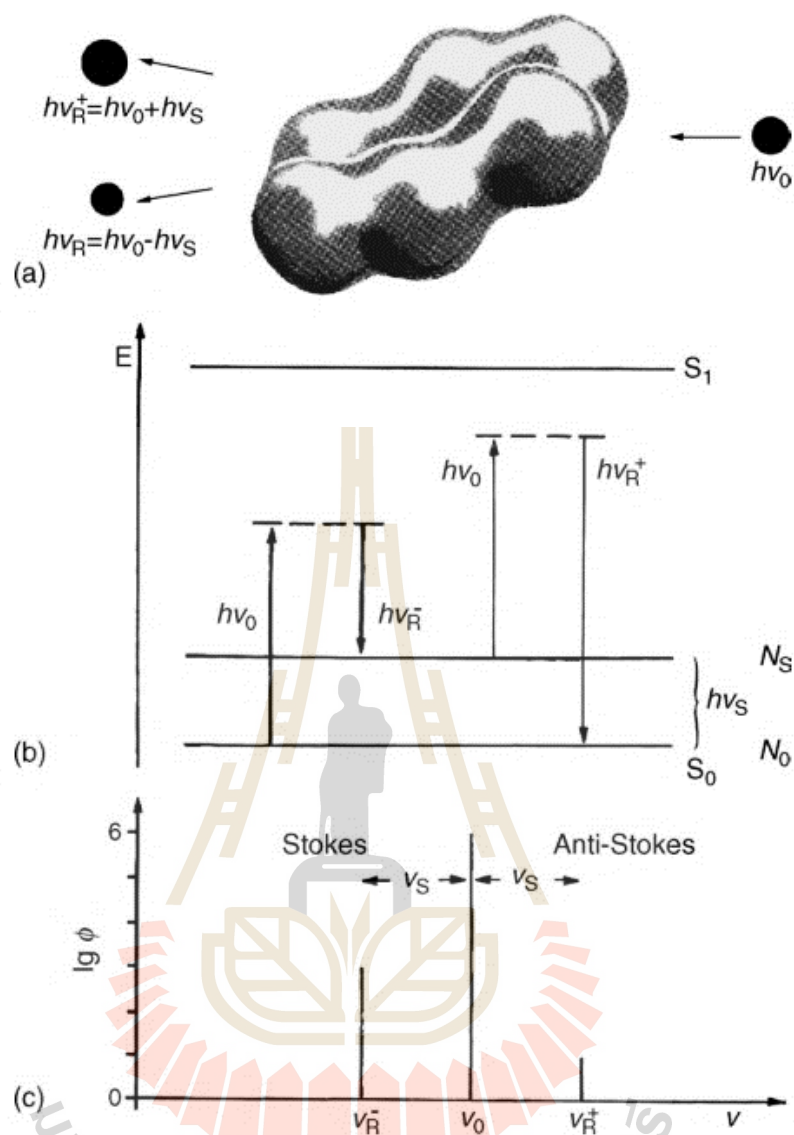


Figure 3.10 Schematic diagram of the principle of Raman scattering: (a) inelastic scattering of an optical quantum hitting the materials; (b) term diagram; (c) Raman spectra. Because the vibration of atoms in the excited state is much less than that of the ground state atoms, the Stokes line is stronger than the anti-Stokes line (Chu and Li, 2006).

3.4.7 X-ray diffraction

X-ray Diffraction (XRD) is an accepted technique to discover the crystalline structures of any materials. The structural parameters, such as the lattice constant (a), the crystallite size (D) and the atomic spacing (d) are obtained from this technique. The basic concept is based on the interference phenomenon of two waves with the same wavelength and traveling in the same direction to the sample. The constructive and destructive interferences occur if a phase difference is $n\lambda$ (in phase) and $n\lambda/2$ (out of phase), respectively. The schematic principle of XRD equipment is presented in Figure 3.11 and these principles obey Bragg's equation:

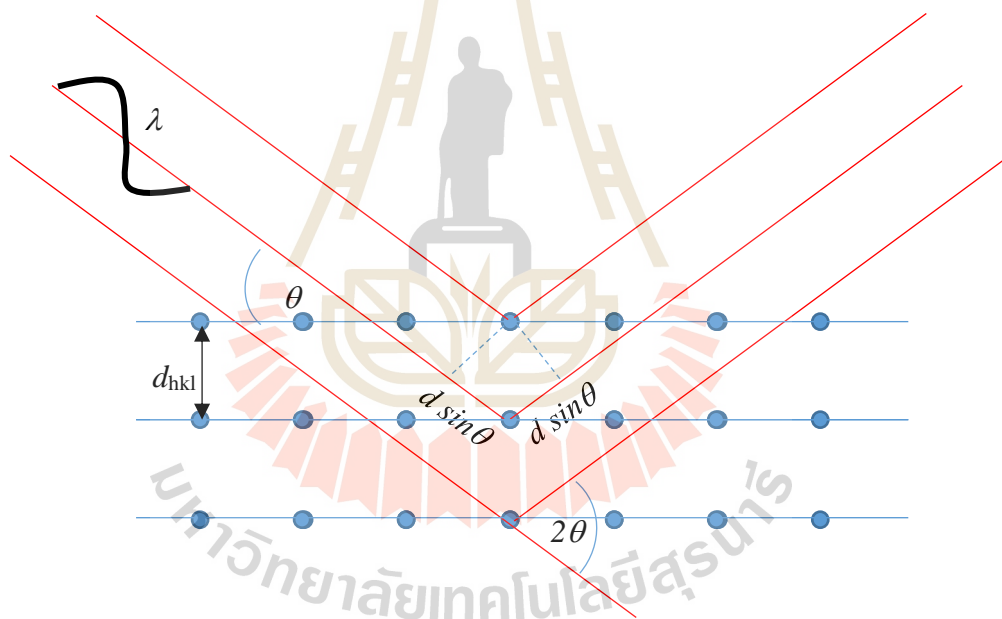


Figure 3.11 Diagram represents the principles of XRD.

In this work, the calcined nanofibers were studied using an X-ray Diffraction Bruker D2 Phaser. The crystal size of the calcined samples was evaluated using the Scherrer equation as follows.

$$D_{hkl} = \frac{K\lambda}{\beta \cos\theta} \quad (3.5)$$

Where: D_{hkl} is the mean size of the ordered (crystalline) domains, which may be smaller or equal to the grain size. K is a dimensionless shape factor with a value close to unity. The shape factor has a typical value of 0.89, but it varies with the actual shape of the crystallite. λ is the X-ray wavelength ($\lambda_{CuK\alpha} = 1.5418 \text{ \AA}$). β is the line broadening at half the maximum intensity (FWHM) after subtracting the instrumental line broadening in radians. This quantity is also sometimes denoted as $\Delta(2\theta)$ and θ is the Bragg angle.

3.4.8 X-ray absorption near edge structure

X-ray absorption near-edge structure (XANES) analysis at the Mn K -edge, Ni K -edge and Ag L_3 -edge were performed at room temperature using a fluorescent spectroscopy beamline available at the Synchrotron Light Research Institute (BL 5.2 SUT-NANOTEC-SLRI XAS) of Thailand. The spectra were measured in the width range of 120 eV with an energy step of 0.2 eV in both the pre- and post-edge regions. The spectra were evaluated using Athena software. Linear combination fitting was also employed to study the metal clusters mapping in as-prepared composite carbon nanofibers.

$$I = I_0 e^{-\mu t} \quad (3.6)$$

X-ray absorption near-edge structure (XANES) analysis at the Mn K -edge, Ni K -edge and Ag L_3 -edge were performed at room temperature using a fluorescent spectroscopy beamline available at the Synchrotron Light Research Institute (BL 5.2 SUT-NANOTEC-SLRI XAS) of Thailand. The spectra were measured in the width range of 120 eV with an energy step of 0.2 eV in the both pre- and post-edge regions. The spectra

were evaluated using Athena software. Linear combination fitting was also employed to study the metal clusters mapping in as-prepared composite carbon nanofibers.

3.5 Electrochemical properties evaluation

3.5.1 Electrode preparation

The as-prepared samples were assembled as working electrodes using 2 mg of each calcined sample sandwiched between the nickel foam (1cm (width)×2cm (length)) without any binder and then pressed at 2 kPa for 1 min using an hydraulic press machine (Ye *et al.*, 2013) following each step in Figure 3.12, the electrodes were kept in a soaked condition in electrolyte for at least 6 h and then they were ready for installing in an electrochemical cell.

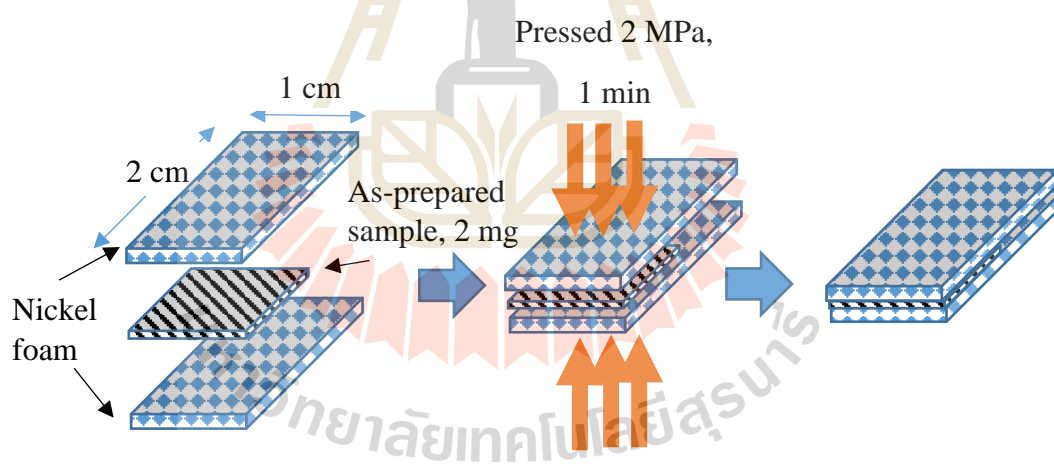


Figure 3.12 Schematic representation of a working electrode preparation.

3.5.2 Electrolyte preparation

In order to study the effect of electrolyte on electro chemical properties of the samples, the various electrolyte solutions consisting of KOH 1.5, NaOH, LiOH, and Na_2SO_4 were used for electrochemical study (Table 3.4). They were prepared based

on an aqueous solution by dissolving the substrate in distilled water. The concentration was calculated by following equation:

$$\text{Molar concentration} = \frac{\text{Amount in mole}}{\text{Volume of solution}} \quad (3.7)$$

Table 3.4 List of materials used for aqueous electrolyte preparation.

Electrolyte	Substrate	Total volume (ml)
	(g)	
KOH 1.5 M	21.04	250
KOH 3 M	42.08	250
KOH 6 M	84.15	250
LiOH 3 M	17.96	250
NaOH 3 M	29.99	250
Na ₂ SO ₄ 1.5 M	53.27	250

3.5.3 Electrochemical cell setup

A three-electrode electrochemical cell was placed in 6 M KOH aqueous solution to study an effect of difference composition while the other electrolyte are used to study the effect of electrolyte on electrochemical properties of the electrode, the high concentration of the alkaline electrolyte was to ensure that no ion starvation occurred during the charge/discharge measurement process (Kandalkar *et al.*, 2010). Platinum wire and Ag/AgCl were counter and reference electrodes, respectively. The as-prepared samples were the working electrodes (Figure 3.13). The cell was connected to Metrohm Autolab PGSTAT302N potentiostat/galvanostat system to

perform the experiment at room temperature (Figure 3.14). The experiment procedures were controlled and evaluated using Nova software.

3.5.4 Cyclic voltammetry

In this study, the CV was measured within potential windows of -1-0 V (Avoidance of oxygen and hydrogen evolution (Conway and Gileadi, 1962)) and scan rates of 2, 5, 10, 20, 50, 100, 200, and 500 mV s^{-1} . The effect of voltage potential windows on specific capacitance was also studied.

3.5.5 Galvanostatic charge/discharge testing

In this study, the GCD testing was observed over the same voltage window as same as CV measurement at the current density ranges of 0.5, 1, 2, 5 and 10 A g^{-1}

3.5.6 Electrochemical impedance spectroscopy

In this study the EIS was monitored over the frequency range, 10 mHz to 100 kHz at 0.1 V using galvanostatic mode. The equivalent circuits of the cells were evaluated using Nova 1.11 software.

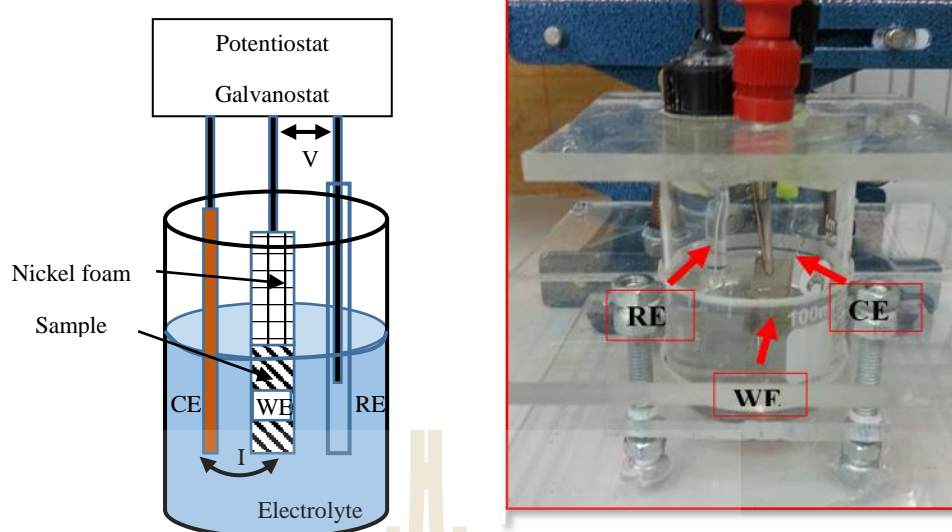


Figure 3.13 Three-electrode electrochemical cell setup. Reference electrode (RE) is Ag/AgCl, counter electrode (CE) is platinum wire, and working electrode (WE) are prepared from the fabricated samples.

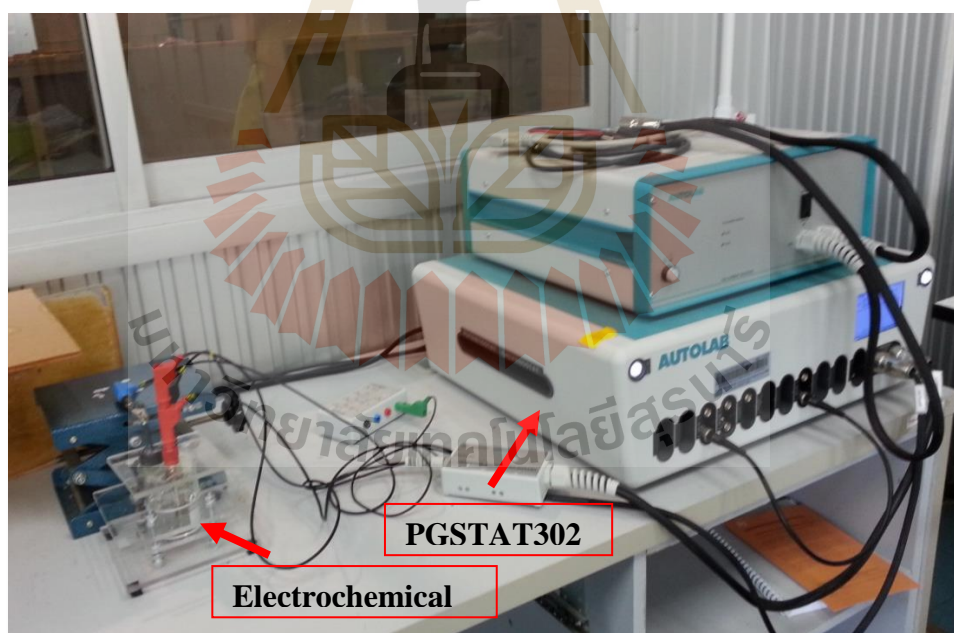


Figure 3.14 Electrochemical experiment setup. Inset: Three-electrode electrochemical cell setup. Reference electrode (RE) is Ag/AgCl, counter electrode (CE) is platinum wire, and working electrode (WE) are prepared from the fabricated samples.

CHAPTER IV

RESULTS AND DISCUSSION

This chapter presents the results and discussion of prepared samples in four main sections depending on the material composition consisting of nickel composite carbon-based nanofibers (NiO_x/CNF), silver composite carbon-based nanofibers (AgO_x/CNF), manganese composite carbon-based nanofibers (MnO_x/CNF), and silver-manganese composite carbon-based nanofibers ($\text{AgO}_x\text{-MnO}_x/\text{CNF}$). Each section consists of fabrication, characterization, and electrochemical study. The effect of electrospinning parameters on fiber formation and its properties were only studied for a group of NiO_x/CNF . The characterization of the samples was done by various techniques in order to understand thermal stability, morphology, microstructure, and porosity using thermogravimetric analysis and differential scanning calorimetry (TGA/DSC), scanning electron microscope (FESEM), Transmission Electron Microscopy (TEM), Fourier Transform Infrared Spectroscopy (FTIR), Raman spectroscopy, X-ray Diffraction (XRD), X-ray absorption near edge structure (XANES), and Brunauer-Emmett-Teller (BET) method. Finally, in order to understand the electrochemical properties of as-prepared samples, three electrochemical techniques including cyclic voltammetry (CV) galvanostatic charge/discharge testing (GCD) and electrochemical impedance spectroscopy (EIS) were evaluated to explain the capacitive behavior, pseudocapacitive behavior, equivalent circuit of the samples, and also cycling stability.

4.1 Fabrication of electrospun carbon-based composite nanofibers.

4.1.1 Effect of applied voltage on the morphology of electrospun nanofibers

The solution of PAN (10 wt.%) and $\text{Ni}(\text{NO}_3)_2$ (5 wt.% of PAN) dissolving in DMF was originated to roughly study the effect of applied voltage on the morphology of electrospun nanofibers. The $\text{Ni}(\text{NO}_3)_2$ /PAN precursor solution was loaded into a 10 ml syringe which was connected with the stainless nozzle tip No.22 and then installed in 4-nozzle electrospinning station. The electrospinning was done at a solution flow rate of 0.5 ml h^{-1} and TCD of 18 cm. The various applied voltages of 8, 10, 12, and 14 kV were decided to study the effect of applied electric field on as-spun nanofibers. The as-spun nanofibers collected on aluminum foil drum as the non-woven nanofibers sheet and it was removed from the foil every 6 h, the flexible sheet had an average thickness of around 40-100 μm Figure 4.1. The morphology of electrospun $\text{Ni}(\text{NO}_3)_2$ /PAN at various conditions was observed using SEM (Figure 4.2). All samples appeared the random arrangement of nanofibers caused by bending process of charge moving in the very high nonuniform electric field before arrived the collector (Yang *et al.*, 2008). The histograms displayed the approximate Gaussian distribution of diameter size for all samples. Even the most as-spun samples show the long uniform fibrous, it can be seen that the nanofibers appeared more beads as the applied voltage increased (Figure 4.3). The average diameter of electrospun $\text{Ni}(\text{NO}_3)_2$ /PAN nanofibers at various applied voltage slightly decreased as applied voltage increased. Even this results indicated that the applied voltages did not significantly effect on the diameter of nanofibers (Beglou and Haghi, 2008), it obviously resulted on more beads formed on nanofibers. However, the affection of the applied voltages on the diameter of

electrospun fibers is a little controversial and it always discussed together with another parameter such as concentration, molecular weight, viscosity, surface tension, flow rate, and TCD (Li and Wang, 2013).

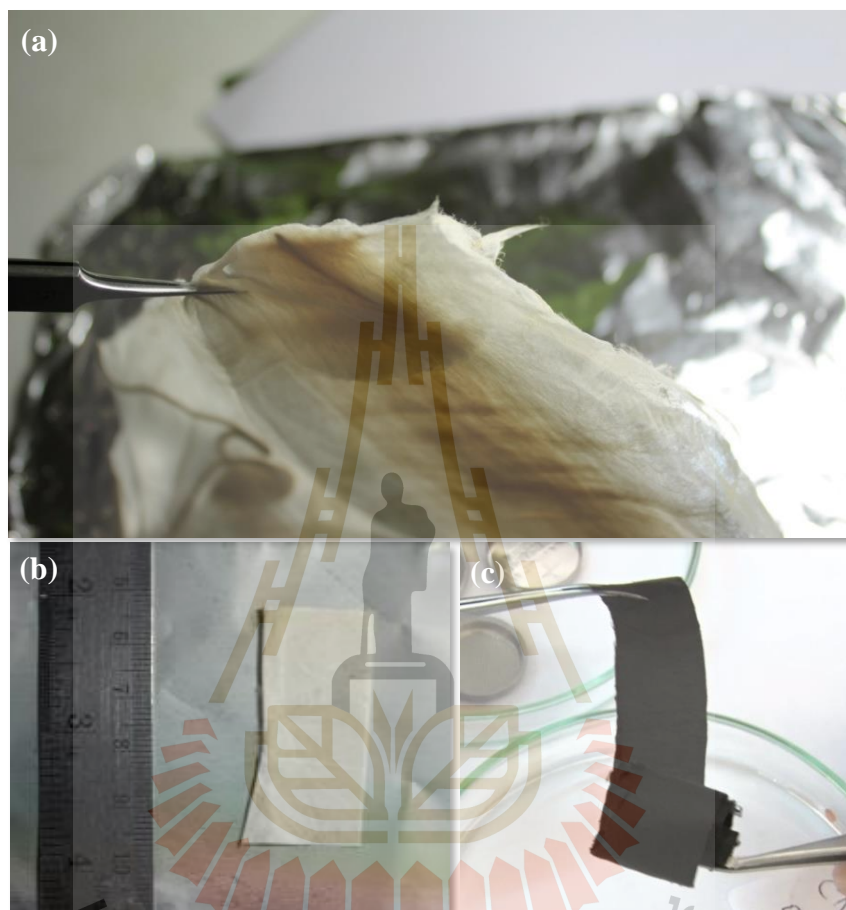


Figure 4.1 (a) The electrospun nanofibers sheet on aluminum foil, (b) it was cut as a dimension of around 1.5×4 cm before putting in the crucible for calcination, and (c) the sample after calcination.

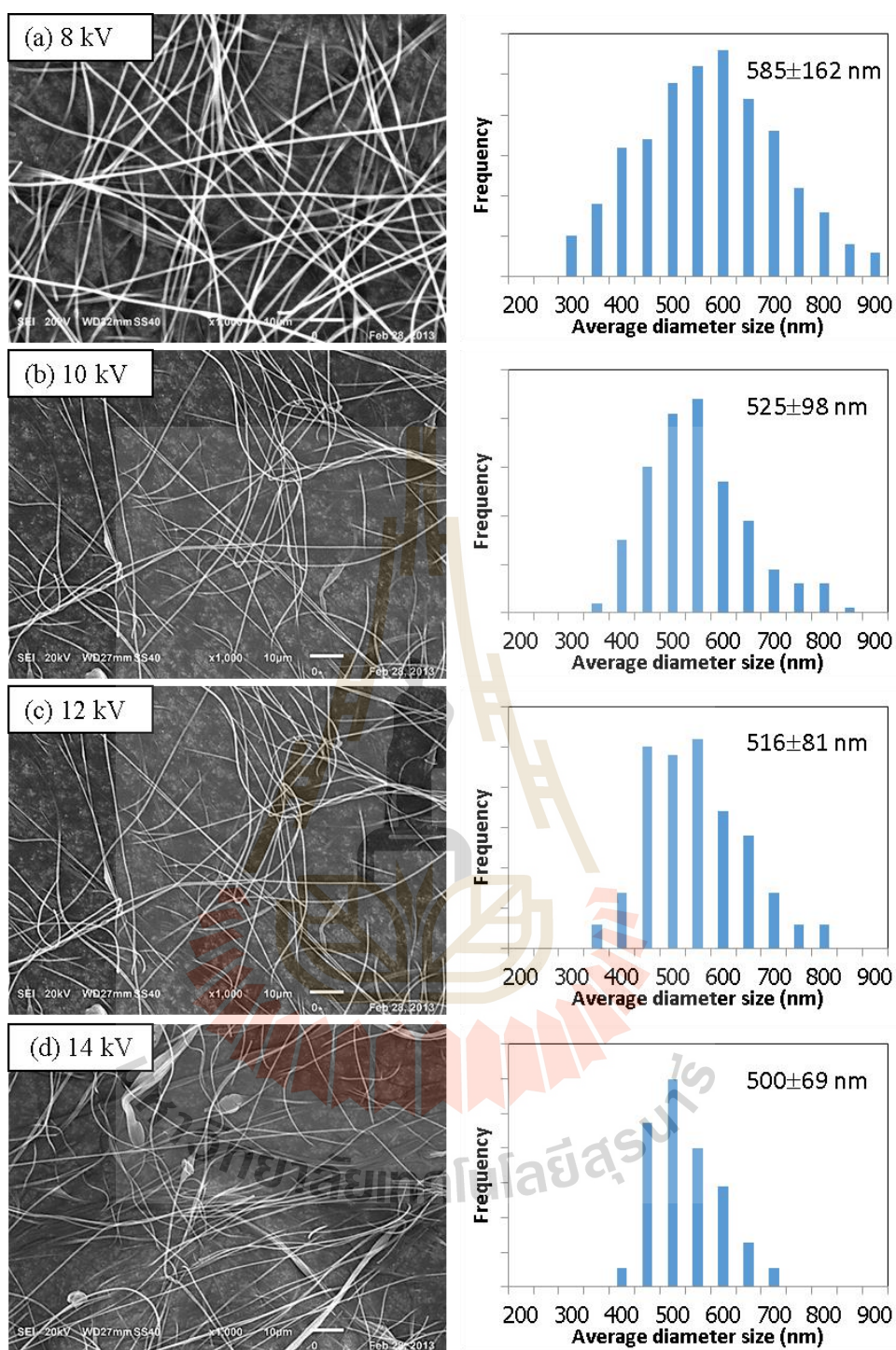


Figure 4.2 SEM images of Ni(NO₃)₂/PAN (5 wt.%) electrospun at various applied voltages of (a) 8 kV, (b) 10 kV, (c) 12 kV, and (d) 14 kV. The histograms on the right-hand side show the average size distribution of each condition (TCD:18 cm; flow rate:0.5 ml h⁻¹).

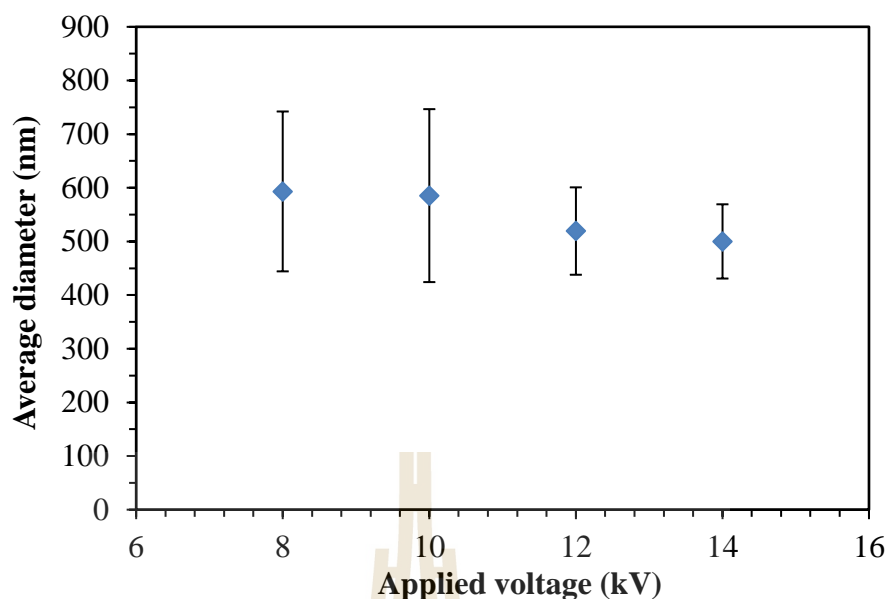


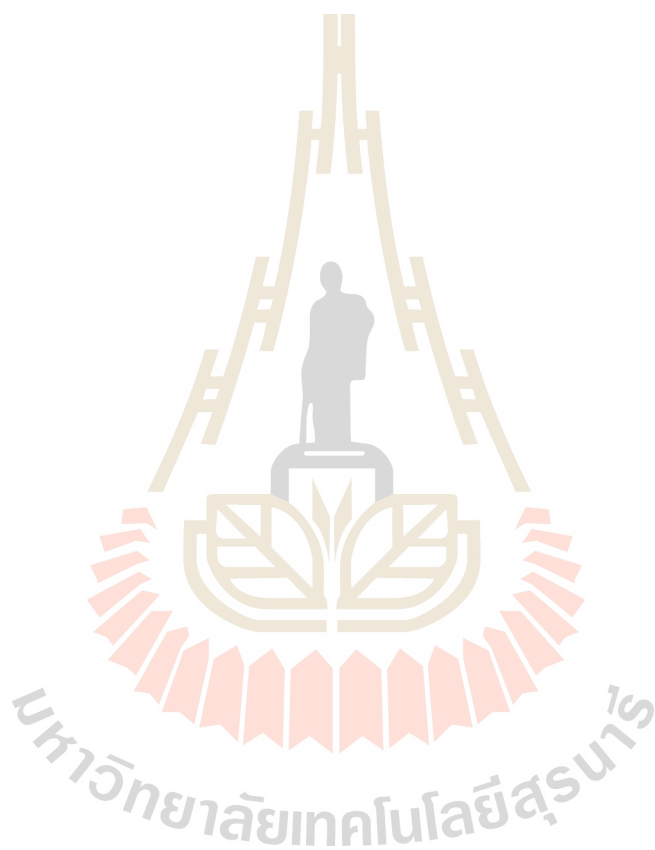
Figure 4.3 Average diameter of the as-spun $\text{Ni}(\text{NO}_3)_2$ -5%/PAN at the various applied voltages of 8, 10, 12, and 14 kV (TCD: 18 cm; flow rate: 0.5 ml h^{-1}).

4.1.2 Effect of nickel concentration on morphology and microstructure of electrospun nanofibers

Effect of reinforcement concentrations on morphologies of electrospun nanofibers was also studied. The various PAN-based solution precursors were prepared by adding of different nickel concentration of 0, 5, 10, and 20 wt.%. They were electrospun at a flow rate of 0.5 ml h^{-1} with TCD of 18 cm. The morphology of electrospun $\text{Ni}(\text{NO}_3)_2$ /PAN -12kV (the electrospinning was done at 12 kV) nanofibers were observed using SEM (Figure 4.3). All samples appeared the random arrangement, long, and uniform nanofibers. The histograms in Figure 4.4 displayed the approximate Gaussian distribution of diameter size for all samples.

Even the diameter sized of the as-spun nanofibers tend to increase with more $\text{Ni}(\text{NO}_3)_2$ concentration, it initially turned down when the concentration of nickel reinforcement reaches 20 wt.% (Figure 4.6). This is possible due to the viscosity of the

precursor solution were increased by adding more reinforcement so caused the larger diameter size of as-spun nanofibers (Min *et al.*, 2004). Moreover, at high nickel concentration of 20 wt.% the effect of charge density had taken the major role than the solution viscosity then reduced the diameter size of as-spun nanofibers as displayed in Figure 4.4 (Beglou and Haghi, 2008).



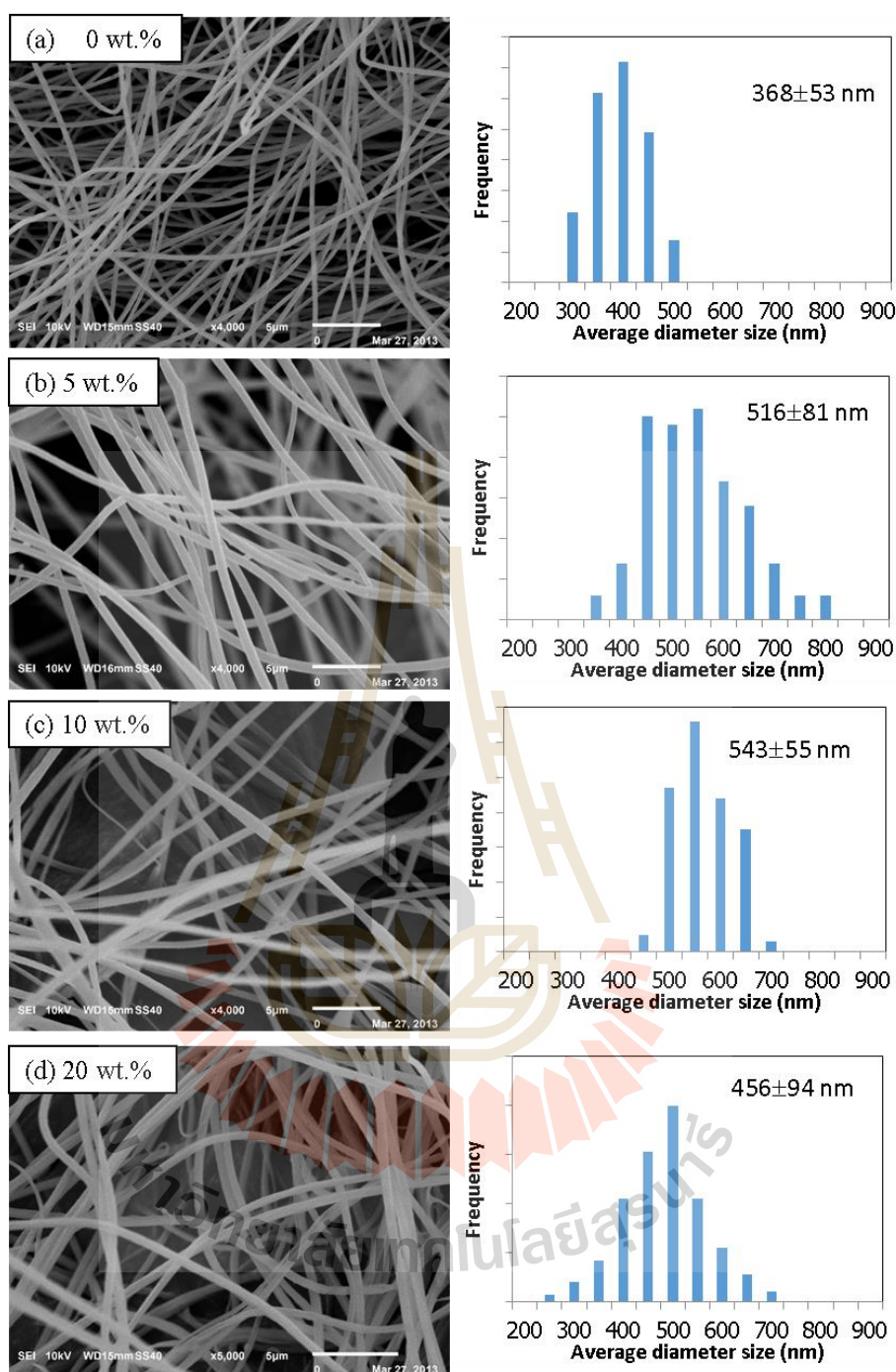


Figure 4.4 SEM images of as-spun $\text{Ni}(\text{NO}_3)_2/\text{PAN}$ fabricated using voltage of 12 kV at the various $\text{Ni}(\text{NO}_3)_2$ concentrations of (a) 0, (b) 5, (c) 10, and (d) 20 wt.%. The histograms on right-hand side show the average size distribution of each species (the samples were spun using a flow rate of 0.5 ml h^{-1} and TCD of 18 cm).

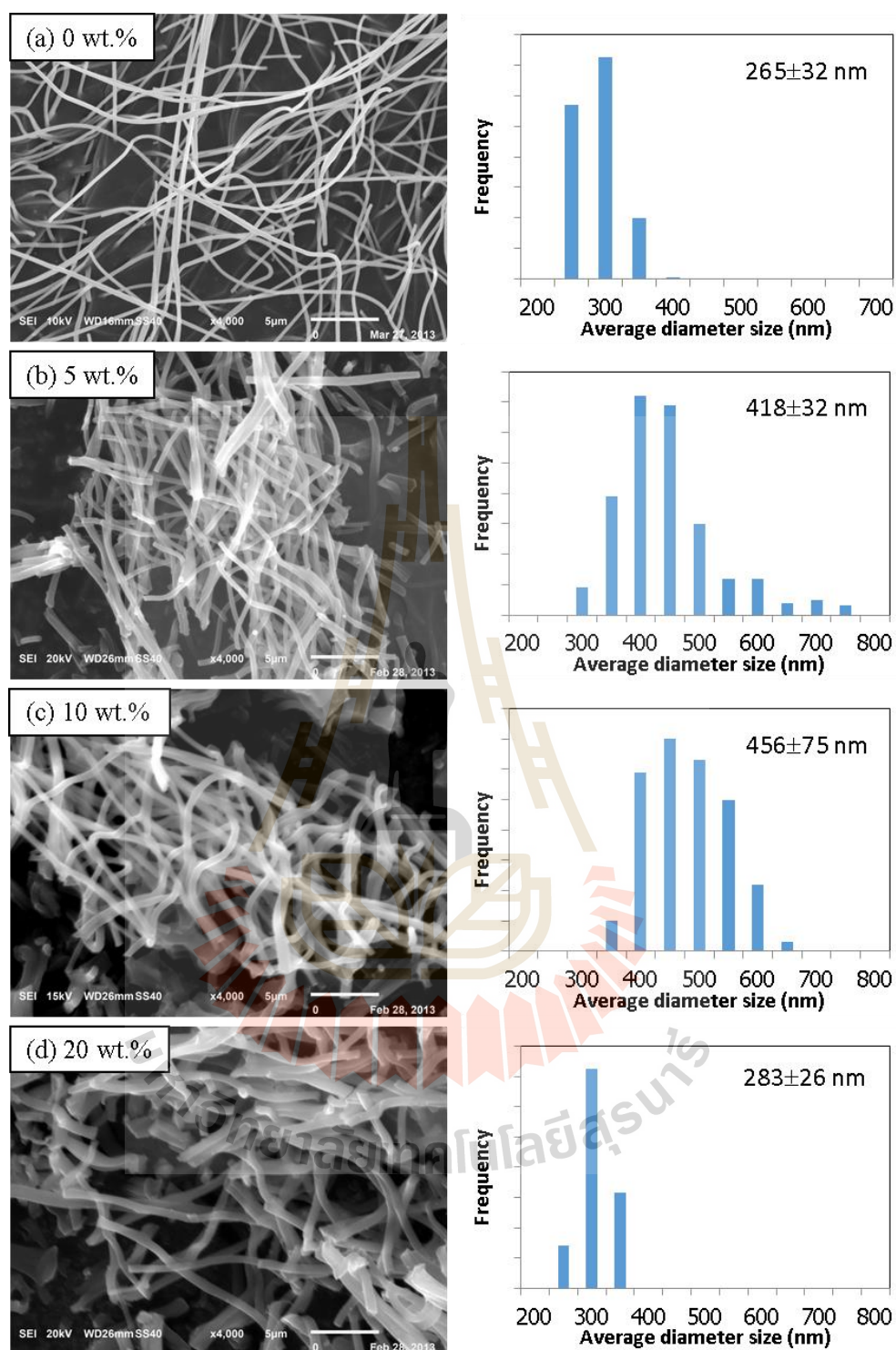


Figure 4.5 SEM images of NiO_x/CNF calcined at 900°C the with the various $\text{Ni}(\text{NO}_3)_2$ precursor concentrations of (a) 0, (b) 5, (c) 10, and (d) 20 wt.%. Right-hand, the histogram of the average size of each species.

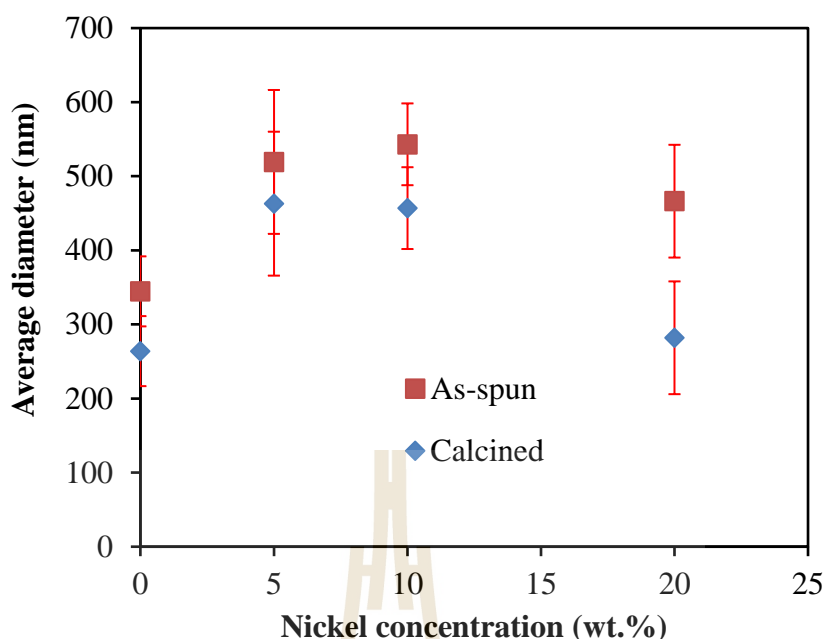


Figure 4.6 Average diameter of the as-spun and calcined $\text{Ni}(\text{NO}_3)_2/\text{PAN}$ at the various $\text{Ni}(\text{NO}_3)_2$ concentrations of 0, 5, 10, and 20 wt.% comparing to PAN (applied voltage: 12 kV; flow rate: 0.05 ml h^{-1} ; TCD: 10 cm).

The average diameters of as-spun and calcined $\text{Ni}(\text{NO}_3)_2/\text{PAN}$ nanofibers in Figure 4.6 were measured from SEM micrographs of each sample using ImageJ software. All nanofibers presented a nonlinear relation in diameter with the embedding of various $\text{Ni}(\text{NO}_3)_2$ concentration of 0, 5, 10, and 20 wt.%. The smallest average diameter of 344.7 ± 47.3 nm was observed for pristine as-spun PAN nanofibers. The average sizes of as-spun nanofibers were increased with existent of $\text{Ni}(\text{NO}_3)_2$ for 5 and 10 wt.% possibly due to an increase of viscosity at a high concentration of metal source reinforcement. For low viscosity liquids, tiny droplets can easily be emitted from the tip result. However, it turns decreased when the $\text{Ni}(\text{NO}_3)_2$ content reaches 20 wt.% implying that the conductivity is also increased with more $\text{Ni}(\text{NO}_3)_2$ adding and then can overcome the effect of viscosity significantly caused a decrease of the average size of as-spun nanofibers as shown in Figure 4.6. The SEM micrographs also show that

the samples calcined at 900 °C in an argon atmosphere for 2 h has a distortion and fracture after heat treatment. The size distribution of each nanofiber is represented by histogram gathered in right-hand side of each figure, the average diameter size of electrospun composite Ni(NO₃)₂/PAN nanofibers shrinks by about 25 % after calcination caused by removal of absorbed water and any solvent, and also changing in polymer structure in cyclization of polymer during heat treatment (Nataraj *et al.*, 2009).

4.2 Characterization and electrochemical properties of nickel clusters composite carbon-based nanofibers (NiO_x/CNF)

4.2.1 Characterization of CNF, NiO/CNF, Ni/CNF, and Ni-NiO/CNF

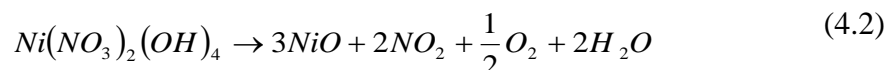
4.2.1.1 Thermal properties of as-spun Ni(NO₂)₃/PAN (where Ni(NO₂)₃ concentrations are 0, 5, 10, and 20 wt.%). The weight loss of all the as-spun nanofibers were studied using TGA and DSC. The tests were operated in N₂ atmosphere at a flow rate of 100 ml min⁻¹ and ranged the temperature from 25 °C up to 1000 °C at a heating rate of 5 °C min⁻¹. Figure 4.7(a) shows the three major weight losses of pure PAN and four major weight loss for all the composite samples during the heating process. The first minor weight loss of all the samples before 175 °C resulted from the removal of the free solvent in the as-spun nanofibers (Yu *et al.*, 2012). The second region, the pre-weight loss only respectively fund observed on samples 5, 10, 20 wt.% 277, 256, and 255 °C were attributed to the decomposition of nickel nitrate into NiO_x (Fréty *et al.*, 2014). The significant weight loss at 306, 293, 290, and 293 °C respectively observed for samples 5, 10, and 20 wt.% can be interpreted as the infusible ladder polymer forming in cyclization of nitrile groups of

matrix PAN before carbonization (Alarifi *et al.*, 2015). Finally, the last weight loss regions of all the samples initiated above 700 °C were related to the decomposition and degradation temperature of carbon structure during pyrolyzed at a high temperature in an inert gas (Fleming *et al.*, 2014).

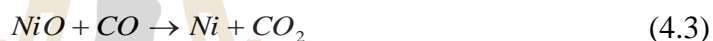
The DSC curves of all the samples were collected as shown in Figure 4.7 (b). Among all samples, only the fibers which were composited with a high concentration of nickel nitrate clearly appeared the first tiny endothermic peaks at around 75 °C involving the release of water and solvent. In the same genus, they appeared the small exothermic peaks of pre-oxidized processes at 277, 256, and 255 °C for samples 5, 10, and 20 wt.%, respectively (Zhang and Li, 2005). The main exothermic reaction peaks were obviously displayed for all the samples located at 306, 293, 290, and 293 °C respectively for as-spun of 0, 5, 10, and 20 wt.%, which were in agreement with the weight losses observed on consistent TGA results.

4.2.1.2 Thermal analysis of CNF, NiO/CNF, Ni/CNF, and Ni-NiO/CNF. In this study, only the as-spun of 20 wt.% of Ni(NO₃)₂ was calcined as the composite carbon nanofibers. After calcination, the TGA of the calcined samples was studied again in air atmosphere up to 1000 °C in order to determine the mass of non-carbon (metal and/or metal oxide) elements loading in nanofibers. As shown in Figure 4.8 (a) the slight weight loss below 100 °C was considered as the removal of absorbed humidity in the porous structure of the sample. The subsequent dramatic weight losses in the temperature range of 350-650 °C were an evidence of the oxidization of carbon components in an oxygen-rich environment, the complete decomposition arose at above 424, 488, 510, and 644 °C for NiO/CNF, Ni-NiO/CNF, Ni/CNF, and CNF,

respectively (Wang *et al.*, 2015). During the heat treatment, Nickel oxide was first obtained by the dehydration of nickel nitrate in composite with water that dissociated at around 200 °C as follows (Nataraj *et al.*, 2009).



And the absence of oxygen during decomposition of the electrospun composite nanofibers suggested that carbon dioxides displace atomic oxygen that was expected to play an important role in the mechanism of decomposition of nickel oxide in nanofibers matrix to reduce metallic nickel as follows.



The non-carbon components loading in nanofibers were determined from residue weight loss at 1000 °C, which was obtained to be 23, 29, and 24% for Ni/CNF, NiO/CNF, and Ni-NiO/CNF, respectively (Figure 4.8(b)).

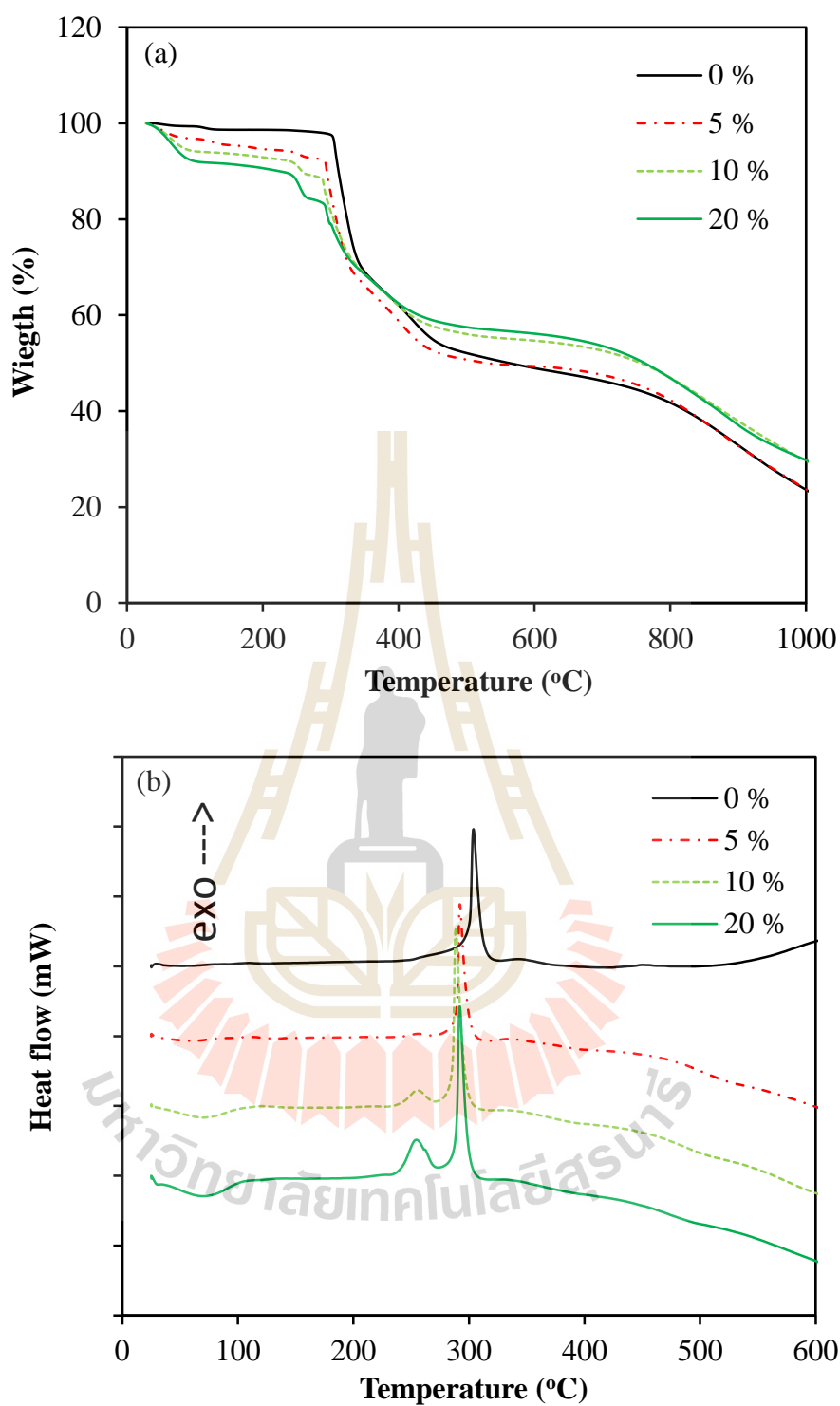


Figure 4.7 (a) TGA and (b) DSC curves of as-spun PAN nanofibers reinforced with different $\text{Ni}(\text{NO}_3)_2$ concentrations of 0, 5, 10, and 20 %. The TGA-DSC analysis was carried out in N_2 atmosphere (heating rate: $10\text{ }^\circ\text{C min}^{-1}$; flow rate: 100 ml min^{-1}).

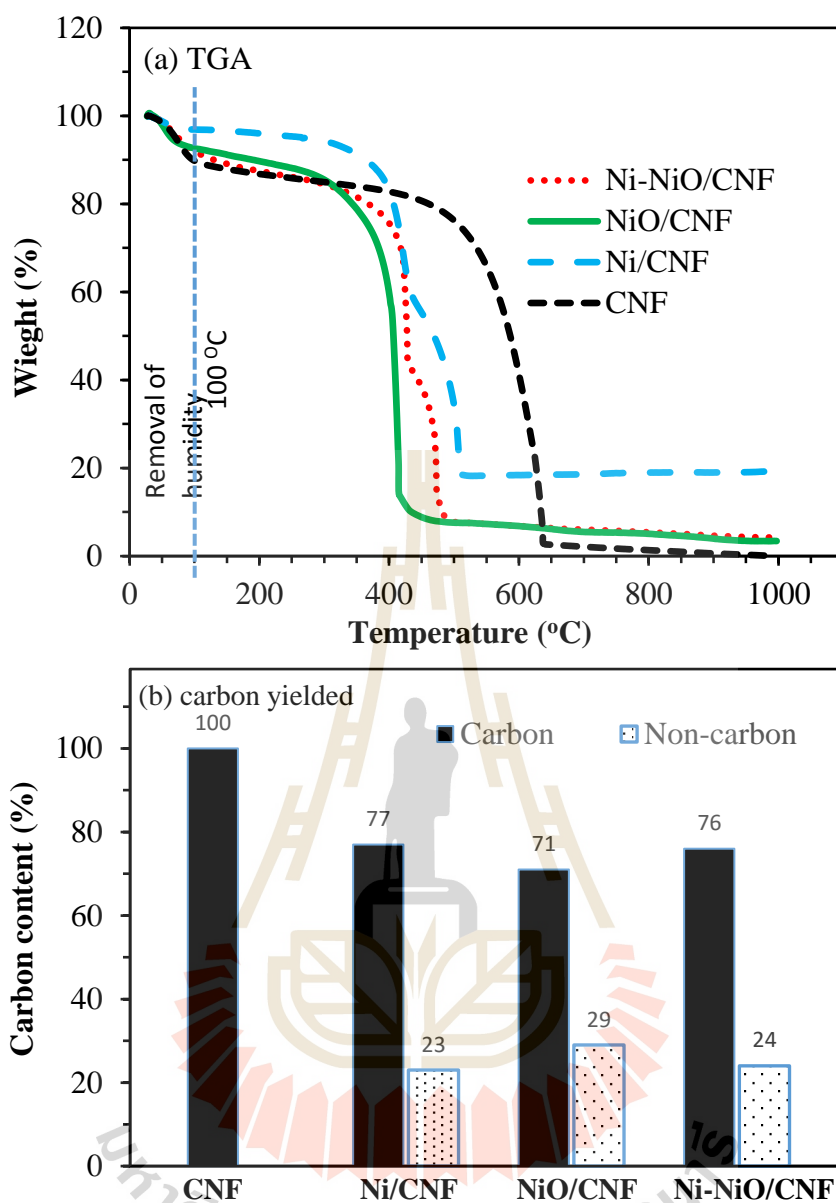


Figure 4.8 (a) TGA of CNF, Ni/CNF, NiO/CNF, and Ni-NiO/CNF carried out in an air atmosphere, the temperature ranged from 25-1000 °C, and a heating rate of 10 °C min⁻¹. (b) The plot of carbon and non-carbon content determined from TGA of various composite CNF.

4.2.2 Morphology of CNF, Ni/CNF, NiO/CNF, and Ni-NiO/CNF

Figure 4.9(a) shows the SEM image of as-spun $\text{Ni}(\text{NO}_3)_2/\text{PAN}$ nonwoven webs. The as-spun webs show smooth surface and uniform fibers with average diameter ~ 456 nm. There are no beads appear on the as-spun webs. After calcination, the average diameter was reduced by removal of solvent and moistures during heat treatment, the average size is ~ 282 - 359 nm as shown in Figure 4.9(b). As observed, all samples still presented likely a smooth surface and uniform fibers. While the surfaces of NiO/CNF Ni-NiO/CNF become decay surface. TEM images in Figure 4.9(c) present that the nanoparticles were observed inside sample which were composited of nickel elements corresponding nickel or nickel oxide nanoparticles forming during heat treatment.

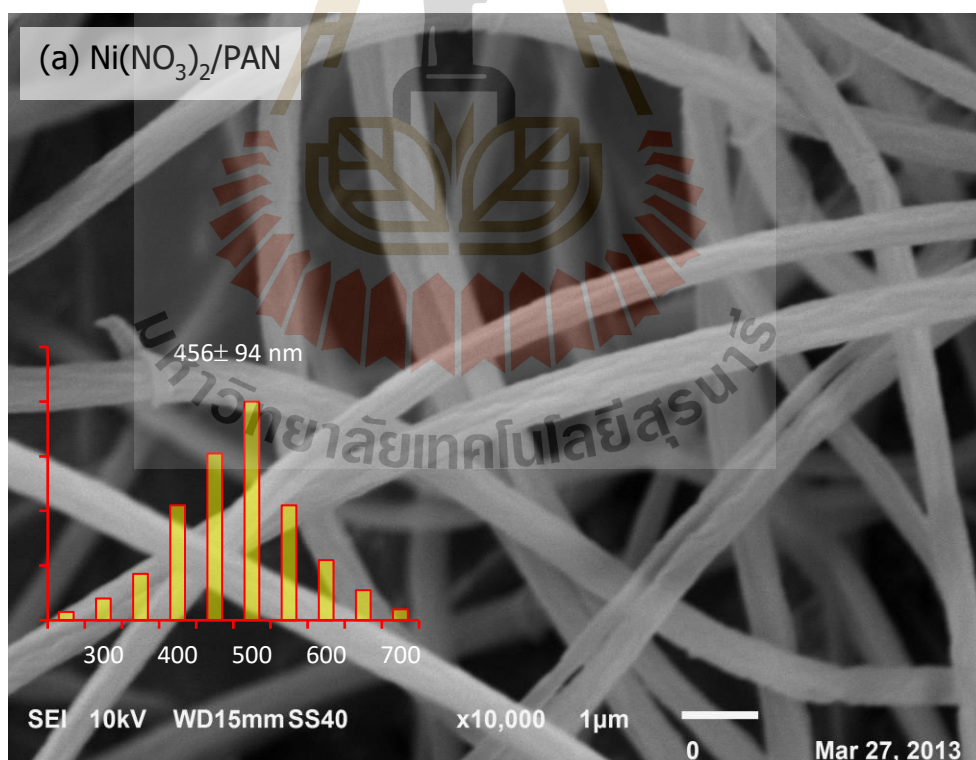


Figure 4.9 SEM images of (a) as-spun $\text{Ni}(\text{NO}_3)_2/\text{PAN}$ (20 wt.%) and (b) calcined samples. (c) TEM images of the calcined sample.

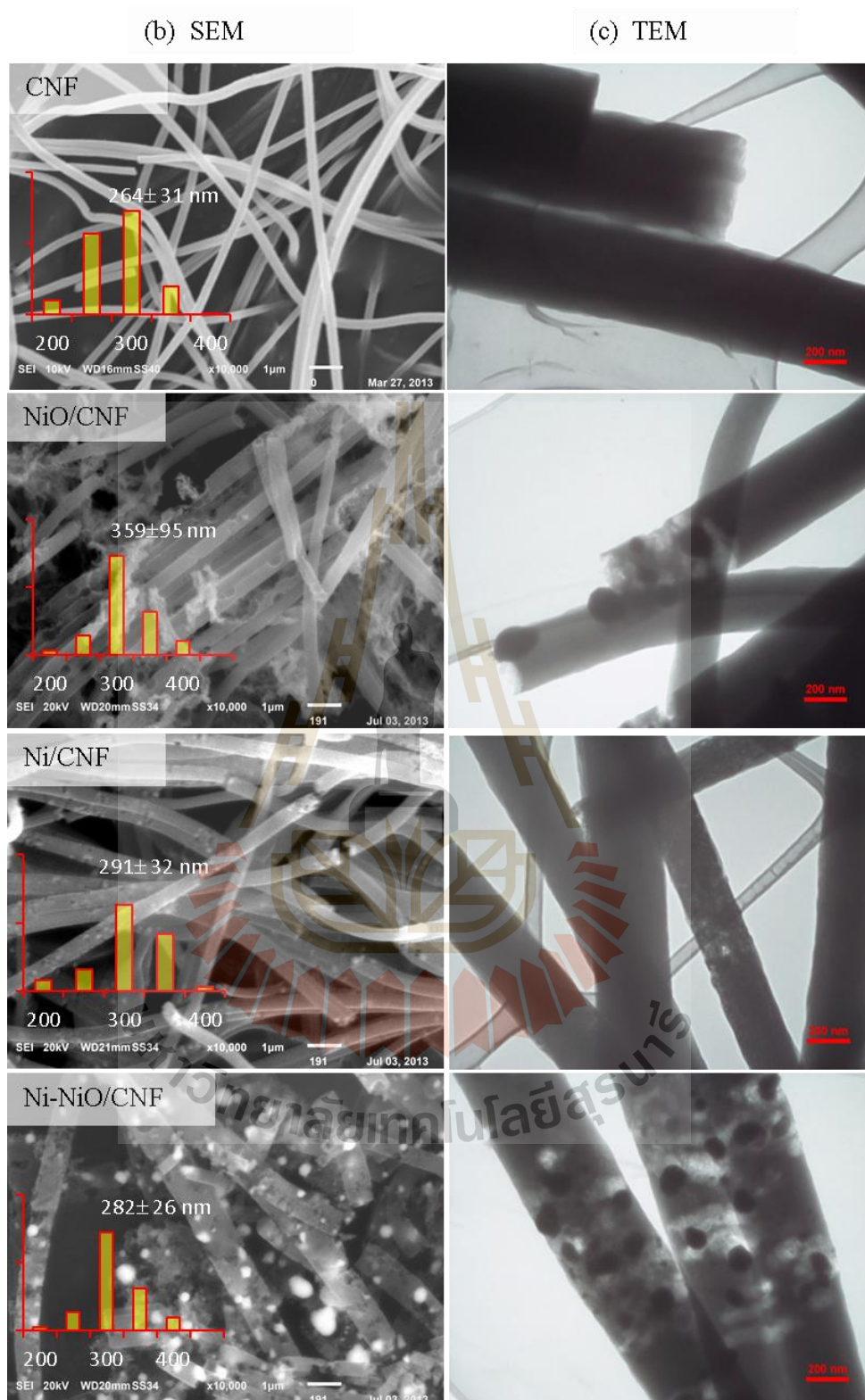


Figure 4.9 SEM images of (a) as-spun $\text{Ni}(\text{NO}_3)_2/\text{PAN}$ (20 wt.%) and (b) calcined samples. (c) TEM images of the calcined sample.(continued)

Table 4.1 Average diameter of all fiber and particle size of CNF, AgO_x/CNF, MnO_x/CNF and AgO_x-MnO_x-CNF nanofibers.

Sample	Fiber size (nm)		Particle size (nm)
	As-spun	Calcined	
CNF	264±31	264±31	-
NiO/CNF	359±95	359±95	93±38
Ni/CNF	381±13	291±32	-
Ni-NiO/CNF	476±39	282±26	56±13

4.2.3 Microstructure of CNF, Ni/CNF, NiO/CNF, and Ni-NiO/CNF

4.2.3.1 XRD analysis

The as-spun Ni(NO₃)₂/PAN (20 wt.%) was calcined with the different condition of 500 °C in argon, 500 °C in air+argon, 500 °C in air, 500 °C in argon → 900 °C in argon, and 500 °C in air+argon → 900 °C in argon atmosphere to hopefully obtain the different phases of metal reinforcements as Ni or/and NiO. The XRD spectra of the calcined samples were measured with Cu K α wavelength of 1.54 Å between 2 θ from 10-80°, step time 0.2 and step size 0.02. As appeared in Figure 4.11, the XRD pattern of CNF, NiO/CNF, Ni/CNF and Ni-NiO/CNF samples show the broad peak of amorphous carbon at around 26° corresponding to plane 002 of carbon layer that indicated the amorphous carbon structures mainly formed during carbonization (Lee *et al.*, 2014). Otherwise, the carbon peaks disappeared for NiO nanofibers because all of the polymer precursors were oxidized in oxygen rich atmosphere during calcination. The diffraction peaks at 37.2°, 43.3°, 62.8° and 75.4° of cubic NiO were clearly seen in

NiO, NiO/CNF, and Ni-NiO/CNF nanofibers which can be steadily indexed respectively to the planes of (001), (200), (111) and (021) (PDF: 03-065-6920), suggesting that the obtained products were consisted of crystalline NiO (

Figure 4.10(b)). This confirms that the oxygen is needed for the formation of cubic NiO (Wu *et al.*, 2012). As expected, metal Ni phase was found in Ni/CNF and also Ni-NiO/CNF, and the peaks at 44.5° , 51.8° and 76.4° indexing planes of (111), (200) and (220) respectively (PDF: 00-004-0850) suggested that the crystalline of metallic nickels were achieved in argon atmosphere at higher temperature than forming of nickel oxides. The structural parameters and crystallite sizes of the composites were presented in Table 1.

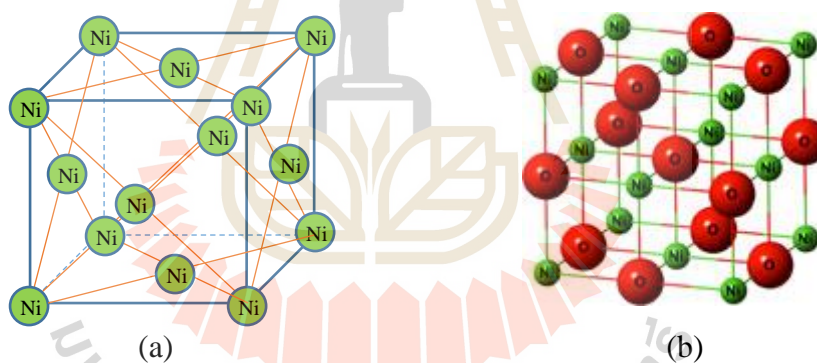


Figure 4.10 A schematic crystal structure of the cubic (a) Ni and (b) NiO (Magyari-Köpe *et al.*, 2012).

Table 4.2 Structural parameters of the carbon, cubic nickel, and cubic nickel oxide observing from electrospun (a) CNF, (b) NiO/CNF, (c) NiO, (d) Ni/CNF, and (e) Ni-NiO/CNF.

Sample	C			Ni						NiO							
	Peak (002)		D_C	Peak (111)		Peak (200)		Peak (220)		D_{Ni}	Peak (111)		Peak (200)		Peak (220)]		D_{NiO}
	2θ	d_{002}		2θ	d_{111}	2θ	d_{200}	2θ	d_{220}		2θ	d_{111}	2θ	d_{200}	2θ	d_{220}	
	(°)	(Å)	(nm)	(°)	(Å)	(°)	(Å)	(°)	(Å)	(nm)	(°)	(Å)	(°)	(Å)	(°)	(Å)	(nm)
CNF	25.57	3.71	1.4	-	-	-	-	-	-	-	-	-	-	-	-	-	
NiO/CNF	25.76	3.46	1.8	-	-	-	-	-	-	-	37.46	2.39	44.25	2.05	63.11	1.47	13.7±7.2
NiO	-	-	-	-	-	-	-	-	-	-	37.42	2.40	43.45	2.08	63.03	1.47	23.2±8.1
Ni/CNF	25.81	3.45	3.2	44.62	2.03	51.98	1.76	76.51	1.24	33.3±4.7	-	-	-	-	-	-	-
NiO-Ni/CNF	26.07	3.41	3.4	44.66	2.03	52.02	1.76	76.53	1.24	25.5±1.1	37.29	2.40	43.33	2.08	62.94	1.48	9.4±0.9

4.2.3.2 XANES study of Ni(NO₃)₂/PAN, NiO/CNF, Ni/CNF, and Ni-NiO/CNF

The series of Ni K-edge XANES were measured at energy range 8,320-8,420 eV to examine the chemical states of nickel element in the samples. The energy edges were evaluated using Athena software, the nickel chemical mapping in each sample was analyzed employing linear combination fitting method. The reference chemical states were measured from commercial Ni metal and NiO. Figure 4.12(a) shows that the spectrum of Ni/CNF ($E_0 = 8344.32$ eV) exhibited nearly to be Ni foil spectrum while the spectra of NiO/CNF ($E_0 = 8343.43$ eV) and Ni-NiO/CNF ($E_0 = 8343.99$ eV) presented closely a standard NiO or Ni(NO₃)₂ precursor. The fitting results showed the factors R were found to be below 0.05 for all samples. Figure 4.12(b) illustrates most Ni metal mapped Ni/CNF valued around 89.6%. In a difference manner (Figure 4.12(c and d)), the NiO/CNF and Ni-NiO/CNF rather present the oxidation of Ni²⁺ of NiO and Ni(NO₃)₂/PAN spectrum. These results revealed more nanophase structures of each sample than that observed in XRD.

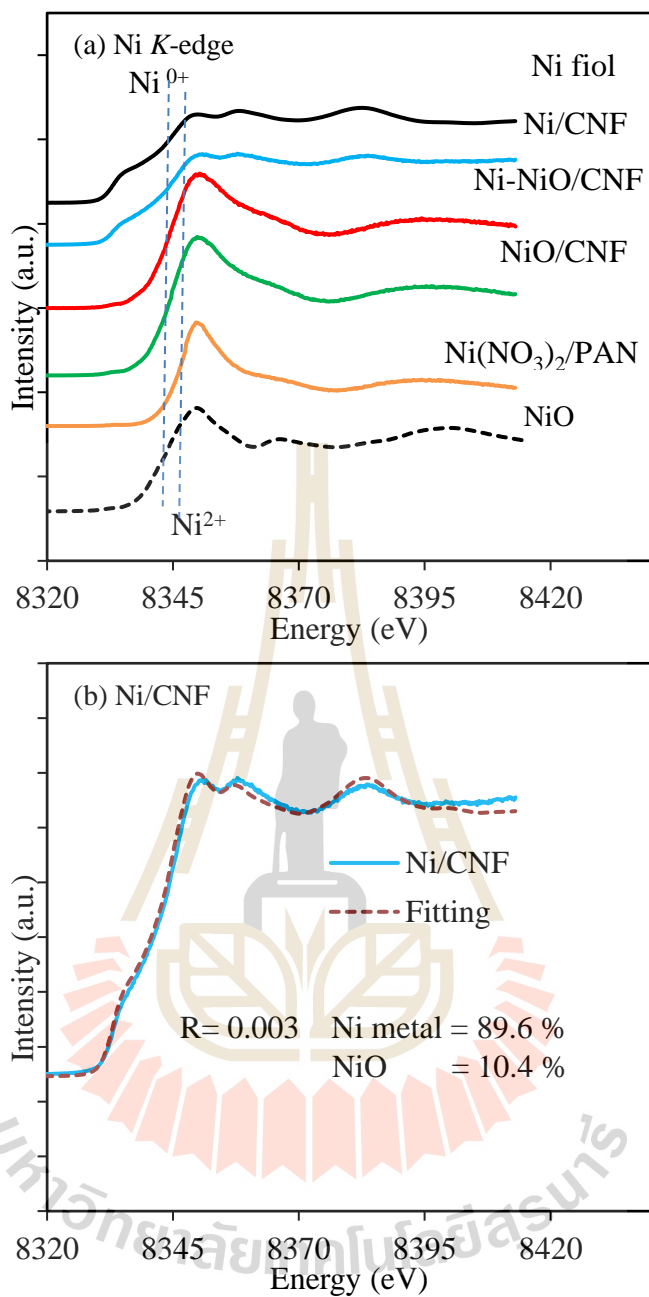


Figure 4.12 (a) Ni K-edge XANES of as-spun Ni(NO₃)₂/PAN, NiO, and Ni foil. (b-d) Ni chemical mapping of each sample using Linear combination fitting.

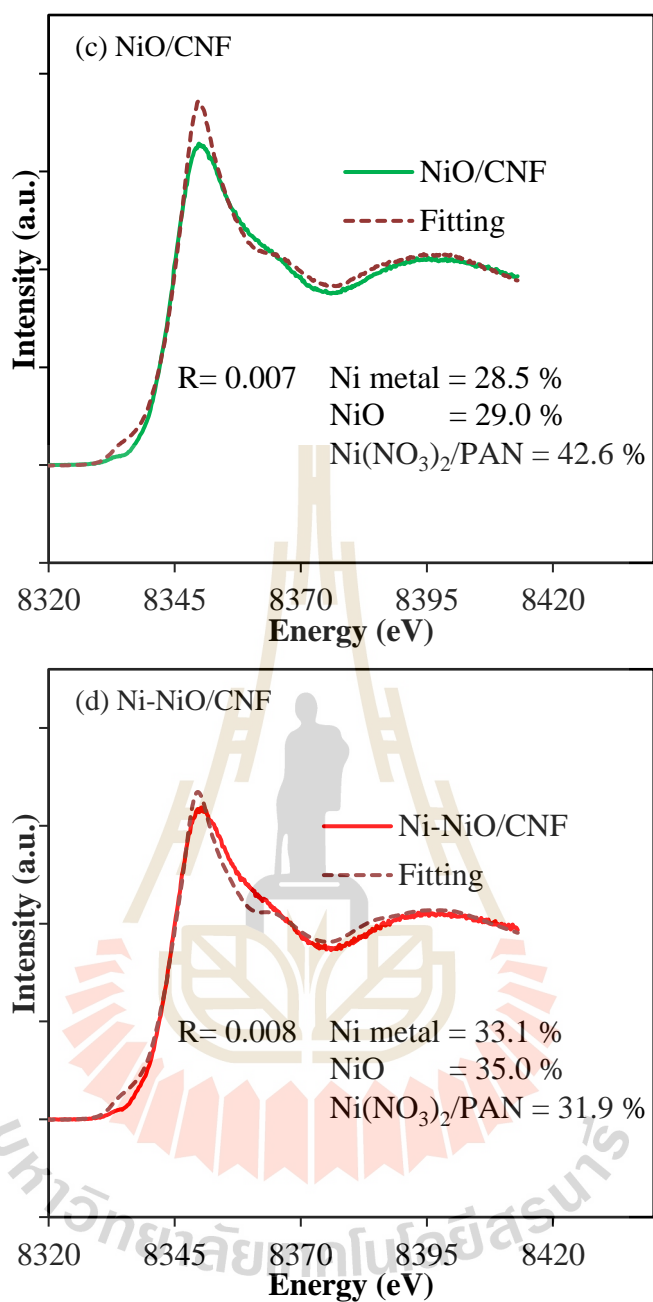
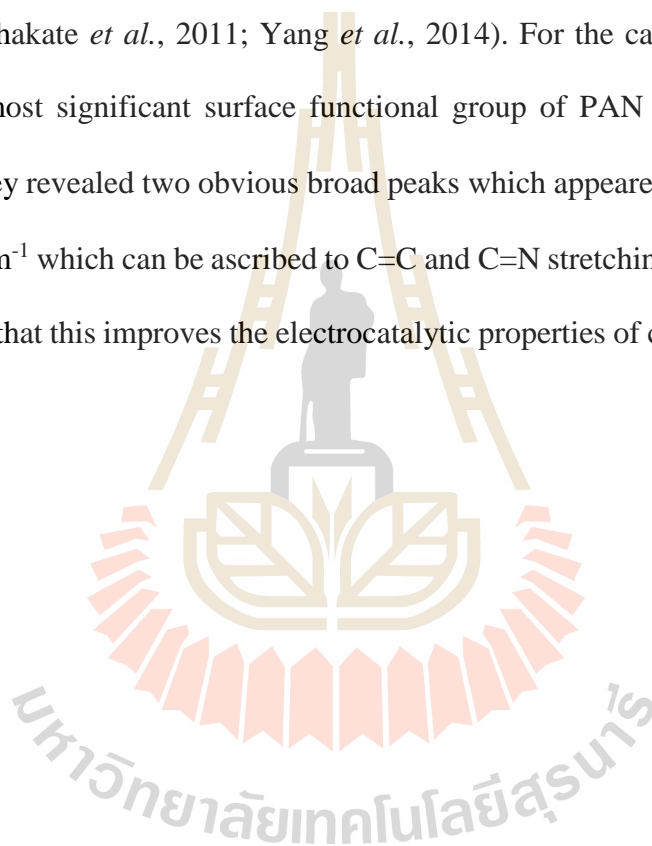


Figure 4.12 (a) Ni K-edge XANES of as-spun Ni(NO₃)₂/PAN, NiO, and Ni foil. (b-d) Ni chemical mapping of each sample using Linear combination fitting. (continued)

4.2.3.3 The surface chemistry of as-spun Ni(NO₃)₂/PAN, CNF, Ni/CNF, NiO/CNF, and Ni-NiO/CNF

The surface function groups of all samples were determined in wave number range between 400-4000 cm^{-1} using FTIR analysis and their spectra are shown in Figure 4.13. The transmittance broad peaks $\sim 3410 \text{ cm}^{-1}$ indicated the O–H stretching vibration of absorbed water. The typical spectrum of PAN nanofibers was specified to peaks of 2938 cm^{-1} , 1450 cm^{-1} , 2243 cm^{-1} , and 1625 cm^{-1} for the $-\text{CH}_2$ asymmetric stretching mode, $-\text{CH}_2$ bending mode, $\text{C}\equiv\text{N}$ stretching vibration, and $\text{C}=\text{O}$ vibration. (Dhakate *et al.*, 2011; Yang *et al.*, 2014). For the calcined samples, even though the most significant surface functional group of PAN were absent by heat treatment, they revealed two obvious broad peaks which appeared at ~ 1600 -1580 and 1300-1100 cm^{-1} which can be ascribed to $\text{C}=\text{C}$ and $\text{C}=\text{N}$ stretching (Zeng *et al.*, 2015). It is possible that this improves the electrocatalytic properties of composite CNF (Li *et al.*, 2014).



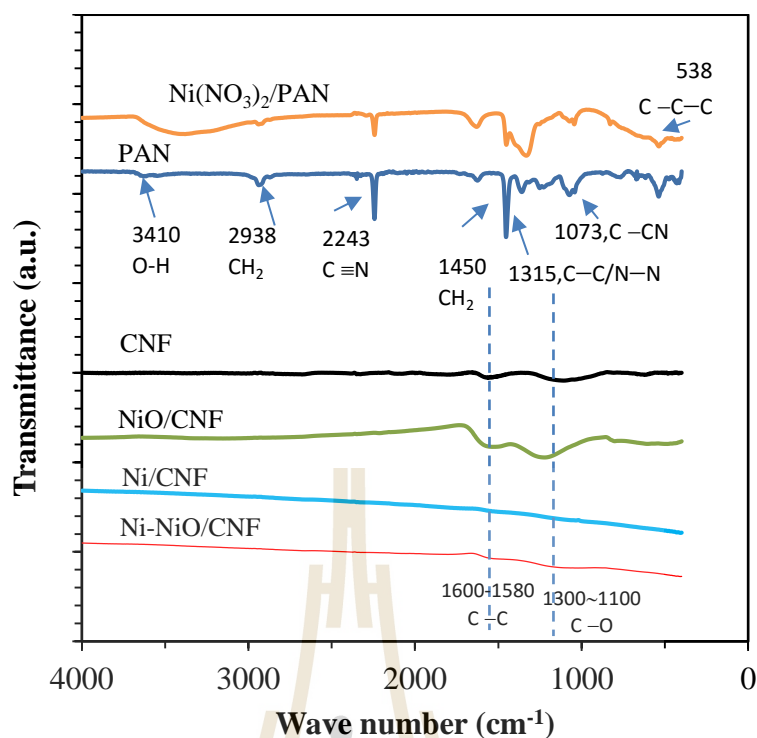
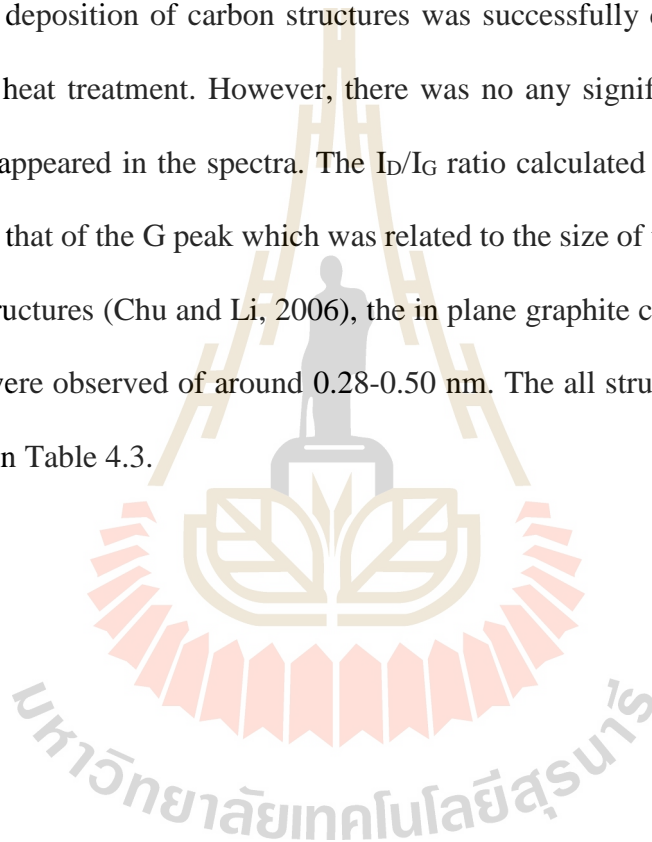


Figure 4.13 FTIR spectra of as-spun PAN, $\text{Ni}(\text{NO}_3)_2/\text{PAN}$ and the calcined samples.

4.2.3.4 Raman spectroscopy

The all calcined samples (CNF, NiO/CNF, Ni/CNF, and Ni-NiO/CNF) were observed between 100 and 4000 cm^{-1} and the spectra are shown in Figure 4.14. All samples allowed five peaks using Gaussian fitting. The first- (D, D'', and G peak) and second-order (G'' and G+D peak) Raman spectra also displayed at around $1340\text{--}1597\text{ cm}^{-1}$ and $2671\text{--}2908\text{ cm}^{-1}$ for all calcined samples. About the first-order region, even the spectra show overlapping between G and D peak which is associated with the amorphous or interstitial defect. However, they were separated as three different peaks of D, D'', and G-band using Gaussian fitting. The first strong peaks at $1340\text{--}1343\text{ cm}^{-1}$ related to well-known D-Breathing Band. This is characteristic of the scattering on disordered of amorphous carbon clusters (sp^3 -bonded carbon atoms). The second small peaks located around $1514\text{--}1535\text{ cm}^{-1}$ were D''-band which was associated with amorphous sp^2 -bonded carbon atoms or interstitial defects. The main strong peaks of

the G-Breathing band appeared at around 1586-1597 cm^{-1} corresponded to the stretching of C-C bonds in the hexagonal ring of sp^2 bonded carbon atom in graphite structures (Ji and Zhang, 2009; Yan *et al.*, 2014; Lisunova *et al.*, 2010). The secondary region, G' and G+D peaks were measurable seen for all samples at 2671- 2908 cm^{-1} corresponding to the phonon oscillation that revealed the infinite crystal of graphite structure in the sample (Colindres *et al.*, 2014; Pimenta *et al.*, 2007). These results indicated the deposition of carbon structures was successfully converted from PAN precursor by heat treatment. However, there was no any significant peak related to nickel oxide appeared in the spectra. The I_D/I_G ratio calculated from the intensity of the D peak to that of the G peak which was related to the size of the graphite planes in the carbon structures (Chu and Li, 2006), the in plane graphite crystalline sizes of the all samples were observed of around 0.28-0.50 nm. The all structural parameters are summarized in Table 4.3.



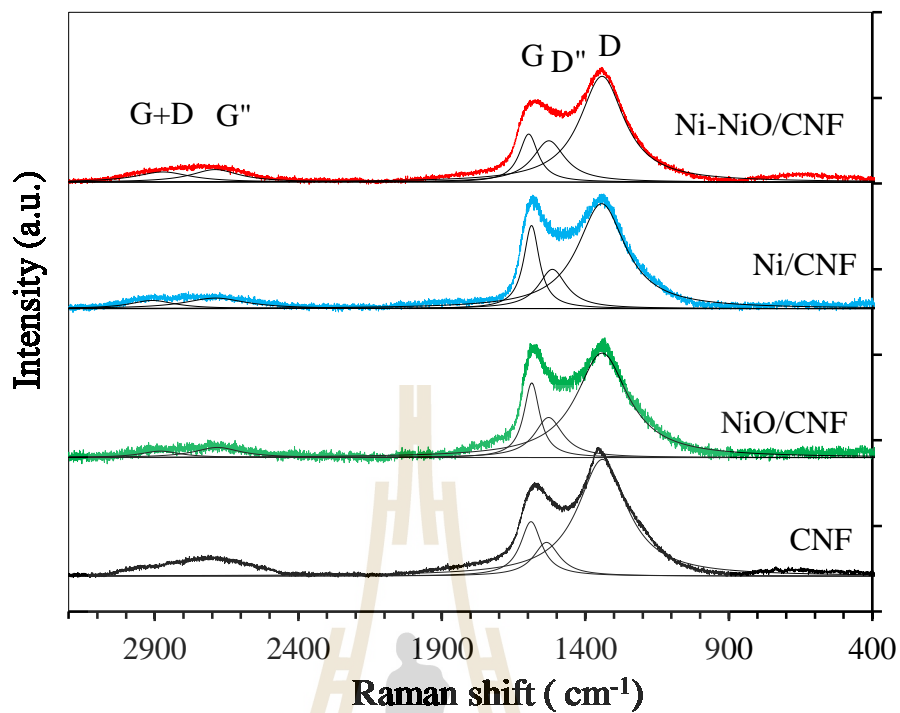


Figure 4.14 Raman spectra of CNF (500 °C in argon), NiO/CNF (500 °C in air+argon), Ni/CNF (500 → 900 °C in argon), and Ni-NiO/CNF (500 °C in air+argon → 900 °C in argon). The dash lines are Gaussian fitting.

Table 4.3 Relevant parameters of the peaks fitted to the Raman spectra of the various composited CNF.

Sample	Peak position (cm ⁻¹)					I _D /I _G	L _a (nm)
	D	D''	G	G''	G+D		
CNF	1340	1535	1589	2671	2832	2.14	0.48
Ni/CNF	1343	1514	1587	2688	2908	1.26	0.28
NiO/CNF	1341	1527	1586	2681	2880	1.40	0.31
Ni-NiO/CNF	1341	1526	1597	2689	2871	2.20	0.50

4.2.4 Surface area and porosity of CNF, Ni/CNF, NiO/CNF, and Ni-NiO/CNF

The specific surface area and pore character of all calcined samples were investigated by measuring N₂ adsorption/desorption at 77 K as shown in Figure 4.15 (a). All spectra exhibit hysteresis loops which are typical type IV isotherms due to capillary condensation of nitrogen in mesopore, and a part of micropore can be attributed by knee-shape at low pressure, the both NiO/CNF and Ni-NiO/CNF spectra show the small N₂ adsorbed volume (V_a) compared to CNF and Ni/CNF implied a small specific surface area (S_{BET}). The pore size distributions of the samples were evaluated using both the BJH and MP methods, which are shown in Figure 4.15(b). The average pores (D_p) of NiO/CNF around 130 nm in diameter is extremely higher than the most other samples. However, the pure CNF displayed the highest S_{BET} of 362 m² g⁻¹ incorporation to the composite sample. The micropores average sizes of around 0.6-0.8 nm were observed for CNF, Ni/CNF, and Ni-NiO/CNF. For the NiO/CNF, it showed a bigger pore size of 1.60 nm. The other textural parameters are evaluated and summarized in Table 4.4.

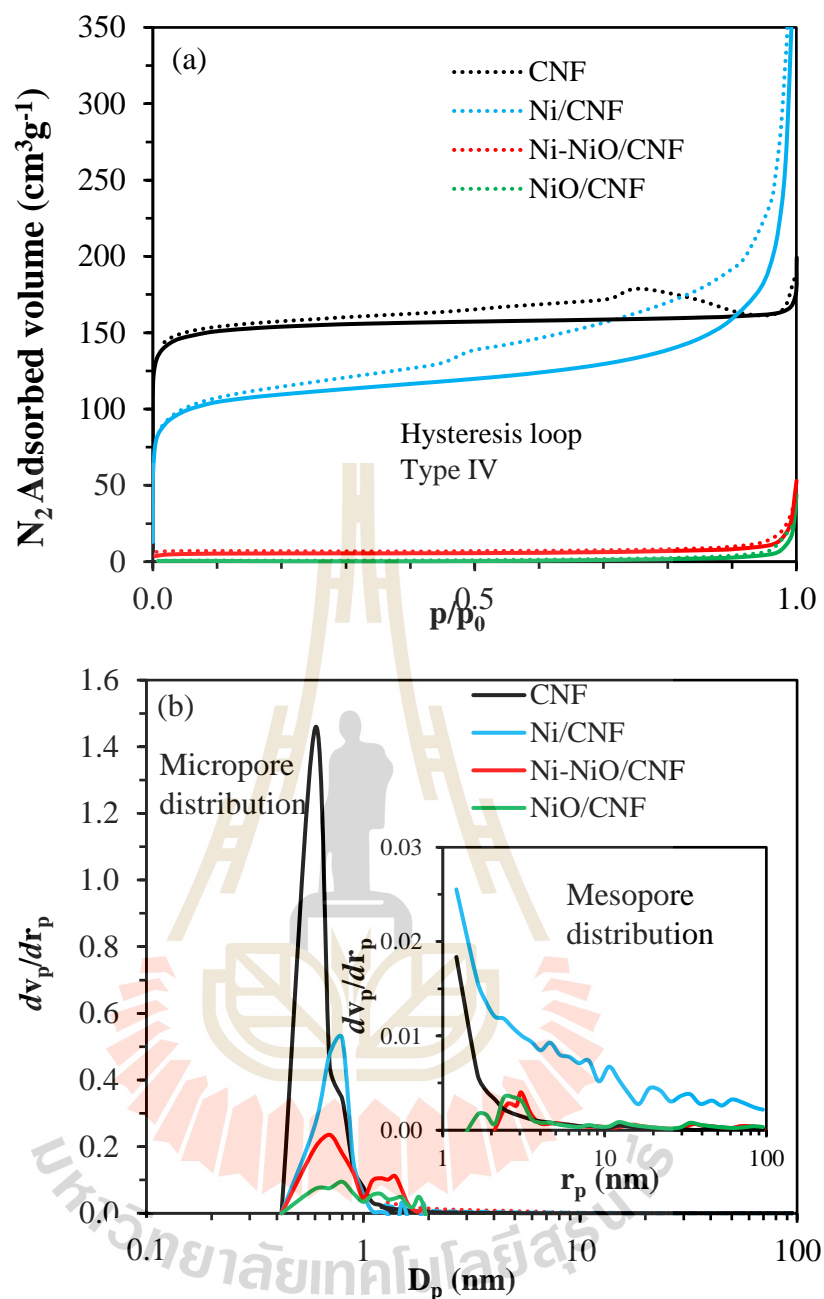


Figure 4.15 (a) N_2 adsorption and desorption isotherm (solid line (ADS) and dash line (DES)), (b) Micropore distribution by MP plot, and (inset) Mesopore distribution from BJH plot of CNF, Ni/CNF, NiO/CNF, and Ni-NiO/CNF.

Table 4.4 The textural parameters of CNF, Ni/CNF, NiO/CNF, and Ni-NiO/CNF, obtained by BET, MP, and BJH method.

Sample	BET			Micropore		Mesopore		$V_{mi}:V_{me}$ (%)
	S_{BET}	D_p	V_{tot}	D_m	V_{mi}	r_p	V_{me}	
	(m^2g^{-1})	(nm)	(cm^3g^{-1})	(nm)	(cm^3g^{-1})	(nm)	(cm^3g^{-1})	
CNF	362	2.89	0.26	0.60	0.21	1.21	0.04	85:15
Ni/CNF	274	7.30	0.50	0.80	0.12	1.22	0.37	25:75
NiO/CNF	77	130.01	0.05	1.60	0.02	2.38	0.03	40:60
Ni-NiO/CNF	130	12.04	0.06	0.70	0.03	2.71	0.03	50:50

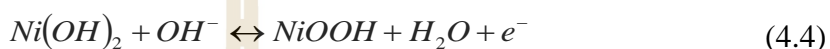
มหาวิทยาลัยเทคโนโลยีสุรนารี

4.2.5 Electrochemical properties of CNF, NiO/CNF, Ni/CNF, and Ni-NiO/CNF

4.2.5.1 Cyclic voltammetry of CNF, NiO/CNF, Ni/CNF, and Ni-NiO/CNF

The CV profiles of all samples in Figure 4.16 were measured in scan rate range of 2-500 mV s^{-1} in order to cover the whole capacitive mechanisms ranges: EDLC at high scan rate value more than 100 mV s^{-1} , surface pseudocapacitance at mid scan rate between 5-100 mV s^{-1} , and also bulk pseudocapacitance at very low scan rate lower than 5 mV s^{-1} . The charged/discharged current of all the electrodes strongly increased with the large scan rate. However, there was no redox peak observed for any samples during the potential becomes more positive and reverse sweeping in the potential windows of 1 V. In this potential voltage window region, the NiO/CNF electrode trendly presented more unstable CV cure due to it showed more resistive behavior at the both low voltage below -0.8 V and high voltage above -0.1 V interpreted to the hydrogen and oxygen evolution from the broken water molecules in aqueous electrolyte (Chen *et al.*, 2013; Seghioer *et al.*, 1998). The specific capacitances of the most samples decreased with increasing of scan rate, except for metallic Ni/CNF electrode that the specific capacitance trendly increased at scan rate below 100 mV s^{-1} and then deceased as the function of scan rate above 100 mV s^{-1} . In Figure 4.16(e), it is noteworthy that the samples which were composited with nickel oxides microstructures; the both NiO/CNF and Ni-NiO/CNF composite presented the same way of high specific capacitance at low scan rate below 10 mV s^{-1} due to the well contribution of pseudocapacitance form redox reaction of nickel oxides and alkaline KOH. This process caused the Ni-NiO/CNF electrode became highest specific

capacitance of nearly 90 F g^{-1} at small scan rate of 2 mV s^{-1} while Ni/CNF became highest value of $\sim 54 \text{ F g}^{-1}$ at high scan rate of 500 mV s^{-1} , these suggested that the Ni-NiO/CNF appropriately used for very slow process like battery whereas Ni/CNF more acceptable for high power density device like supercapacitor. The faradaic redox reaction of nickel or nickel oxide in aqueous KOH solution are offered as follows (Seghioer *et al.*, 1998);



The effect of applied potential voltage window (ΔV) on a CV behavior of the samples was also investigated by expanding the applied voltage window ($\Delta V = 1, 1.0, 1.2, 1.4, \text{ and } 1.5 \text{ V}$). As shown in Figure 4.17, the specific current has tendency to be increased with the wider potential windows but the CV curve of each electrode began to show the unstable curve for applied potential window above 1.4 V related to the hydrogen and oxygen evolution from broken water molecule in aqueous electrolyte (Chen *et al.*, 2013). Moreover, there was small anodic current peak observing at around -0.1 V for the NiO/CNF electrodes at the potential voltage windows more than 1.4 V indicated that the wider potential windows provided more redox reaction of the active materials (Seghioer *et al.*, 1998; Al-Enizi *et al.*, 2014). However, the specific capacitance and energy density were calculated allowing this effect, to cause the increase with the increasing of potential window as displayed in Figure 4.18. The specific capacitance and energy density of the various samples were increased around 40% and 200%, respectively, when the voltage window was adjusted from 1.0 V to be 1.5 V .

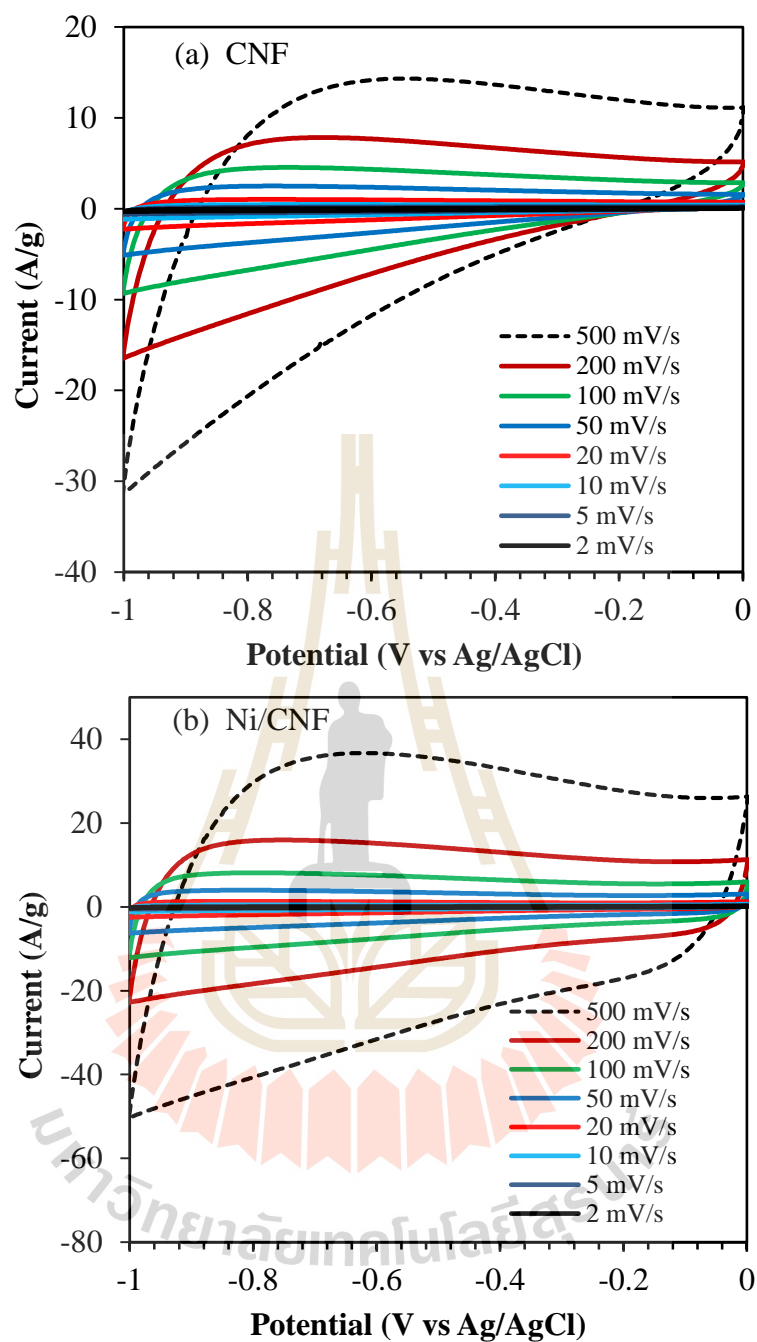


Figure 4.16 Cyclic voltammograms of (a) CNF, (b) Ni/CNF, (c) NiO/CNF, (d) Ni-NiO/CNF, and (e) specific capacitance as a function of scan rate ($\Delta V = 1.0$ V).

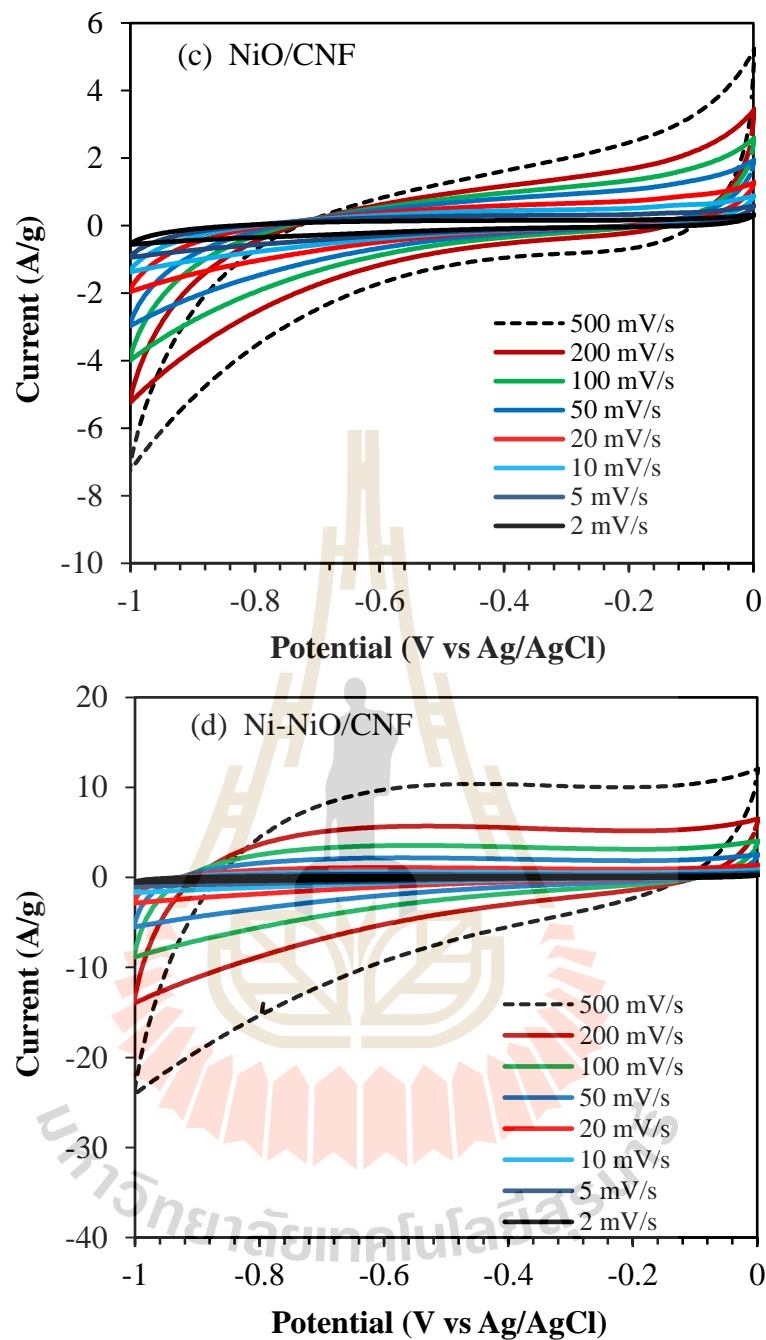


Figure 4.16 Cyclic voltammograms of (a) CNF, (b) Ni/CNF, (c) NiO/CNF, (d) Ni-NiO/CNF, and (e) specific capacitance as a function of scan rate ($\Delta V = 1.0$ V).
(continued)

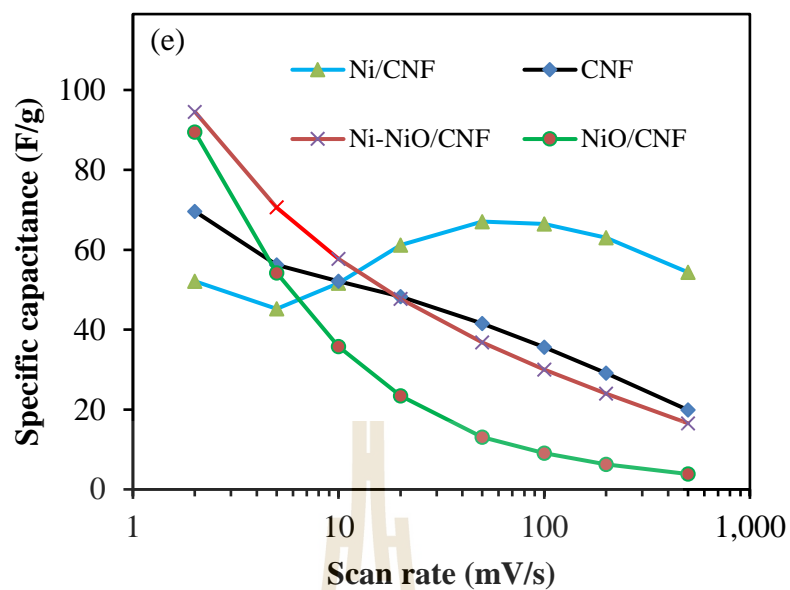


Figure 4.16 Cyclic voltammograms of (a) CNF, (b) Ni/CNF, (c) NiO/CNF, (d) Ni-NiO/CNF, and (e) specific capacitance as a function of scan rate ($\Delta V = 1.0$ V).

(continued)

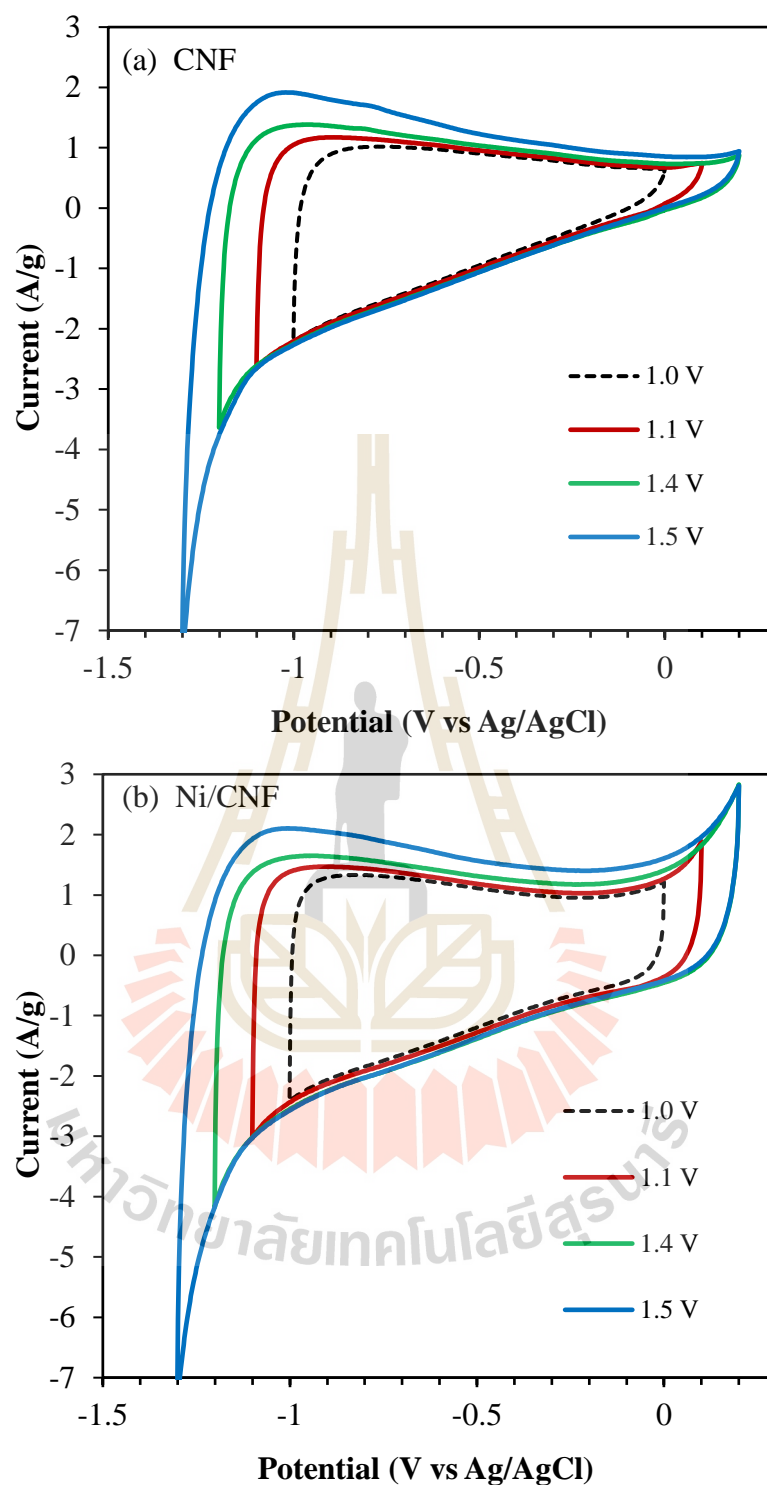


Figure 4.17 Cyclic voltammograms of (a) CNF, (b) Ni/CNF, (c) NiO/CNF, (d) Ni-NiO/CNF measuring for different potential windows of 1.0, 1.2, 1.4, and 1.5 V at scan rate of 20 mV s^{-1} .

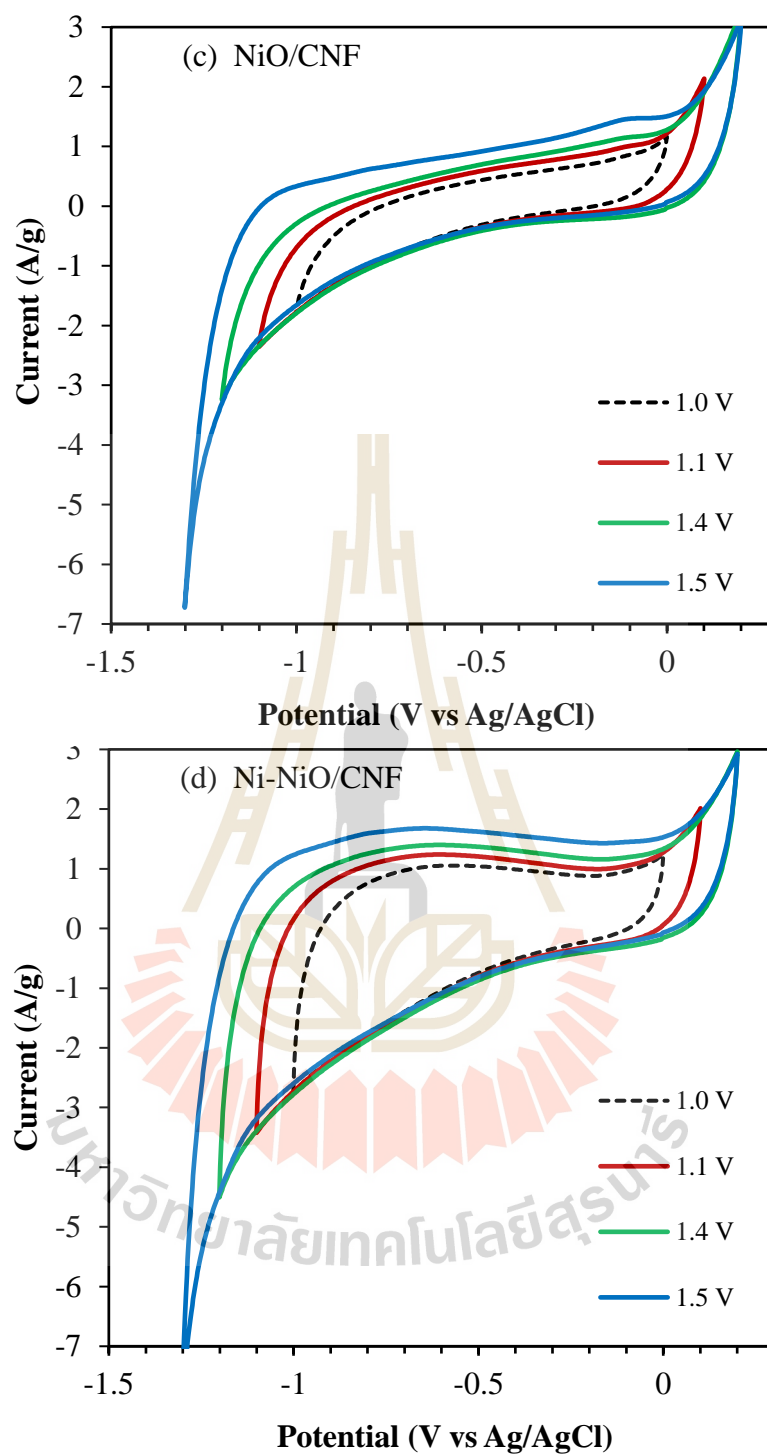


Figure 4.17 Cyclic voltammograms of (a) CNF, (b) Ni/CNF, (c) NiO/CNF, (d) Ni-NiO/CNF measuring for different potential windows of 1.0, 1.2, 1.4, and 1.5 V at scan rate of 20 mV s^{-1} . (continued)

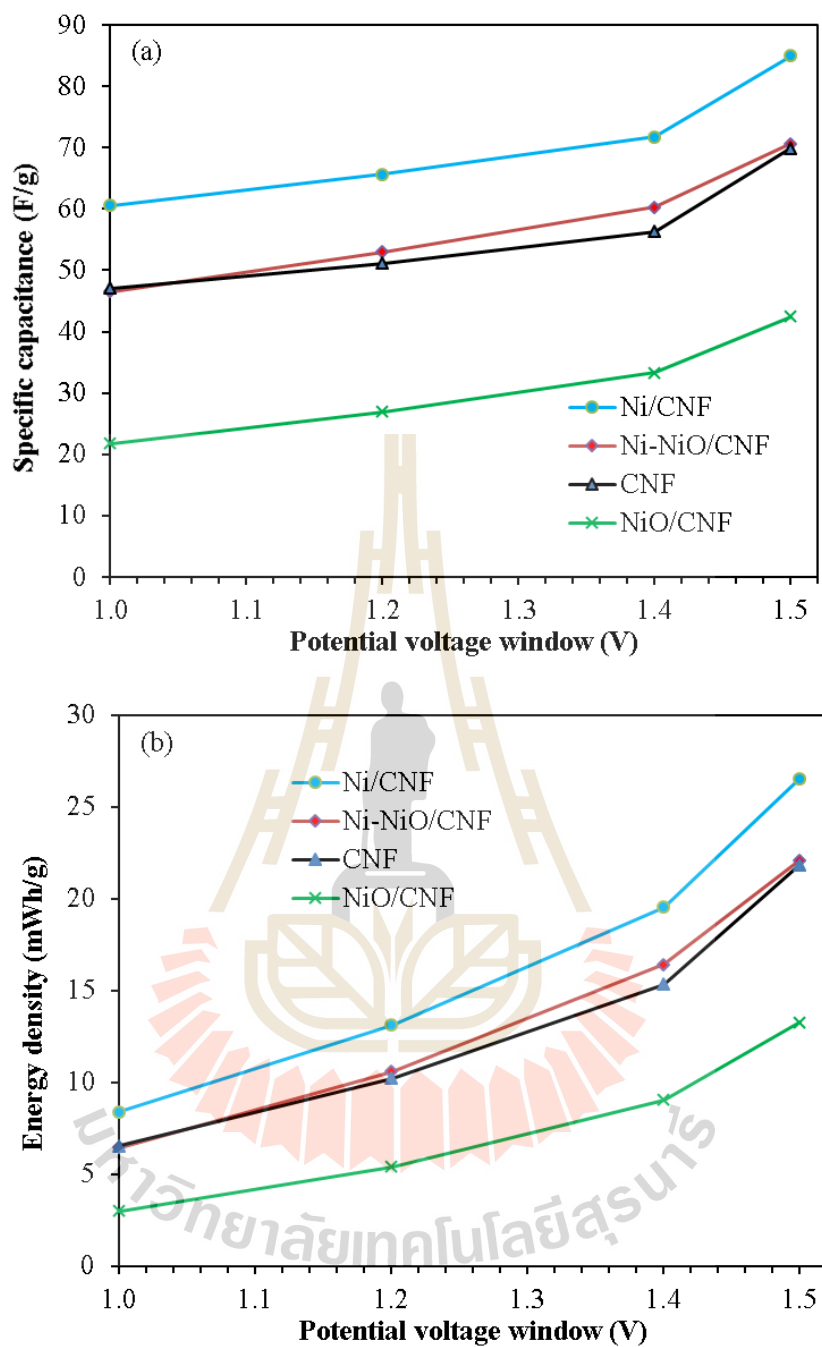


Figure 4.18 (a) Specific capacitance and (b) energy density of CNF, Ni/CNF, NiO/CNF, and Ni-NiO/CNF at different applied potential windows of 1.0, 1.2, 1.4, 1.5 V.

4.2.5.2 Galvanostatic charge/discharge testing of CNF, NiO/CNF, Ni/CNF, and Ni-NiO/CNF

Figure 4.19 represents linear voltage-time profiles of all electrodes measurement at the current density of 0.5, 1, 2, 5, and 10 A g⁻¹. Among all samples, the Ni-NiO/CNF electrode displayed the longest duration time of ions charging/discharging at each high current density. Whereas the adverse property about a leak current due to a large series resistance effect (Wang *et al.*, 2015), which was observed from the distortion discharge curve be dissimilar to ideal liner-curve of EDLC (dash line), was clearly seen from all electrodes and rather present high value with the existence of nickel oxide structure of NiO/CNF and Ni-NiO/CNF samples.

Inset of Figure 4.19(b) shows the advantage of nickel composited in carbon nanofibers expressed by small IR-drop, which was occurred from the accumulation of DC internal resistance, even though the IR-drop of all samples was increased with the large current density, it was significantly decreased by adding of metallic nickel. By taking into account of nonlinear curve due to series resistance effect, the specific capacitance was calculated from a half-maximum region as suggested by Stoller and Ruoff method (Stoller and Ruoff, 2010), thus the specific capacitances of all electrodes tend to decrease when the current density increased. Among them, the Ni/CNF electrode yielded a value of 63.69 F g⁻¹ at a current density of 0.5 A g⁻¹ and kept a value of 44.12 F g⁻¹ at a current density of 10 A g⁻¹ that appeared to be much higher than the other electrodes (In Figure 4.20(a)). A comparison of power and energy density of all electrodes is represented by the well-known Ragone plot as shown in Figure 4.21(a). The Ni/CNF electrode outstripped the efficiency of the other electrodes, because it stored maximum energy of ~2.25 mWh g⁻¹ at a high power

density of $\sim 126 \text{ mW g}^{-1}$ for potential voltage windows of 1 V demonstrating a faster charging/discharging.

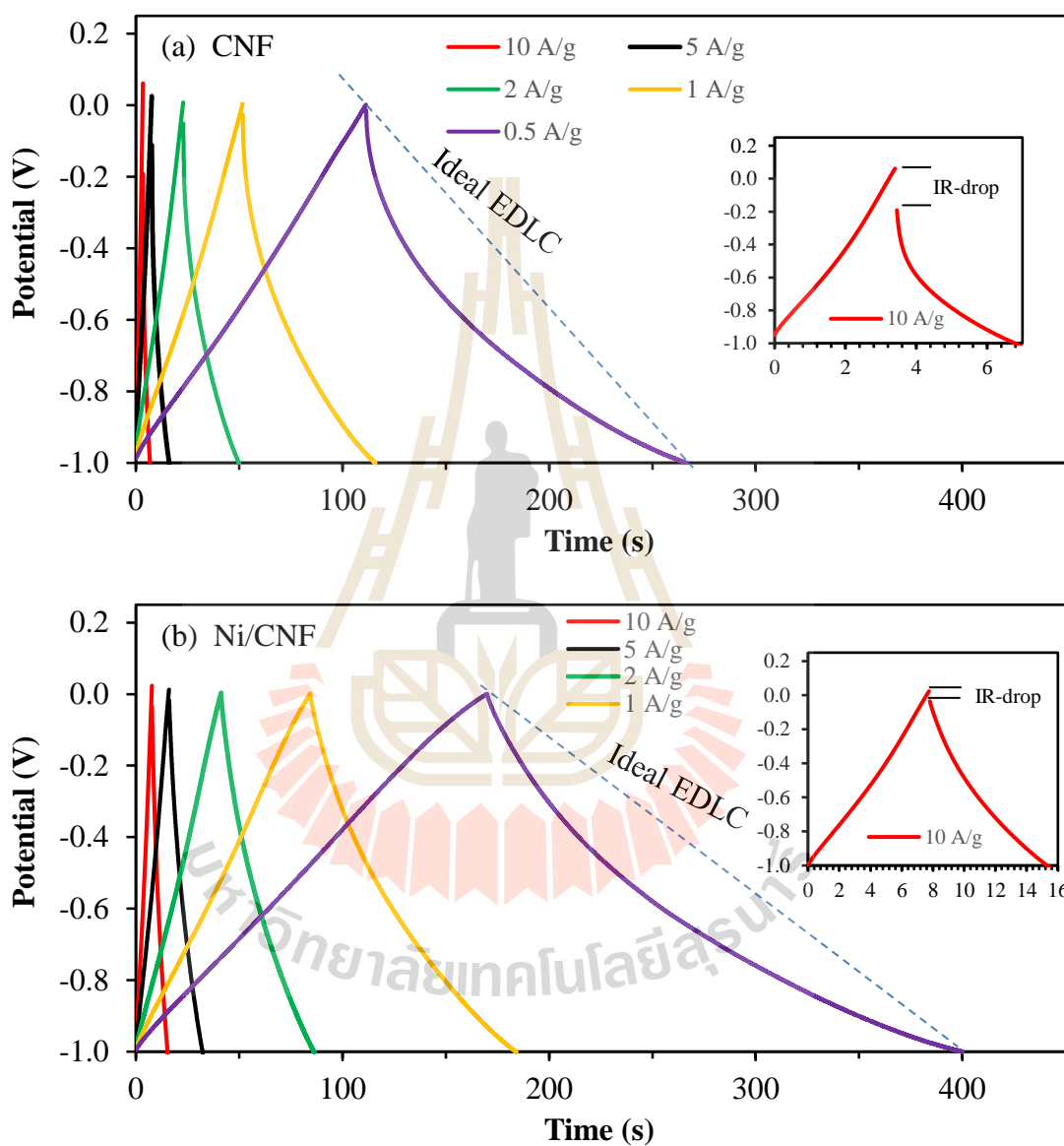


Figure 4.19 The linear voltage-time profiles of GCD measurement of (a) CNF, (b) Ni/CNF, (c) NiO/CNF, and (d) Ni-NiO/CNF as the function of current density.

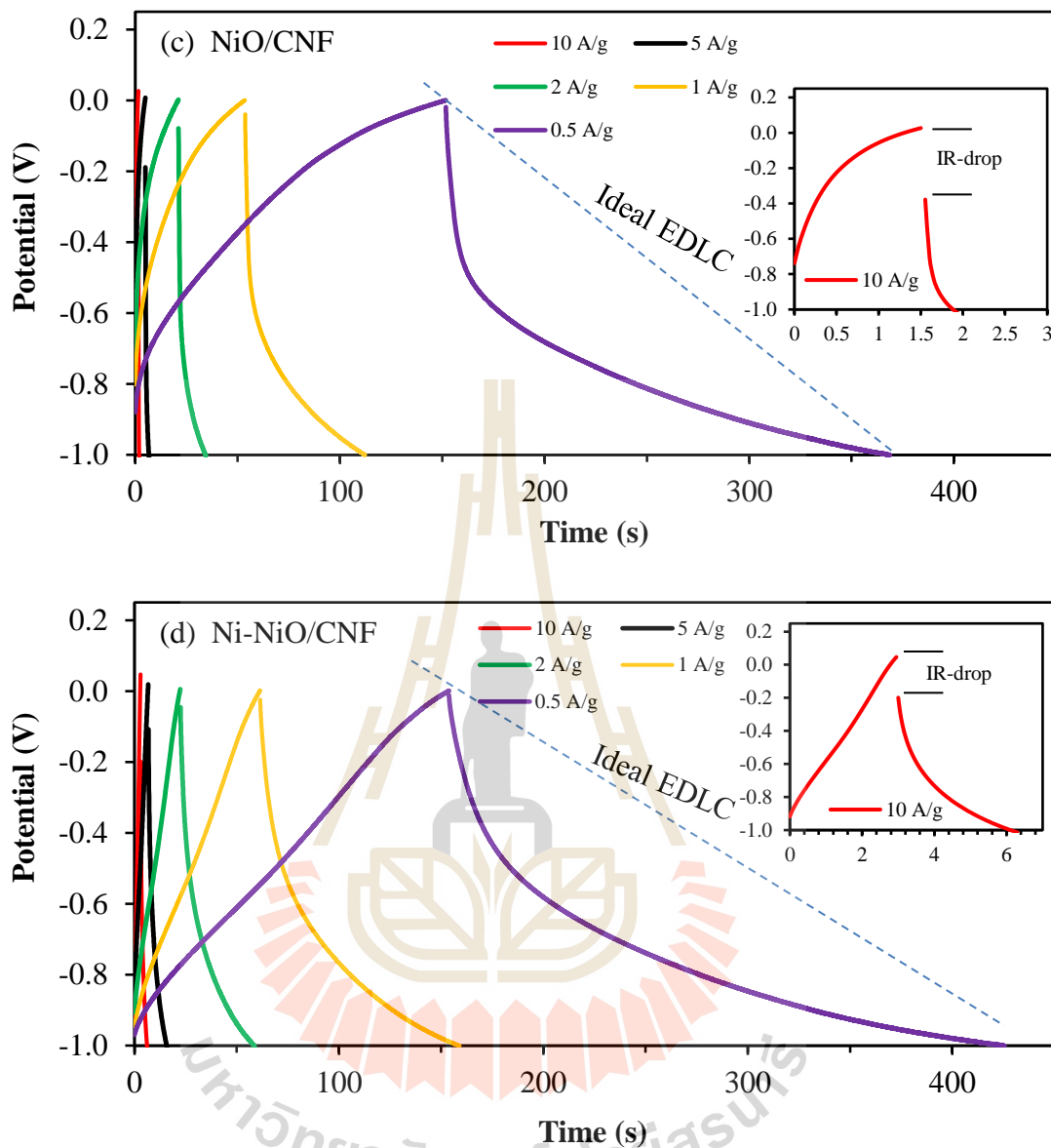


Figure 4.19 The linear voltage-time profiles of GCD measurement of (a) CNF, (b) Ni/CNF, (c) NiO/CNF, and (d) Ni-NiO/CNF as the function of current density.

(continued)

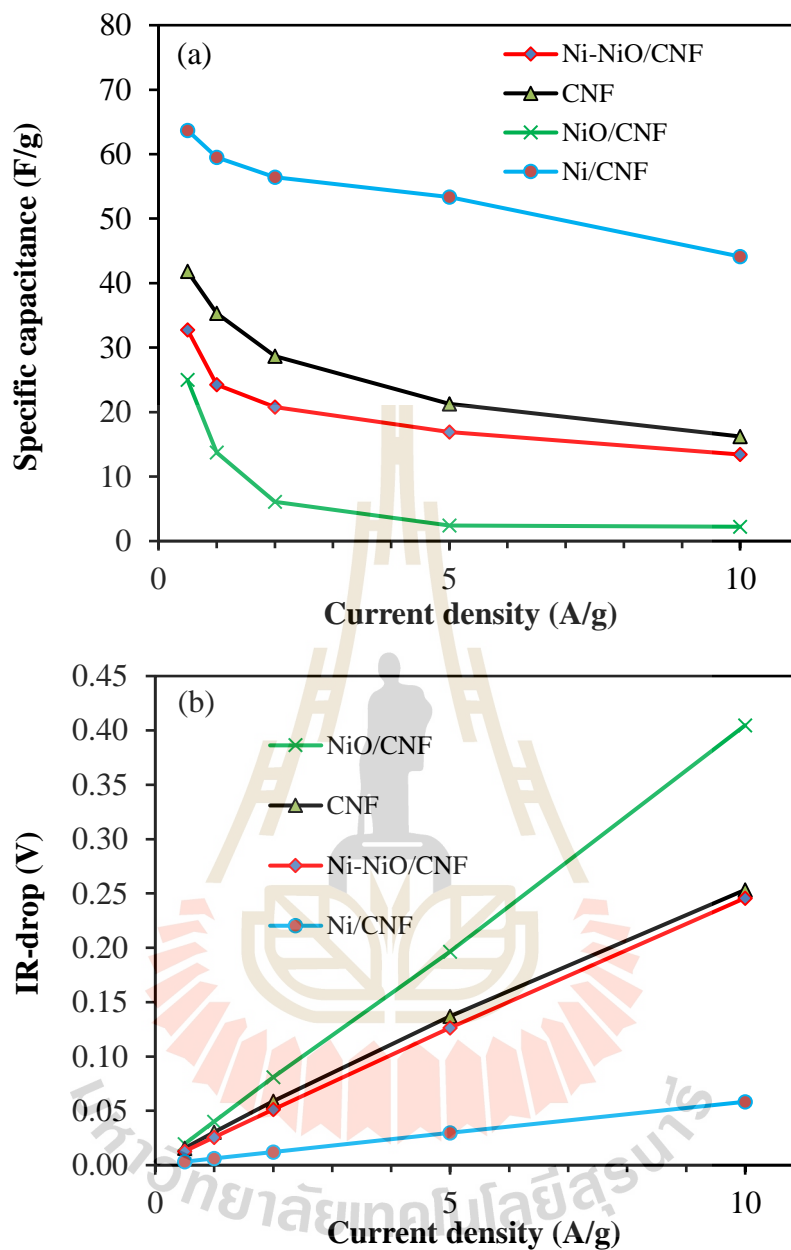


Figure 4.20 (a) Discharged specific capacitance and (b) IR-drop of CNF, Ni/CNF, NiO/CNF, and Ni-NiO/CNF as a function of current density.

4.2.5.3 Cycling stability of CNF, NiO/CNF, Ni/CNF, and Ni-NiO/CNF electrodes

The cycling capability of the electrodes were investigated using galvanostatic charge/discharge method, the measurement was processed at least 1000 cycles at a constant current density of 5 A g^{-1} . The charge/discharge voltage profiles as a function of duration times were display in inset of Figure 4.22. The capacity retention of each sample was calculated and normalized in percentage to compare with the other sample. As displayed in Figure 4.21(b), the capacitances of all electrode were decreased as a function of cycling time. The pure CNF electrode still exhibited the excellent stability of carbon by presenting the highest normalized capacitance remained of around 97% after cycling at 1000 cycles (Ra *et al.*, 2009). The samples which were contained of nickel reinforcement also retained the high capacitance value more than 83% after 1000 cycles of charge/discharging. The slight decrease in the capacitance during cycling process was interpreted to the depreciation of a faradaic reaction of the nickel or nickel oxide in charge/discharged process (Wu *et al.*, 2009; Lai and Lo, 2015). Figure 4.22 shows the comparison of charged/discharged voltage curve at various cycles of 2nd, 10th, 100th, 500th, and 1000th, all electrodes exhibited slight more charging times when repeated several cycles while the discharging periods lightly turned down. These indicated the lower power on charging and lower energy on discharging indicated that the performance was dropped from charge/discharge repeatedly. However, the normalized capacitance of all the prepared electrodes still presented great value more than 83 % that kept a high value comparing to the other works such as Si/Ni/CNF (82 % at 40 cycles) (Xu *et al.*, 2014), CNF@Ni-Co (51.1 %

at 1000 cycles) (Lai *et al.*, 2015), and Ni(OH)₂/CNF (90 % at 500 cycles) (Miao *et al.*, 2014).

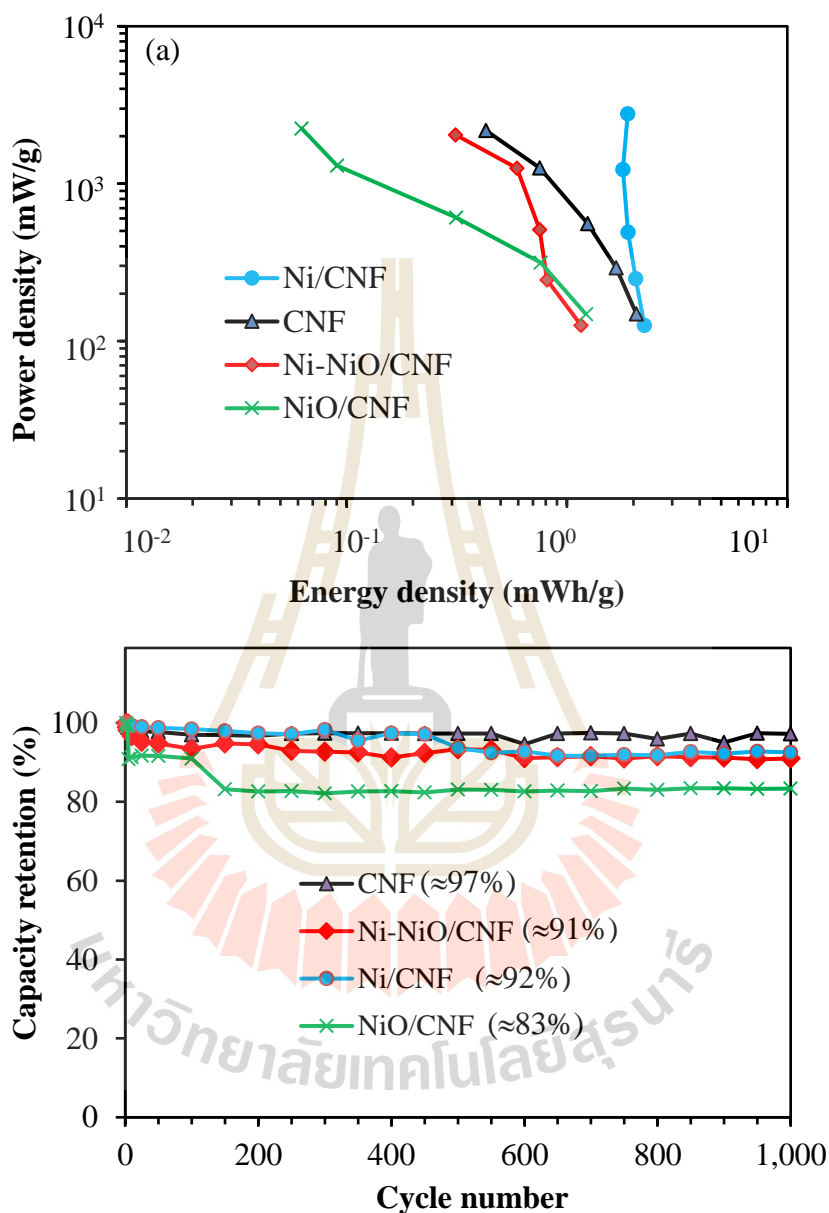


Figure 4.21 (a) A Ragone plot comparing between energy and power density of each electrode varying the discharge current density of 0.5, 1, 2, 5, and 10 A g⁻¹. (b) Cycling stability at a current density of 5 A g⁻¹ for up to 1000 cycles.

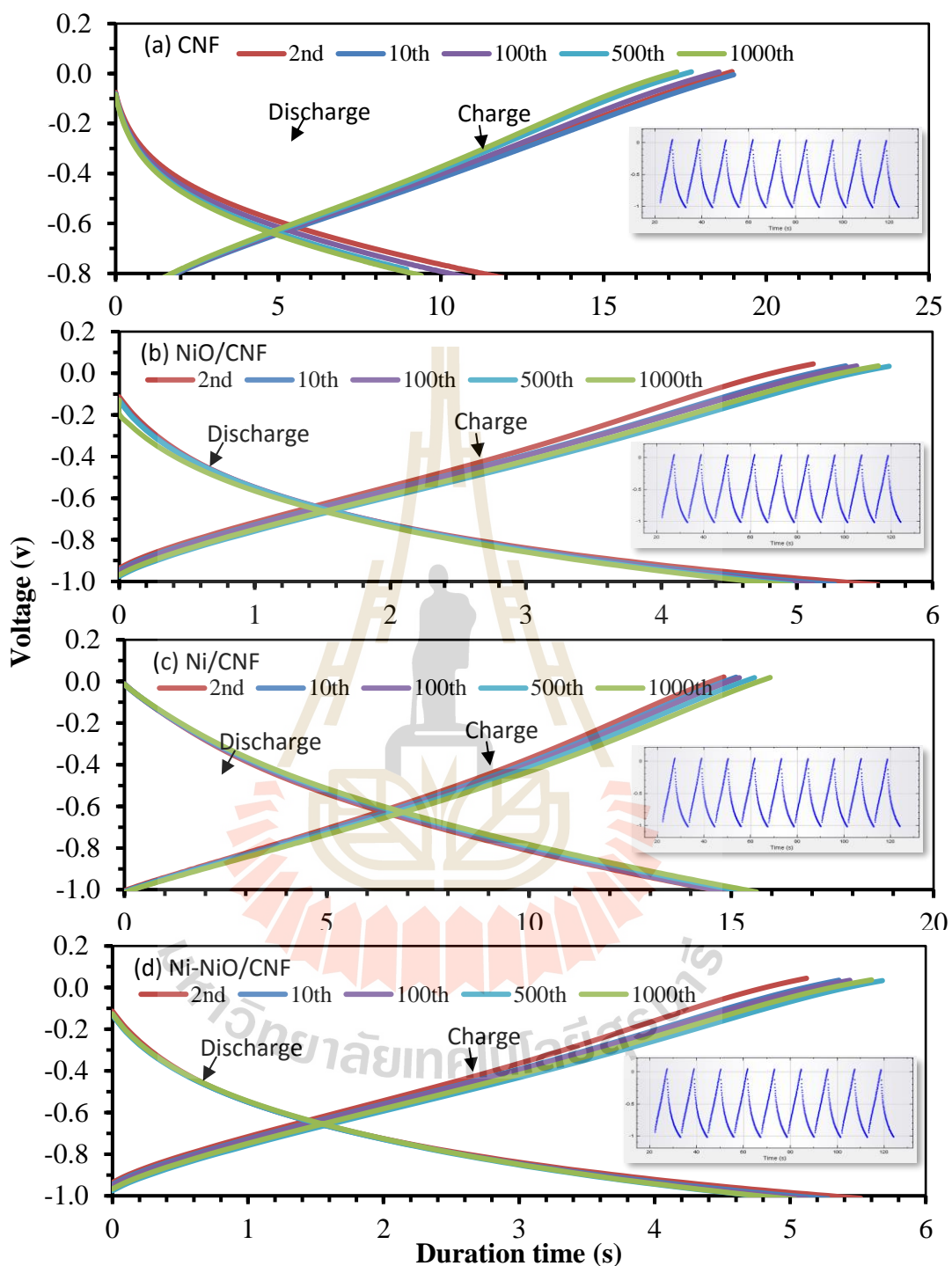


Figure 4.22 Charge/discharge profile at -1.0 V at various cycles of 2nd, 10th, 100th, 500th, and 1000th of (a) CNF, (b) NiO/CNF, (c) Ni/CNF, and (d) Ni-NiO/CNF electrode, insets presented typical continued cycling.

4.2.5.4 Electrochemical impedance spectroscopy of CNF, NiO/CNF, Ni/CNF, and Ni-NiO/CNF

Nyquist plots of EIS measurement in Figure 4.23 provide further evidence of the restriction of all samples. All spectra showed the interception on the real axis at high-frequency (Kötz and Carlen, 2000) indicated the small total effective series resistance (ESR) including bulk electrolyte and electrode resistance around 440-627 m Ω that small than previous work of Al-Enizi *et al.* (2014). Among the samples, Ni/CNF expressed closest to be ideal SC spectrum with the small semi cycle like in the mid frequency (Figure 4.23(g)) which represents the parallel combination of charge-transfer resistance (R_{ct}) and constant phase element (Q). The knee-region at low frequency is a consequence of the diffusion and transporting of electrolyte in the porous electrode which is known as Warburg impedance (Z_W) confirmed the narrow inlet of bubble pores as mentioned in CV result (inset in Figure 4.39(c)) (Keiser *et al.*, 1976). In the low frequency region, only the Ni/CNF electrode presented nearly a vertical plot behind the Warburg region indicating the SC pattern, which is modeled by the constant phase element (Q_f) or combination of constant phase element (Q_f) and diffusion element (T). The kinetic parameters derived from the Nyquist plots for CNF, NiO/CNF, Ni/CNF and Ni-NiO/CNF electrodes are summarized in Table 4.5. Figure 4.24(a) shows the plot of capacitance as a function of frequency, the capacitance of Ni/CNF electrode appeared higher than the others, and rapidly decreased during 1-10 Hz. However, there were no capacitive behaviors observed above 100 Hz for the all electrodes. The character frequency ($f_\omega = 1.68$ Hz, $\tau = 0.60$ s) was only found for Ni/CNF electrode in frequency range of 0.1-100,000 Hz (Figure 4.24(b)). The

improvements on capacitance of the sample possibly helpful for energy storage application.

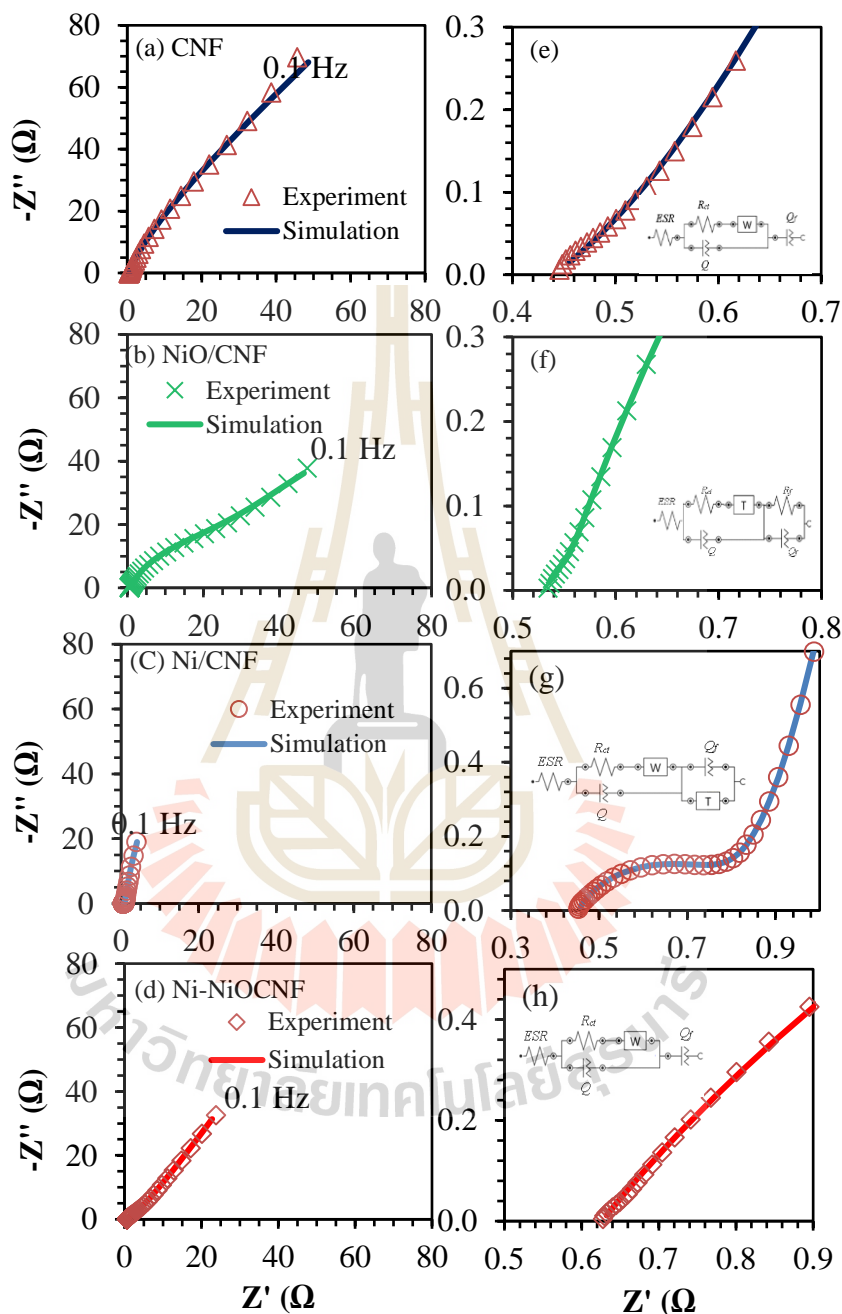


Figure 4.23 Nyquist plot and an equivalent circuit of (a – d) CNF, NiO/CNF, Ni/CNF, and Ni-NiO/CNF at a perturbation amplitude of 0.1 V. (e – h) Enlarged picture of each sample at high-frequency region.

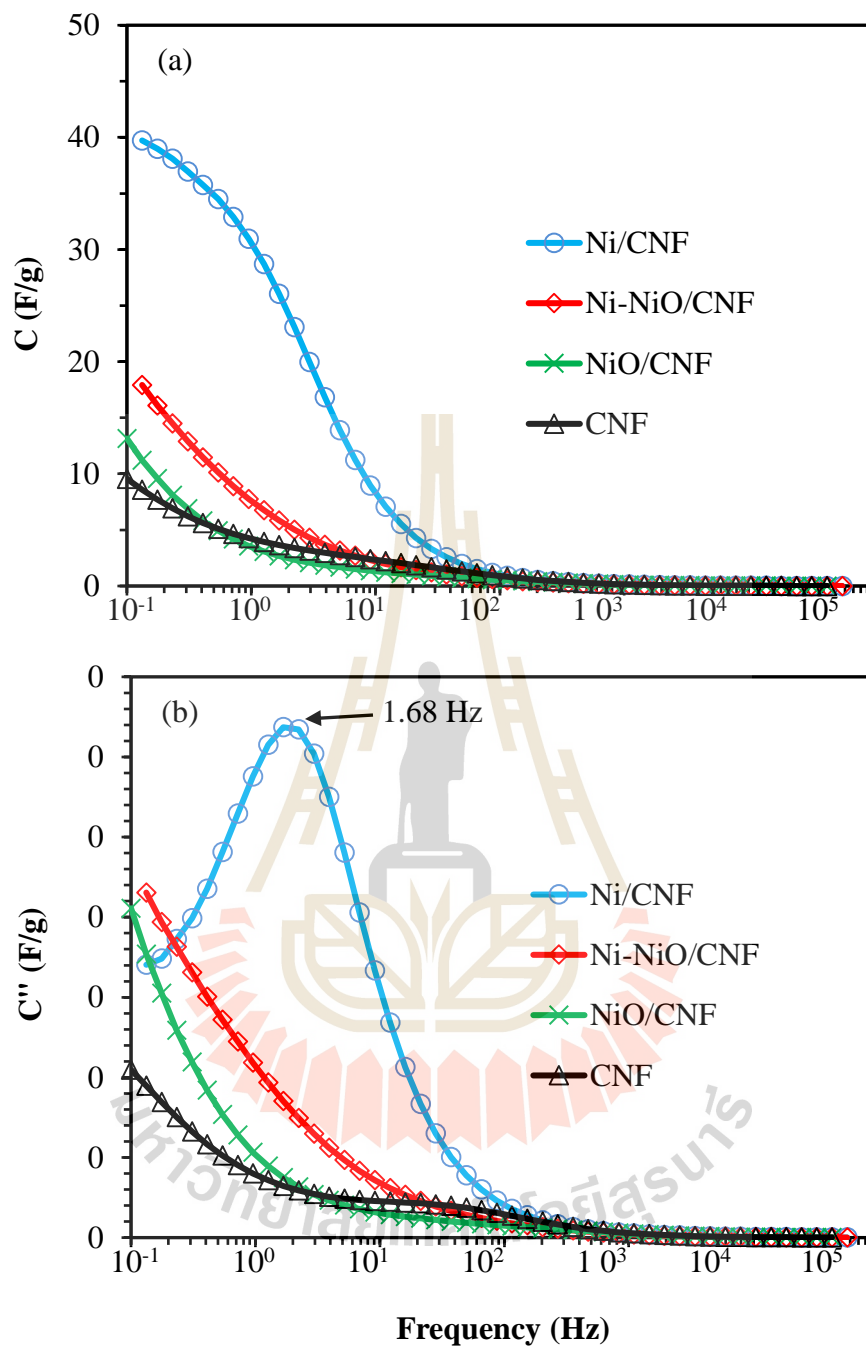
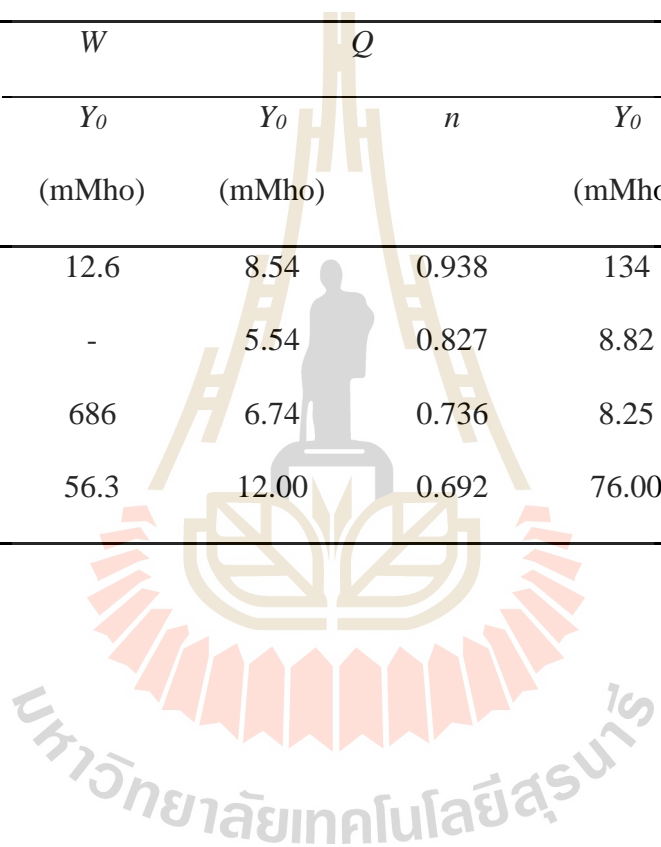


Figure 4.24 (a) Capacitance as a function of frequency. (b) The imaginary part in impedance of all electrodes.

Table 4.5 Kinetic parameters derived from the Nyquist plots for CNF, NiO/CNF, Ni/CNF and Ni-NiO/CNF electrodes.

Sample	ESR ($m\Omega$)	R_{ct} (Ω)	W		Q		Q_f		T	
			Y_0	Y_0	n	Y_0	n	Y_0	B	
			($mMho$)	($mMho$)		($mMho$)		($mMho$)		
CNF	440	15.60	12.6	8.54	0.938	134	0.472	-	-	
NiO/CNF	533	25.60	-	5.54	0.827	8.82	0.858	25.6	4.6	
Ni/CNF	453	0.34	686	6.74	0.736	8.25	0.298	5500	0.0015	
Ni-NiO/CNF	627	3.21	56.3	12.00	0.692	76.00	0.745	-	-	



4.3 Characterization and electrochemical properties of silver and/or manganese cluster composite carbon-based nanofibers ($\text{AgO}_x\text{-MnO}_x\text{/CNF}$)

4.3.1 Fabrication of CNF, $\text{AgO}_x\text{/CNF}$, $\text{MnO}_x\text{/CNF}$, and $\text{AgO}_x\text{-MnO}_x\text{/CNF}$.

4.3.1.1 Solution preparation

Figure 4.5 represents the whole procedure of material preparation including preparation of the solution, electrospinning, and calcination. The precursor solutions were prepared by dissolving 10 wt.% PAN and 20 wt.% metal sources (the metal content was compared to PAN content) in DMF separately. After being strongly stirred at room temperature for 3 h, each solution was then mixed together and further stirred for 0.5 h before being ultrasonicated for 3 h at 50 °C and subsequently stirred overnight at room temperature to obtain the homogeneous solution, which was ready for electrospinning. Four different conditions; PAN, $\text{AgNO}_3\text{/PAN}$, $\text{Mn}(\text{NO}_3)_2\text{/PAN}$ and $\text{AgNO}_3\text{-Mn}(\text{NO}_3)_2\text{/PAN}$, were prepared for comparison.

4.3.1.2 Electrospinning of pure CNF, $\text{AgO}_x\text{/CNF}$, $\text{MnO}_x\text{/CNF}$, and $\text{AgO}_x\text{-MnO}_x\text{/CNF}$

The homogeneous precursor solution was loaded into 10 ml plastic syringes and then installed on the four-nozzle electrospinning system. The solution was fed at 0.4-0.5 ml h⁻¹, the applied voltage was controlled between 10-12 kV, and the TDC was 18 cm. The solution jets were stretched and moved along electric field to form nanofibers and collected on an aluminum foil rotating drum as a paper sheet. The sheet was then removed from the drum every 6 h and stored in an incubator at 70 °C at least one day before characterization and calcination.

4.3.2 Characterization of as-spun and calcined pure PAN, AgNO₃/PAN, Mn(NO₃)₂/PAN, and AgNO₃-Mn(NO₃)₂/PAN.

4.3.2.1 Thermal analysis of as-spun and calcined pure PAN, AgNO₃/PAN, Mn(NO₃)₂/PAN, and AgNO₃-Mn(NO₃)₂/PAN

The weight losses of all as-spun PAN, AgNO₃/PAN, Mn(NO₃)₂/PAN, and AgNO₃-Mn(NO₃)₂/PAN were studied using TGA and DSC, and the experiment were operated in N₂ atmosphere at flow rate of 100 ml min⁻¹ and ranged the temperature from 25 up to 1000 °C at heating rate of 5 °C min⁻¹. Figure 4.4(a) shows the three majors weight loss of pure PAN and four major weight loss for the all composite samples during the heating process. Figure 4.3(a) shows the three major weight losses of pure PAN and four major weight losses for the all composite samples during the heating process. The first minor weight loss of all samples before 175 °C resulted from the removal of the free solvent in the as-spun nanofibers, which were in agreement with the weight losses observed on consistent TGA results of as-spun nickel composite PAN-based nanofibers. The second region was the pre-weight loss only observed respectively fund on as-spun of composite samples of AgNO₃/PAN, Mn(NO₃)₂/PAN, and AgNO₃-Mn(NO₃)₂/PAN nanofibers for 200, 252, and 253 °C which were attributed to the decomposition of silver and/or manganese into silver and/or manganese oxide (Nohman *et al.*, 1995; Preisler, 1980) compounds, respectively. The significant weight loss at 306, 312, 281, and 297 °C respectively observed for as-spun PAN, AgNO₃/PAN, Mn(NO₃)₂/PAN, and AgNO₃-Mn(NO₃)₂/PAN nanofibers can be interpreted as the infusible ladder polymer forming in cyclization of nitrile groups of matrix PAN during carbonization (Alarifi *et al.*, 2015; Shi *et al.*, 2015). Finally, the last weight loss regions of all samples initiated

above 700 °C and continued till 1000 °C related to the decomposition and degradation temperature of carbon structure during pyrolyzed at a high temperature in an inert gas which is in agreement with the DSC results (Fleming *et al.*, 2014; Maensiri *et al.*, 2006; Dhakate *et al.*, 2011).

The DSC of all as-spun nanofibers were observed at the temperature ranged from 25 to 1000 °C with a heating rate of 10 °C min⁻¹ under a nitrogen atmosphere flow rate of 100 ml min⁻¹. As displayed in Figure 4.25(b), the PAN curve appeared with its main exothermic peak at around 301 °C, the main peaks of both AgNO₃-Mn(NO₃)₂/PAN and Mn(NO₃)₂/PAN curves shifted to a lower temperature and centered at around 297 and 280 °C, respectively, whereas the AgNO₃/PAN curve exhibited different features with the peak slightly shifted to the higher temperature in comparison with the chaste PAN nanofibers and centered at around 310 °C. These features suggest that the embedding of Mn(NO₃)₂ encouraged a greater cyclization reaction of nitride groups resulting in a lower decomposition temperature, which was interpreted to be the cause of the high graphite structure forming in MnO_x/CNF as observed agreeable with TEM results (Liu *et al.*, 2009; Liu *et al.*, 2012).

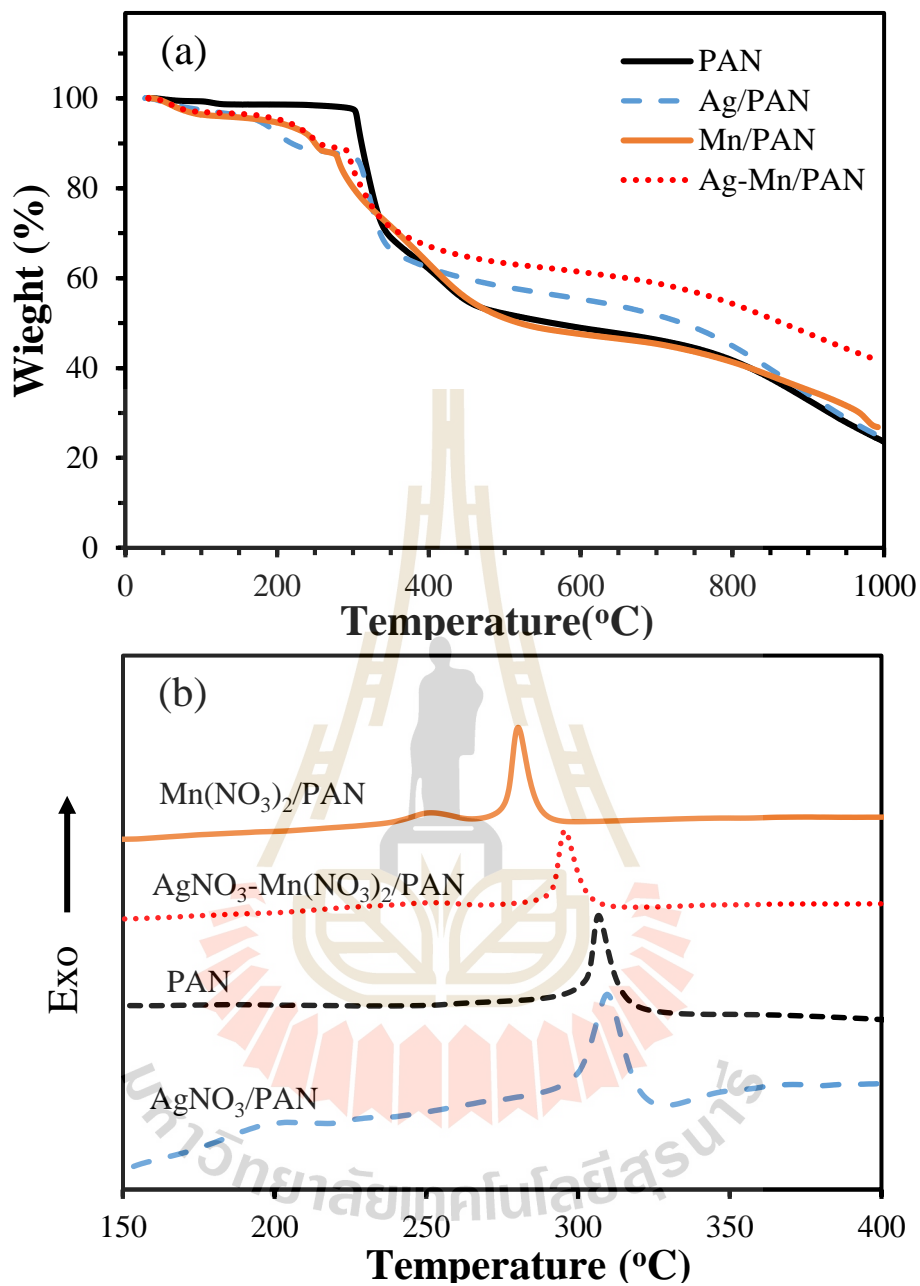
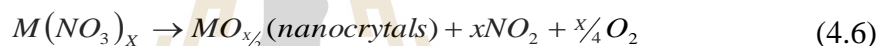


Figure 4.25 (a) TGA and (b) DSC curves of as-spun PAN, AgNO₃/PAN, Mn(NO₃)₂/PAN, and AN/AgNO₃-Mn(NO₃)₂.

After calcination, the TGA of the calcined samples was studied again in air atmosphere up to 1000 °C in order to determine the mass of non-carbon (metal and/or metal oxide) elements loading in nanofibers. As shown in Figure 4.26(a), the slight weight loss below 100 °C was considered as the removal of absorbed humidity in the porous structure of the sample. The subsequent dramatic weight losses in the temperature range of 350-650 °C were evidence of the oxidization of carbon components in an oxygen-rich environment, and the complete decomposition arose at above 378, 538, 590, and 640 °C for AgO_x-MnO_x/CNF, AgO_x/CNF, MnO_x/CNF, and CNF, respectively (Wang *et al.*, 2015). The simple process of thermal decomposition of metal nitrate in metal oxide were described as follows (Wang *et al.*, 2008).



Where *M* are Mn and Ag. Especially for silver nitrate, it was easily formed as metallic silver during heating as a following process (Mayer *et al.*, 2002).



The non-carbon components loading in nanofibers were determined from residue weight loss at 1000 °C, which was obtained values of 14%, 16%, and 17% for AgO_x-MnO_x/CNF, MnO_x/CNF, and AgO_x/CNF, respectively (Figure 4.26(b)).

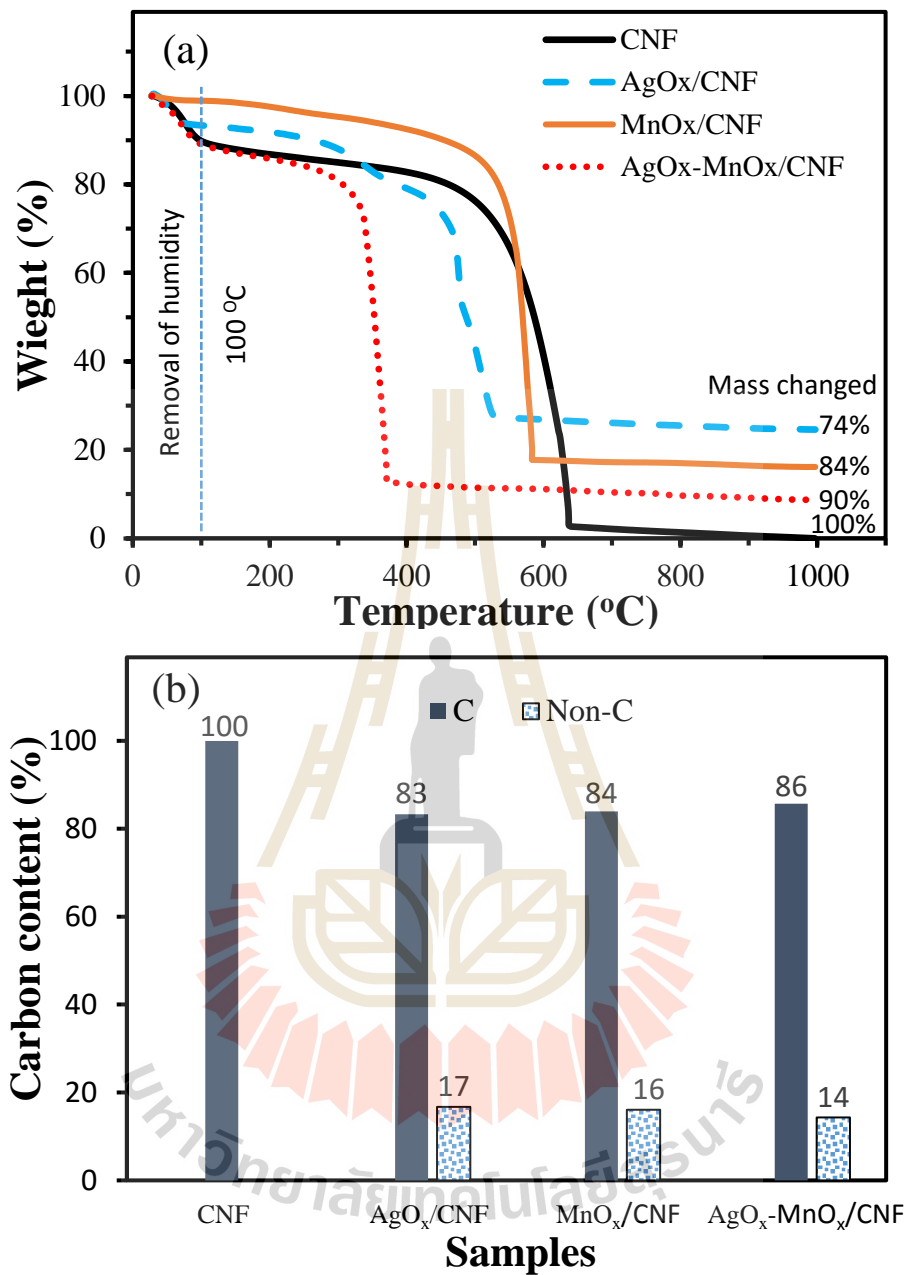


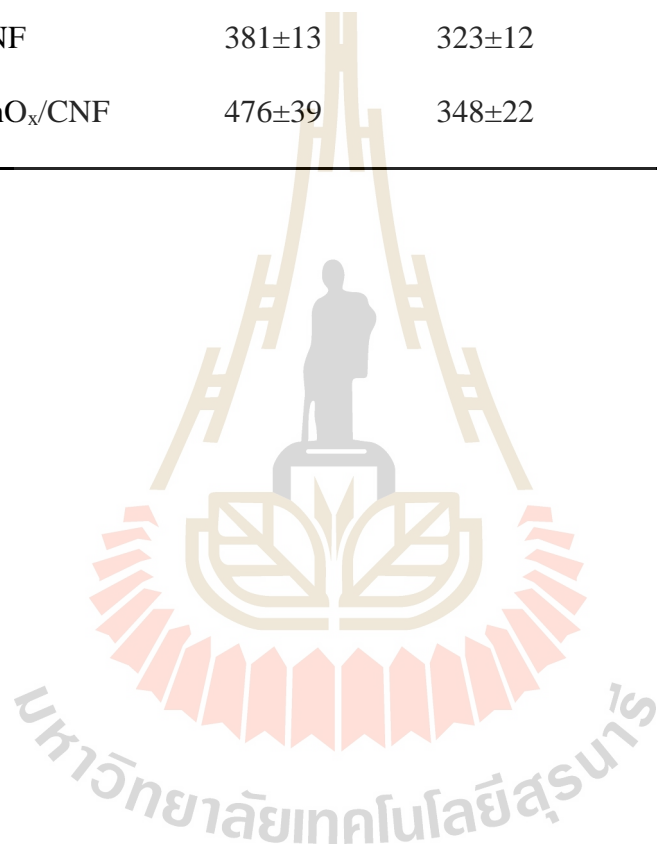
Figure 4.26 (a) TGA of CNF, AgO_x/CNF, MnO_x/CNF, and AgO_x-MnO_x/CNF carried out at the temperature ranged from 25-1000 °C in an air atmosphere and a heating rate of 10 °C min⁻¹. (b) The plot of carbon and non-carbon content determined from TGA of various composite CNF.

4.3.2.2 Morphology of pure CNF, AgO_x/CNF, MnO_x/CNF, and AgO_x-MnO_x/CNF

Figure 4.27(a-d) shows the high magnification SEM images of the as-spun nanofibers. All products exhibit a few rough surfaces of long uniform, and randomly arranged nanofibers. There are the significant changes on composite as-spun nanofibers because the embedding of metallic precursors causes a different net charge density and force repulsion during electrospinning (Rajzer *et al.*, 2012). PAN without metal addition still remains the smallest size of 295 ± 11 nm. The mixture of metal precursors in both AgNO₃-Mn(NO₃)₂/PAN and Mn(NO₃)₂/PAN yielded the average size of 381 ± 13 and 476 ± 39 nm, respectively, whereas a significant increase in the average diameter was observed on AgNO₃/PAN nanofibers for 836 ± 108 nm. After calcination, only the pure CNF was significantly distorted and tended to fuse together with other fibers yielding brittle and inflexible properties (Figure 4.28 (e)). Whereas Figure 4.28(f) and (g) display the separated uniform fibers and relatively smooth surfaces of AgO_x/CNF and AgO_x-MnO_x/CNF. On the other hand, MnO_x/CNF became a rough surface. Overall, the measurable decrease in the diameter sizes was found to be of around 15-25% compared to the as-spun, and there were other effects including loss of solvent, phase transition of the polymer into carbon structures, and some parts of the matrix carbon were oxidized during CO₂ activation. The average sizes of overall as-spun and calcined nanofibers are summarized in Table 4.6.

Table 4.6 Average diameter of all fiber and particle size of CNF, AgO_x/CNF, MnO_x/CNF and AgO_x-MnO_x-CNF nanofibers.

Sample	Fiber size (nm)		Particle size (nm)
	As-spun	Calcined	
CNF	295±11	237±8	-
AgO _x /CNF	836±108	643±41	13.5±1.4
MnO _x /CNF	381±13	323±12	33.1±6.9
AgO _x -MnO _x /CNF	476±39	348±22	15.2±0.8



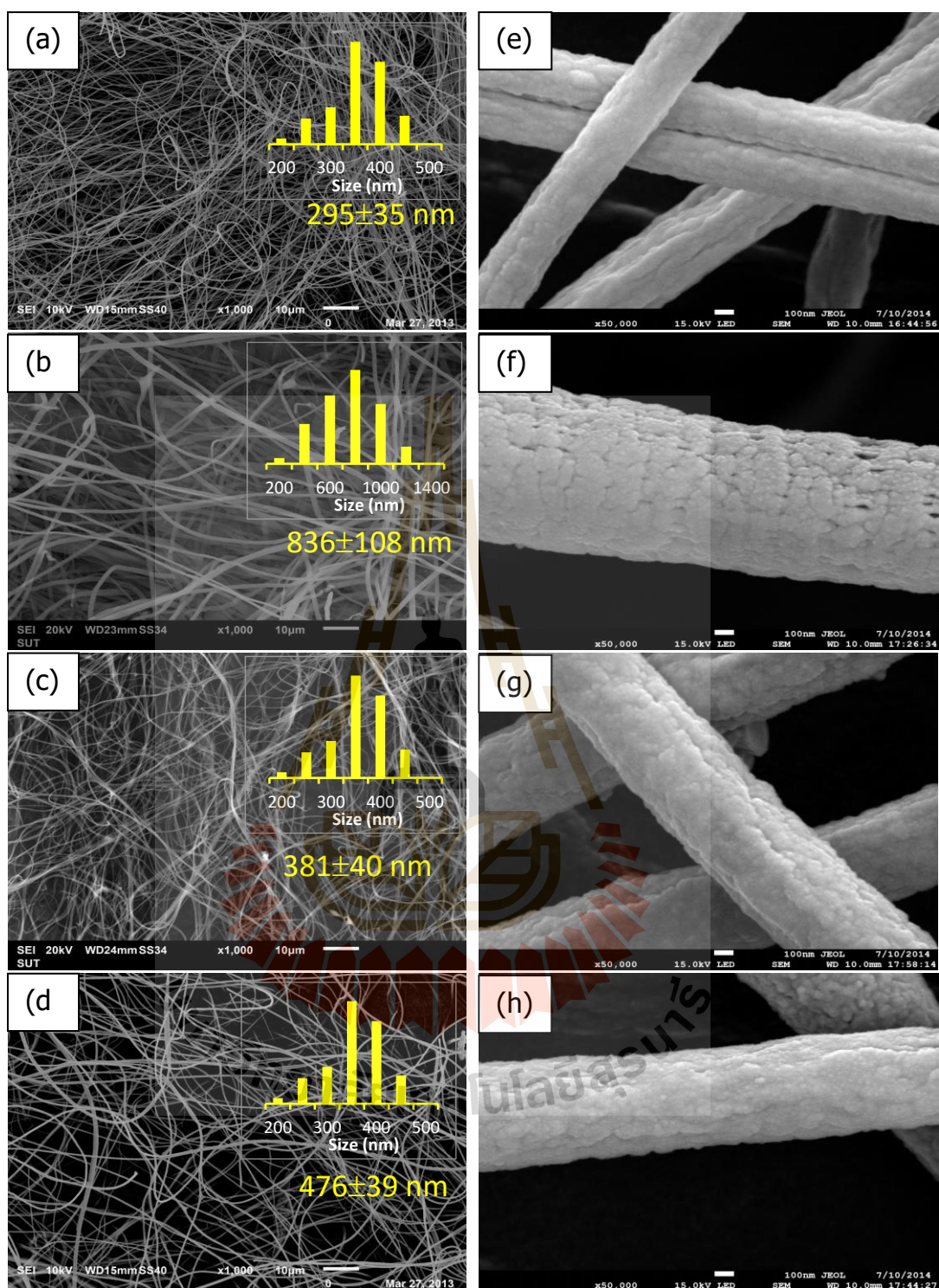


Figure 4.27 SEM images of as-spun (a,e) PAN, (b,f) AgNO_3/PAN , (c,g) $\text{Mn}(\text{NO}_3)_2/\text{PAN}$, and (d,h) $\text{AgNO}_3\text{-Mn}(\text{NO}_3)_2/\text{PAN}$ (flow rate: 0.35 ml h^{-1} , TDC: 18 cm, applied voltage: 12 kV)

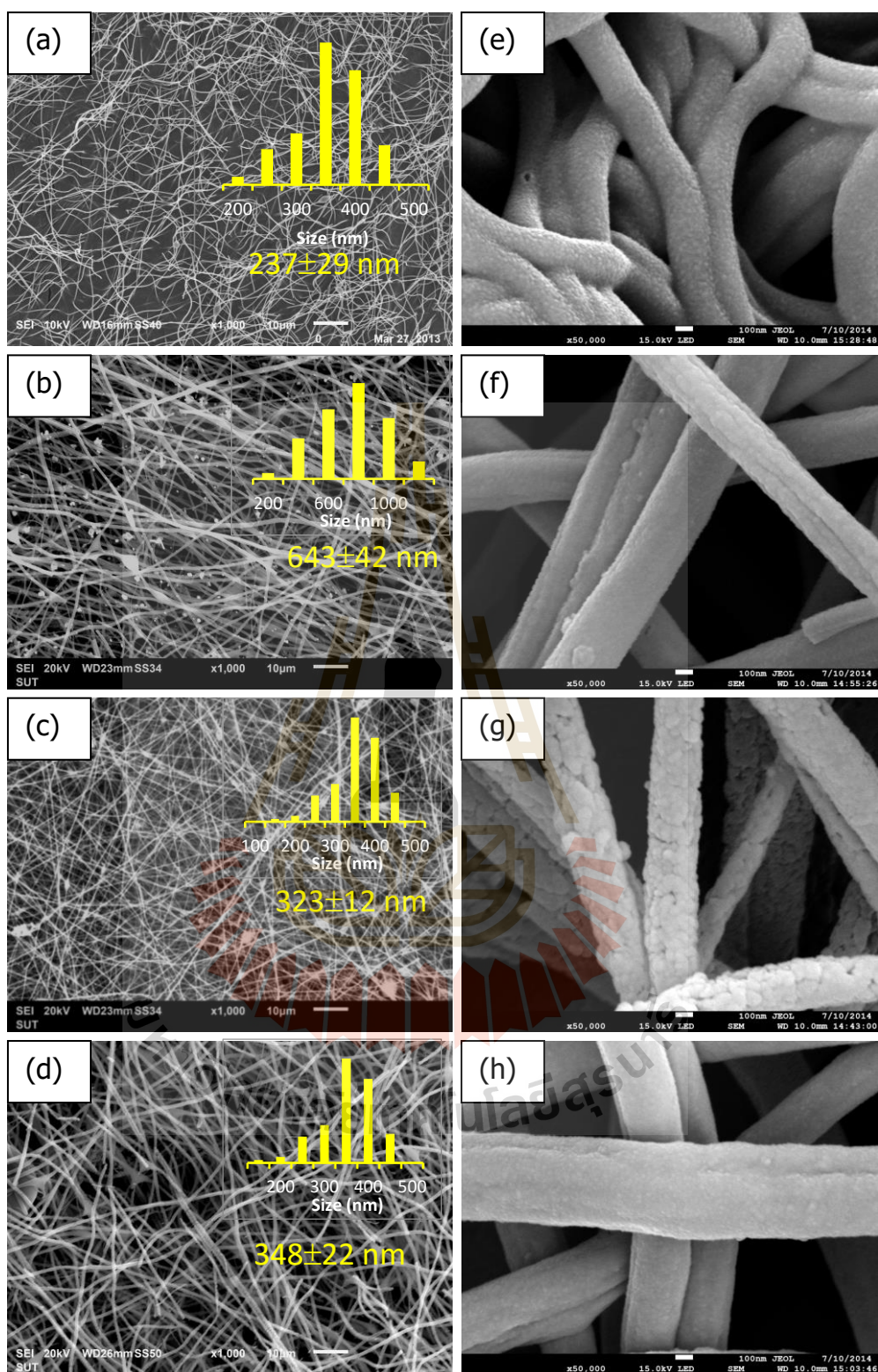


Figure 4.28 SEM images of (a,e) CNF, (b,f) AgO_x/CNF , (c,g) MnO_x/CNF , and (d,h) $\text{AgO}_x\text{-MnO}_x/\text{CNF}$.

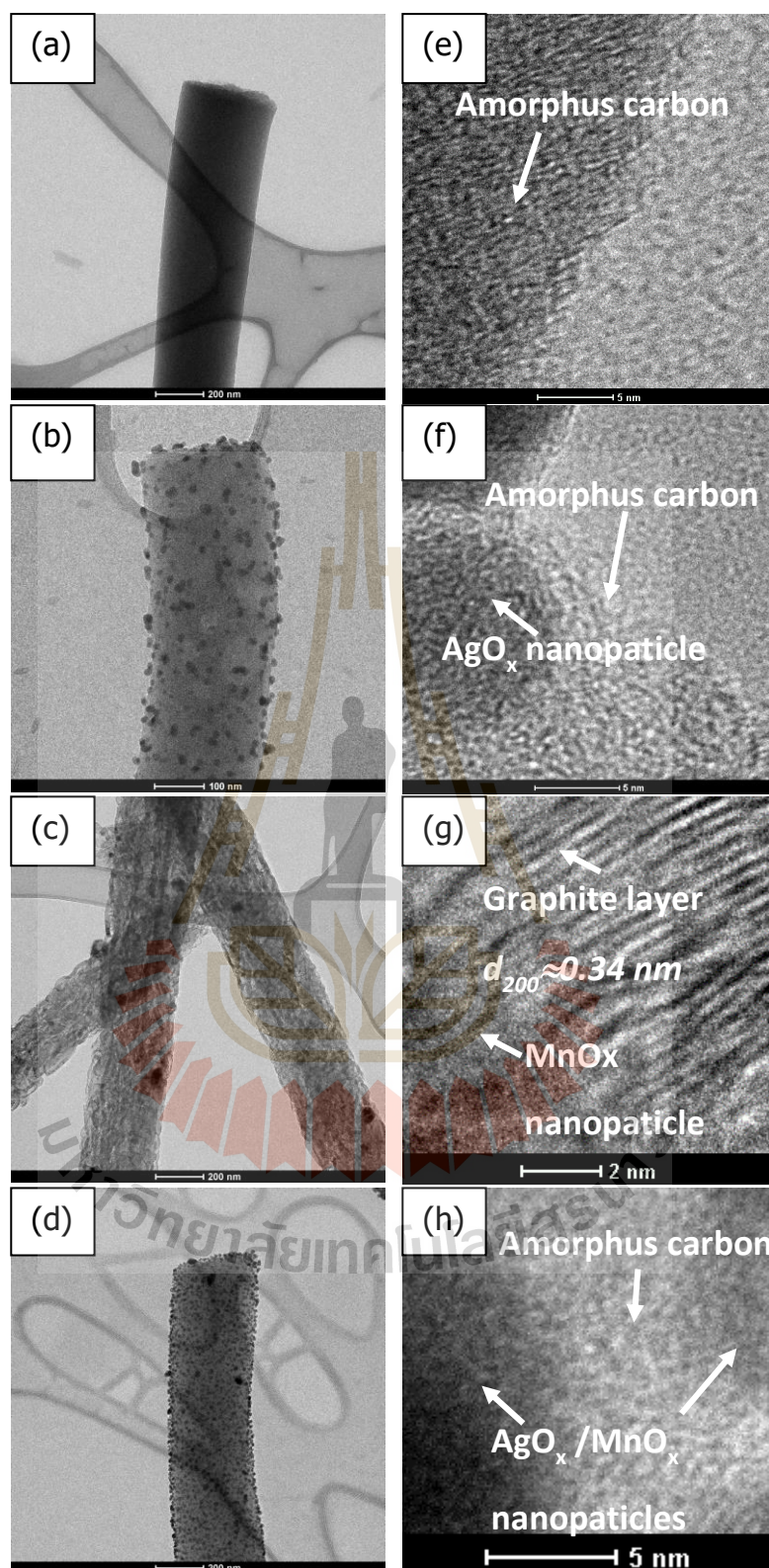


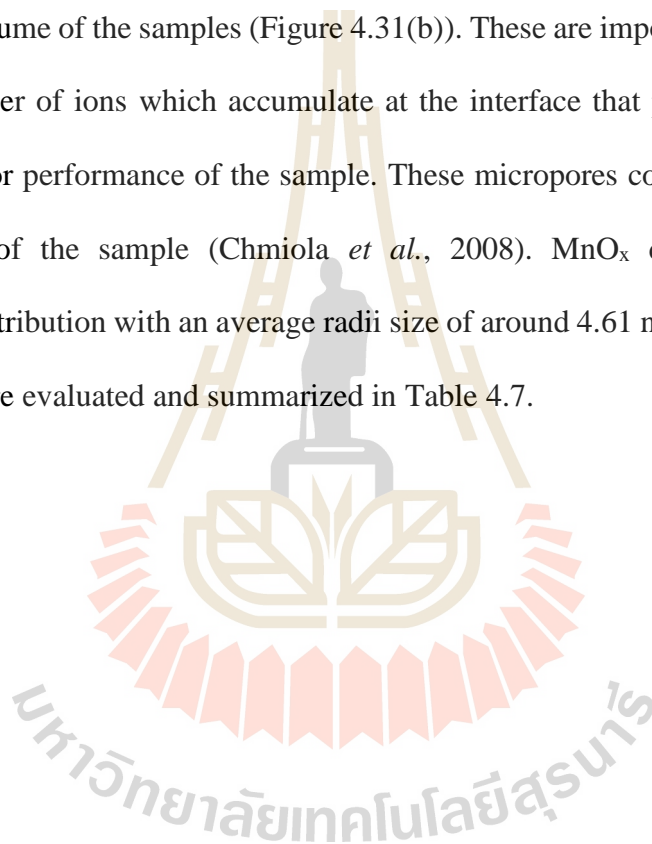
Figure 4.29 TEM images of (a) CNF, (b) AgO_x/CNF, (c) MnO_x/CNF, and (d) AgO_x-MnO_x/CNF. Figures e, f, g, and h are a high magnification of each sample.

The internal structures of the calcined samples were further investigated using TEM. As shown in Figure 4.29, the AgO_x/CNF and AgO_x-MnO_x/CNF were composed of metal nanoparticles with an average size of 13.5±1.4 nm that were located on the inner and outer surfaces and distributed homogeneously along the fibers. Whereas most the MnO_x/CNF nanoparticles with average size of 33.1±6.9 nm were encapsulated in carbon nanofibers (Figure 4.29(c)). It is noteworthy that the enlarged picture of MnO_x/CNF (Figure 4.29(g)) in the absence of Ag clusters displayed the typical graphite reflection of the plane (200) with *d*-spacing of ~ 0.34 nm, which suggests that only the adding of Mn component causes the high graphite structure of nanofibers. Furthermore, the existence of nanoparticles possibly reduces the fusion of fibers during calcination, which was observed for pure CNF.

4.3.2.3 Surface area and porosity of pure CNF, AgO_x/CNF, MnO_x/CNF, and AgO_x-MnO_x/CNF

The specific surface area and pore character of pristine CNF, AgO_x/CNF, MnO_x/CNF, and AgO_x-MnO_x/CNF were investigated by measuring N₂ adsorption/desorption. As shown in Figure 4.30(a), all samples exhibit hysteresis loops which are typical type IV isotherms due to capillary condensation of nitrogen in mesopore and a part of micropore can be attributed by knee-shape at low pressure. In detail, MnO_x/CNF displayed type H3 hysteresis loop possibly due to the nonuniform pore, the denseness graphitic structures as postulate in Figure 4.31(c) resulting in poor specific surface area of 112 m² g⁻¹. Whereas the CNF, AgO_x/CNF, and AgO_x-MnO_x/CNF present type H4 hysteresis loop of uniform slit pores shape existing in each sample (Leofanti *et al.*, 1998). The pore size distributions of the samples were evaluated using both the BJH and MP methods, which are shown in Figure 4.30(b) and

the inset. The broken amorphous structure of carbon matrix (Figure 4.1(a)) in CNF, AgO_x/CNF and AgO_x-MnO_x/CNF have mainly micropores with average diameter sizes of around 0.6-0.7 nm. Both the highest specific surface area of 812 m² g⁻¹ and the total pore volume of 0.45 cm³ g⁻¹ were observed for AgO_x-MnO_x/CNF possibly due to the nanoparticles reinforcement which were dispersed over the samples cannot bond with textural matrix carbon then created the space around the nanoparticles resulting high pore volume of the samples (Figure 4.31(b)). These are important as they provide a large number of ions which accumulate at the interface that possibly enhance the supercapacitor performance of the sample. These micropores could be optimized the capacitance of the sample (Chmiola *et al.*, 2008). MnO_x displayed significant mesopore distribution with an average radii size of around 4.61 nm. The other textural parameters are evaluated and summarized in Table 4.7.



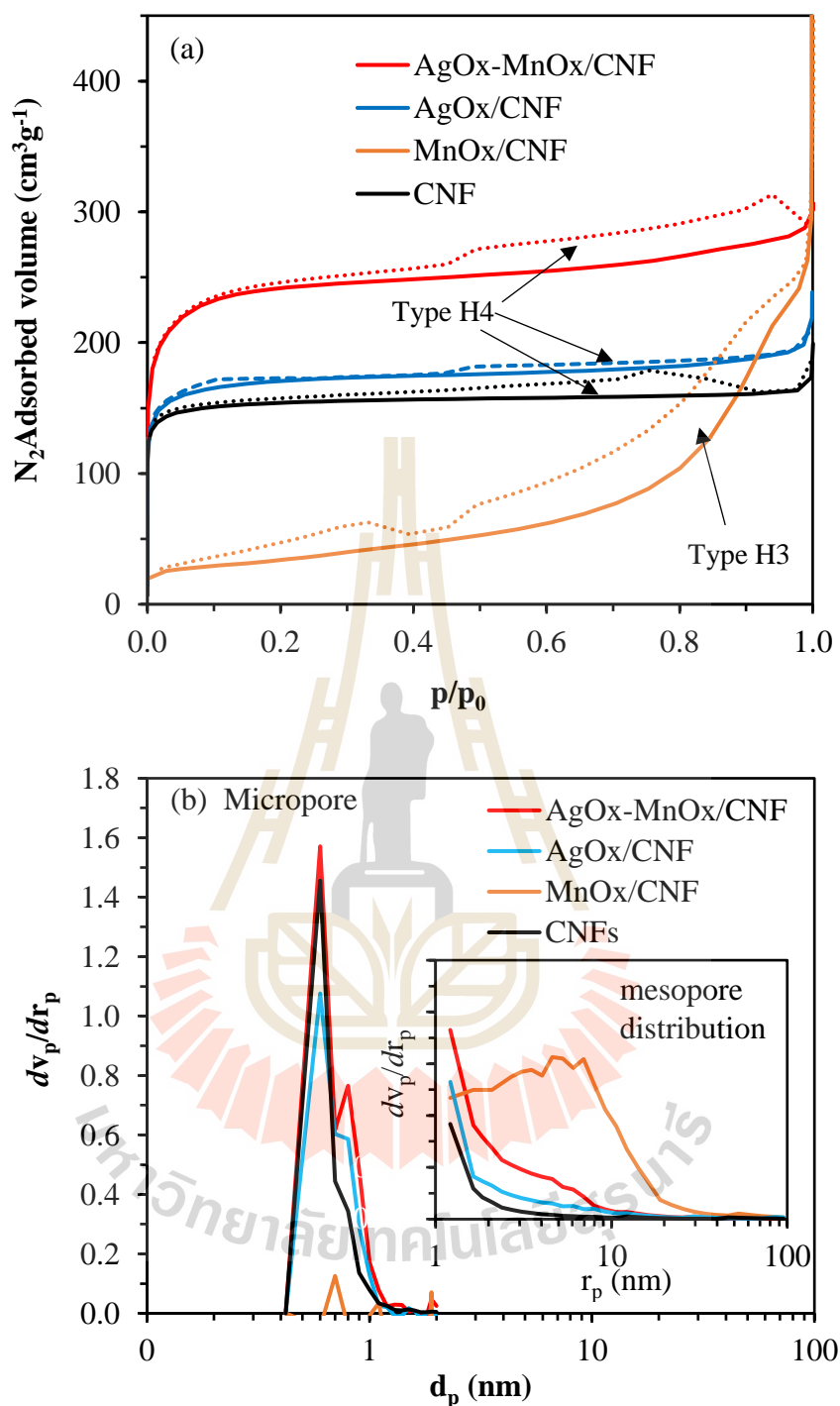


Figure 4.30 (a) N_2 adsorption and desorption isotherm (solid line (ADS) and dash line (DES)), (b) Micropore distribution by MP plot, and (inset) Mesopore distribution from BJH plot of CNF, AgO_x/CNF, MnO_x/CNF, and AgO_x-MnO_x/CNF.

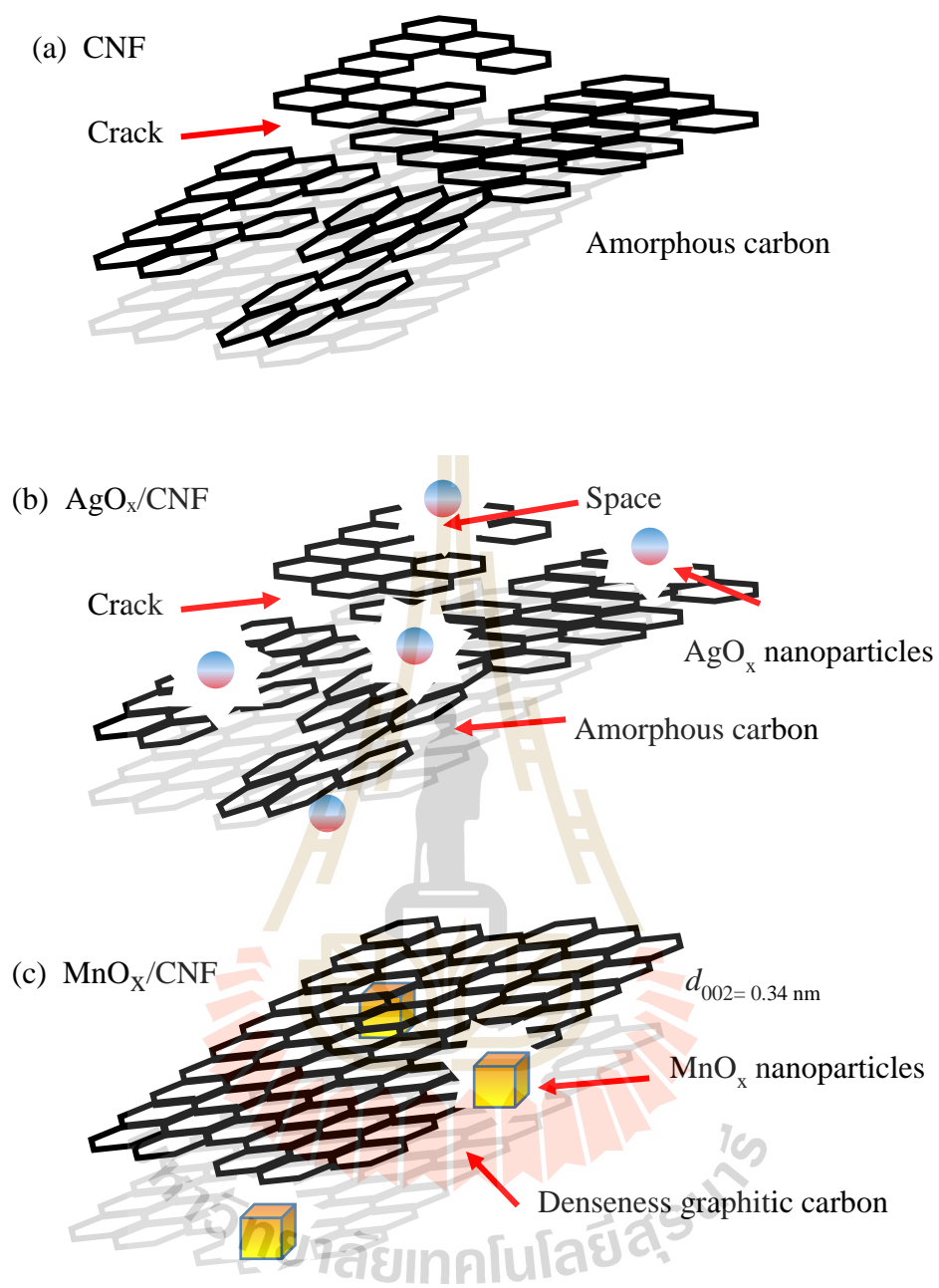
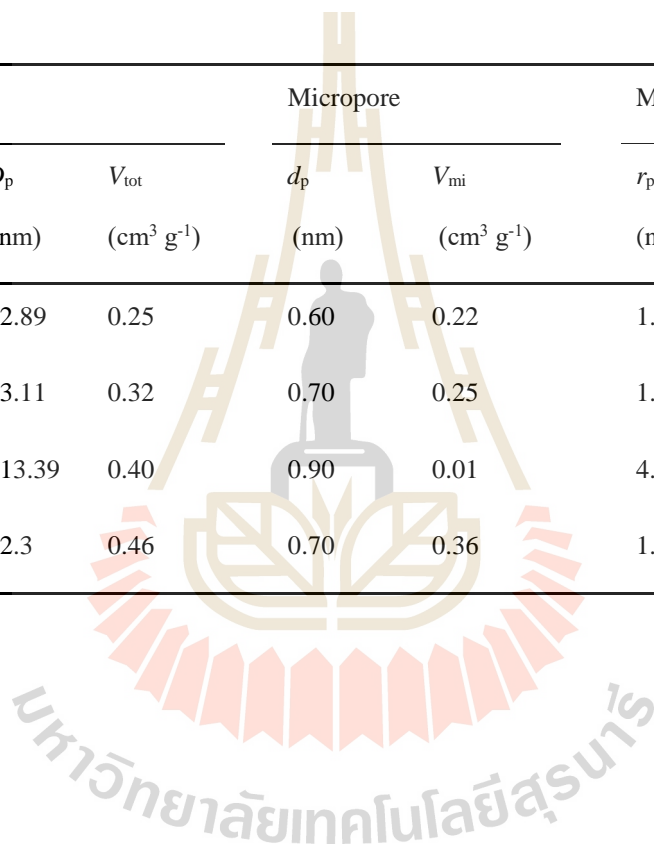


Figure 4.31 Schematic represents the textural carbon structure and the reinforcement of (a) CNF, (b) AgO_x/CNF or AgO_x-MnO_x/CNF, and (c) MnO_x/CNF.

Table 4.7 The textural parameters of CNF, AgO_x/CNF, MnO_x/CNF, and AgO_x-MnO_x/CNF, obtained by BET, MP, and BJH method.

Sample	BET			Micropore		Mesopore		$V_{mi}: V_{me}$ (%)
	S_{BET}	D_p	V_{tot}	d_p	V_{mi}	r_p	V_{me}	
	(m ² g ⁻¹)	(nm)	(cm ³ g ⁻¹)	(nm)	(cm ³ g ⁻¹)	(nm)	(cm ³ g ⁻¹)	
CNF	362	2.89	0.25	0.60	0.22	1.21	0.04	85:15
AgO _x /CNF	405	3.11	0.32	0.70	0.25	1.22	0.07	78:22
MnO _x /CNF	119	13.39	0.40	0.90	0.01	4.61	0.39	3:97
AgO _x - MnO _x /CNF	812	2.3	0.46	0.70	0.36	1.21	0.10	78:22



4.3.2.4 Microstructure and component analysis of pure CNF, AgO_x/CNF, MnO_x/CNF, and AgO_x-MnO_x/CNF

The surface functional groups of all the as-spun (PAN, Mn(NO₃)₂/PAN, AgNO₃/PAN, and AgNO₃-Mn(NO₃)₂/PAN) and calcined samples (CNF, AgO_x/CNF, MnO_x/CNF, and AgO_x-MnO_x/CNF) were determined using FTIR analysis. The spectra of all the as-spun fibers are shown in Figure 4.32(a). The transmittance broad peaks ~ 3410 cm⁻¹ indicated the O–H stretching vibration of absorbed water. The typical spectrum of PAN nanofibers was specified to peaks of 2938, 1450, 2243, and 1625 cm⁻¹ for the –CH₂ asymmetric stretching mode, –CH₂ bending mode, C≡N stretching vibration, and C=O vibration. (Dhakate *et al.*, 2011; Yang *et al.*, 2014). For the calcined samples (Figure 4.32(b)), even though the most significant surface functional groups of PAN were absent by heat treatment, they revealed two obvious broad peaks which appeared at ~ 1600-1580 and 1300-1100 cm⁻¹ which can be ascribed to C=C and C=N stretching (Zeng *et al.*, 2015). It is possible that these two stretchings play an important role in the improvement of the electrocatalytic properties of composite CNF (Li *et al.*, 2014).

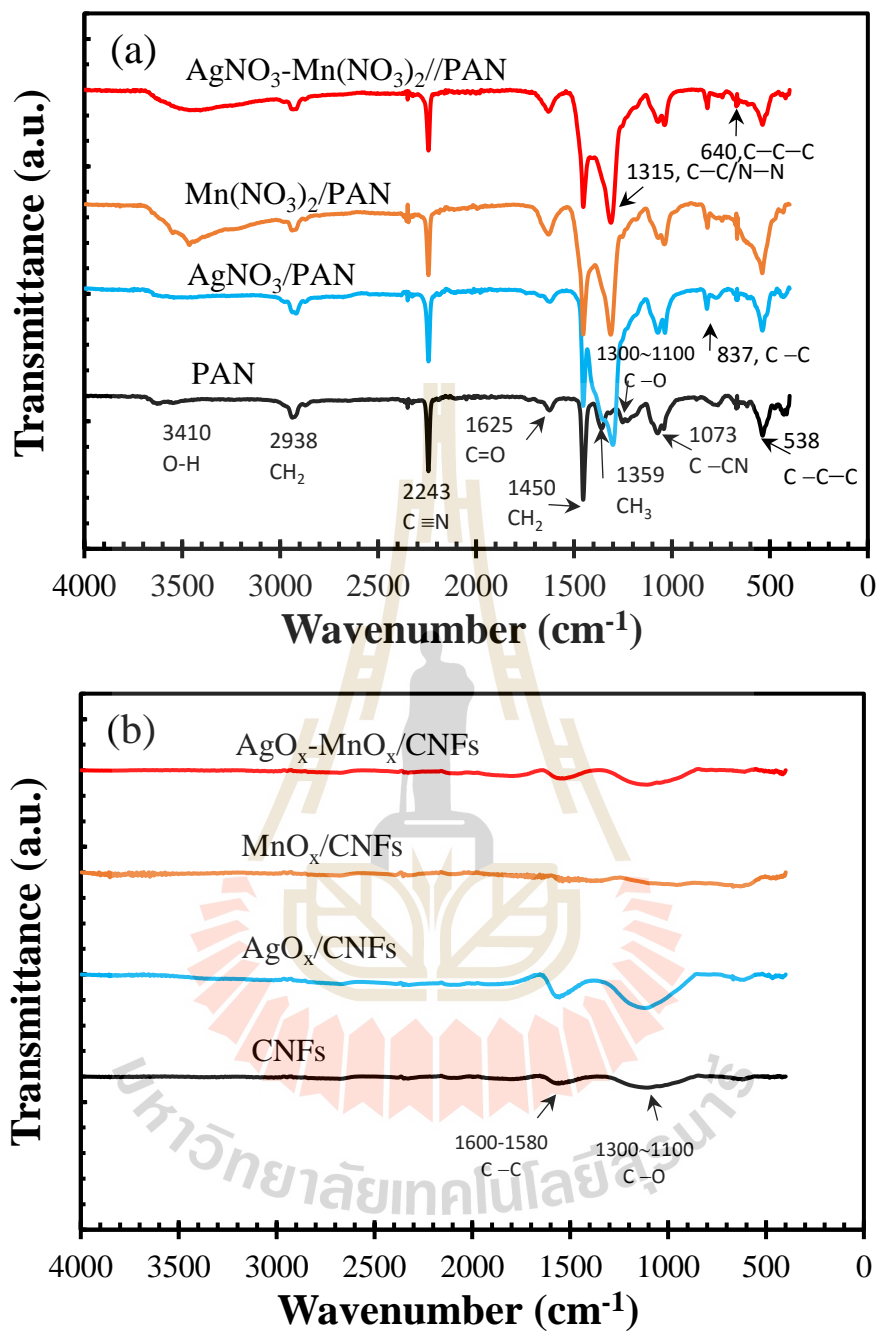


Figure 4.32 (a) FTIR spectra of as-spun PAN, Mn(NO₃)₂/PAN, AgNO₃/PAN, and AgNO₃-Mn(NO₃)₂/PAN and (b) CNF, AgO_x/CNF, MnO_x/CNF, and AgO_x-MnO_x/CNF.

A carbon feature of as-prepared samples was further investigated by Raman analysis, which was observed between 100 and 4000 cm^{-1} . The band positions were analyzed using a Lorentzian curve fitting (Yan *et al.*, 2014). As shown in Figure 4.33, two strong peaks at $\sim 1341\text{-}1350 \text{ cm}^{-1}$ (D-Breathing Band) and $1574\text{-}1591 \text{ cm}^{-1}$ (G-Breathing Band) were observed for all products that related to the scattering on disordered amorphous carbon clusters (sp^3 bonded carbon atoms) and the stretching of C-C bonds in the hexagonal ring of graphite structures (sp^2 bonded carbon atom) (Lisunova *et al.*, 2010). The fitting yields the highest I_D/I_G of 1.42 for $\text{AgO}_x\text{-MnO}_x/\text{CNF}$ mostly indicated amorphous structures, whereas the spectrum MnO_x/CNF revealed the separated D and G peaks with the smallest I_D/I_G of 0.98 indicating high graphitic carbon forming in the fibers. The secondary region of G' and G+D peaks were hardly seen for the pristine CNF and MnO_x/CNF at $\sim 2600\text{-}2800 \text{ cm}^{-1}$ corresponding to the phonon oscillation that revealed the infinite crystal of graphite structure in the sample (Colindres *et al.*, 2014). The in plane crystalline sizes of graphite of the all samples were observed around 0.20.32 nm. The all relevant parameters of the peaks fitted to the Raman spectra are summarized in Table 4.8.

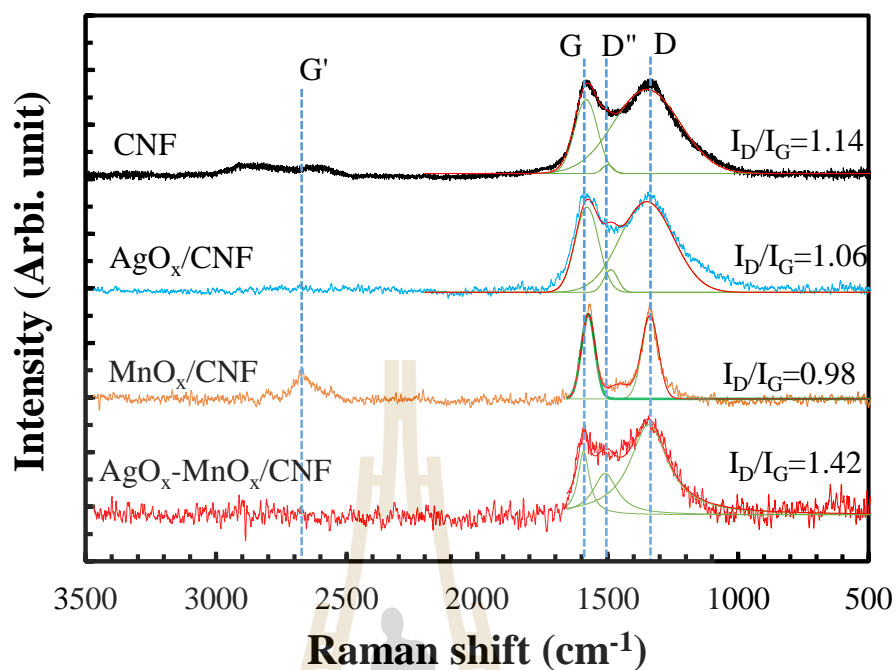


Figure 4.33 Raman shift of CNF, AgO_x/CNF, MnO_x/CNF, and AgO_x-MnO_x/CNF.

Table 4.8 Relevant parameters of the peaks fitted to the Raman spectra of the various CNF, AgO_x/CNF, MnO_x/CNF, and AgO_x-MnO_x/CNF.

Sample	Peak position (cm ⁻¹)					I _D /I _G	I _D /I _G (nm)
	D	D''	G	G''	G+D		
CNF	1350	1499	1582	2615	2849	1.14	0.25
AgO _x /CNF	1349	1487	1578	-	-	1.06	0.24
MnO _x /CNF	1337	1454	1574	2661	-	0.98	0.22
AgO _x -MnO _x /CNF	1342	1509	1591	-	-	1.42	0.32

The XRD spectra of prepared samples in Figure 4.35 were measured with Cu K α wavelength of 1.54 Å between 2 θ from 10 to 80°, step time 0.2 and step size 0.02.

The MnO_x/CNF pattern presents rather strong and sharp peaks of hexagonal graphite at 26.6 and 44.6° corresponding to the plane (002) and (101), whereas the other composite CNF still display the diffraction broad peaks of amorphous carbon structure at $\sim 23 - 28$ and $42 - 47^\circ$ and these are consistent with the preceding high resolution TEM and Raman results. However, these carbon peaks in the AgO_x/CNF and $\text{AgO}_x\text{-MnO}_x/\text{CNF}$ were somewhat overshadowed by the high intensity peaks of plane (111), (200), (220), and (311) of cubic Ag (PDF:01-087-0780) located at 38.3 , 44.5 , 64.7 , and 77.4° , respectively (Aussawasathien and Sancaktar, 2008). In the case of Mn-doping, the various phases of oxide were formed during heat treatment (Robinson *et al.*, 2013). The MnO_x/CNF pattern present rather the planes (111), (200), (220), and (311) of cubic MnO (PDF:01-075-0257) structure having peaks at 35.2 , 40.9 , 59.2 , and 70.8° , respectively (Wang *et al.*, 2015), whereas the $\text{AgO}_x\text{-MnO}_x/\text{CNF}$ pattern mainly adopts spinel Mn_3O_4 structure (PDF:00-024-0734) (Lee *et al.*, 2014).

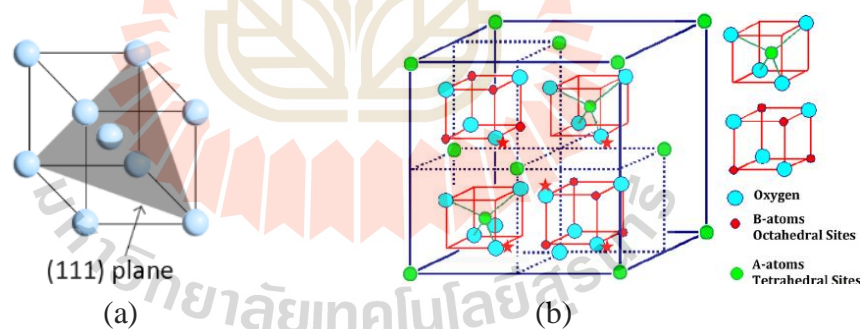


Figure 4.34 A schematic picture of the (a) cubic and (b) spinel structure; star means the intermediary cation sites that denote considerable cation disorder (Ghasemi and Mousavinia, 2014).

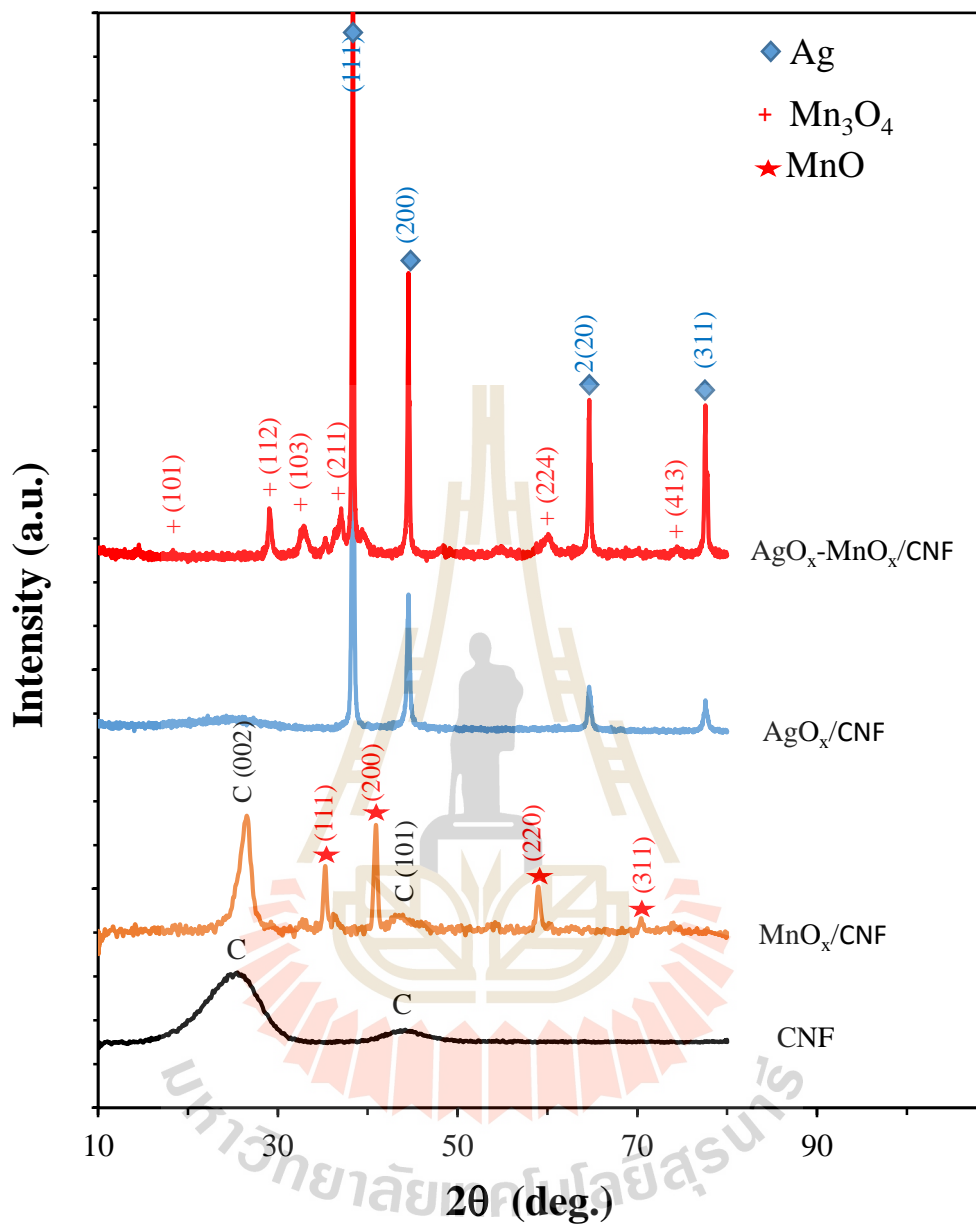


Figure 4.35 XRD patterns of CNF, AgO_x/CNF, MnO_x/CNF, and AgO_x-MnO_x/CNF.

The series of Ag L_3 -edge and Mn K -edge XANES were further measured to examine the various chemical states of each element in the samples. The energy edges were evaluated using Athena software, the Ag and Mn chemical mapping nanofibers were analyzed employing linear combination fitting method. The reference oxidation states Ag metal, Ag¹⁺, Ag²⁺, Mn metal, Mn²⁺, Mn^{2.67+}, Mn³⁺, and Mn⁴⁺ were measured from commercial samples of Ag, Ag₂O, AgO, Mn, MnO, Mn₃O₄, Mn₂O₃, and MnO₂, respectively. Figure 4.36(a) shows the Ag L_3 spectra of both AgO_x-MnO_x/CNF and AgO_x/CNF exhibited nearly to be Ag metal spectrum and energy edges appeared at 3.349 keV and 3.350 keV, respectively. In the case of Mn element (Figure 4.37(a)), the spectrum of MnO_x/CNF exhibits the features and energy edges (6.545 eV) similar to standard MnO, whereas the AgO_x-MnO_x/CNF spectrum with an energy edge of 6.548 eV presents rather the Mn₃O₄ component, and these are consistent with the preceding XRD analysis. The fitting results show the factor R that was found to be below 0.05 for both Ag and Mn elements for all samples. Figure 4.36(b) illustrates most Ag metals mapping including AgO_x-MnO_x/CNF and AgO_x/CNF valued ~81% of whole Ag clusters in the samples. In a different manner (Figure 4.37 (b)), the MnO_x/CNF showed various phases of Mn metal (8.7%), Mn²⁺ (72.1%), and Mn^{2.67+} (19.2%), whereas AgO_x-MnO_x/CNF appeared in various states of Mn²⁺ (22.3%), Mn^{2.67+} (50.9%), and Mn⁴⁺ (26.8%) existed in each sample. It is noteworthy that the embedding of silver nanoparticles possibly affect a high degree Mn₃O₄ forming in fibers and possibly enhances the pseudocapacitance resulting in a good supercapacitor performance of the sample (Bauer *et al.*, 2015; Behrens *et al.*, 1999). The element chemical mapping in composite nanofibers are summarized in Table 4.9.

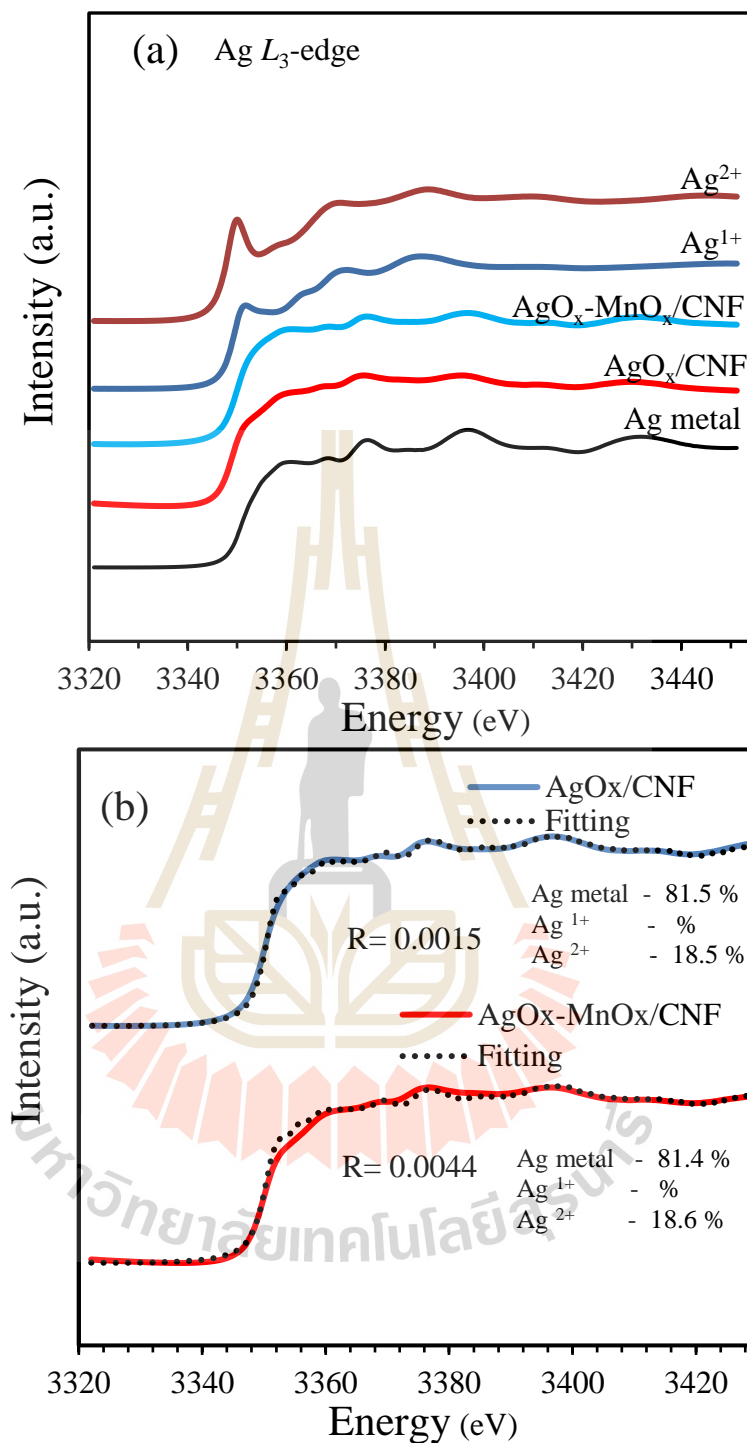


Figure 4.36 (a) Ag L_3 -edge XANES of the as-prepared samples and various oxide compounds. (b) Ag chemical mapping of the nanofibers using Linear combination fitting.

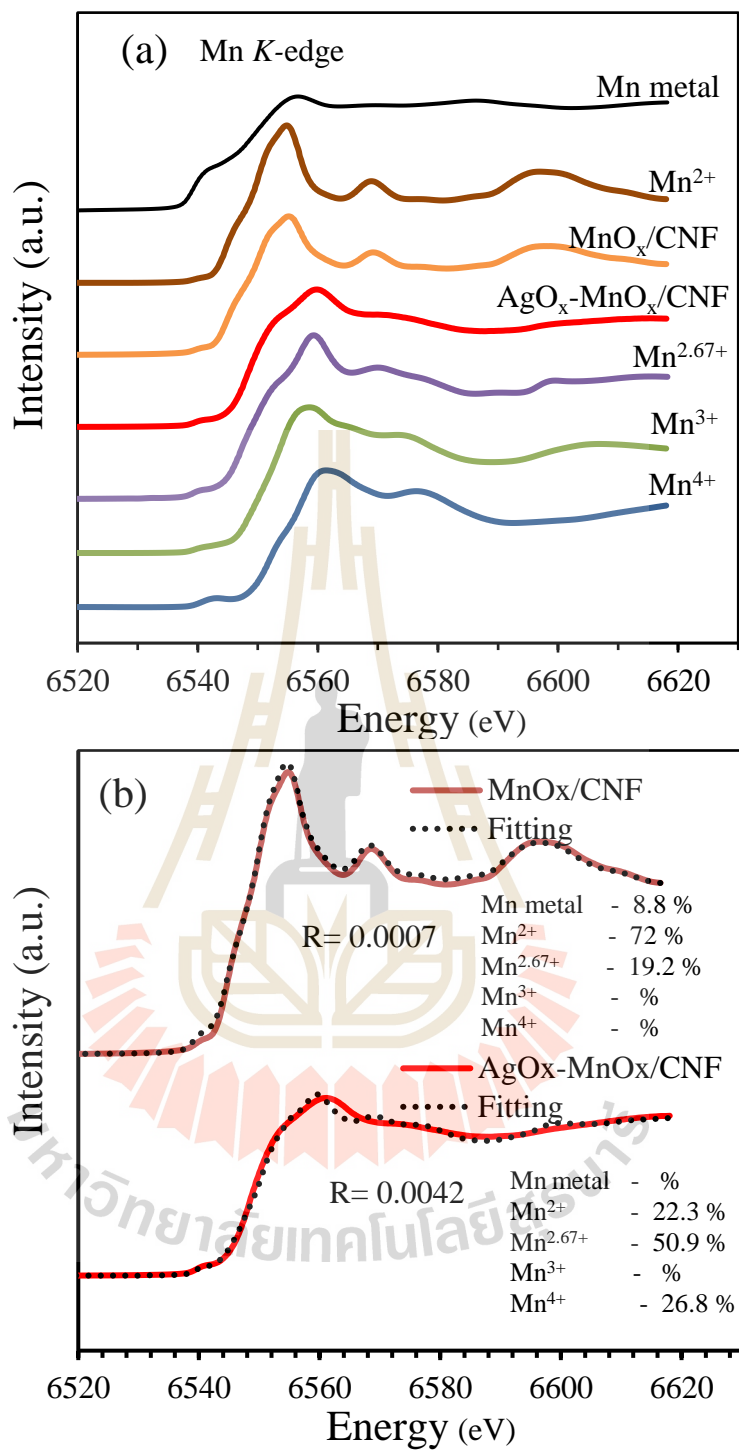


Figure 4.37 (a) Mn K-edge XANES of the as-prepared samples and various oxide compounds. (b) Mn chemical mapping of the nanofibers using Linear combination fitting.

Table 4.9 Element chemical states mapping in AgO_x/CNF, MnO_x/CNF, and AgO_x-MnO_x/CNF obtaining from linear combination fitting.

Sample	Ag L ₃ -edge		Mn K-edge			
	Ag metal	Ag ²⁺	Mn metal	Mn ²⁺	Mn ^{2.67+}	Mn ⁴⁺
	(%)	(%)	(%)	(%)	(%)	(%)
AgO _x /CNF	81.5	18.5	-	-	-	-
MnO _x /CNF	-	-	8.8	72.0	19.2	-
AgO _x -MnO _x /CNF	81.4	18.6	-	22.3	50.9	26.8



4.3.3 Electrochemical properties of pure CNF, AgO_x/CNF, MnO_x/CNF, and AgO_x-MnO_x/CNF electrodes

4.3.3.1 Cyclic voltammetry of pure CNF, AgO_x/CNF, MnO_x/CNF, and AgO_x-MnO_x/CNF electrodes

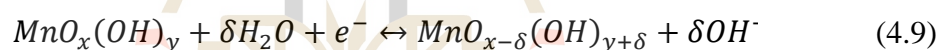
The CV profiles of all samples in Figure 4.38 were measured in scan rate range of 2-500 mV s⁻¹ in order to cover the whole capacitive mechanisms ranges: EDLC at high scan rate value more than 100 mV s⁻¹, surface pseudocapacitance at mid scan rate between 5-100 mV s⁻¹, and also bulk pseudocapacitance at very low scan rate lower than 5 mV s⁻¹. The measure current (*i*) at the fixed potential voltage window of 1.0 V of all the electrodes are increased with increasing of scan rate (*v*) obeyed the equation (4.8) (Wang *et al.*, 2016).

$$i = av^b \quad (4.8)$$

Where *a* and *b* is the constant.

At high scan rate, the CV curves of CNF and AgO_x/CNF electrodes behave nearly as a rectangular curve of an ideal capacitor without significant redox peak, indicating that the double layer capacitive processes mainly stored the charges of the electrodes. The CV profiles of MnO_x/CNF and AgO_x-MnO_x/CNF electrodes present a pair of cathodic and anodic peaks corresponding to the oxidation and reduction processes of various MnO_x clusters in the samples (Yano *et al.*, 2013), which indicate the contribution of the double layer and pseudocapacitance. It worth noting that there was no any current peak observed for the samples without Mn. Especially, the CV curves at 20 and 2 mV s⁻¹ represent the pseudocapacitive behavior of the electrodes. In the case of the small scan rate of 2 mV s⁻¹ (Figure 4.39(b) and (c)), even

though MnO_x/CNF and $\text{AgO}_x\text{-MnO}_x/\text{CNF}$ electrodes obviously exhibit a couple of cathodic and anodic peaks, the bare CNF and AgO_x/CNF electrodes still present only a background loop of double layer capacitance. It is noted that only the CNF electrode starts to display resistive behavior at the operating potential above -0.1 V, which is the cathodic current from the decomposition of the aqueous electrolyte (Chen *et al.*, 2013). This phenomenon indicates an overpotential region that implies the limitation of the bare CNF. In particular, the existence of many structures including MnO, Mn_3O_4 , and MnO_2 in $\text{AgO}_x\text{-MnO}_x/\text{CNF}$ and MnO_x/CNF provide more chemical reactions as seen from each more than one cathodic and anodic peaks. As seen in Figure 4.39(c) and (d), the redox mechanism is possibly considered to be a transformation of $\text{Mn}^{2+} \leftrightarrow \text{Mn}^{3+}$ and $\text{Mn}^{3+} \leftrightarrow \text{Mn}^{4+}$, which is proposed by reversible redox reaction as follows (Yano *et al.*, 2013; Brock *et al.*, 1998; Zhou *et al.*, 2011):



where $\text{MnO}_x(\text{OH})_y$ and $\text{MnO}_{x-\delta}(\text{OH})_{y+\delta}$ denote interfacial manganese oxide under oxidation and reduction states, respectively. The Mn ions transformations are also more described in term of oxygen intercalated into MnO_x structures, initially oxygen vacancies are filled through intercalation of an electrolyte oxygen ion and diffusion of O^{2-} along octahedral edges through the crystal concomitant with the oxidation of two Mn^{2+} center to two Mn^{3+} corresponding to the anodic current peak at around -0.48 V of cyclic voltammogram of $\text{AgO}_x\text{-MnO}_x/\text{CNF}$ and MnO_x/CNF . In the next step of reaction, excess oxygen is intercalated at the surface through diffusion of manganese to the surface and oxidation of Mn^{3+} centers to two Mn^{4+} corresponding to anodic peak at around -0.3 V. The cathodic peaks present in backward scan are the reduction of each step. Moreover, the intercalation of oxygen ions into vacancy sites is

accompanied by proton transfer to electrolyte hydroxide ions yielding water as a product (Mefford *et al.*, 2014). However, there is no significant redox peak related to AgO_x that was observed in this experiment. The specific capacitances as the scan rate range 2-500 mV s^{-1} are displayed in Figure 4.39(e). Except for the MnO_x/CNF electrode, the specific capacitance of the other samples increased with the scan rate from 2 to 20 mV s^{-1} , then reached a maximum value between 20-50 mV s^{-1} and the decreases of capacitance were found above 100 mV s^{-1} indicating the diffusion of electrolyte ions was limited due to the time constraint and only the outer surface provided charge accumulation (Park *et al.*, 2012; Lang *et al.*, 2011). In this work, we postulate the model of capacitive mechanisms for each scan rate region as demonstrated in Figure 4.41. At low scan rate below 5 mV s^{-1} (Figure 4.41(a)), the outer ions located outside the pore then moved slowly into the pore by an influent of applied voltage. The Helmholtz double layer also formed simultaneously faster than the large numbers of outer ions through the pore channel and then the pore was closed. Thus, the double layer growth and blocked the ions before they fully accessed in the micropores which was not observed on mesopore structure of MnO_x/CNF . However, this processes occurring slow enough for the bulk pseudocapacitance from electrosorption (Lang *et al.*, 2011). At mid scan rate of 5-100 mV s^{-1} (Figure 4.1(b)), even the bulk storage does not support the total capacitance in this region, the EDLC contributed more total capacitance because the charges move faster and more accumulated inside the pores. The large number of micropores volume around $0.36 \text{ cm}^3 \text{ g}^{-1}$ with the average size of around 0.7 nm of $\text{AgO}_x\text{-MnO}_x/\text{CNF}$ resulted in the highest value of $\sim 155 \text{ F g}^{-1}$ at a scan rate of 20 mV s^{-1} is in agreement with Wang's report as exhibited in Figure 4.40 (Wang *et al.*, 2016). The specific capacitance of the

MnO_x/CNF electrode decreases with an increase of all scan rate ranges at the fixed potential window of 1.0 V due to pseudocapacitance as a result of redox processes associated with the surface adsorption of cations or incorporation of cation into the oxide structure in the electrode (Li *et al.*, 2008). At high scan rate above 100 mV s⁻¹ (Figure 4.41(c)), the process was very fast then limited the diffusion and migration of electrolyte ions within electrodes, resulting in a low electrochemical utilization of active materials (Lai and Lo, 2015).



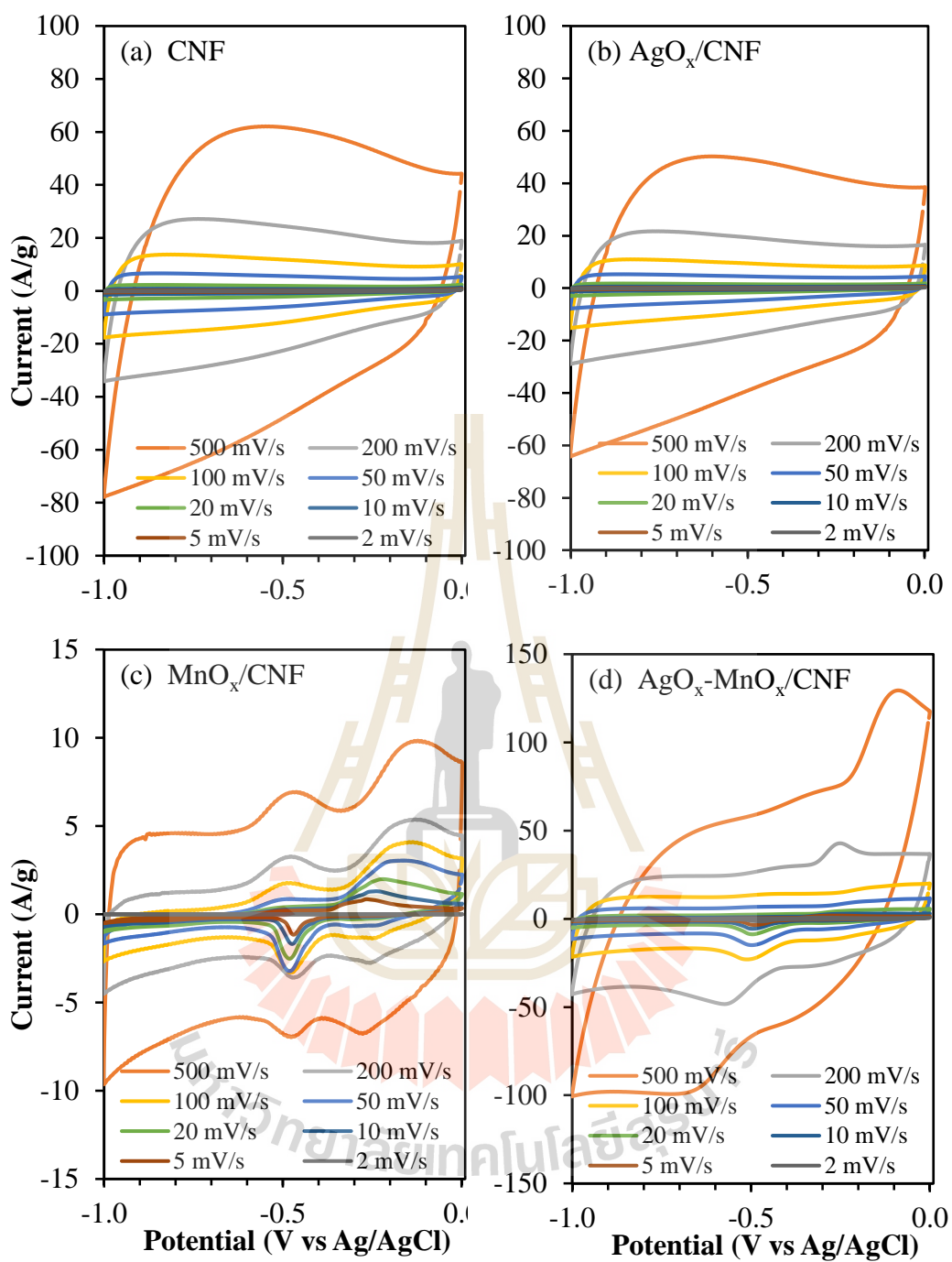


Figure 4.38 Cyclic voltammograms of (a) CNF, (b) AgO_x/CNF, (c) MnO_x/CNF, and (d) AgO_x-MnO_x/CNF as the function of scan rate.

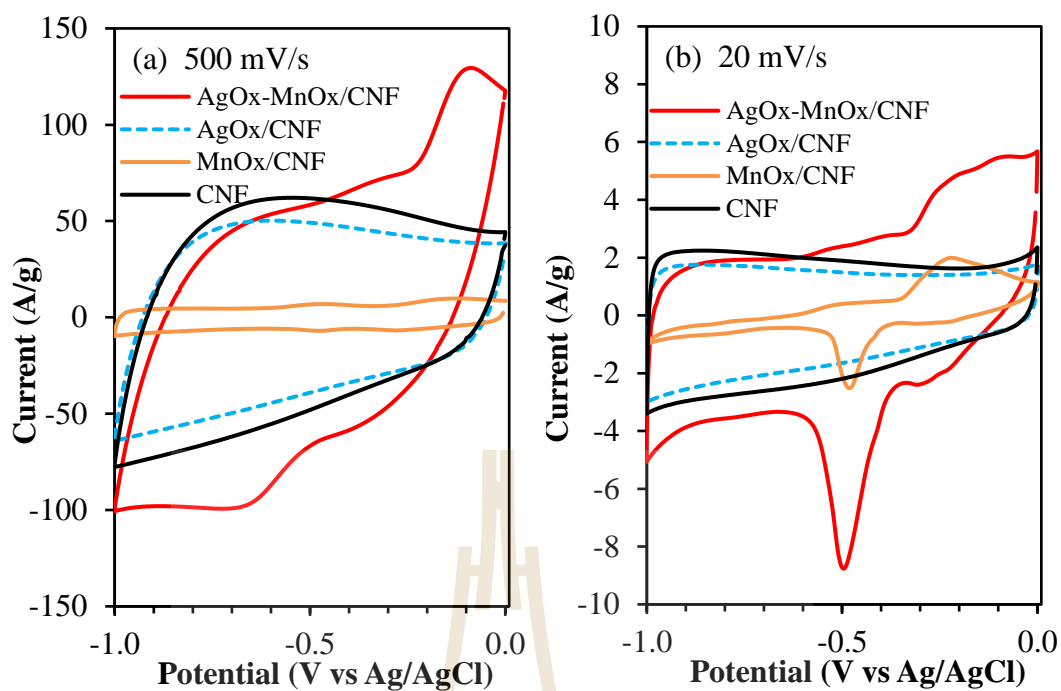


Figure 4.39 Cyclic voltammograms of CNF, AgO_x/CNF, MnO_x/CNF, and AgO_x-MnO_x/CNF at (a) 500, (b) 20, and (d) 2 mV s⁻¹. (d) Mechanism of oxygen intercalation into MnO_x structures (Zhong *et al.*, 2016; Mefford *et al.*, 2014). (e) The specific capacitance as the function of scan rate.

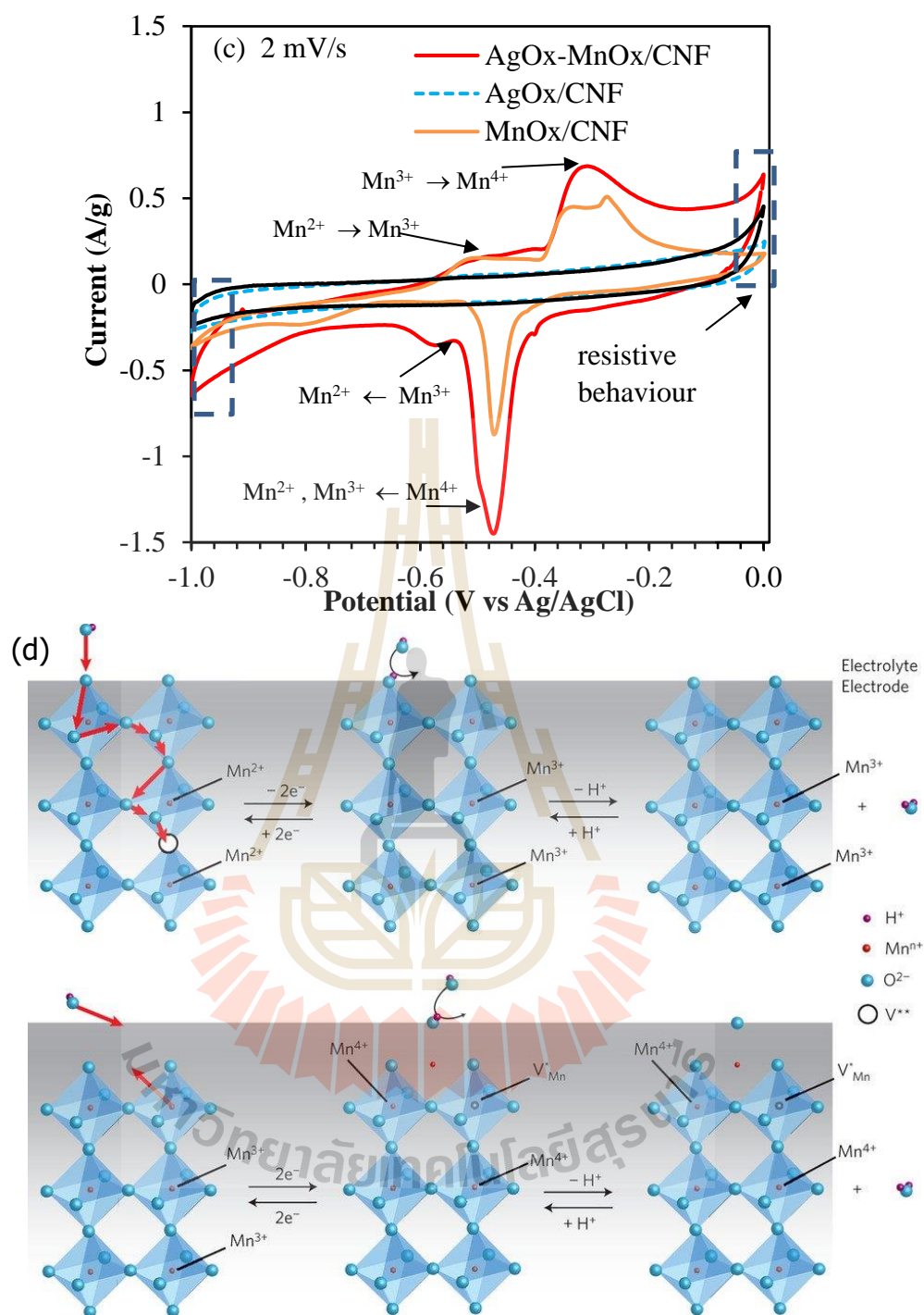


Figure 4.39 Cyclic voltammograms of CNF, AgO_x/CNF, MnO_x/CNF, and AgO_x-MnO_x/CNF at (a) 500, (b) 20, and (d) 2 mV s⁻¹. (d) Mechanism of oxygen intercalation into MnO_x structures (Zhong *et al.*, 2016; Mefford *et al.*, 2014). (e) The specific capacitance as the function of scan rate. (continued)

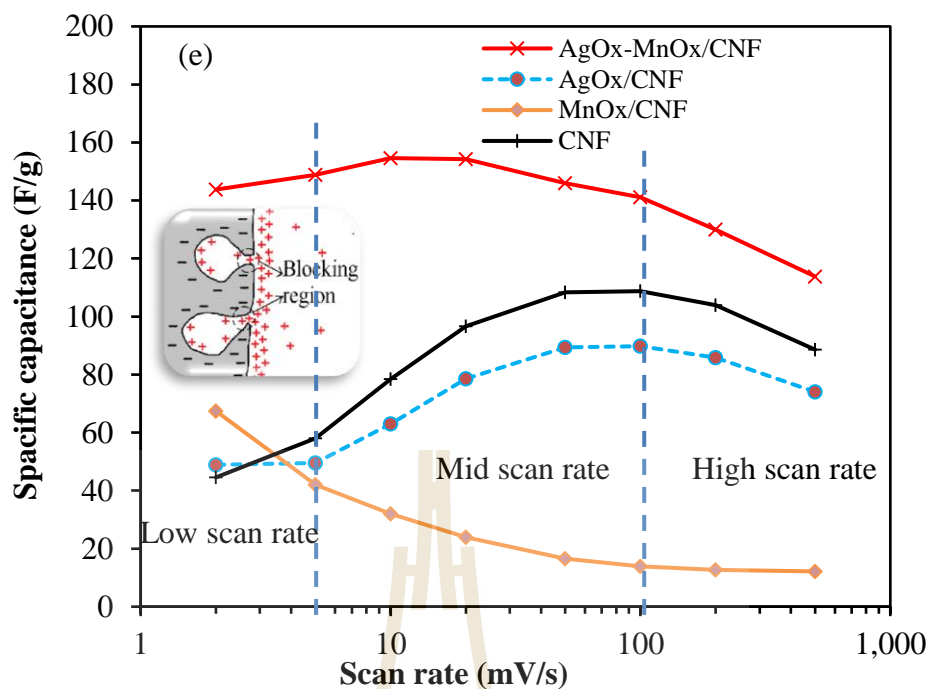


Figure 4.39 Cyclic voltammograms of CNF, AgO_x/CNF, MnO_x/CNF, and AgO_x-MnO_x/CNF at (a) 500, (b) 20, and (d) 2 mV s⁻¹. (d) Mechanism of oxygen intercalation into MnO_x structures (Zhong *et al.*, 2016; Mefford *et al.*, 2014). (e) The specific capacitance as the function of scan rate. (continued)

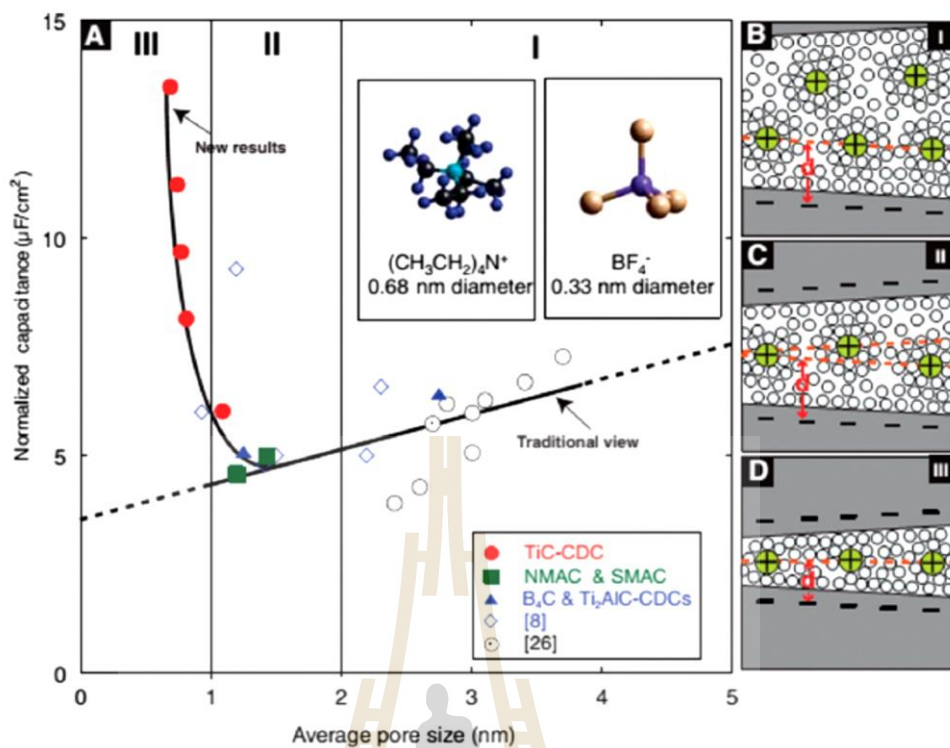


Figure 4.40 (A) Specific capacitance normalized by BET surface area and average pore size for carbon. Drawing of solvated ions residing in pores structure (B) greater than 2 nm, (C) between 1 and 2 nm, and (D) less than 1 nm (Wang *et al.*, 2016).

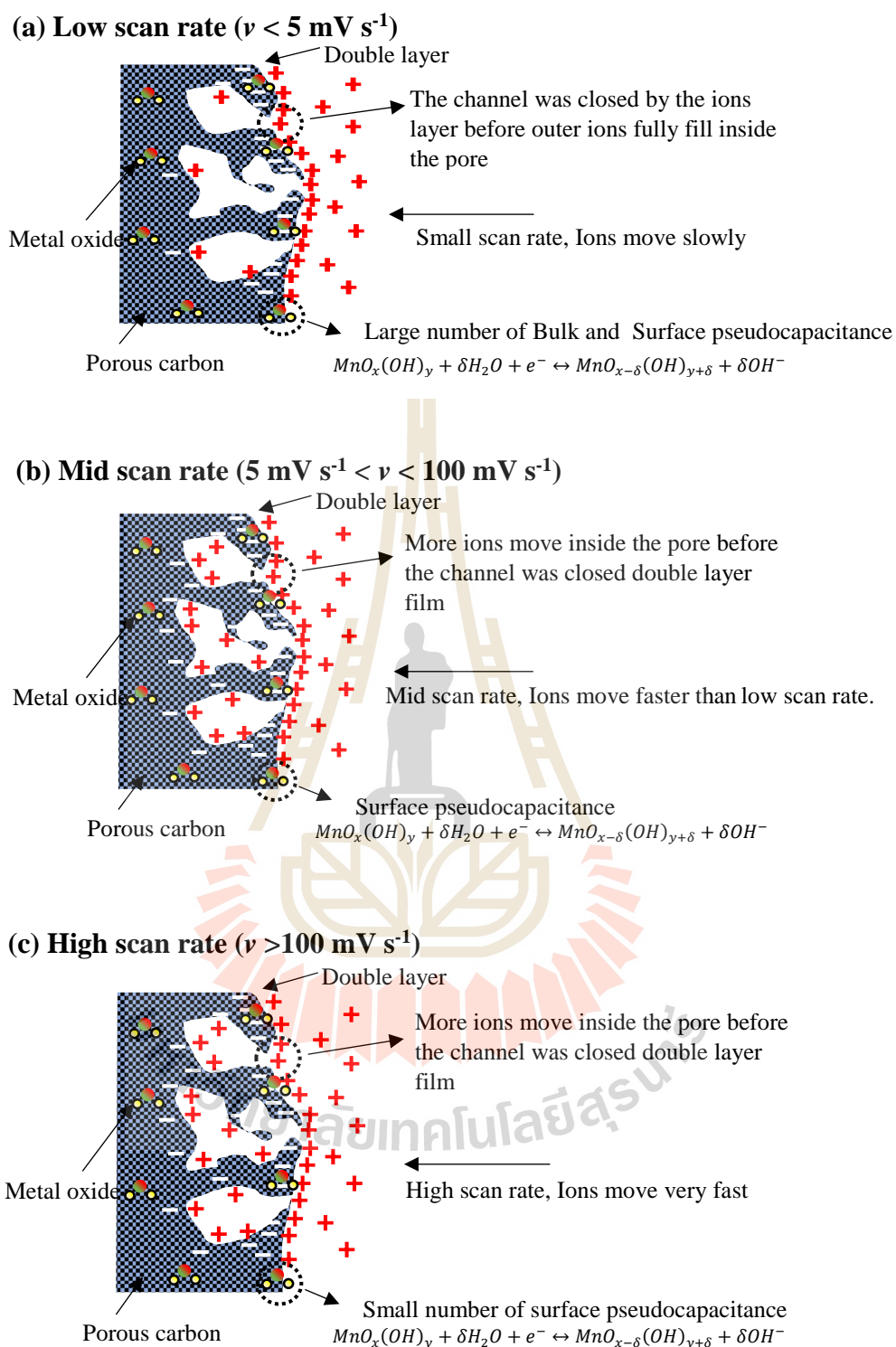


Figure 4.41 A schematic represents the capacitive mechanism of the composite carbon nanofibers of this work in three scan rate regions of (a) low ($v < 10 \text{ mV s}^{-1}$), (b) mid ($10 \text{ mVs}^{-1} < v < 100 \text{ mV s}^{-1}$), and (c) high ($v > 100 \text{ mV s}^{-1}$) scan rate.

4.3.3.2 Galvanostatic charge/discharge testing of pure CNF, AgO_x/CNF, MnO_x/CNF, and AgO_x-MnO_x/CNF electrodes

Figure 4.42 represents linear voltage-time profiles of all electrodes measured at the current density of 0.5, 1, 2, 5, and 10 A g⁻¹. Among all the samples, the AgO_x-MnO_x/CNF electrode displays the longest duration time of ions charging/discharging at each current density. Whereas the adverse property is still observed for the pristine CNF electrode, which tends to reach the full charging state above -0.1 V which is earlier than the other electrodes. In Figure 4.42(c), the non-uniform curve was observed for MnO_x/CNF, a voltage-mound around 0.4 V of charging and 0.5 V of discharging attributed the large numbers of faradaic charge from chemical redox reaction between MnO_x and KOH electrolyte. Figure 4.43(b) shows that the specific capacitances decrease with an increasing of current density and then remains approximately constant above 2 A g⁻¹. The specific capacitance of AgO_x-MnO_x/CNF electrode yields a value of ~204 F g⁻¹ at current density of 0.5 A g⁻¹ and keeps a high value of 145 F g⁻¹ at a current density of 10 A g⁻¹ that appears to be much higher than the other electrodes (Lang *et al.*, 2011).

A comparison of power and energy density of all electrodes is represented by the well-known Ragone plot as shown in Figure 4.45(a). The AgO_x-MnO_x/CNF electrode still outstrips the efficiency of the other electrodes, because it stores maximum energy of ~28 mWh g⁻¹ at a high-power density of ~250 mW g⁻¹ demonstrating faster charging/discharging. Moreover, Figure 4.45(b) exhibits the greatest cycling stability of AgO_x-MnO_x/CNF electrode observed at ~99% remaining after 1000 cycles.

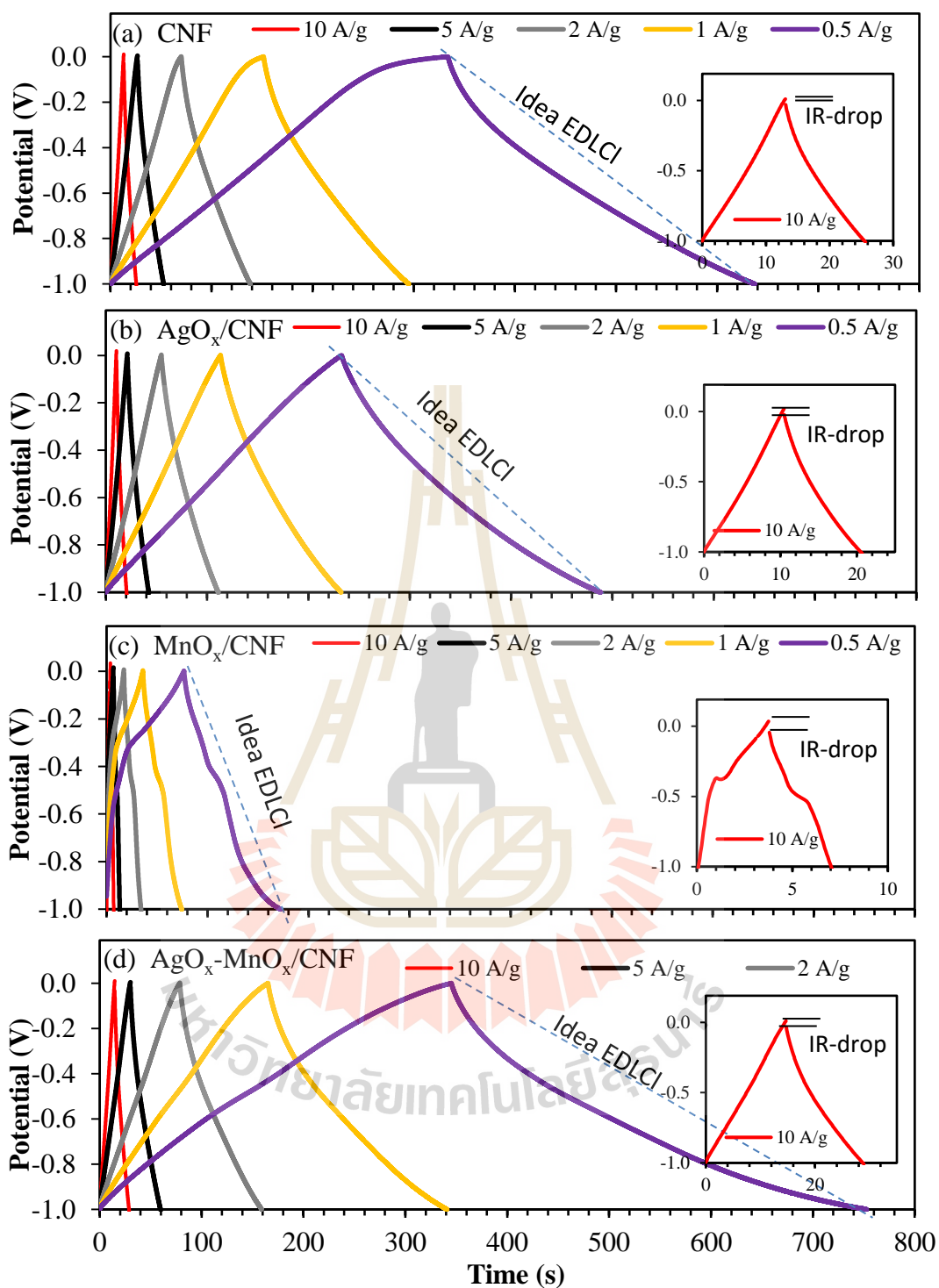


Figure 4.42 The linear voltage-time profiles of GCD measurement of (a) CNF, (b) AgO_x/CNF, (c) MnO_x/CNF, and (d) AgO_x-MnO_x/CNF as the function of current density.

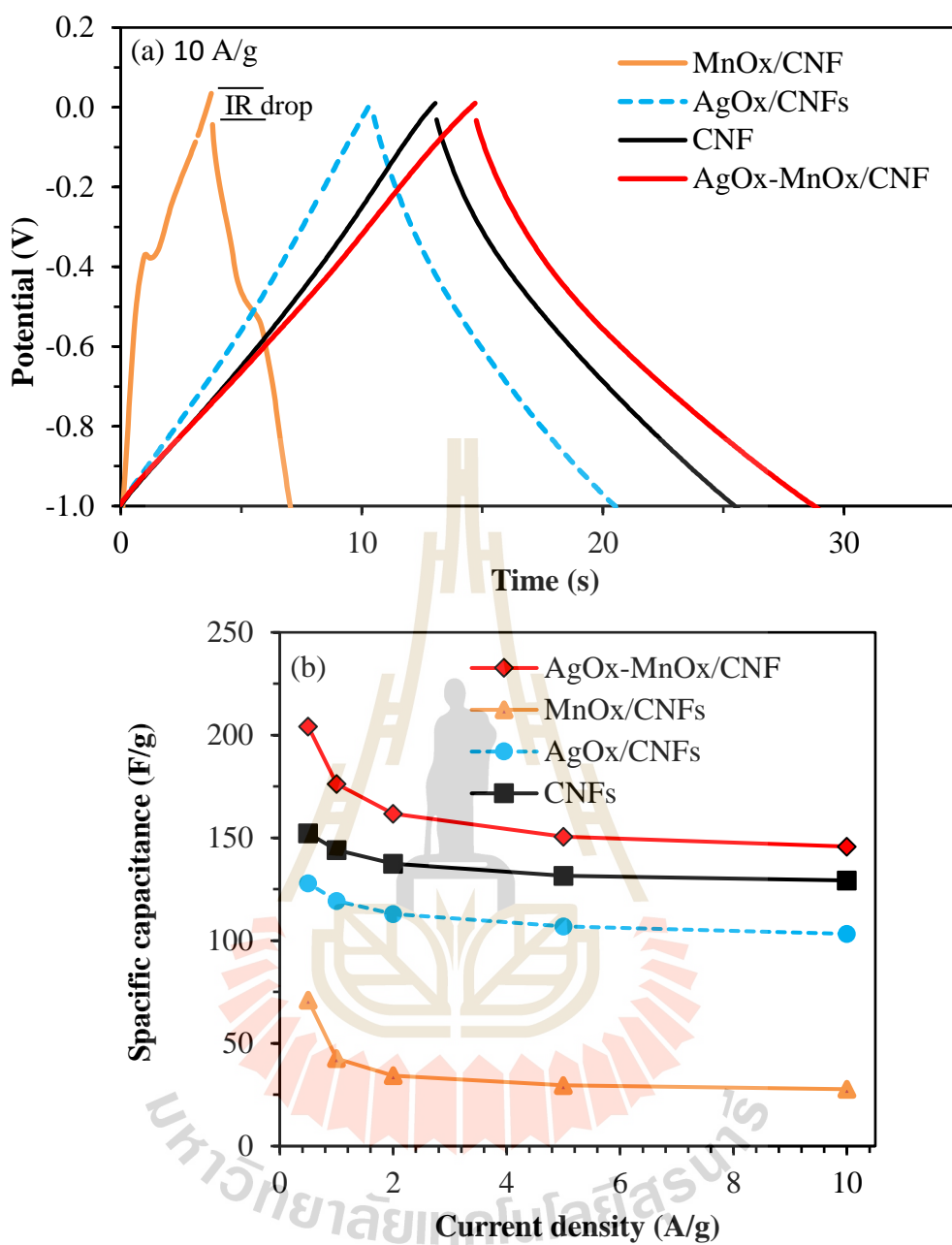


Figure 4.43 (a) The comparison of linear voltage-time profiles of CNF, AgO_x/CNF, MnO_x/CNF, and AgO_x-MnO_x/CNF at a current density of 10 A g⁻¹. (b) The specific capacitance as the function of current density.

Figure 4.44 shows the changing of charge/discharged voltage curves upon cycling at the difference cycles of 2nd, 10th, 100th, 500th, and 1000th cycle, most

sample likewise presented a slight decrease of duration charged/discharged timing. Except for MnO_x/CNF electrode, it displayed a gradually sloping charge profile of the high-voltage plateau associated with reversible redox reaction of MnO_x (Lin *et al.*, 2014) is consistent with the CV results. However, the imperfect reversible redox reaction of MnO_x nanoparticle and electrolyte causing in significant degradation of the total normalized capacitance in 1st-100th cycle. Above 100th cycles of testing the normalized capacitance became be constant that attributed only the EDLC (Pang *et al.*, 2000; Wei *et al.*, 2011). As a result of TGA-DSC, the average carbon matrix content around 80 % in the composite nanofibers resulted in the high capacity retention more than 95 % after 1000 cycles observed for CNF, AgO_x/CNF, and AgO_x-MnO_x/CNF electrodes. Except for MnO_x/CNF, carbon itself poorly stores the charge due to low surface area as mention above thus the total capacitance mainly from redox reaction of MnO_x then rapidly dropped when arising more charge/discharge cycle. The comparison of electrochemical performance of the prepared electrodes and the other reports are shown in (4.9).

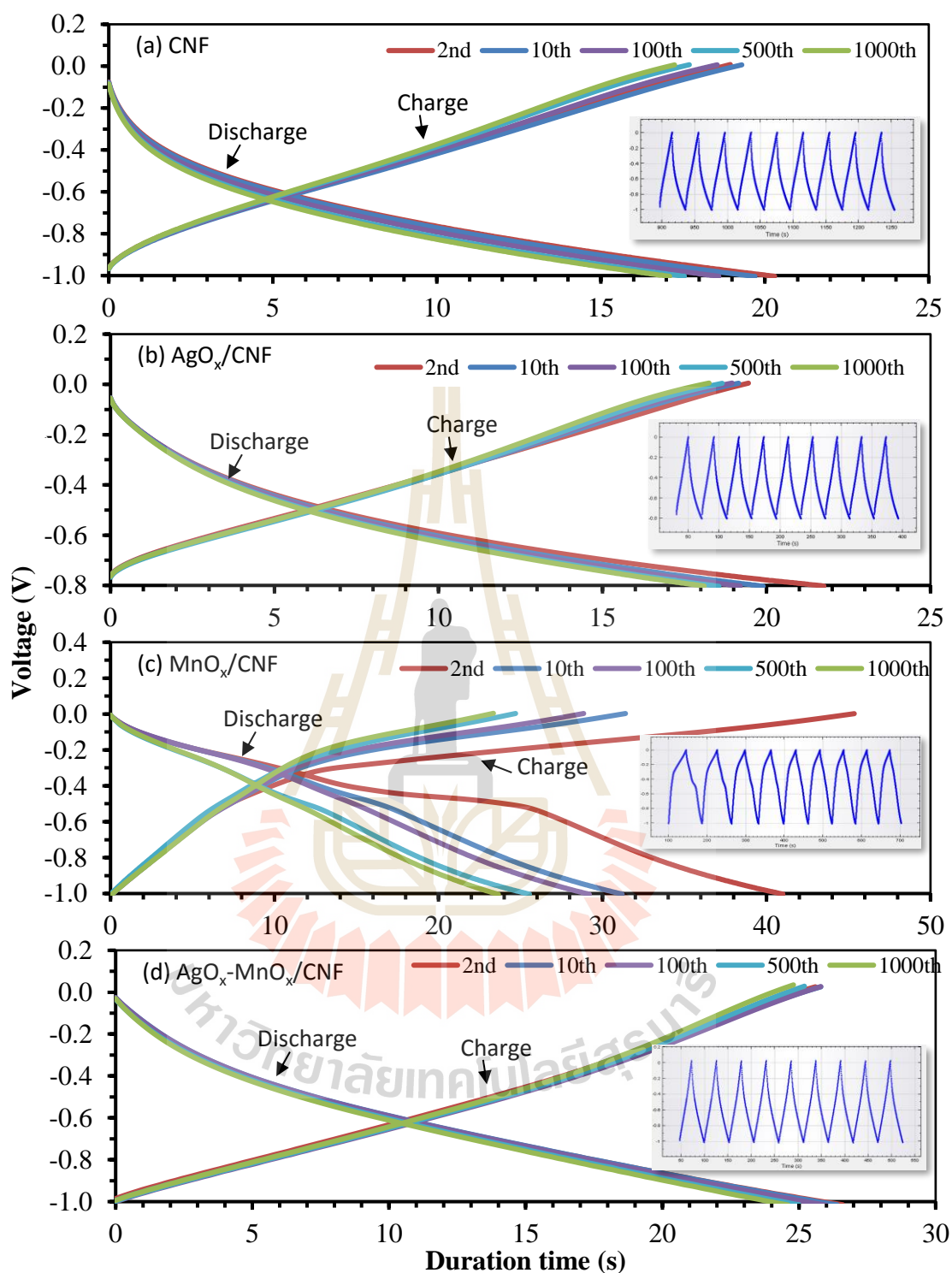


Figure 4.44 Charge/discharge profile at -1-0 V at various cycles of 2nd, 10th, 100th, 500th, and 1000th of (a) CNF, (b) AgO_x/CNF, (c) MnO_x/CNF, and (d) AgO_x-MnO_x/CNF electrode, insets presented typical continued cycling.

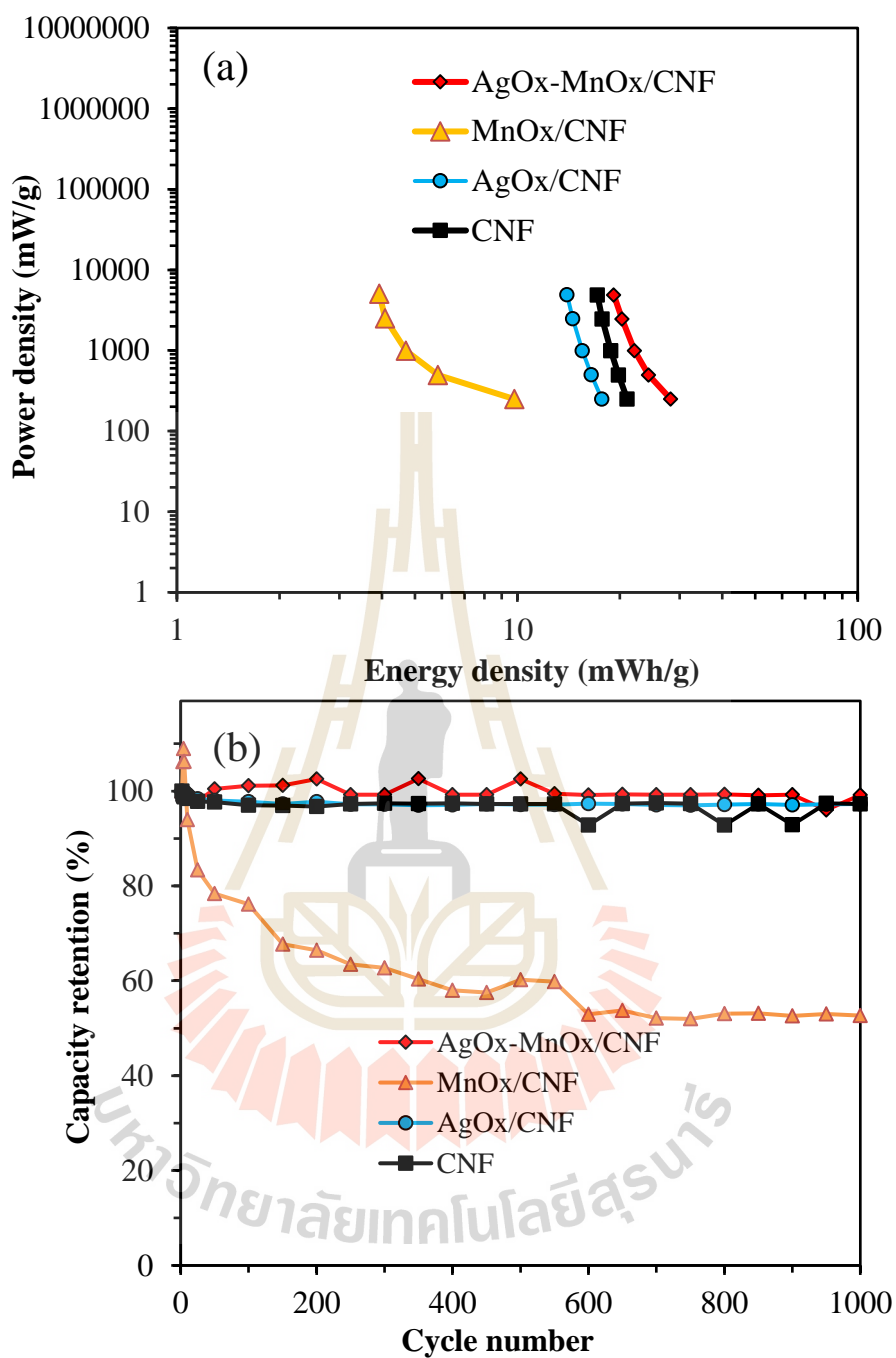


Figure 4.45 (a) A Ragone plot for CNF, AgO_x/CNF, MnO_x/CNF, and AgO_x-MnO_x/CNF varying the discharge current density of 0.5, 1, 2, 5, and 10 A g⁻¹. (b) Cycling stability at a current density of 5 A g⁻¹ for up to 1000 cycles.

Table 4.10 Comparison of specific capacitance and cycle life of composite CNF-based related to MnO_x . All values are measured using the three-electrode system (Wang *et al.*, 2015).

Samples	Specific capacitance (F g^{-1})	Cycle life
$\text{MnO}_2/\text{CNTs-CNF}$	374, 2 mV s^{-1}	94 %, 1000 cycles 4 A g^{-1}
$\text{MnO}_2/\text{CNTs-Textile}$	410, 0.05 mV s^{-1}	80 %, 200 cycles
Coaxial CNFs/ MnO_2	557, 1 A g^{-1}	94 %, 1500 cycles 100 mV s^{-1}
MnO_2/CNFs	365, 1 A g^{-1}	95.3 %, 1000 cycles 1 A g^{-1}
$\text{AgO}_x\text{-MnO}_x/\text{CNF}$	204, 0.5 A g^{-1}	99 %, 1000 cycles
(This work)		5 A g^{-1}

4.3.3.3 Electrochemical impedance spectroscopy of pure CNF, AgO_x/CNF , MnO_x/CNF , and $\text{AgO}_x\text{-MnO}_x/\text{CNF}$ electrodes

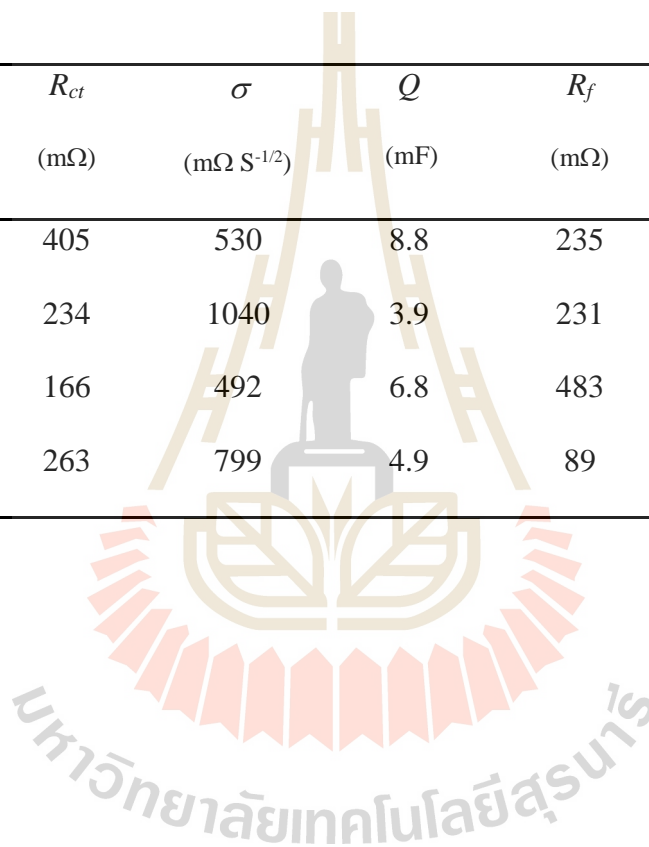
Nyquist plots of EIS measurement in Figure 4.46(a) provide further evidence of the restriction of the bare CNF and composite samples. All spectra expressed as a pattern of SC. The interception on the real axis at high-frequency corresponds to the total effective series resistance (ESR) including bulk electrolyte and electrode resistance (Kötz and Carlen, 2000). The semi cycle like in the mid frequency (shown in Figure 4.46(b)) represents the parallel combination of charge-transfer resistance (R_{ct}) and constant phase element (Q). The knee-region at low frequency is

a consequence of the diffusion and transporting of electrolyte in the porous electrode which is known as Warburg impedance (Z_W) confirmed the narrow inlet of bubble pores as mentioned in CV result (inset in Figure 4.39(c)) (Keiser *et al.*, 1976). In the low frequency region, all electrodes present nearly a vertical plot behind the Warburg region are modeled by a parallel combination of resistance (R_f) and constant phase element (Q_f) which indicate the internal structures are completely wetted by the electrolyte (Wang *et al.*, 2013; Ra *et al.*, 2009). By fitting the impedance spectra to the proposed equivalent circuit (inset of Figure 4.46(b)) employing Nova software, the fitted parameters are summarized in Table 4.10. The small R_f (89 m Ω) and R_{ct} (263 m Ω) of AgOx-MnOx/CNF will result in a small IR drop during CD measurement especially at a high scan rate. Moreover, the largest Q_f , \approx 147 mF, was also observed for AgOx-MnOx/CNF, which was consistent with the preceding specific capacitances of CV and CD results. In addition, the smallest Z_W , \approx 492 m Ω S^{-1/2}, of MnOx/CNF facilitated fast mass transport within the mesopore of the electrode (Xing *et al.*, 2014). Complex capacitance analysis generated from EIS spectra, have been emerged as an acceptable technique for investigation of bulk and interfacial electrochemical properties of various solid or liquid materials. Figure 4.48 shows both the real part (C') and the imaginary part (C'') of the complex capacitance derived from the EIS spectra of the samples. Figure 4.48(a) shows the plots of capacitance as a function of frequency, the overall electrodes reached full capacitance at low frequency below 1 Hz, then rapidly decreased during 1-10 Hz and no capacitive behaviors were observed above 100 Hz. The value of C' at 0.1 Hz were also calculated and summarized in Table 4.10. The highest value of 64.1 F observed for AgO_x-MnO_x/CNF is in agreement with capacitance of MnO₂/C around 79-233 F g⁻¹ at 10 mHz (Yang *et al.*, 2013). The

characteristic frequency of each electrode is shown in Figure 4.48 (b), and the characteristic frequency of all composite electrodes had a higher value than pristine CNF ($f_{\omega} = 1.1$ Hz, $\tau = 0.91$ s). The small time constants of the AgO_x/CNF ($\tau = 0.48$ s), MnO_x/CNF ($\tau = 0.19$ s), and AgO_x-MnO_x/CNF ($\tau = 0.77$ s) imply that they are able to deliver energy faster than the bare CNF. However, the smallest time constant of 0.19 s observed for MnO_x/CNF is possibly due to the fact that the ion of electrolyte can access the mesopore of the material easily (Zhi *et al.*, 2012). The accession of electrolyte charges on the interface of the microporous electrode is also described corresponding to Keiser's work (Keiser *et al.*, 1976), they explained that the EIS profile are related to the pore morphologies as displayed in Figure 4.47. The high value of slope of EIS curve at mid frequency (Warburg region). The EIS curves of MnO_x/CNF can be interpreted as feature (1) or (2) which the electrolyte charges move easily into the pores resulting in the fast accession. While the other electrodes present likely to be a bubble pore shape of feature (4) with the narrow entry and the small average total pore size around 2.3-3.1 nm of CNF, AgO_x/CNF, and AgO_x-MnO_x/CNF as discussed before. As a result, the charges move into the pore structures of CNF, AgO_x/CNF, and AgO_x-MnO_x/CNF electrodes slower than that of MnO_x/CNF electrode (Yang *et al.*, 2013).

Table 4.11 Kinetic parameters derived from the Nyquist plots for CNF, AgO_x/CNF, MnO_x/CNF, and AgO_x-MnO_x/CNF electrodes.

Sample	<i>ESR</i>	<i>R_{ct}</i>	σ	<i>Q</i>	<i>R_f</i>	<i>Q_f</i>	<i>C'</i>	τ
	(mΩ)	(mΩ)	(mΩ S ^{-1/2})	(mF)	(mΩ)	(mF)	(F)	(s ⁻¹)
CNF	273	405	530	8.8	235	105	45.7	0.95
AgO _x /CNF	393	234	1040	3.9	231	115	48.8	0.48
MnO _x /CNF	410	166	492	6.8	483	34	16.8	0.19
AgO _x -MnO _x /CNF	428	263	799	4.9	89	147	64.1	0.79



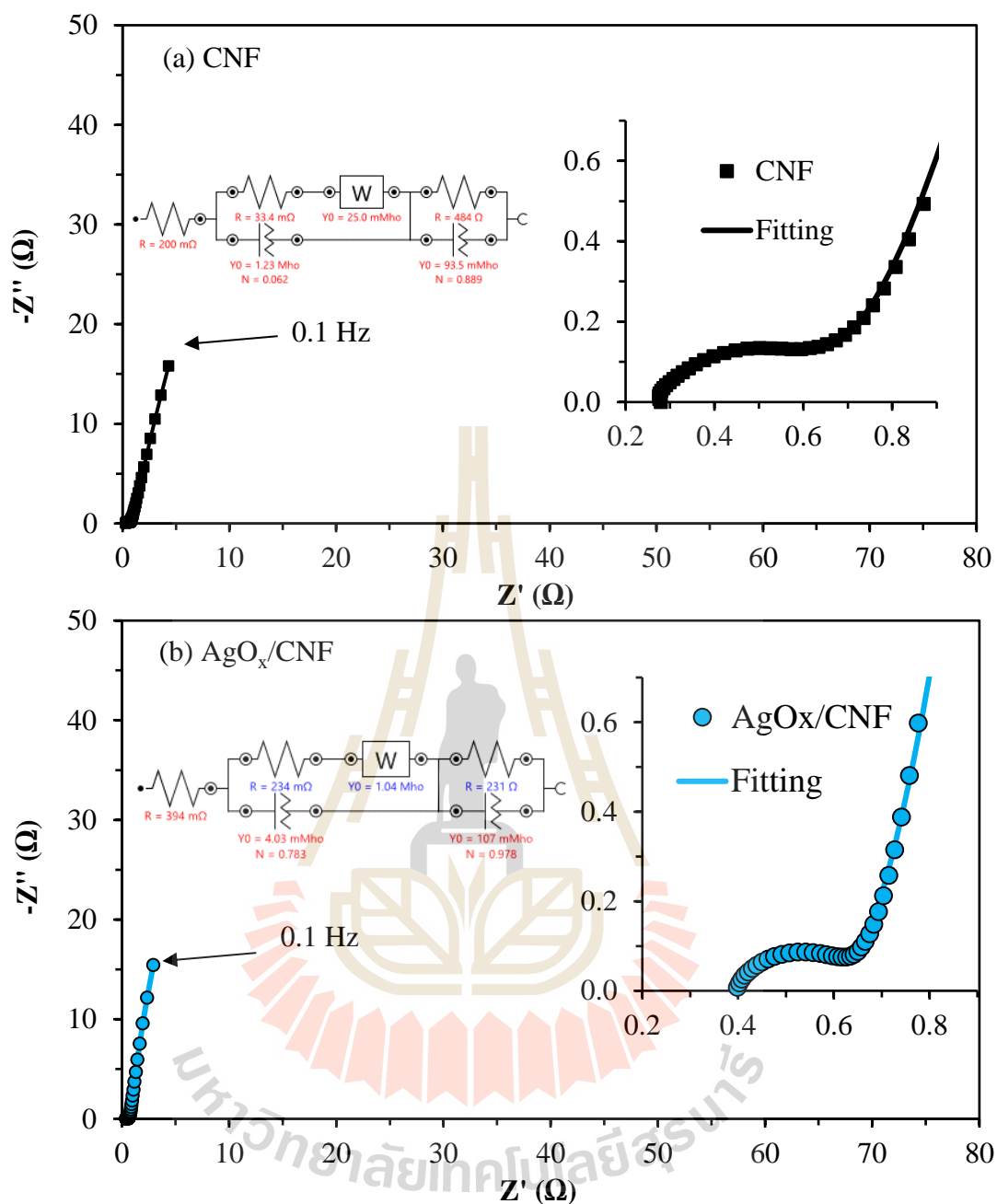


Figure 4.46 (a) Nyquist plot of all electrodes at a perturbation amplitude of 0.1 V and (b) enlarged spectra at high frequency (inset is the equivalent circuit using for impedance fitting).

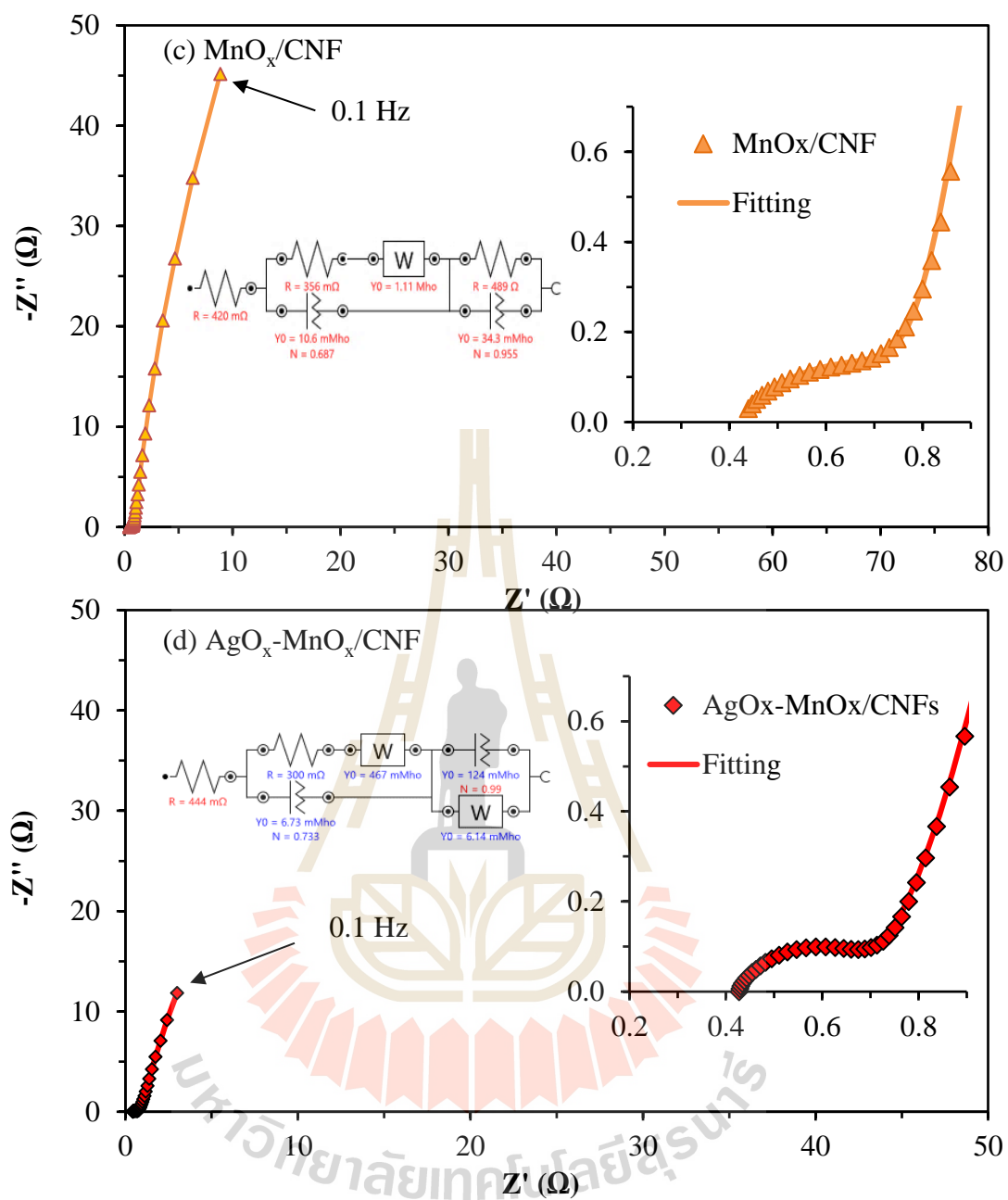


Figure 4.46 (a) Nyquist plot of all electrodes at a perturbation amplitude of 0.1 V and (b) enlarged spectra at high frequency (inset is the equivalent circuit using for impedance fitting). (continued)

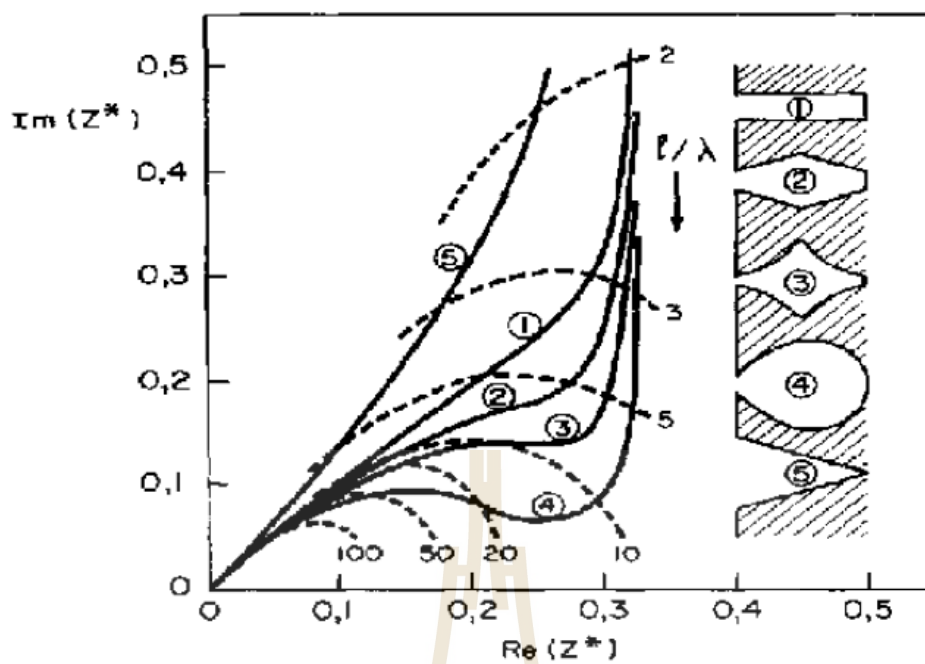


Figure 4.47 The relationship between pore features and impedance curves obtaining from EIS (Keiser *et al.*, 1976).

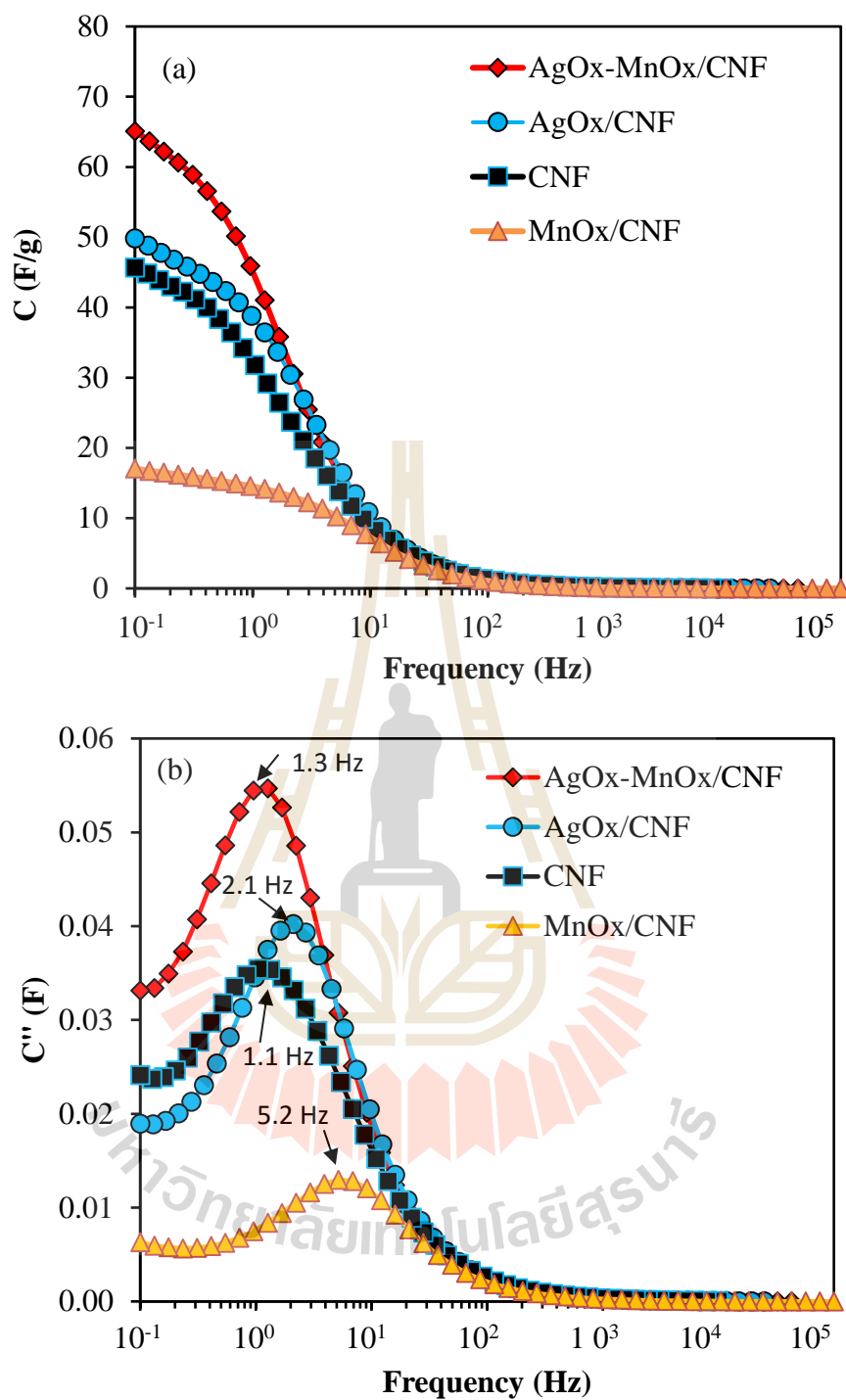


Figure 4.48 (a) Capacitance as a function of frequency. (b) The imaginary part in impedance of all electrodes.

4.3.4 Effect of calcination temperature on physical and electrochemical properties of AgO_x-MnO_x/CNF

4.3.4.1 Porosity of AgO_x-MnO_x/CNF fabricated at different temperatures of 500, 700, and 900 °C

Figure 4.49 shows the nitrogen adsorption/desorption isotherms for the AgO_x-MnO_x/CNF prepared at different calcination temperatures of 500, 700, and 900 °C. According to the IUPAC, the long plateau of curves principally attribute the adsorption characteristics of microporous adsorbent. The adsorption isotherm in the low-relative-pressure region of AgO_x-MnO_x/CNF-900 and -700 is attributed to the surface of the micropores, whereas the hysteresis loops varying from P/P₀ 0.45 to 0.95 indicating typical type IV isotherms due to the mesopore structure (Liu and Zhang, 2009). Among all the samples, the AgO_x-MnO_x/CNF-900 exhibits the biggest loop indicating large number of mesopore and micropores volume, and this results in the highest specific surface area of the AgO_x-MnO_x/CNF-900 (Tavanai *et al.*, 2009).

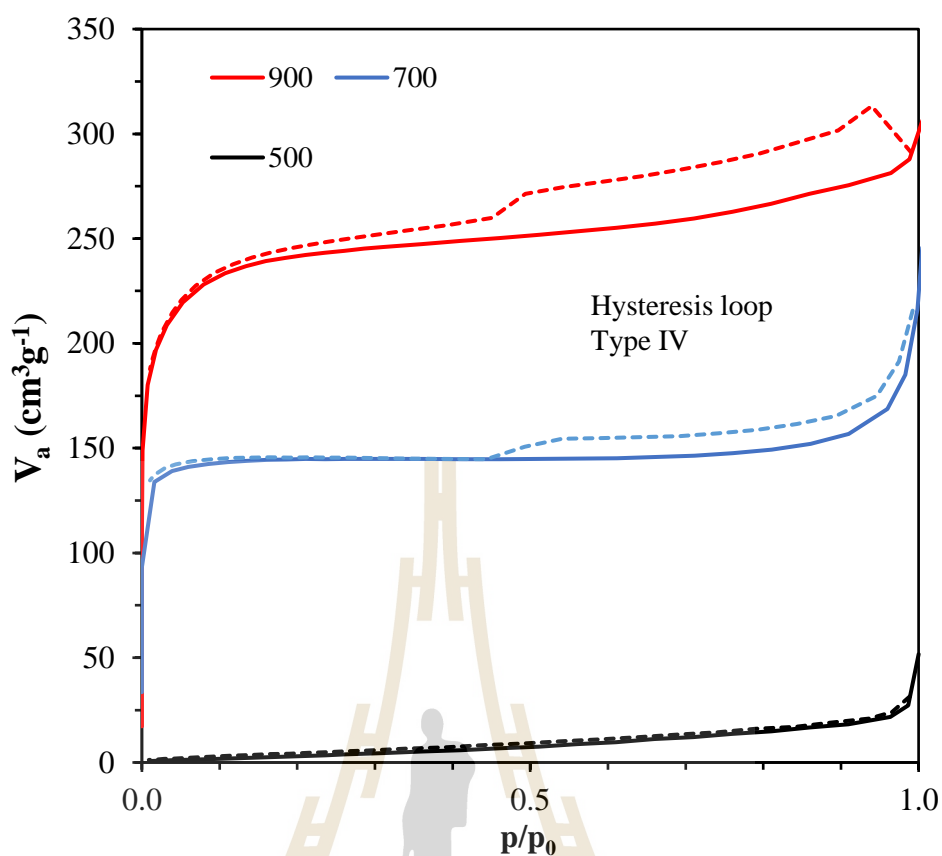


Figure 4.49 N₂ adsorption/desorption isotherm of AgO_x-MnO_x/CNF calcined at 500, 700, and 900 °C.

Table 4.12 The textural parameter of AgO_x-MnO_x/CNF calcined at 500, 700, and 900 °C.

Sample	S_{BET} ($\text{m}^2 \text{g}^{-1}$)	D_p (nm)	V_{tot} ($\text{cm}^3 \text{g}^{-1}$)
AgO _x -MnO _x /CNF-900	812	2.21	186.66
AgO _x -MnO _x /CNF-700	334	3.68	76.94
AgO _x -MnO _x /CNF-500	20	10.35	4.61

4.3.4.2 Microstructures of AgO_x-MnO_x/CNF fabricated at different temperatures of 500, 700, and 900 °C

The XRD patterns in Figure 4.50 present a broad peak of (002) plane of carbon around 26° for all samples (Lai and Lo, 2015) and the d_{002} spacing slightly decreases from 0.366 to 0.359 with increasing calcination temperature from 500 to 900 °C (Table 4.13) is in consistent with the report of Andrews *et al.* (2001). While only pattern of AgO_x-MnO_x/CNF-900 displays the diffraction peak of cubic Ag metal at 38.7, 44.5, 64.7, and 77.7 ° of the planes (111), (200), (220), and (311), respectively. The diffraction peaks at 18.29, 28.9, 32.7, 36.3, 50.9, 58.7, and 60.1 ° attributed to the planes (110), (112), (111), (211), (105), (321), and (224) of spinel Mn₃O₄ in the sample. These results confirm that the AgNO₃ and Mn(NO₃)₂ precursor added in nanofibers are more converted to cubic Ag and spinel Mn₃O₄, and thus forming more nanocrystals with higher calcination temperature (Cai *et al.*, 2016). The TEM micrograph of the sample are displayed in Figure 4.50(b-d), small dark black nanoparticles greatly distributed overall the fibers calcined at 900 °C in Figure 4.50 (b) were identified to be silvers nanoparticles as mentioned above. Whereas the nanoparticles obviously decreased nanofiber calcined at 700 °C and no any particle observed for sample 500 °C. These confirmed the strong effect of calcination temperature on matrix carbon and nano-reinforcement forming during heat treatment. This growth of particles with increasing calcination temperature is due to agglomeration of particles and has been consistently reported of Ud Din *et al.* (2015).

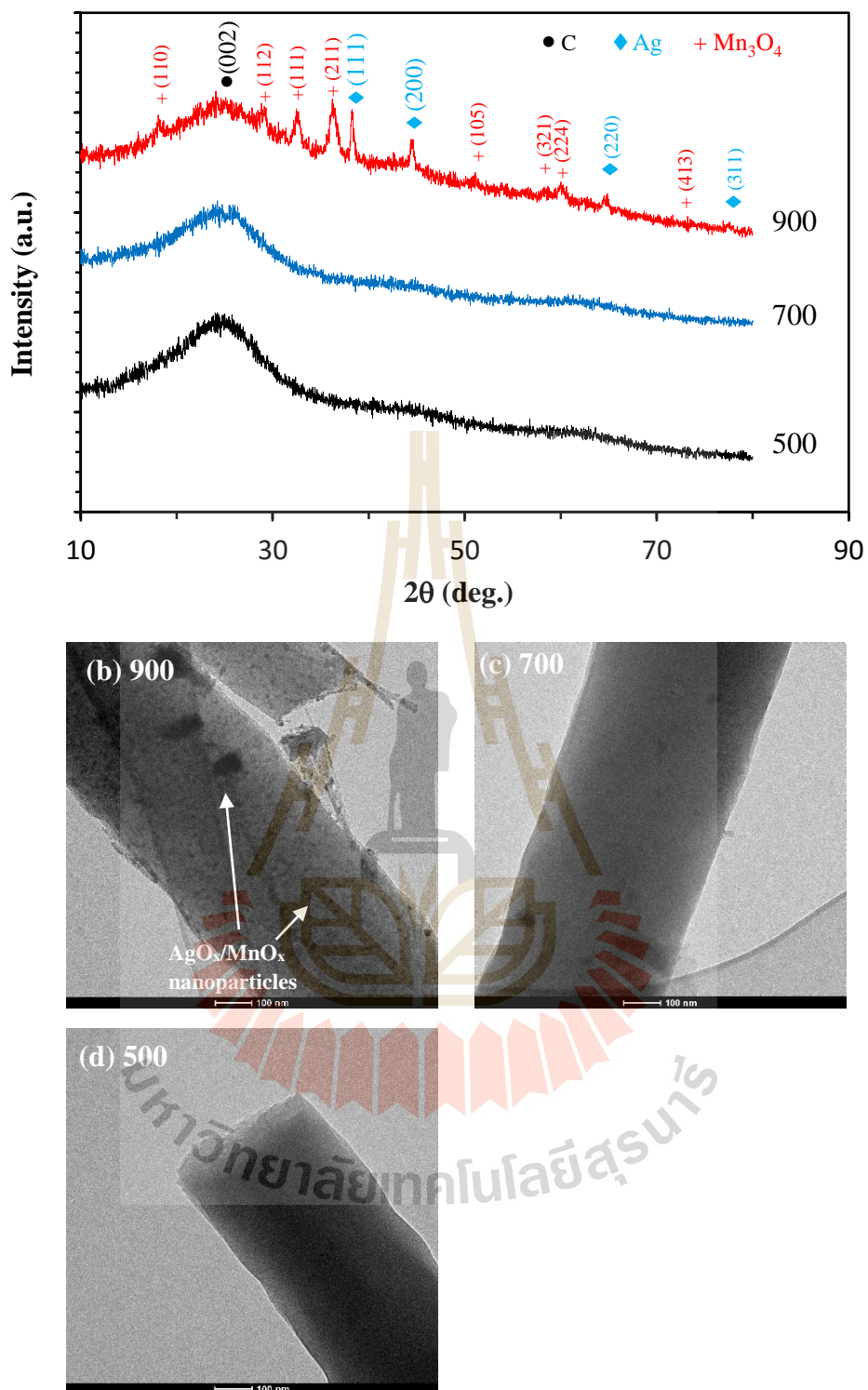
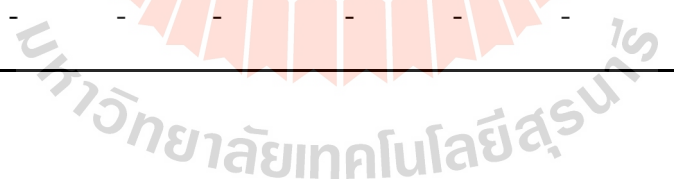


Figure 4.50 (a) XRD patterns and TEM pictures of AgO_x-MnO_x/CNF prepared at different calcination temperature of (b) 500, (c) 700, and (d) 900 °C.

Table 4.13 Structural parameters of the carbon, cubic Ag, and spinel Mn₃O₄ observing from electrospun AgO_x-MnO_x/CNF prepared at different calcination temperatures of 500, 700, and 900 °C.

Sample		C	Ag					Mn ₃ O ₄					
		(002)	(111)	(200)	(220)	(311)	(110)	(112)	(111)	(211)	(105)	(321)	(224)
900	2θ (deg.)	24.79	38.73	44.55	64.69	77.19	18.29	28.89	32.65	36.31	50.96	58.74	60.11
	<i>d</i> (nm)	0.359	0.232	0.203	0.144	0.123	0.485	0.309	0.274	0.247	0.179	0.157	0.154
700	2 θ (deg.)	24.44	-	-	-	-	-	-	-	-	-	-	-
	<i>d</i> (nm)	0.364	-	-	-	-	-	-	-	-	-	-	-
500	2 θ (deg.)	24.36	-	-	-	-	-	-	-	-	-	-	-
	<i>d</i> (nm)	0.366	-	-	-	-	-	-	-	-	-	-	-



4.3.4.3 Cyclic voltammetry of AgO_x-MnO_x/CNF fabricated at different temperatures of 500, 700, and 900 °C

The CV profiles of AgO_x-MnO_x/CNF calcined at 500, 700, and 900 °C were measured in KOH 6 M aqueous electrolyte at scan rate range of 2-500 mV s⁻¹ at potential voltage windows of 1.0 V in order to cover the whole capacitive mechanisms ranges: EDLC (C_{dl}) at high scan rate value more than 100 mV s⁻¹, surface pseudocapacitance (C_{ps-S}) at mid scan rate between 5-100 mV s⁻¹, and also bulk pseudocapacitance (C_{ps-B}) at very low scan rate lower than 5 mV s⁻¹. The all electrodes showed an increasing of current density at higher scan rate and behaved nearly as a rectangular curve of an ideal capacitor. This indicates that the double layer capacitive processes mainly stores the charges of the electrodes, while only sample calcined at 900 °C clearly presents a pair of cathodic and anodic peaks corresponding to the oxidation and reduction processes of MnO_x clusters in the samples (Yano *et al.*, 2013). The comparison of CV profiles at 500, 50, and 2 mV s⁻¹ are presented in Figure 4.51 (e-f) to describe the detail of capacitive behavior at each scan rate region. At high scan rate of 500 mV s⁻¹, the CV plot of AgO_x-MnO_x/CNF-900 rather presents the bigger current loop than the others corresponding to the best EDLC behavior due to greatest specific surface area and strong redox reaction peaks, indicating surface pseudo capacitance due to the more MnO_x nano structures. However, the CV loop of AgO_x-MnO_x/CNF-700 became bigger than the others at mid scan rate of 50 mV s⁻¹ because the EDLC was tendy dropped as scan rate decreased and surface pseudocapacitance from MnO_x nanoparticles originated to contribute the total capacitance (Figure 4.52). At low scan rate of 2 mV s⁻¹, the CV plot of AgO_x-MnO_x/CNF-500 clearly appeared the two pairs of redox reaction peak possibly originated from bulk and surface

pseudocapacitance. However the background loop of EDLC behavior became smallest value. The specific capacitances as a function of scan rate are shown in Figure 4.52.

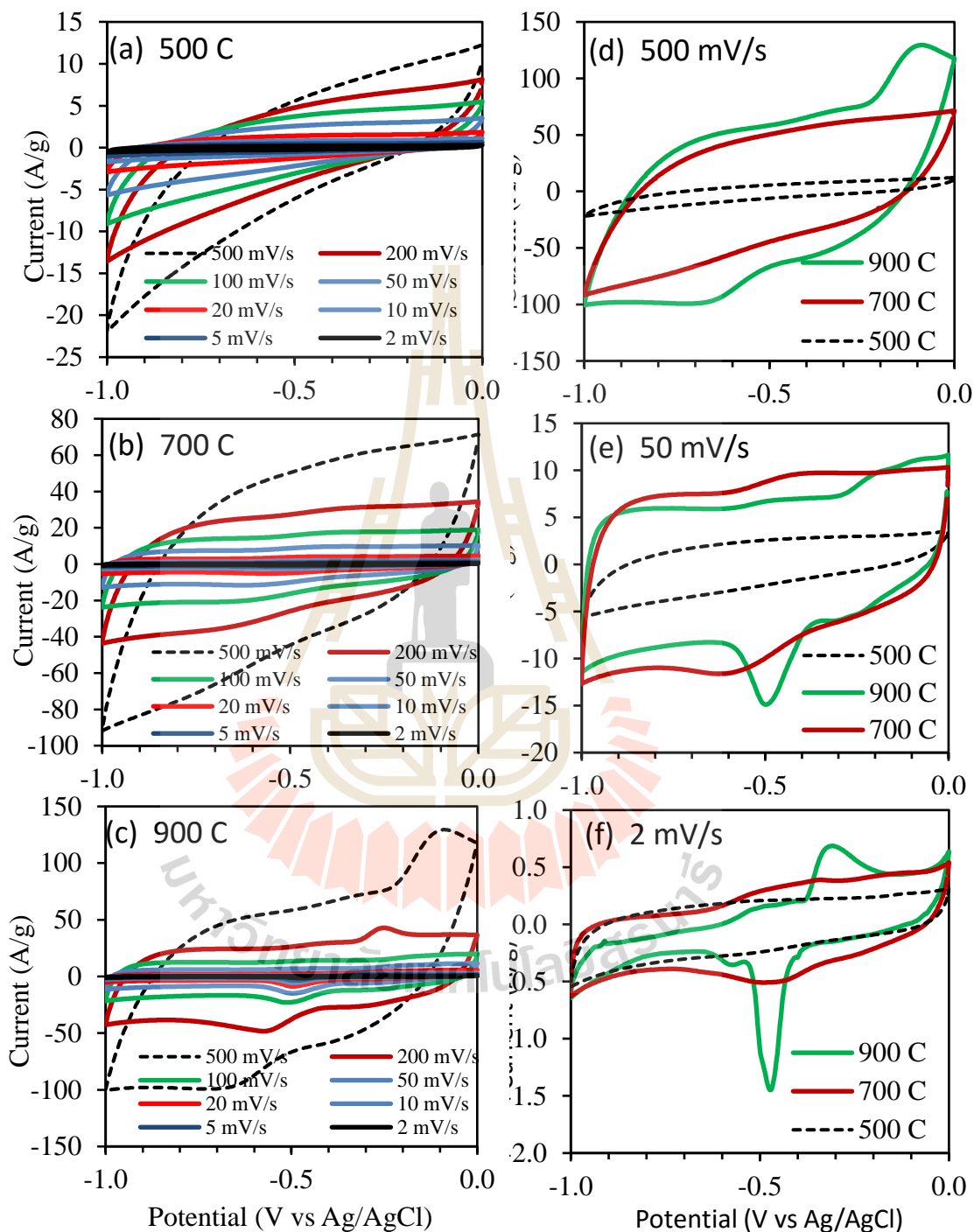


Figure 4.51 Cyclic voltammograms of the $\text{AgO}_x\text{-MnO}_x/\text{CNFs}$ which were calcined at differences temperature of 500, 700, and 900 °C.

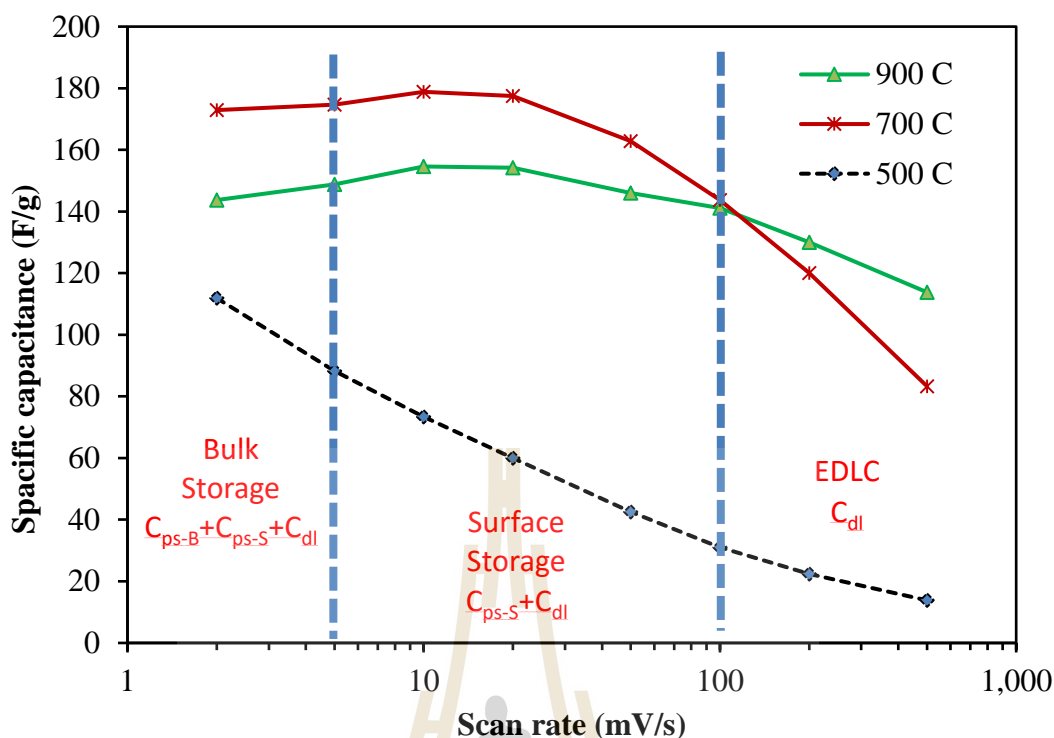


Figure 4.52 The specific capacitance as the function of scan rate of $\text{AgO}_x\text{-MnO}_x/\text{CNF}$ calcined at difference temperature of 500, 700, and 900 °C.

4.3.5 Effect of electrolyte on electrochemical properties of $\text{AgO}_x\text{-MnO}_x/\text{CNF}$

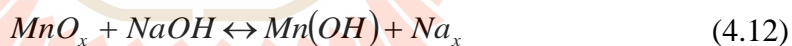
In the previous experiments, the cation was always K^+ and it is known that the main energy storage mechanism in supercapacitors arises from the reversible electrostatic accumulation of electrolyte ions on the surface of porous carbon, the influence of electrolyte on the capacitance is demonstrated by equation (4.10) (Béguin *et al.*, 2014). Therefore, to further investigate the roles of cations and anions in charge storage for Mn clusters in active materials, cyclic voltammetry was performed on the oxygen-excess material in four aqueous electrolytes; 3 M LiOH, 3 M NaOH, 3 M KOH, and 1.5 M Na_2SO_4 , varying the cation and anions size ratios between $\text{Li}^+ < \text{Na}^+ < \text{K}^+$ and $\text{OH}^- < \text{SO}_4^{2-}$ as summarized in Table 4.14. The CV profiles of samples were measured

at scan rate range of 2-500 mV s^{-1} with potential voltage windows of -1-0 V (Figure 4.53(a-d)). The comparisons of the cyclic voltammogram at low (2 mV s^{-1}), mid (50 mV s^{-1}), and high (500 mV s^{-1}) scan rate in Figure 4.53(e-g) present clearly the different pseudocapacitive mechanism due to varied electrolytes. At high scan rate, the CV current can be found that the supercapacitors in their voltage range exhibited parallelogram because the large DC resistance at high scan rate. The absence of any redox peaks of faradaic current from electrochemical reaction between MnO_x nanoparticles and the electrolytes due to the purely physical forming of the EDLC without electrochemical reactions in this scan rate range (Béguin *et al.*, 2014). At mid scan rate, the CV current appeared closely to be the rectangular EDLC behavior including a broad redox reaction peaks of MnO_x in the samples. However, there was no any redox peak found for Na_2SO_4 electrolyte is in consistent with the several reports such as Hassan *et al.* (2012), Li *et al.* (2008), Li and Zhitomirsky (2009), Pang *et al.* (2000), and Peng *et al.* (2010). More details about redox reaction peak of the sample measured in each electrolyte were observed at low scan rate of 2 mV s^{-1} and the unstable curve of oxygen evolution was observed for Na_2SO_4 electrolyte above -0.2 V (Chen *et al.*, 2013). Essentially, the quiet difference of cyclic voltammogram measured in NaOH and Na_2SO_4 possibly on account of the pseudocapacitive charge storage in MnO_x structures is dominated by anion intercalation. This can be explained by the presence of OH^- or SO_4^{2+} ions that are readily accessible from the electrolyte, while mobile protons must be formed through the dissociation of water (Mefford *et al.*, 2014). The plot of specific capacitance as a function of scan rate in Figure 4.54 exhibited the high EDLC of the electrode for KOH electrolyte due to high conductivity of 65 S m^{-1} . However, the LiOH electrolyte rather affected on high capacitance because the large

numbers of smallest Li^+ ionic radius (Table 4.14) can easily access inside the micropores and the lithium is also known as the best alkaline reactant. Therefore, these caused more total capacitance from the both EDLC and pseudocapacitance at low scan rate below 10 mV s^{-1} (Zhang *et al.*, 2012; Wang *et al.*, 2016).

$$C_H = \varepsilon_0 \varepsilon_r \frac{A}{d} \quad (4.10)$$

Where C_H is capacitance corresponding to Hemholtz layer, ε_0 is the vacuum permittivity ($= 8.854 \times 10^{-12} \text{ F m}^{-1}$), ε_r is the relative permittivity of the electrolyte, A is the electrode surface area, and d is the effective thickness of the electric double layer of Hemholtz model (Béguin *et al.*, 2014). The typical electrochemical redox reaction between MnO_x nanoparticles composited in the electrode and the electrolytes can be interpreted to equation (4.9) for KOH, equation (4.11) for LiOH (Yuan and Zhang, 2006), and equation (4.12) (Brock *et al.*, 1998) or (4.13) (Wang *et al.*, 2013) for NaOH.



Or



Table 4.14 Kinetic parameters of the electrolytes.

Electrolyte (M)	Ionic radius		Conductivity		
	Positive	Negative	Electrolyte (S m ⁻¹)	Selected ions	
	(nm)	(nm)		(S L mol ⁻¹ cm ⁻¹)	
KOH, 3 M	0.133 (K ⁺)	0.133 (OH ⁻)	65	0.0735 (K ⁺)	0.1986 (OH ⁻)
NaOH, 3 M	0.095 (Na ⁺)	0.133 (OH ⁻)	0.8	0.0501 (Na ⁺)	0.1986 (OH ⁻)
Na ₂ SO ₄ , 1.5 M	0.095 (Na ⁺)	0.258 (SO ₄ ²⁻)	0.11	0.0501 (Na ⁺)	0.1596 (SO ₄ ²⁻)
LiOH, 3 M	0.060 (Li ⁺)	0.133 (OH ⁻)	0.04	0.0387 (Li ⁺)	0.1986 (OH ⁻)



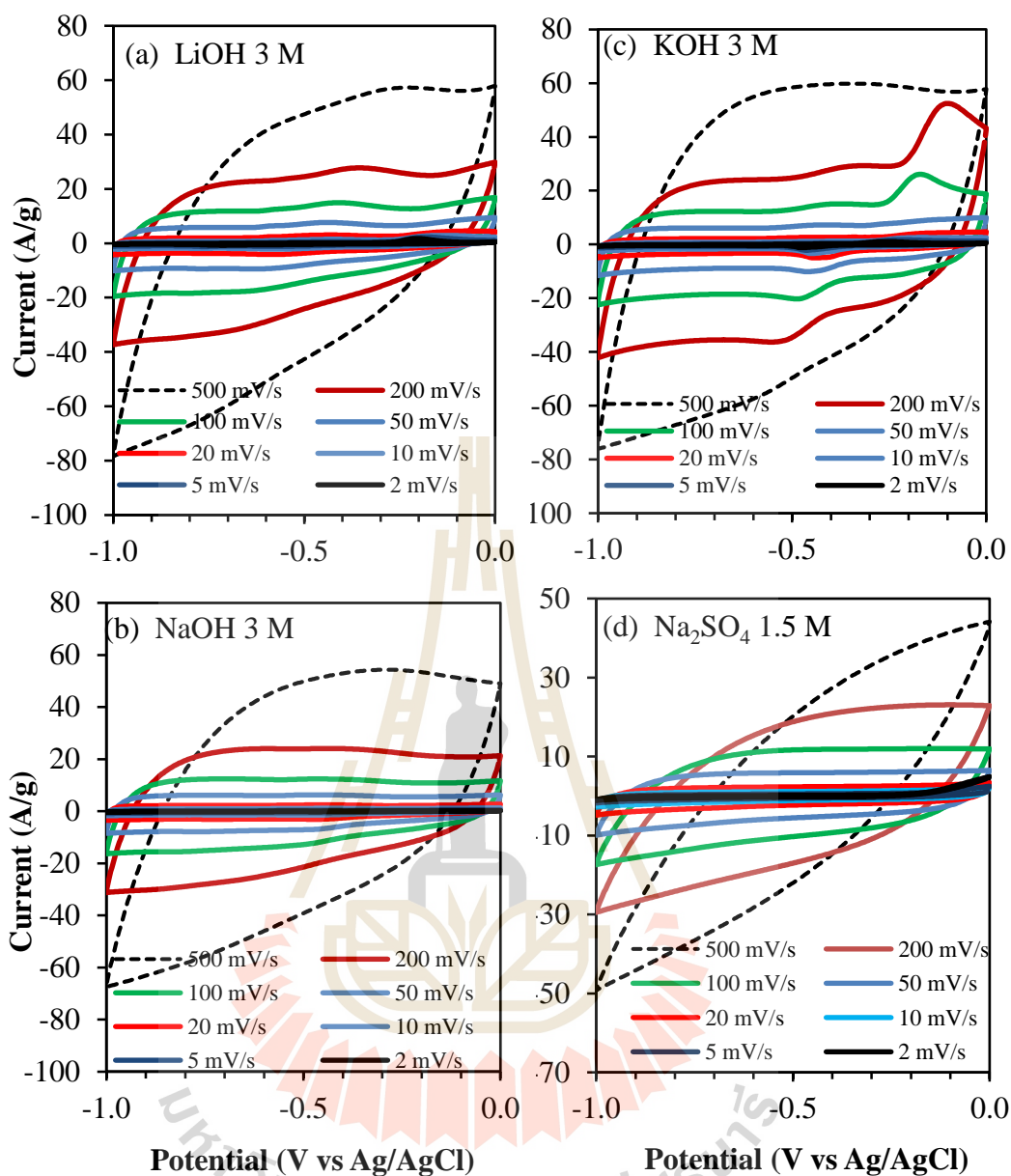


Figure 4.53 (a-d) CV profiles of AgO_x-MnO_x/CNF electrode in the different electrolytes as scan rate range between 2-500 mV s⁻¹. (e-g) Comparison of CV profiles at high, mid, and small scan rate.

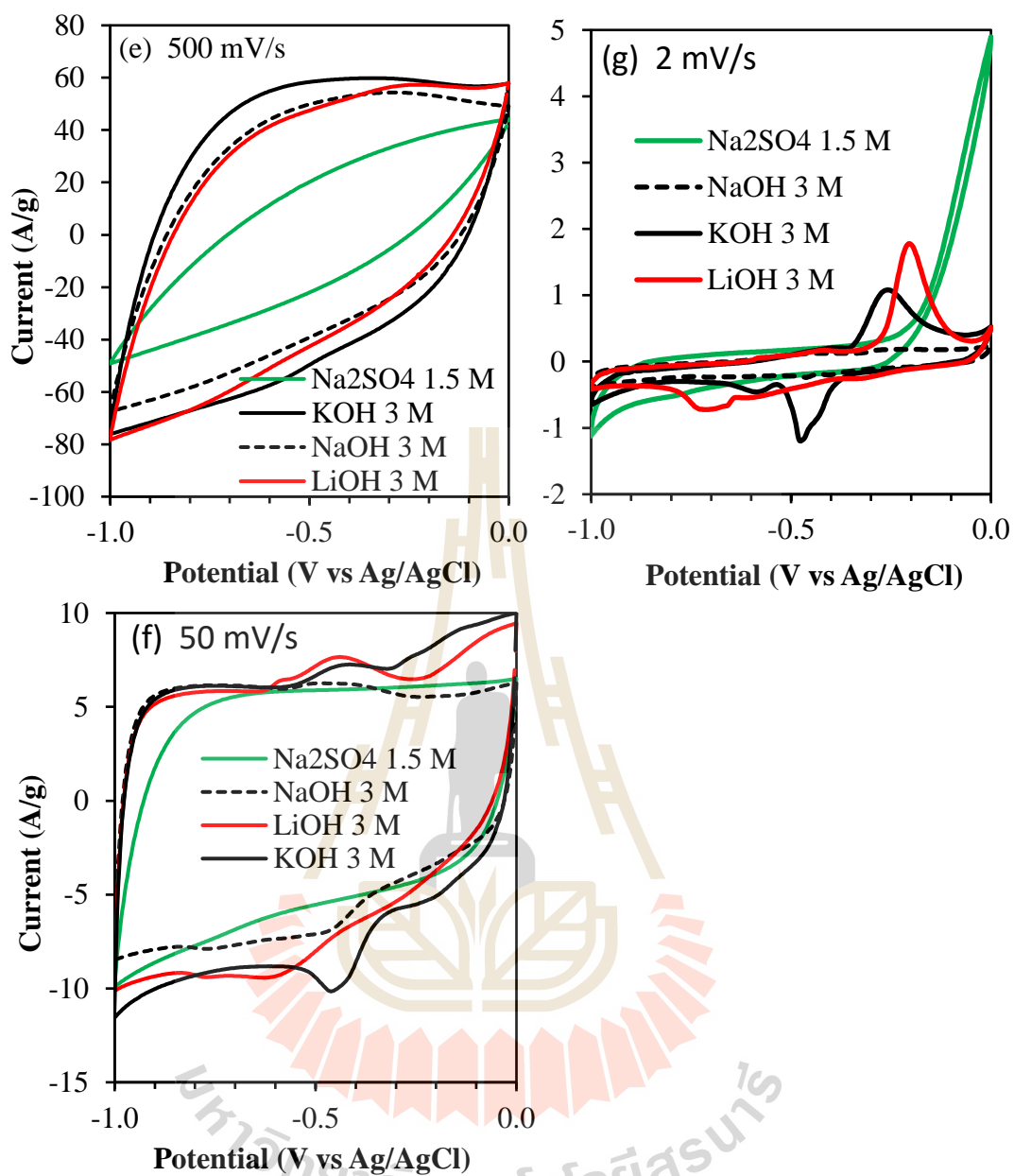


Figure 4.53 (a-d) CV profiles of AgO_x-MnO_x/CNF electrode in the different electrolytes as scan rate range between 2-500 mV s⁻¹. (e-g) Comparison of CV profiles at high, mid, and small scan rate.

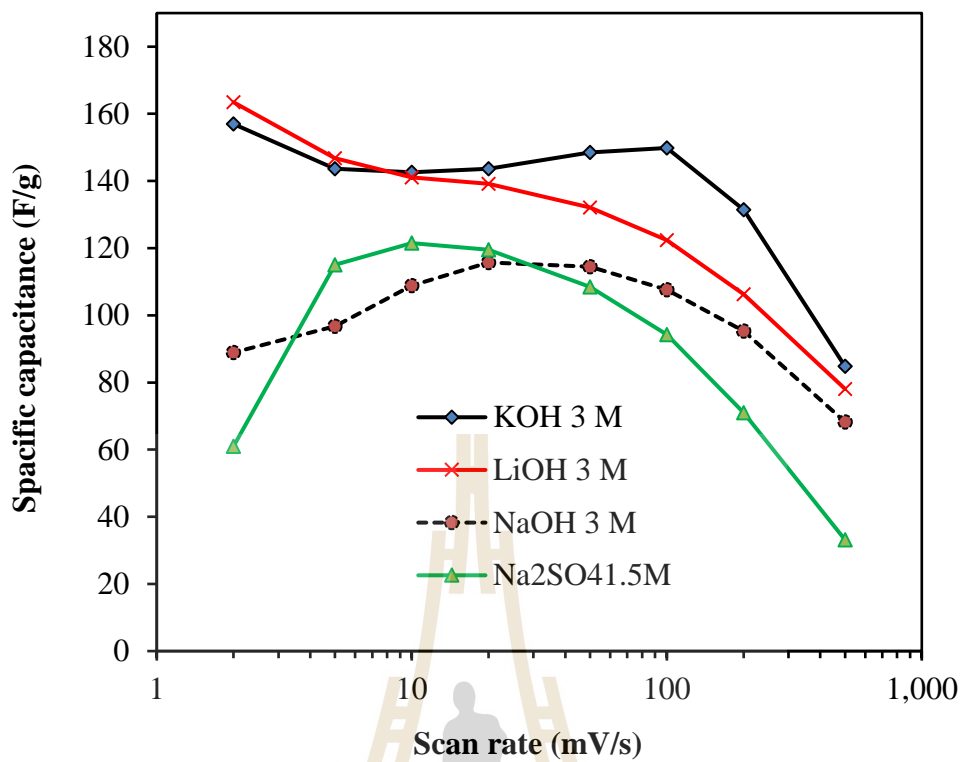
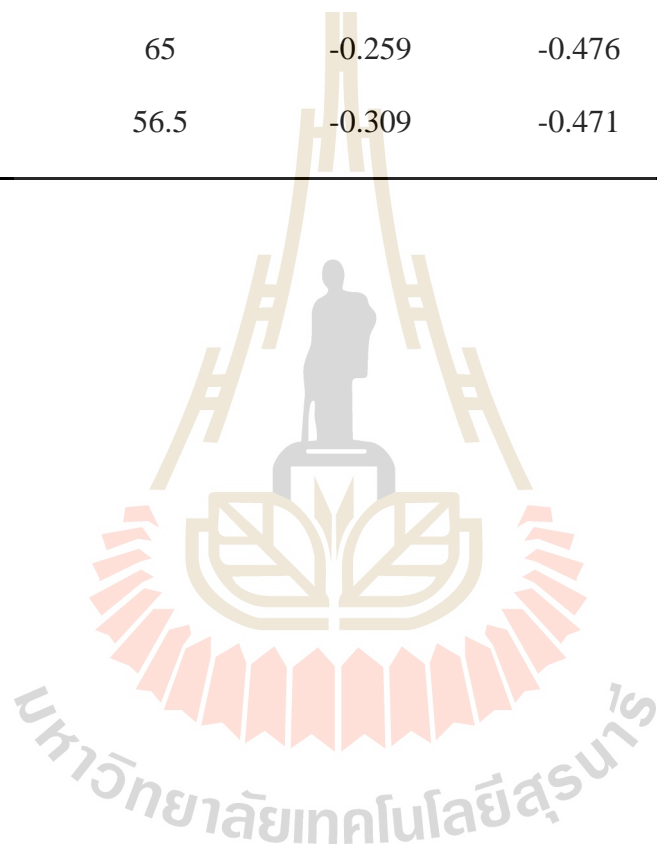


Figure 4.54 Specific capacitance of AgO_x-MnO_x/CNF electrode measured in different electrolytes as the function of scan rate.

The CV profiles of AgO_x-MnO_x/CNF electrode were also measured in different KOH concentrations of 1.5, 3, and 6 M in potential windows of 1.0 V at 2-500 mV s⁻¹ to study the effect of the concentration on the electrochemical properties. The results are shown in Figure 4.55(a-c). The both anodic and cathodic peaks related to oxygen intercalation using electrolyte hydroxide ions corresponding to Mn²⁺ ↔ Mn³⁺ as oxygen vacancy sites are filled, and the higher voltage peak corresponding to Mn³⁺ ↔ Mn⁴⁺ as excess oxygen is intercalated into the MnO_x structure. The CV measured in 6 M KOH trendly presented higher value than the other concentration at high and mid scan rate (Figure 4.55(d) and (e)), but the peaks measured in 1.5 M became higher at low scan rate of 2 mV s⁻¹ (Figure 4.55(f)). In this scan rate range, the anodic and cathodic voltages were slightly shifted to higher voltage and the potential difference (ΔV) between the two peaks also increase as the concentration decreased. These results show a strong influence of electrolyte concentration on chemical redox reaction of MnO_x in each electrode (Martinez *et al.*, 2014). The specific capacitances as a function of scan rate for each concentration are shown in Figure 4.56. It was found that the high concentration of 6 M KOH resulted in the highest capacitance of 113 F g⁻¹ at high scan rate of 500 mV s⁻¹, nevertheless it became smallest value of 144 F g⁻¹ at small scan rate of 2 mV s⁻¹.

Table 4.15 The difference between anodic and cathodic potentials at small scan rate of 2 mV s^{-1} .

Concentration (M)	Conductivity (mS cm^{-1})	Anodic peak (V vs Ag/AgCl)	Cathodic peak (V vs Ag/AgCl)	Potential difference (ΔV)
1.5	20	-0.195	-0.417	0.222
3	65	-0.259	-0.476	0.217
6	56.5	-0.309	-0.471	0.162



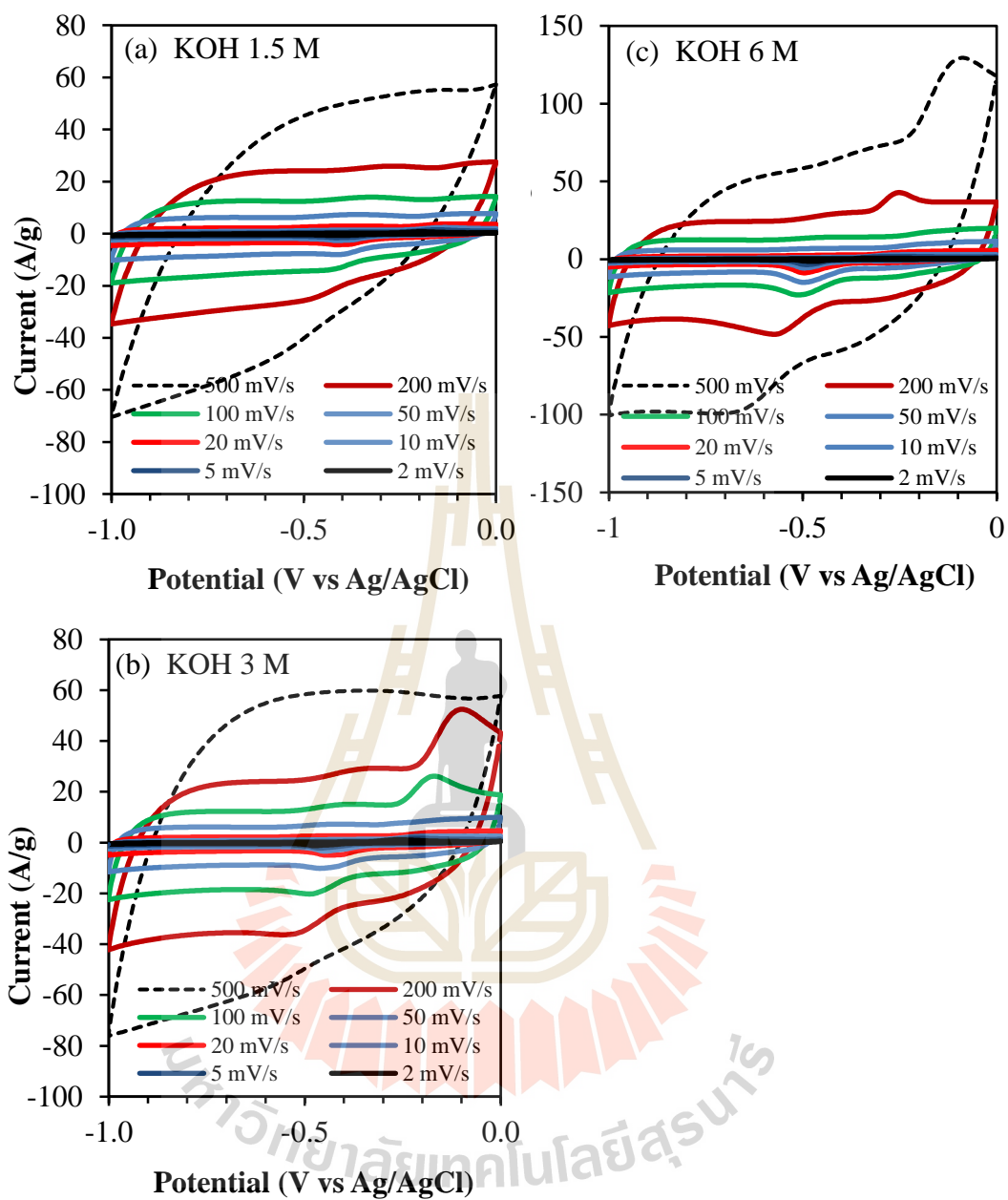


Figure 4.55 (a-c) CV profiles of AgO_x-MnO_x/CNF electrode in the difference KOH molarities as the scan rate range between 2-500 mV s⁻¹. (d-f) Comparison of CV profile at high, mid, and small scan rate.

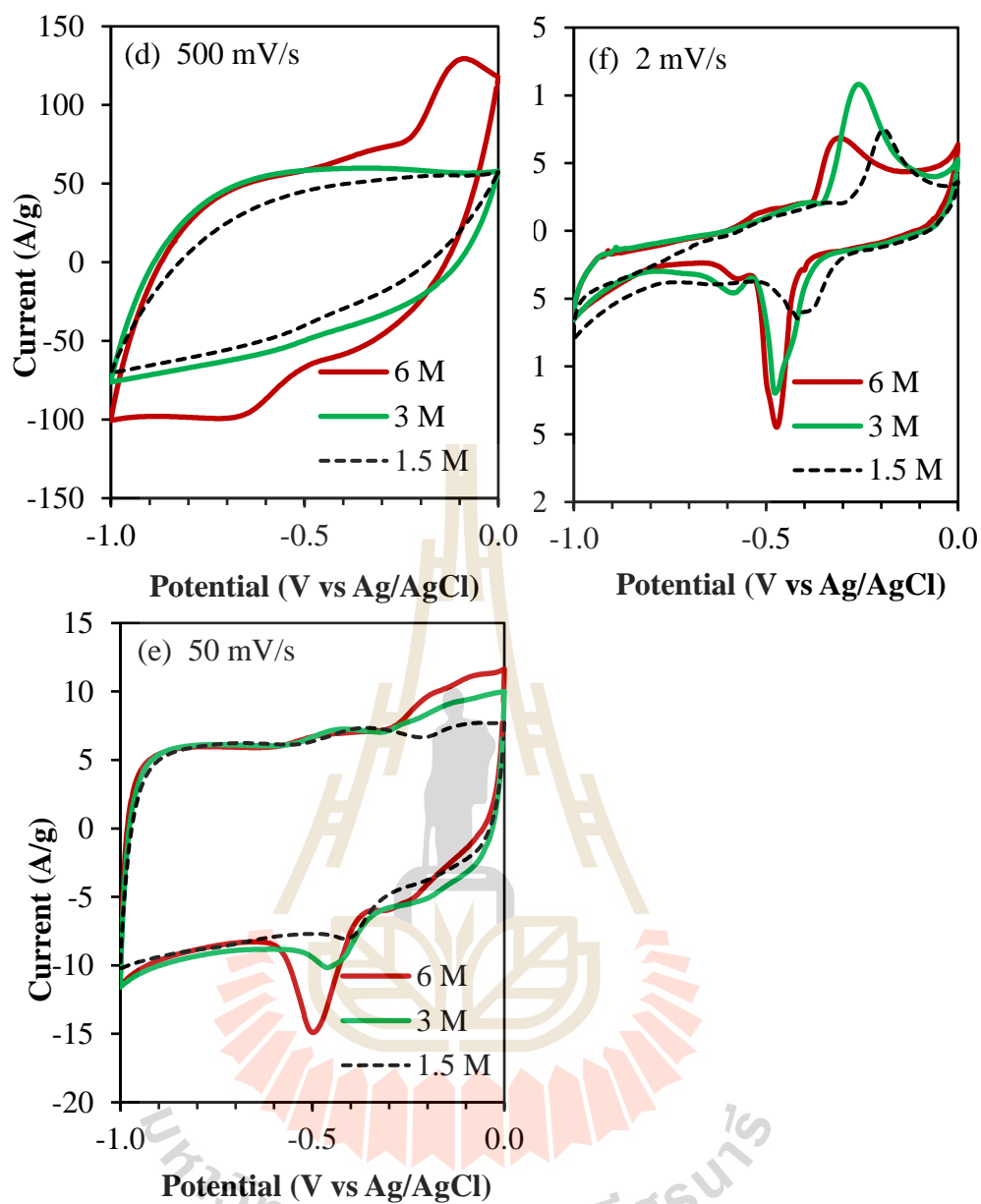


Figure 4.55 (a-c) CV profiles of $\text{AgO}_x\text{-MnO}_x/\text{CNF}$ electrode in the difference KOH molarities as the scan rate range between 2-500 mV s^{-1} . (d-f) Comparison of CV profile at high, mid, and small scan rate.

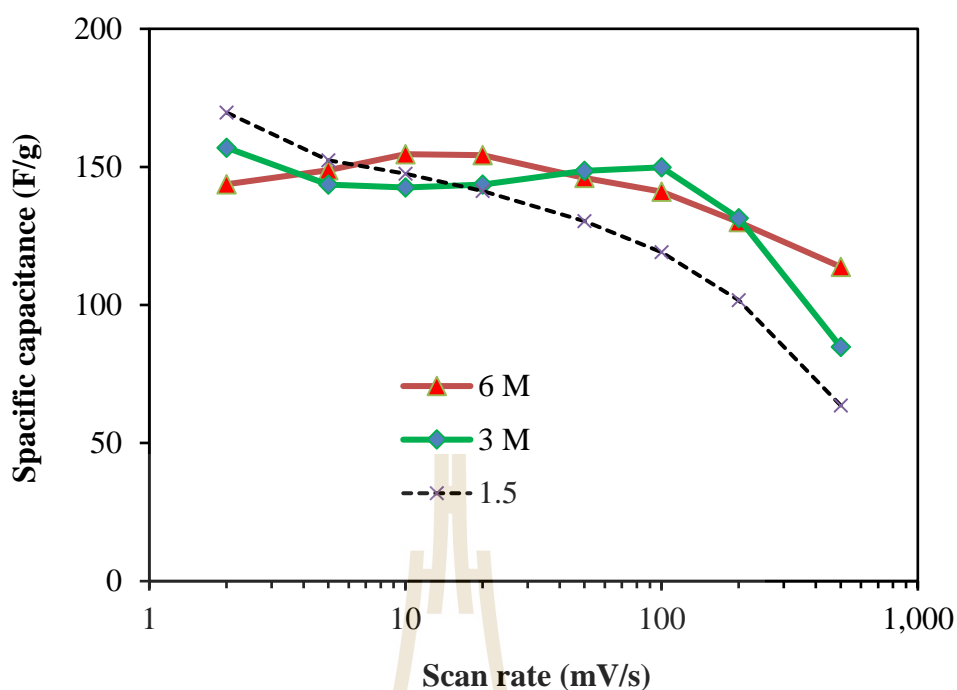


Figure 4.56 Specific capacitance of $\text{AgO}_x\text{-MnO}_x/\text{CNF}$ electrode measured in different molar of KOH as the function of scan rate.

4.3.6 $\text{AgO}_x\text{-MnO}_x/\text{CNF}$ electrode comparing to the commercial capacitors

In this study, the $\text{AgO}_x\text{-MnO}_x/\text{CNF}$ was prepared as the electrodes of supercapacitor and measured the capacitance comparing to the commercial devices. The 50 mg of $\text{AgO}_x\text{-MnO}_x/\text{CNF}$ was pressed on nickel foam current collectors as the electrodes of supercapacitor (Figure 4.57(a)). By the sandwich technique (Zhao *et al.*, 2013), the filter paper was placed between two $\text{AgO}_x\text{-MnO}_x/\text{CNF}$ electrodes to protect the short circuit of electrode from one another as shown in Figure 4.57(b). The cyclic voltammogram of a $\text{AgO}_x\text{-MnO}_x/\text{CNF}$ -supercapacitor was measured comparing to 7000 μF and 1.2 F commercial capacitors. The measurement was carried out under room condition.

The cell was immersed in 6 M KOH electrolyte. The supercapacitor performances were evaluated by measuring of CV behaviour comparing to 7,000 μF and 1.2 F commercial capacitors. The CV measurement was operated at voltage potential window ranged of -1.5-0.5 V at the sweep scan rate of 5 and 50 mV s^{-1} to compare with 7,000 μF and 1.2 F commercial capacitors, respectively, the measurement was carried out under room condition.

Figure 4.58(a) shows the comparison of CV profiles of the $\text{AgO}_x\text{-MnO}_x/\text{CNF}$ supercapacitor and commercial 7000 μF capacitor, the CV loop of a created capacitor displayed a bigger loop than the commercial at the sweep scan rate of 50 mV s^{-1} in voltage potential windows range of -1.5-0.5 V and it also gave a higher capacitance of 19,500 μF . While Figure 4.58(b) shows the CV measured at a low scan rate of 2 mV s^{-1} that compare to 1.2 F commercial supercapacitor, the $\text{AgO}_x\text{-MnO}_x/\text{CNF}$ supercapacitor also had the bigger CV loop than the commercial and obtained more capacitance of 2.2 F. However, the commercial products still kept more stable CV curves with no current leaked during charge/discharge process while the created $\text{AgO}_x\text{-MnO}_x/\text{CNF}$ supercapacitor displayed more resistive behaviour at low voltage region below -1.0 V possibly due to the simple manufacturing in the lab.

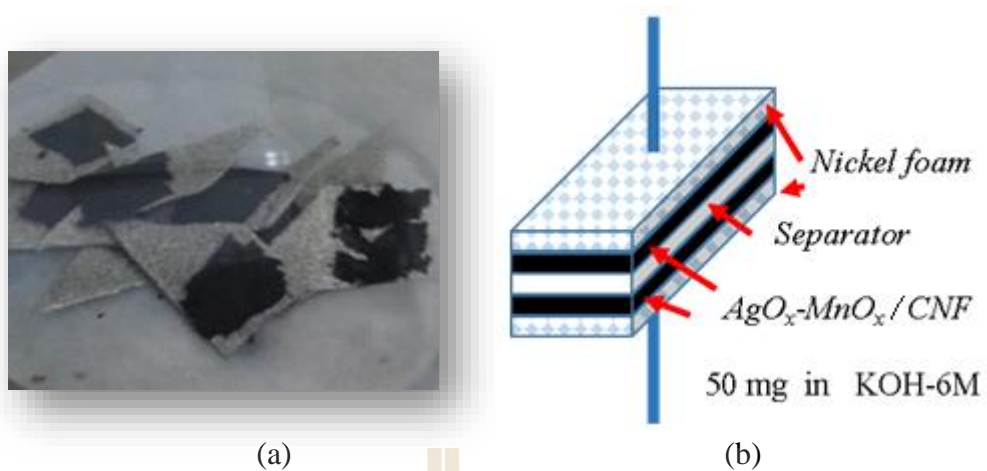


Figure 4.57 (a) Pressed-AgO_x-MnO_x/CNF nickel foam for the supercapacitor electrode. (B) A schematic represented a manufacturing of two-electrode AgO_x-MnO_x/CNF supercapacitor.

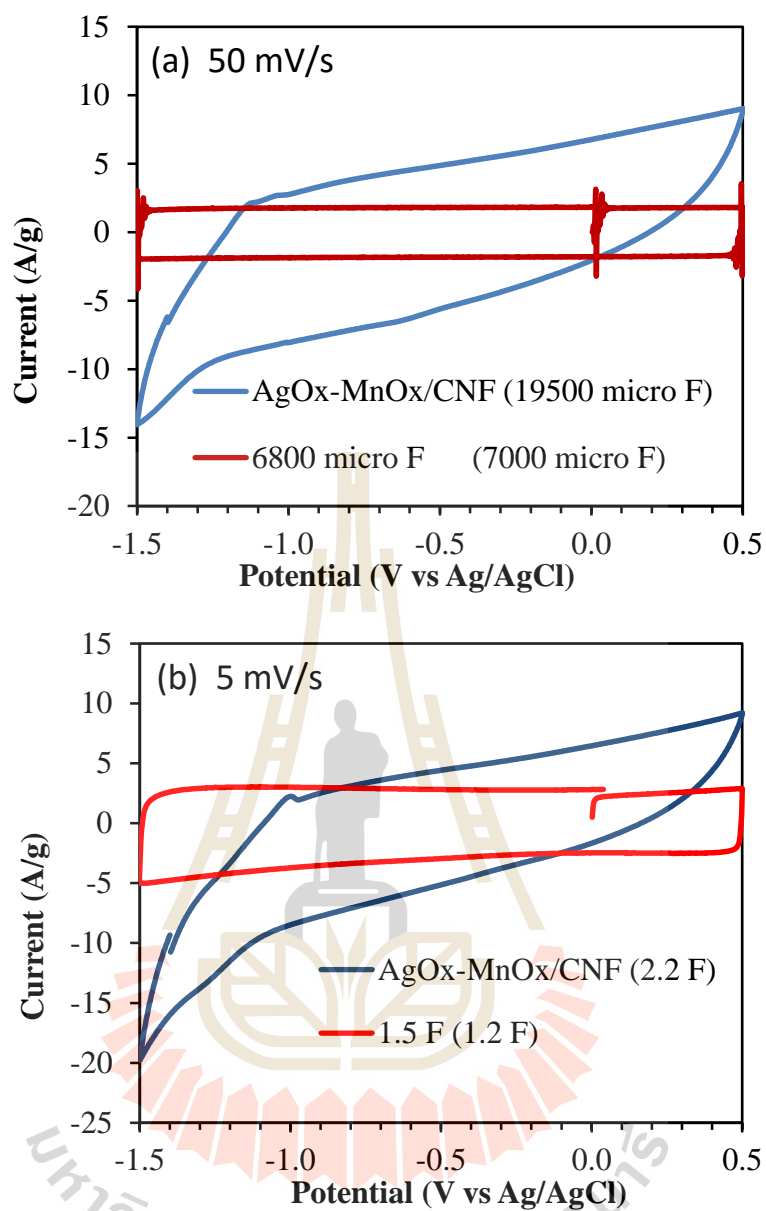


Figure 4.58 CV of AgO_x-MnO_x/CNF supercapacitor measured compared to commercial products.

CHAPTER V

CONCLUSIONS

In this study, carbon-based composite nanofibers (CNF, NiO_x/CNF, AgO_x/CNF, MnO_x/CNF, and AgO_x-MnO_x/CNF) have been successfully fabricated using simple electrospinning and successively calcined using three steps of stabilization, carbonization, and activation to obtain as composited CNF. The polymer source was fixed at 10 wt.%, while the metal sources were varied as 0, 5, 10, and 20 wt.%. The morphology, thermal stability, surface chemistry, microstructures, porosity, and chemical state were investigated by SEM, TEM, TGA, FTIR, XRD, Raman spectroscopy, BET, and XAS techniques. The electrochemical properties were studied via three electrochemical techniques including CV, GCD, and EIS. From the results and discussion, the conclusions of the whole thesis can be drawn as follows.

5.1 CNF

The electrospinning of PAN nanofibers was processed to be the precursor of the bare CNF fabrication. The PAN nanofibers have an average diameter of 368±53 nm and the average size was decreased as 265±32 nm after calcination. The thermal analysis suggested that the proper temperature on carbon fabrication should be above 350 °C. The high porosity with average pore diameter of 2.89 nm and specific surface area of 362 m² g⁻¹ of CNF can be obtained by activating in CO₂ at high temperature. However, this study found that the CO₂ activation above 900 °C caused the samples

burning off. The most carbon microstructures were found to be the amorphous structure.

The electrochemical performance of pure carbon electrode displayed no redox activity and the specific capacitance trendy independent on applied scan rate attributed an EDLC behavior. After a long lifetime of galvanostatic charge/discharge testing, the CNF showed the great capacity retention more than 98 %.

5.2 NiO_x/CNF

The electrospun Ni(NO₃)₂/PAN nanofibers were prepared as the precursor of various NiO_x/CNF composite. Morphology of fibers and distribution of fiber diameter were investigated at various applied voltage and polymer source concentration. Uniform PAN-based nanofibers with average diameters of 585±162--500±69 nm were obtained at an applied voltage of 8-14 kV, and the sizes were significantly decreased as the voltage increased and more beads also formed at high voltage. For various Ni(NO₃)₂ concentration at an applied voltage of 12 kV, the uniform nanofibers had an average diameter of 368±53-543±55 nm but not a linear relationship between diameter size and concentration, the biggest size of 543±55 nm was observed for 10 wt.%. The different nickel phase structures can be obtained by using different gas and temperature conditions. The cubic NiO forming need some oxygen while the most oxygen was rejected to form cubic Ni that led to the various composition of NiO/CNF, Ni/CNF, and Ni-NiO/CNF. The nickel element loading after calcination for all samples was found to be 23-24 % comparing to matrix carbon in each composite. The crystalline sizes of NiO and Ni in the composite were obtained to be 9.4±0.9--23.2±8.1 and 25.5±1.1--33.3±4.7 nm. All composite presented lower porosity and surface area than

pure CNF. Especially, the CNF matrix that consisted of NiO nanostructures. The amorphous carbon was also observed in all the composites which was in agreement with pure CNF.

The electrochemical performance revealed that the existence of metallic Ni resulted in high specific capacitance of the electrode at operating scan rate above 10 mV s^{-1} due to the high conductivity of conductive nickel. However, the specific capacitance of electrode which consisted of NiO nanostructures became higher at low scan rate below 10 mV s^{-1} indicating that the contribution of EDLC from porous carbon matrix and pseudocapacitance from redox reactions between NiO and electrolyte. All composites also exhibited high cycling stability of capacity retention over 83 % after 1000 cycles.

5.3 AgO_x/CNF

The electrospun $\text{Ag}(\text{NO}_3)/\text{PAN}$ nanofibers was fabricated at the $\text{Ag}(\text{NO}_3)$ concentration of 20 wt.%. The uniform as-spun nanofibers had an average of 836 ± 108 nm and it was later reduced by heat treatment to be 643 ± 41 nm. By adding of the silver precursor, the main decomposition temperature of the as-spun sample was slightly shifted to the higher temperature of 310 °C comparing to pure PAN nanofibers. The composite sample consisted of metallic Ag nanoparticles with the average size of 13.5 ± 6.9 nm reinforced on an amorphous carbon matrix. Moreover, addition of Ag reinforcement led to higher porosity and specific surface area than that of the bare CNF. However, the addition of Ag nanoparticles did not improve the electrochemical

properties, such as specific capacitance, energy density, power density, and cycling capability of the electrode.

5.4 MnO_x/CNF

The electrospun of Ag(NO₃)/PAN nanofibers was fabricated at a Mn(NO₃)₂ concentration of 20 wt.%. The uniform as-spun nanofibers had an average of 381±13 nm and it was later reduced during calcination to be 323±12 nm. The entry of manganese reinforcement induced the decomposition temperature of the composite to low temperature of 281 °C. The MnO_x/CNF consisted of two main products carbon and MnO_x. The carbon matrix by dropping of decomposition temperature obtained as quiet different structure comparing to the other samples. The most carbon was formed as very high graphite structure and only this one that presented I_D/I_G less than 1 with the value of 0.98. A higher density and well-ordered of graphite structure resulted in low porosity and surface area of 119 m² g⁻¹. Secondly, the manganese reinforcement was mostly formed as cubic MnO with the average particle size of 33.1±6.9 nm.

Even the existence of MnO provided a high pseudocapacitance from redox with a high reaction rate, the total specific capacitance obtained just a small value comparing to the other composite nanofibers in this work. This is because the small surface area caused a very small EDLC. However, the capacitance became larger than AgO_x/CNF and MnO_x/CNF at very low scan rate below 5 mV s⁻¹. This is the appropriate region of bulk pseudocapacitive behavior.

5.5 AgO_x-MnO_x/CNF

The electrochemical results revealed that the electrochemical capacitance of carbon-based electrode can be enhanced by improving the specific surface area with CO₂ activation and also doping with transition metal oxide with a high redox activity, such as AgO_x, NiO_x, and MnO_x as presented in this work. Among all composites, the AgO_x-MnO_x/CNF exhibited the best electrochemical performance in terms of specific capacitance as high as 204 F g⁻¹ at a current density of 5 A g⁻¹, maximizing the energy density of 28 mW h g⁻¹ at a high power density of 250 mW g⁻¹. And it also retained the incredible cycling capability of more than 99% at 1000 cycles.

In addition, the different calcination temperature of AgO_x-MnO_x/CNF also effected on the electrochemical performance. Even the high temperature of 900 °C can result in a highest specific surface area of 812 m² g⁻¹, it does not support the high specific capacitance at low scan rate below 100 mV s⁻¹. Moreover, the electrochemical performance of different aqueous electrolytes of 3 M KOH, 3 M NaOH, 3 M LiOH, and 1.5 M Na₂SO₄ revealed that the alkaline KOH trendy presents a high capacitance value above mid scan rate above 10 mV s⁻¹ due to a high conductivity causing on faster double layer forming at the interface of the electrolyte and active material that resulted in high EDLC. In this case, the presence of numerous derivatives of oxygen ion in the electrolyte solution accelerates oxygen evolution resulting in a narrower working potential voltage windows causing a low energy density. The difference in KOH concentrations of 1.5, 3, and 6 M showed that the high concentration proper for fast process of EDLC at high scan rate above 200 mV s⁻¹ but it became negative effect when the scan rate was less than 2 mV s⁻¹.

5.6 Suggestion

Enhanced energy storage could be obtained by designing electrode materials as a combination of EDLC together with pseudocapacitance. In this thesis, the improvement on specific capacitance by introducing composite to a carbon matrix also results in high energy and power density during the electrochemical performance of the materials. However, the obtaining of both EDLC and pseudocapacitance by the heating process is still receptive for the other composites, and the carbon and metal oxide are achieved from the quiet different gas condition, no oxygen and oxygen rich, respectively. Therefore, designing proper composite materials for a hybrid system in large scale to apply in the commercial area is a very interesting research in next decades. Moreover, the development of new materials should be considered the important factors, such as cost, toxicity, light weight, lifetime etc. However, perhaps the super capacitor is insufficient for electric vehicle application unless it is developed in conjunction with batteries or fuel cells.



REFERENCES

มหาวิทยาลัยเทคโนโลยีสุรนารี

REFERENCES

- Al-Enizi, A. M., Elzatahry, A. A., Abdullah, A. M., AlMaadeed, M. A., Wang, J., Zhao, D. and Al-Deyab, S. (2014). Synthesis and electrochemical properties of nickel oxide/carbon nanofiber composites. **Carbon**. 71: 276-283.
- Al-Saleh, M. H. and Sundararaj, U. (2009). A review of vapor grown carbon nanofiber/polymer conductive composites. **Carbon**. 47(1): 2-22.
- Alarifi, I. M., Alharbi, A., Khan, W. S., Swindle, A. and Asmatulu, R. (2015). Thermal, electrical and surface hydrophobic properties of electrospun polyacrylonitrile nanofibers for structural health monitoring. **Materials**. 8(10): 7017-7031.
- Andrews, R., Jacques, D., Qian, D. and Dickey, E. (2001). Purification and structural annealing of multiwalled carbon nanotubes at graphitization temperatures. **Carbon**. 39(11): 1681-1687.
- Anton, F. (1934) Process and apparatus for preparing artificial threads. (pp. 1-4)Richard, Schreiber Gastell, Anton, Formhals, United States.
- Aryal, S., Kim, C. K., Kim, K.-W., Khil, M. S. and Kim, H. Y. (2008). Multi-walled carbon nanotubes/TiO₂ composite nanofiber by electrospinning. **Materials Science and Engineering: C**. 28(1): 75-79.
- Aussawasathien, D. and Sancaktar, E. (2008). Electrospun polyacrylonitrile-based carbon nanofibers and their silver modifications: surface morphologies and properties. **Current Nanoscience**. 4(2): 130-137.

- Barbieri, O., Hahn, M., Herzog, A. and Kötz, R. (2005). Capacitance limits of high surface area activated carbons for double layer capacitors. **Carbon**. 43(6): 1303-1310.
- Bauer, S., Biasi, L. d., Glatthaar, S., Toukam, L., Ge and Baumbach, T. (2015). In operando study of the high voltage spinel cathode material $\text{LiNi}_{0.5}\text{Mn}_{1.5}\text{O}_4$ using two dimensional full-field spectroscopic imaging of Ni and Mn. **Physical Chemistry Chemical Physics**. 17(25): 16388-16397.
- Beachley, V. and Wen, X. (2009). Effect of electrospinning parameters on the nanofiber diameter and length. **Materials Science and Engineering: C**. 29(3): 663-668.
- Beglou, M. and Haghi, A. (2008). Electrospun biodegradable and biocompatible natural nanofibers: a detailed review. **Cellulose Chemistry & Technology**. 42(9): 441.
- Béguin, F., Presser, V., Balducci, A. and Frackowiak, E. (2014). Carbons and electrolytes for advanced supercapacitors. **Advanced Materials**. 26(14): 2219-2251.
- Behrens, P., Assmann, S., Bilow, U., Linke, C. and Jansen, M. (1999). Electronic structure of silver oxides investigated by AgL XANES spectroscopy. **Zeitschrift für Anorganische und Allgemeine Chemie**. 625: 111-116.
- Belenkov, E. (2001). Formation of graphite structure in carbon crystallites. **Inorganic Materials**. 37(9): 928-934.
- Bosworth, L. and Downes, S. (2011). **Electrospinning for tissue regeneration**. Elsevier.

- Brock, S. L., Duan, N., Tian, Z. R., Giraldo, O., Zhou, H. and Suib, S. L. (1998). A review of porous manganese oxide materials. **Chemistry of Materials**. 10(10): 2619-2628.
- Cai, J., Xin, W., Liu, G., Lin, D. and Zhu, D. (2016). Effect of calcination temperature on structural properties and photocatalytic activity of Mn-C-codoped TiO₂. **Materials Research**. (AHEAD): 401-407.
- Chen, L., Guo, Z., Xia, Y. and Wang, Y. (2013). High-voltage aqueous battery approaching 3 V using an acidic–alkaline double electrolyte. **Chemical Communications**. 49(22): 2204-2206.
- Chen, X. H., Chen, C. S., Xiao, H. N., Cheng, F. Q., Zhang, G. and Yi, G. J. (2005). Corrosion behavior of carbon nanotubes–Ni composite coating. **Surface and Coatings Technology**. 191(2–3): 351-356.
- Chmiola, J., Largeot, C., Taberna, P. L., Simon, P. and Gogotsi, Y. (2008). Desolvation of Ions in Subnanometer Pores and Its Effect on Capacitance and Double-Layer Theory. **Angewandte Chemie**. 120(18): 3440-3443.
- Chronakis, I. S. (2005). Novel nanocomposites and nanoceramics based on polymer nanofibers using electrospinning process—A review. **Journal of Materials Processing Technology**. 167(2–3): 283-293.
- Chu, P. K. and Li, L. (2006). Characterization of amorphous and nanocrystalline carbon films. **Materials Chemistry and Physics**. 96(2): 253-277.
- Colindres, S. C., Aguir, K., Cervantes Sodi, F., Vargas, L. V., Salazar, J. A. M. and Febles, V. G. (2014). Ozone sensing based on palladium decorated carbon nanotubes. **Sensors**. 14(4): 6806-6818.

- Conway, B. and Gileadi, E. (1962). Kinetic theory of pseudo-capacitance and electrode reactions at appreciable surface coverage. **Transactions of the Faraday Society**. 58: 2493-2509.
- Conway, B. E. (2013). **Electrochemical supercapacitors: scientific fundamentals and technological applications**. New York, Springer Science & Business Media.
- Conway, B. E., Bockris, J. O. M. and Ammar, I. A. (1951). The dielectric constant of the solution in the diffuse and Helmholtz double layers at a charged interface in aqueous solution. **Transactions of the Faraday Society**. 47(0): 756-766.
- Crabtree, G. W. and Lewis, N. S. (2007). Solar energy conversion. **Physics today**. 60(3): 37-42.
- Dhakate, S. R., Gupta, A., Chaudhari, A., Tawale, J. and Mathur, R. B. (2011). Morphology and thermal properties of PAN copolymer based electrospun nanofibers. **Synthetic Metals**. 161(5-6): 411-419.
- Dzubiella, J. and Hansen, J.-P. (2005). Electric-field-controlled water and ion permeation of a hydrophobic nanopore. **The Journal of chemical physics**. 122(23): 234706.
- Endo, M., Nishimura, K., Kim, Y., Hakamada, K., Matushita, T., Dresselhaus, M. and Dresselhaus, G. (1999). Raman spectroscopic characterization of submicron vapor-grown carbon fibers and carbon nanofibers obtained by pyrolyzing hydrocarbons. **Journal of Materials Research**. 14(12): 4474-4477.
- Fleaca, C. T. and Le Normand, F. (2014). Ni-catalysed carbon nanotubes and nanofibers assemblies grown on TiN/Si(1 0 0) substrates using hot-filaments

- combined with d.c. plasma CVD. **Physica E: Low-dimensional Systems and Nanostructures**. 56: 435-440.
- Fleming, R., Pardini, L. C., Alves, N., Garcia, E. and Brito Júnior, C. (2014). Synthesis and thermal behavior of polyacrylonitrile/vinylidene chloride copolymer. **Polímeros**. 24(3): 259-268.
- Fréty, R., Santos, M. R., Sales, R. F., Silva, A. O., Barbosa, C. and Pacheco, J. G. (2014). Flash pyrolysis of oleic acid as a model compound adsorbed on supported nickel catalysts for biofuel production. **Journal of the Brazilian Chemical Society**. 25(12): 2433-2443.
- Fripp, H. (1876). On the limits of the optical capacity of the microscope. **The Monthly microscopical journal**. 16(1): 15-39.
- Fritsch, S., Sarrias, J., Brieu, M., Couderc, J. J., Baudour, J. L., Snoeck, E. and Rousset, A. (1998). Correlation between the structure, the microstructure and the electrical properties of nickel manganite negative temperature coefficient (NTC) thermistors. **Solid State Ionics**. 109(3-4): 229-237.
- Fujimoto, H., Mabuchi, A., Tokumitsu, K., Kasuh, T. and Akuzawa, N. (1994). Effect of crystallite size on the chemical compositions of the stage 1 alkali metal-graphite intercalation compounds. **Carbon**. 32(2): 193-198.
- Ghasemi, A. and Mousavinia, M. (2014). Structural and magnetic evaluation of substituted NiZnFe₂O₄ particles synthesized by conventional sol-gel method. **Ceramics International**. 40(2): 2825-2834.
- Girgis, B. S., Khalil, L. B. and Tawfik, T. A. (2002). Porosity development in carbons derived from olive oil mill residue under steam pyrolysis. **Journal of Porous Materials**. 9(2): 105-113.

- Gong, G. and Wu, J. (2012) **Novel Polyimide Materials Produced by Electrospinning**. In High Performance Polymers-Polyimides Based-From Chemistry to Applications, Intech, pp. 127.
- Gopalan, A. I., Santhosh, P., Manesh, K. M., Nho, J. H., Kim, S. H., Hwang, C.-G. and Lee, K.-P. (2008). Development of electrospun PVdF-PAN membrane-based polymer electrolytes for lithium batteries. **Journal of Membrane Science**. 325(2): 683-690.
- Gu, S. Y., Ren, J. and Vancso, G. J. (2005). Process optimization and empirical modeling for electrospun polyacrylonitrile (PAN) nanofiber precursor of carbon nanofibers. **European Polymer Journal**. 41(11): 2559-2568.
- Gu, S. Y., Ren, J. and Wu, Q. L. (2005). Preparation and structures of electrospun PAN nanofibers as a precursor of carbon nanofibers. **Synthetic Metals**. 155(1): 157-161.
- Gualous, H., Bouquain, D., Berthon, A. and Kauffmann, J. M. (2003). Experimental study of supercapacitor serial resistance and capacitance variations with temperature. **Journal of Power Sources**. 123(1): 86-93.
- Gubbins, K. E. (2009). Hysteresis Phenomena in Mesoporous Materials.
- Haider, A., Haider, S. and Kang, I.-K. (2015). A comprehensive review summarizing the effect of electrospinning parameters and potential applications of nanofibers in biomedical and biotechnology. **Arabian Journal of Chemistry**.
- Han, S. and Hyeon, T. (1999). Simple silica-particle template synthesis of mesoporous carbons. **Chemical Communications**. (19): 1955-1956.

- Hassan, S., Suzuki, M. and El-Moneim, A. A. (2012). Effect of Ag-Doping on the Capacitive Behavior of Amorphous Manganese Dioxide Electrodes. **Electrical and Electronic Engineering**. 2: 18-22.
- Huang, J., Sumpter, B. G. and Meunier, V. (2007). Theoretical model for nanoporous carbon supercapacitors. **Angewandte Chemie International Edition**. 47(3): 520-524.
- Huang, X. (2009). Fabrication and properties of carbon fibers. **Materials**. 2(4): 2369-2403.
- Huang, Z.-M., Zhang, Y.-Z., Kotaki, M. and Ramakrishna, S. (2003). A review on polymer nanofibers by electrospinning and their applications in nanocomposites. **Composites Science and Technology**. 63(15): 2223-2253.
- Inagaki, M., Kaneko, K. and Nishizawa, T. (2004). Nanocarbons—recent research in Japan. **Carbon**. 42(8): 1401-1417.
- Inagaki, M., Kang, F., Toyoda, M. and Konno, H. (2013). **Advanced materials science and engineering of carbon**. Oxford, Butterworth-Heinemann.
- Inagaki, M. and Radovic, L. R. (2002). Nanocarbons. **Carbon**. 40(12): 2279-2282.
- Jang, J., Bae, J., Choi, M. and Yoon, S.-H. (2005). Fabrication and characterization of polyaniline coated carbon nanofiber for supercapacitor. **Carbon**. 43(13): 2730-2736.
- Ji, L. and Zhang, X. (2009). Generation of activated carbon nanofibers from electrospun polyacrylonitrile-zinc chloride composites for use as anodes in lithium-ion batteries. **Electrochemistry Communications**. 11(3): 684-687.
- JINTAO, Z. (2012) Transition-Metal-Oxide-Based Nanostructures as Supercapacitor Electrodes. (Vol. A thesis submitted for the degree of doctor of phillosophy,

pp. Department of Chemical & Biomolecular Engineering, National University of Singapore.

- Ju, Y.-W., Choi, G.-R., Jung, H.-R. and Lee, W.-J. (2008). Electrochemical properties of electrospun PAN/MWCNT carbon nanofibers electrodes coated with polypyrrole. **Electrochimica Acta**. 53(19): 5796-5803.
- Jung, H.-R., Cho, S. J., Kim, K. N. and Lee, W.-J. (2011). Electrochemical properties of electrospun Cu_xO ($x = 1, 2$)-embedded carbon nanofiber with EXAFS analysis. **Electrochimica Acta**. 56(19): 6722-6731.
- Kalayci, V. E., Patra, P. K., Kim, Y. K., Ugbolue, S. C. and Warner, S. B. (2005). Charge consequences in electrospun polyacrylonitrile (PAN) nanofibers. **Polymer**. 46(18): 7191-7200.
- Kandalkar, S. G., Dhawale, D. S., Kim, C.-K. and Lokhande, C. D. (2010). Chemical synthesis of cobalt oxide thin film electrode for supercapacitor application. **Synthetic Metals**. 160(11–12): 1299-1302.
- Katepalli, H., Bikshapathi, M., Sharma, C. S., Verma, N. and Sharma, A. (2011). Synthesis of hierarchical fabrics by electrospinning of PAN nanofibers on activated carbon microfibers for environmental remediation applications. **Chemical Engineering Journal**. 171(3): 1194-1200.
- Keiser, H., Beccu, K. D. and Gutjahr, M. A. (1976). Abschätzung der porenstruktur poröser elektroden aus impedanzmessungen. **Electrochimica Acta**. 21(8): 539-543.
- Kidkhunthod, P., Nilmoung, S., Mahakot, S., Rodporn, S., Phumying, S. and Maensiri, S. (2016). A structural study and magnetic properties of electrospun

- carbon/manganese ferrite (C/MnFe₂O₄) composite nanofibers. **Journal of Magnetism and Magnetic Materials**. 401: 436-442.
- Kim, B.-H., Kim, C. H., Yang, K. S., Rahy, A. and Yang, D. J. (2012). Electrospun vanadium pentoxide/carbon nanofiber composites for supercapacitor electrodes. **Electrochimica Acta**. 83: 335-340.
- Kim, B.-H., Yang, K. S., Kim, Y. A., Kim, Y. J., An, B. and Oshida, K. (2011). Solvent-induced porosity control of carbon nanofiber webs for supercapacitor. **Journal of Power Sources**. 196(23): 10496-10501.
- Kim, B.-H., Yang, K. S. and Woo, H.-G. (2011). Thin, bendable electrodes consisting of porous carbon nanofibers via the electrospinning of polyacrylonitrile containing tetraethoxy orthosilicate for supercapacitor. **Electrochemistry Communications**. 13(10): 1042-1046.
- Kim, B.-H., Yang, K. S., Woo, H.-G. and Oshida, K. (2011). Supercapacitor performance of porous carbon nanofiber composites prepared by electrospinning polymethylhydrosiloxane (PMHS)/polyacrylonitrile (PAN) blend solutions. **Synthetic Metals**. 161(13-14): 1211-1216.
- Kim, B.-H., Yang, K. S. and Yang, D. J. (2013). Electrochemical behavior of activated carbon nanofiber-vanadium pentoxide composites for double-layer capacitors. **Electrochimica Acta**. 109: 859-865.
- Kim, B. H., Bui, N. N., Yang, K. S., dela Cruz, M. E. D. and Ferraris, J. P. (2009). Electrochemical properties of activated polyacrylonitrile/pitch carbon fibers produced using electrospinning. **Bulletin of the Korean Chemical Society**. 30(9): 1967-1972.

- Kim, C., Park, S.-H., Lee, W.-J. and Yang, K.-S. (2004). Characteristics of supercapacitor electrodes of PBI-based carbon nanofiber web prepared by electrospinning. **Electrochimica Acta**. 50(2–3): 877-881.
- Kim, C. and Yang, K. (2003). Electrochemical properties of carbon nanofiber web as an electrode for supercapacitor prepared by electrospinning. **Applied Physics Letters**. 83(6): 1216-1218.
- Kim, J.-H., Jeong, E. and Lee, Y.-S. (2015). Preparation and characterization of graphite foams. **Journal of Industrial and Engineering Chemistry**. 32: 21-33.
- Kim, S. Y., Kim, B.-H. and Yang, K. S. (2013). Preparation and electrochemical characteristics of a polyvinylpyrrolidone-stabilized Si/carbon composite nanofiber anode for a lithium ion battery. **Journal of Electroanalytical Chemistry**. 705: 52-56.
- Kim, S. Y., Kim, B.-H., Yang, K. S. and Oshida, K. (2012). Supercapacitive properties of porous carbon nanofibers via the electrospinning of metal alkoxide-graphene in polyacrylonitrile. **Materials Letters**. 87: 157-161.
- Knight, D. S. and White, W. B. (1989). Characterization of diamond films by Raman spectroscopy. **Journal of Materials Research**. 4(2): 385-393.
- Kötz, R. and Carlen, M. (2000). Principles and applications of electrochemical capacitors. **Electrochimica Acta**. 45(15–16): 2483-2498.
- Laforgue, A. (2011). All-textile flexible supercapacitors using electrospun poly(3,4-ethylenedioxythiophene) nanofibers. **Journal of Power Sources**. 196(1): 559-564.

- Laforgue, A., Simon, P., Sarrazin, C. and Fauvarque, J.-F. (1999). Polythiophene-based supercapacitors. **Journal of Power Sources**. 80(1): 142-148.
- Lai, C.-C. and Lo, C.-T. (2015). Effect of Temperature on Morphology and Electrochemical Capacitive Properties of Electrospun Carbon Nanofibers and Nickel Hydroxide Composites. **Electrochimica Acta**. 174: 806-814.
- Lai, F., Huang, Y., Miao, Y.-E. and Liu, T. (2015). Controllable preparation of multi-dimensional hybrid materials of nickel-cobalt layered double hydroxide nanorods/nanosheets on electrospun carbon nanofibers for high-performance supercapacitors. **Electrochimica Acta**. 174: 456-463.
- Lang, X., Hirata, A., Fujita, T. and Chen, M. (2011). Nanoporous metal/oxide hybrid electrodes for electrochemical supercapacitors. **Nat Nano**. 6(4): 232-236.
- Lee, B.-S., Son, S.-B., Park, K.-M., Seo, J.-H., Lee, S.-H., Choi, I.-S., Oh, K.-H. and Yu, W.-R. (2012). Fabrication of Si core/C shell nanofibers and their electrochemical performances as a lithium-ion battery anode. **Journal of Power Sources**. 206: 267-273.
- Lee, E., Lee, T. and Kim, B.-S. (2014). Electrospun nanofiber of hybrid manganese oxides for supercapacitor: Relevance to mixed inorganic interfaces. **Journal of Power Sources**. 255: 335-340.
- Lee, H.-M., Kim, H.-G., Kang, S.-J., Park, S.-J., An, K.-H. and Kim, B.-J. (2014). Effects of pore structures on electrochemical behaviors of polyacrylonitrile (PAN)-based activated carbon nanofibers. **Journal of Industrial and Engineering Chemistry**. 25: 736-740.
- Lee, K. J., Shiratori, N., Lee, G. H., Miyawaki, J., Mochida, I., Yoon, S.-H. and Jang, J. (2010). Activated carbon nanofiber produced from electrospun

polyacrylonitrile nanofiber as a highly efficient formaldehyde adsorbent.

Carbon. 48(15): 4248-4255.

Leofanti, G., Padovan, M., Tozzola, G. and Venturelli, B. (1998). Surface area and pore texture of catalysts. **Catalysis Today.** 41(1): 207-219.

Li, D., Pang, Z., Chen, X., Luo, L., Cai, Y. and Wei, Q. (2014). A catechol biosensor based on electrospun carbon nanofibers. **Beilstein Journal of Nanotechnology.** 5(1): 346-354.

Li, J., Yang, Q. M. and Zhitomirsky, I. (2008). Nickel foam-based manganese dioxide-carbon nanotube composite electrodes for electrochemical supercapacitors. **Journal of Power Sources.** 185(2): 1569-1574.

Li, J. and Zhitomirsky, I. (2009). Electrophoretic deposition of manganese dioxide-carbon nanotube composites. **Journal of Materials Processing Technology.** 209(7): 3452-3459.

Li, X., Hao, X., Yu, H. and Na, H. (2008). Fabrication of Polyacrylonitrile/polypyrrole (PAN/Ppy) composite nanofibres and nanospheres with core-shell structures by electrospinning. **Materials Letters.** 62(8-9): 1155-1158.

Li, Z. and Wang, C. (2013) **Effects of working parameters on electrospinning.** In *One-Dimensional Nanostructures*, Springer, Berlin, pp. 15-28.

Lin, F., Markus, I. M., Nordlund, D., Weng, T.-C., Asta, M. D., Xin, H. L. and Doeff, M. M. (2014). Surface reconstruction and chemical evolution of stoichiometric layered cathode materials for lithium-ion batteries. **Nature communications.** 5.

- Lisunova, M., Hildmann, A., Hatting, B., Datsyuk, V. and Reich, S. (2010). Nanofibres of CA/PAN with high amount of carbon nanotubes by core-shell electrospinning. **Composites Science and Technology**. 70(11): 1584-1588.
- Liu, J., Chen, G., Gao, H., Zhang, L., Ma, S., Liang, J. and Fong, H. (2012). Structure and thermo-chemical properties of continuous bundles of aligned and stretched electrospun polyacrylonitrile precursor nanofibers collected in a flowing water bath. **Carbon**. 50(3): 1262-1270.
- Liu, J., Zhou, P., Zhang, L., Ma, Z., Liang, J. and Fong, H. (2009). Thermo-chemical reactions occurring during the oxidative stabilization of electrospun polyacrylonitrile precursor nanofibers and the resulting structural conversions. **Carbon**. 47(4): 1087-1095.
- Liu, Y. and Zhang, X. (2009). Effect of calcination temperature on the morphology and electrochemical properties of Co_3O_4 for lithium-ion battery. **Electrochimica Acta**. 54(17): 4180-4185.
- Lu, M., Beguin, F. and Frackowiak, E. (2013). **Supercapacitors: Materials, Systems and Applications**. Weinheim, Germany, John Wiley & Sons.
- Maensiri, S., Nuansing, W., Klinkaewnarong, J., Laokul, P. and Khemprasit, J. (2006). Nanofibers of barium strontium titanate (BST) by sol-gel processing and electrospinning. **Journal of Colloid and Interface Science**. 297(2): 578-583.
- Magyari-Köpe, B., Park, S. G., Lee, H.-D. and Nishi, Y. (2012). First principles calculations of oxygen vacancy-ordering effects in resistance change memory materials incorporating binary transition metal oxides. **Journal of Materials Science**. 47(21): 7498-7514.

- Manickam, S. S., Karra, U., Huang, L., Bui, N.-N., Li, B. and McCutcheon, J. R. (2013). Activated carbon nanofiber anodes for microbial fuel cells. **Carbon**. 53: 19-28.
- Martinez, J. G., Otero, T. F. and Jager, E. W. (2014). Effect of the electrolyte concentration and substrate on conducting polymer actuators. **Langmuir**. 30(13): 3894-3904.
- Mayer, B., Boyer, E. W., Goodale, C., Jaworski, N. A., Van Breemen, N., Howarth, R. W., Seitzinger, S., Billen, G., Lajtha, K. and Nadelhoffer, K. (2002). Sources of nitrate in rivers draining sixteen watersheds in the northeastern US: Isotopic constraints. **Biogeochemistry**. 57(1): 171-197.
- Mefford, J. T., Hardin, W. G., Dai, S., Johnston, K. P. and Stevenson, K. J. (2014). Anion charge storage through oxygen intercalation in LaMnO₃ perovskite pseudocapacitor electrodes. **Nat Mater**. 13(7): 726-732.
- Mi, H., Zhang, X., Ye, X. and Yang, S. (2008). Preparation and enhanced capacitance of core-shell polypyrrole/polyaniline composite electrode for supercapacitors. **Journal of Power Sources**. 176(1): 403-409.
- Miao, F., Shao, C., Li, X., Zhang, Y., Lu, N., Wang, K. and Liu, Y. (2014). One-dimensional heterostructures of beta-nickel hydroxide nanoplates/electrospun carbon nanofibers: Controlled fabrication and high capacitive property. **International Journal of Hydrogen Energy**. 39(28): 16162-16170.
- Min, B.-M., Lee, G., Kim, S. H., Nam, Y. S., Lee, T. S. and Park, W. H. (2004). Electrospinning of silk fibroin nanofibers and its effect on the adhesion and spreading of normal human keratinocytes and fibroblasts in vitro. **Biomaterials**. 25(7-8): 1289-1297.

- Nataraj, S. K., Kim, B. H., Yun, J. H., Lee, D. H., Aminabhavi, T. M. and Yang, K. S. (2009). Effect of added nickel nitrate on the physical, thermal and morphological characteristics of polyacrylonitrile-based carbon nanofibers. **Materials Science and Engineering: B**. 162(2): 75-81.
- Nataraj, S. K., Yang, K. S. and Aminabhavi, T. M. (2012). Polyacrylonitrile-based nanofibers—A state-of-the-art review. **Progress in Polymer Science**. 37(3): 487-513.
- Nohman, A. K. H., Ismail, H. M. and Hussein, G. A. M. (1995). Thermal and chemical events in the decomposition course of manganese compounds. **Journal of Analytical and Applied Pyrolysis**. 34(2): 265-278.
- Ohzuku, T. and Ueda, A. (1994). Why transition metal (di) oxides are the most attractive materials for batteries. **Solid State Ionics**. 69(3-4): 201-211.
- Palmer, L., Cunliffe, A. and Hough, J. (1952). Dielectric constant of water films.
- Pandolfo, A. G. and Hollenkamp, A. F. (2006). Carbon properties and their role in supercapacitors. **Journal of Power Sources**. 157(1): 11-27.
- Pang, S. C., Anderson, M. A. and Chapman, T. W. (2000). Novel electrode materials for thin-film ultracapacitors: comparison of electrochemical properties of sol-gel-derived and electrodeposited manganese dioxide. **Journal of the Electrochemical Society**. 147(2): 444-450.
- Park, S.-J., Park, S. and Kim, S. (2012). Preparation and capacitance behaviors of cobalt oxide/graphene composites. **Carbon Letters**. 13(2): 130-132.
- Peng, Y., Chen, Z., Wen, J., Xiao, Q., Weng, D., He, S., Geng, H. and Lu, Y. (2010). Hierarchical manganese oxide/carbon nanocomposites for supercapacitor electrodes. **Nano Research**. 4(2): 216-225.

- Pimenta, M. A., Dresselhaus, G., Dresselhaus, M. S., Cancado, L. G., Jorio, A. and Saito, R. (2007). Studying disorder in graphite-based systems by Raman spectroscopy. **Physical Chemistry Chemical Physics**. 9(11): 1276-1290.
- Prahsarn, C., Klinsukhon, W. and Roungpaisan, N. (2011). Electrospinning of PAN/DMF/H₂O containing TiO₂ and photocatalytic activity of their webs. **Materials Letters**. 65(15–16): 2498-2501.
- Preisler, E. (1980). Moderne verfahren der großchemie: braunstein. **Chemie in unserer Zeit**. 14(5): 137-148.
- Qing, R. and Sigmund, W. (2014). Morphological and crystallite size impact on electrochemical performance of electrospun rutile and rutile/multiwall carbon nanotube nanofibers for lithium ion batteries. **Ceramics International**. 40(4): 5665-5669.
- Ra, E. J., Raymundo-Piñero, E., Lee, Y. H. and Béguin, F. (2009). High power supercapacitors using polyacrylonitrile-based carbon nanofiber paper. **Carbon**. 47(13): 2984-2992.
- Rajzer, I., Kwiatkowski, R., Piekarczyk, W., Biniś, W. and Janicki, J. (2012). Carbon nanofibers produced from modified electrospun PAN/hydroxyapatite precursors as scaffolds for bone tissue engineering. **Materials Science and Engineering: C**. 32(8): 2562-2569.
- Ren, B., Fan, M., Liu, Q., Wang, J., Song, D. and Bai, X. (2013). Hollow NiO nanofibers modified by citric acid and the performances as supercapacitor electrode. **Electrochimica Acta**. 92: 197-204.
- Robinson, D. M., Go, Y. B., Mui, M., Gardner, G., Zhang, Z., Mastrogiovanni, D., Garfunkel, E., Li, J., Greenblatt, M. and Dismukes, G. C. (2013).

- Photochemical water oxidation by crystalline polymorphs of manganese oxides: Structural requirements for catalysis. **Journal of the American Chemical Society**. 135(9): 3494-3501.
- San Miguel, G., Fowler, G. D. and Sollars, C. J. (2003). A study of the characteristics of activated carbons produced by steam and carbon dioxide activation of waste tyre rubber. **Carbon**. 41(5): 1009-1016.
- Sarlak, N., Nejad, M. A. F., Shakhesi, S. and Shabani, K. (2012). Effects of electrospinning parameters on titanium dioxide nanofibers diameter and morphology: An investigation by Box–Wilson central composite design (CCD). **Chemical Engineering Journal**. 210: 410-416.
- Seghioer, A., Chevalet, J., Barhoun, A. and Lantelme, F. (1998). Electrochemical oxidation of nickel in alkaline solutions: a voltammetric study and modelling. **Journal of Electroanalytical Chemistry**. 442(1–2): 113-123.
- Sharma, P. and Bhatti, T. S. (2010). A review on electrochemical double-layer capacitors. **Energy Conversion and Management**. 51(12): 2901-2912.
- Shi, Y., Li, Y., Zhang, J., Yu, Z. and Yang, D. (2015). Electrospun polyacrylonitrile nanofibers loaded with silver nanoparticles by silver mirror reaction. **Materials Science and Engineering: C**. 51: 346-355.
- Shukla, A. K., Banerjee, A., Ravikumar, M. K. and Jalajakshi, A. (2012). Electrochemical capacitors: Technical challenges and prognosis for future markets. **Electrochimica Acta**. 84: 165-173.
- Simon, F., Jacobasch, H.-J. and Spange, S. (1998). The versatile surface properties of poly (cyclopentadiene)-modified silica particles (PCPD–silica): XPS and electrokinetic studies. **Colloid and Polymer Science**. 276(10): 930-939.

- Singh, P., Mondal, K. and Sharma, A. (2013). Reusable electrospun mesoporous ZnO nanofiber mats for photocatalytic degradation of polycyclic aromatic hydrocarbon dyes in wastewater. **J Colloid Interface Sci.** 394: 208-215.
- Song, M., Jin, B., Xiao, R., Yang, L., Wu, Y., Zhong, Z. and Huang, Y. (2013). The comparison of two activation techniques to prepare activated carbon from corn cob. **Biomass and Bioenergy.** 48: 250-256.
- Stojek, Z. (2010) **The electrical double layer and its structure.** In Electroanalytical methods, Springer, Berlin, pp. 3-9.
- Stoller, M. D. and Ruoff, R. S. (2010). Best practice methods for determining an electrode material's performance for ultracapacitors. **Energy & Environmental Science.** 3(9): 1294-1301.
- Subramania, A. and Devi, S. L. (2008). Polyaniline nanofibers by surfactant-assisted dilute polymerization for supercapacitor applications. **Polymers for Advanced Technologies.** 19(7): 725-727.
- Tanimura, A., Kovalenko, A. and Hirata, F. (2003). Molecular theory of an electrochemical double layer in a nanoporous carbon supercapacitor. **Chemical Physics Letters.** 378(5-6): 638-646.
- Tavanai, H., Jalili, R. and Morshed, M. (2009). Effects of fiber diameter and CO₂ activation temperature on the pore characteristics of polyacrylonitrile based activated carbon nanofibers. **Surface and Interface Analysis.** 41(10): 814-819.
- Tekmen, C., Tsunekawa, Y. and Nakanishi, H. (2010). Electrospinning of carbon nanofiber supported Fe/Co/Ni ternary alloy nanoparticles. **Journal of Materials Processing Technology.** 210(3): 451-455.

- Terasawa, N. and Takeuchi, I. (2013). Electrochemical and electromechanical properties of high-performance polymer actuators containing vapor grown carbon nanofiber and metal oxide. **Sensors and Actuators B: Chemical**. 176: 1065-1073.
- Teschke, O. and De Souza, E. (1999). Dielectric exchange: The key repulsive or attractive transient forces between atomic force microscope tips and charged surfaces. **Applied Physics Letters**. 74(12): 1755-1757.
- Thakur, D. B., Tiggehaar, R. M., Gardeniers, J. G. E., Lefferts, L. and Seshan, K. (2009). Growth of carbon nanofiber coatings on nickel thin films on fused silica by catalytic thermal chemical vapor deposition: On the use of titanium, titanium–tungsten and tantalum as adhesion layers. **Surface and Coatings Technology**. 203(22): 3435-3441.
- Ud Din, I., Shaharun, M. S., Subbarao, D. and Naeem, A. (2015). Synthesis, characterization and activity pattern of carbon nanofibers based copper/zirconia catalysts for carbon dioxide hydrogenation to methanol: Influence of calcination temperature. **Journal of Power Sources**. 274: 619-628.
- Wang, D. S., Xie, T., Peng, Q., Zhang, S. Y., Chen, J. and Li, Y. D. (2008). Direct thermal decomposition of metal nitrates in octadecylamine to metal oxide nanocrystals. **Chemistry–A European Journal**. 14(8): 2507-2513.
- Wang, J.-G., Yang, Y., Huang, Z.-H. and Kang, F. (2013). Effect of temperature on the pseudo-capacitive behavior of freestanding MnO₂@carbon nanofibers composites electrodes in mild electrolyte. **Journal of Power Sources**. 224: 86-92.

- Wang, J.-G., Yang, Y., Huang, Z.-H. and Kang, F. (2015). MnO-carbon hybrid nanofiber composites as superior anode materials for lithium-ion batteries. **Electrochimica Acta**. 170: 164-170.
- Wang, J.-G., Zhang, C., Jin, D., Xie, K. and Wei, B. (2015). Synthesis of ultralong MnO/C coaxial nanowires as freestanding anodes for high-performance lithium ion batteries. **Journal of Materials Chemistry A**. 3(26): 13699-13705.
- Wang, S., Bai, J., Li, C. and Zhang, J. (2012). Functionalization of electrospun β -cyclodextrin/polyacrylonitrile (PAN) with silver nanoparticles: Broad-spectrum antibacterial property. **Applied Surface Science**. 261(0): 499-503.
- Wang, T., Song, D., Zhao, H., Chen, J., Zhao, C., Chen, L., Chen, W., Zhou, J. and Xie, E. (2015). Facilitated transport channels in carbon nanotube/carbon nanofiber hierarchical composites decorated with manganese dioxide for flexible supercapacitors. **Journal of Power Sources**. 274: 709-717.
- Wang, Y., Song, Y. and Xia, Y. (2016). Electrochemical capacitors: mechanism, materials, systems, characterization and applications. **Chemical Society Reviews**. 45(21): 5925-5950.
- Wei, W., Cui, X., Chen, W. and Ivey, D. G. (2011). Manganese oxide-based materials as electrochemical supercapacitor electrodes. **Chemical Society Reviews**. 40(3): 1697-1721.
- Wu, M.-S., Huang, C.-Y. and Jow, J.-J. (2009). Electrophoretic deposition of network-like carbon nanofiber as a conducting substrate for nanostructured nickel oxide electrode. **Electrochemistry Communications**. 11(4): 779-782.

- Wu, M.-S., Lin, Y.-P., Lin, C.-H. and Lee, J.-T. (2012). Formation of nano-scaled crevices and spacers in NiO-attached graphene oxide nanosheets for supercapacitors. **Journal of Materials Chemistry**. 22(6): 2442.
- Xiang, J., Shen, X., Song, F., Liu, M., Zhou, G. and Chu, Y. (2011). Fabrication and characterization of Fe–Ni alloy/nickel ferrite composite nanofibers by electrospinning and partial reduction. **Materials Research Bulletin**. 46(2): 258-261.
- Xing, Y., Fang, B., Bonakdarpour, A., Zhang, S. and Wilkinson, D. P. (2014). Facile fabrication of mesoporous carbon nanofibers with unique hierarchical nanoarchitecture for electrochemical hydrogen storage. **International Journal of Hydrogen Energy**. 39(15): 7859-7867.
- Xu, J., Donohoe, J. P. and Pittman Jr, C. U. (2004). Preparation, electrical and mechanical properties of vapor grown carbon fiber (VGCF)/vinyl ester composites. **Composites Part A: Applied Science and Manufacturing**. 35(6): 693-701.
- Xu, Z.-L., Zhang, B., Zhou, Z.-Q., Abouali, S., Akbari Garakani, M., Huang, J., Huang, J.-Q. and Kim, J.-K. (2014). Carbon nanofibers containing Si nanoparticles and graphene-covered Ni for high performance anodes in Li ion batteries. **RSC Advances**. 4(43): 22359-22366.
- Yan, H., Mahanta, N. K., Wang, B., Wang, S., Abramson, A. R. and Cakmak, M. (2014). Structural evolution in graphitization of nanofibers and mats from electrospun polyimide–mesophase pitch blends. **Carbon**. 71: 303-318.
- Yang, C., Zhou, M. and Xu, Q. (2013). Three-dimensional ordered macroporous MnO₂/carbon nanocomposites as high-performance electrodes for asymmetric

- supercapacitors. **Physical Chemistry Chemical Physics**. 15(45): 19730-19740.
- Yang, H., Gao, P. F., Wu, W. B., Yang, X. X., Zeng, Q. L., Li, C. and Huang, C. Z. (2014). Antibacterials loaded electrospun composite nanofibers: release profile and sustained antibacterial efficacy. **Polymer Chemistry**. 5(6): 1965-1975.
- Yang, Q. B., Li, D. M., Hong, Y. L., Li, Z. Y., Wang, C., Qiu, S. L. and Wei, Y. (2003). Preparation and characterization of PAN nanofiber containing Ag nanoparticles via electrospinning. **Synthetic Metals**. 137(1-3): 973-974.
- Yang, Y., Jia, Z., Liu, J., Li, Q., Hou, L., Wang, L. and Guan, Z. (2008). Effect of electric field distribution uniformity on electrospinning. **Journal of Applied Physics**. 103(10): 104307.
- Yano, M., Suzuki, S., Miyayama, M. and Ohgaki, M. (2013). Effects of Microstructure on Electrode Properties of Nanosheet-Derived $H_x(Ni_{1/3}Co_{1/3}Mn_{1/3})O_2$ for Electrochemical Capacitors. **Nanomaterials**. 3(2): 204-220.
- Yarin, A., Koombhongse, S. and Reneker, D. (2001). Taylor cone and jetting from liquid droplets in electrospinning of nanofibers. **Journal of Applied Physics**. 90(9): 4836-4846.
- Ye, S., Feng, J. and Wu, P. (2013). Deposition of three-dimensional graphene aerogel on nickel foam as a binder-free supercapacitor electrode. **ACS Applied Materials & Interfaces**. 5(15): 7122-7129.
- Yoon, S. H., Lim, S., Song, Y., Ota, Y., Qiao, W., Tanaka, A. and Mochida, I. (2004). KOH activation of carbon nanofibers. **Carbon**. 42(8): 1723-1729.

- Yu, H., Guo, J., Zhu, S., Li, Y., Zhang, Q. and Zhu, M. (2012). Preparation of continuous alumina nanofibers via electrospinning of PAN/DMF solution. **Materials Letters**. 74: 247-249.
- Yu, X., Xiang, H., Long, Y., Zhao, N., Zhang, X. and Xu, J. (2010). Preparation of porous polyacrylonitrile fibers by electrospinning a ternary system of PAN/DMF/H₂O. **Materials Letters**. 64(22): 2407-2409.
- Yuan, A. and Zhang, Q. (2006). A novel hybrid manganese dioxide/activated carbon supercapacitor using lithium hydroxide electrolyte. **Electrochemistry Communications**. 8(7): 1173-1178.
- Zeng, L., Wei, X., Wang, J., Jiang, Y., Li, W. and Yu, Y. (2015). Flexible one-dimensional carbon-selenium composite nanofibers with superior electrochemical performance for Li-Se/Na-Se batteries. **Journal of Power Sources**. 281: 461-469.
- Zhang, C., Liu, Q., Zhan, N., Yang, Q., Song, Y., Sun, L., Wang, H. and Li, Y. (2010). A novel approach to prepare silver chloride nanoparticles grown on the surface of PAN nanofibre via electrospinning combined with gas-solid reaction. **Colloids and Surfaces A: Physicochemical and Engineering Aspects**. 353(1): 64-68.
- Zhang, L. and Hsieh, Y.-L. (2009). Carbon nanofibers with nanoporosity and hollow channels from binary polyacrylonitrile systems. **European Polymer Journal**. 45(1): 47-56.
- Zhang, L. L. and Zhao, X. (2009). Carbon-based materials as supercapacitor electrodes. **Chemical Society Reviews**. 38(9): 2520-2531.

- Zhang, W. and Li, M. (2005). DSC study on the polyacrylonitrile precursors for carbon fibers. **Journal of Materials Science and Technology-Shenyang**. 21(4): 581.
- Zhang, X., Wang, X., Jiang, L., Wu, H., Wu, C. and Su, J. (2012). Effect of aqueous electrolytes on the electrochemical behaviors of supercapacitors based on hierarchically porous carbons. **Journal of Power Sources**. 216: 290-296.
- Zhang, Y., Feng, H., Wu, X., Wang, L., Zhang, A., Xia, T., Dong, H., Li, X. and Zhang, L. (2009). Progress of electrochemical capacitor electrode materials: A review. **International Journal of Hydrogen Energy**. 34(11): 4889-4899.
- Zhao, L., Qiu, Y., Yu, J., Deng, X., Dai, C. and Bai, X. (2013). Carbon nanofibers with radially grown graphene sheets derived from electrospinning for aqueous supercapacitors with high working voltage and energy density. **Nanoscale**. 5(11): 4902-4909.
- Zhao, X., Lv, L., Pan, B., Zhang, W., Zhang, S. and Zhang, Q. (2011). Polymer-supported nanocomposites for environmental application: A review. **Chemical Engineering Journal**. 170(2-3): 381-394.
- Zhi, M., Manivannan, A., Meng, F. and Wu, N. (2012). Highly conductive electrospun carbon nanofiber/MnO₂ coaxial nano-cables for high energy and power density supercapacitors. **Journal of Power Sources**. 208: 345-353.
- Zhi, M., Xiang, C., Li, J., Li, M. and Wu, N. (2013). Nanostructured carbon-metal oxide composite electrodes for supercapacitors: a review. **Nanoscale**. 5(1): 72-88.
- Zhong, C., Deng, Y., Hu, W., Sun, D., Han, X., Qiao, J. and Zhang, J. (2016). **Electrolytes for Electrochemical Supercapacitors**. Florida, CRC Press.

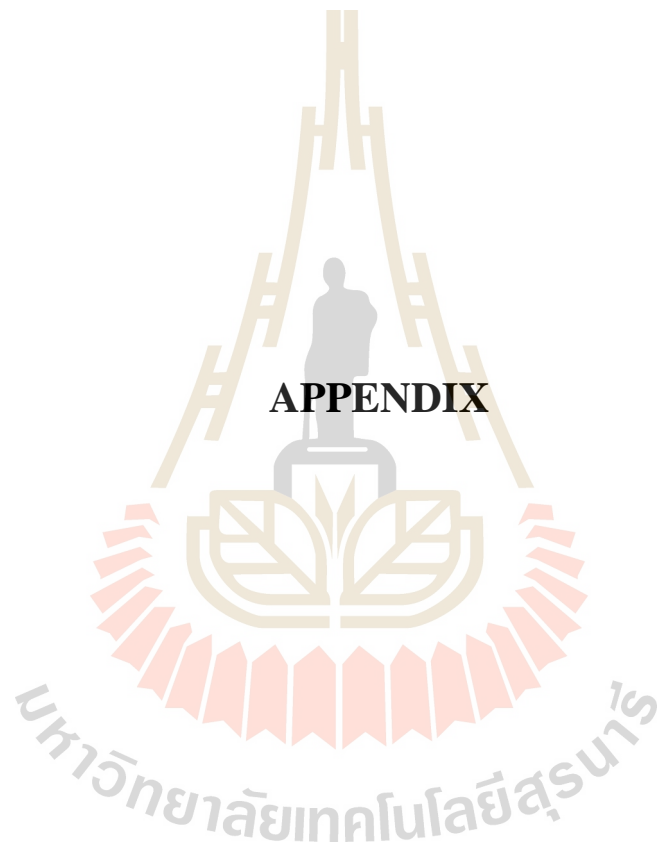
Zhou, T., Mo, S., Zhou, S., Zou, W., Liu, Y. and Yuan, D. (2011). Mn₃O₄/worm-like mesoporous carbon synthesized via a microwave method for supercapacitors.

Journal of Materials Science. 46(10): 3337-3342.

Zussman, E., Chen, X., Ding, W., Calabri, L., Dikin, D. A., Quintana, J. P. and Ruoff, R. S. (2005). Mechanical and structural characterization of electrospun PAN-derived carbon nanofibers. **Carbon.** 43(10): 2175-2185.



APPENDIX



APPENDIX A

PUBLICATION AND PRESENTATION

A.1 List of publication

Sinprachim, T., Phumying, S. and Maensiri, S. (2016). Electrochemical energy storage performance of electrospun AgOx-MnOx/CNF composites. **Journal of Alloys and Compounds**. 677: 1-11.

A.2 List of oral presentations

Sinprachim, T. and Maensiri, S. (2014). Fabrication, characterization, and electrochemical properties of electrospun Ag-Mn_xO_y/CNFs composite nanofibers. In **The 27th International Microprocesses and Nanotechnology Conference (MNC 2014)**. Fukuoka, Japan.

Sinprachim, T. and Maensiri, S. (2014). Fabrication, characterization and supercapacitor behavior of electrospun Ag-Mn_xO_y/CNFs composite nanofibers. In **The 4th Thailand International Nanotechnology Conference (Nano Thailand 2014)**. Thailand Science Park, Pathumthani, Thailand.

Sinprachim, T. and Maensiri, S. (2015). Silver and Manganese Oxide Clusters Embedded Electrospun Carbon Nanofiber for High Performance Supercapacitor. In **The 41st Congress on Science and Technology of Thailand (STT41)**. Nakhon Ratchasima, Thailand.

A.3 List of poster presentations

Sinprachim, T. and Maensiri, S. (2013). Fabrication and Characterization of Ni-NiO/Carbon Composite Nanofibers for Energy Storage Application. In **The 26th International Microprocesses and Nanotechnology Conference (MNC 2013)**. Hokkaido, Japan.

Sinprachim, T. and Maensiri, S. (2013). In **The 3rd Academic Conference on Natural Science of Masterand PhD. Students from ASEAN countries (CASEAN-2013)**. Phnom Penh, Cambodia.



CURRICULUM VITAE

Name Mr. Tanayt Sinprachim

Date of Birth December 4, 1974

Place of Birth 44 Moo 2, Tambol Bangsak, Kantang District, Trang, 92110, Thailand.

Education

1992-1996 Prince of Songkla University, Pattani, Thailand.
B.S. in Education(Physics)

1999-2003 Prince of Songkla University, Songkla, Thailand.
M.Sc. in Physics

2011-2016 Suranaree University of Technology, Nakhon Ratchasima, Thailand.
Ph.D. in Physics

Position and Place of Work

University Lecturer
Department of Physical Science, Faculty of Science and Fisheries Technology,
Rajamangala University of Technology Srivijaya, Trang, Thailand.